First-principles Theoretical Prediction and Analysis of Materials with Nontrivial Electronic Topology

A Thesis

Submitted For the Degree of

DOCTOR OF PHILOSOPHY

in the Faculty of Science

by

Koushik Pal

CHEMISTRY AND PHYSICS OF MATERIALS UNIT
JAWAHARLAL NEHRU CENTRE FOR ADVANCED SCIENTIFIC RESEARCH
Bangalore – 560 064

AUGUST 2017

To my parents

DECLARATION

I hereby declare that the matter embodied in the thesis entitled "**First-principles Theoretical Prediction and Analysis of Materials with Nontrivial Electronic Topology**" is the result of investigations carried out by me at the Chemistry and Physics of Materials Unit, Jawaharlal Nehru Centre for Advanced Scientific Research, Bangalore, India under the supervision of Prof. Umesh V. Waghmare and that it has not been submitted elsewhere for the award of any degree or diploma.

In keeping with the general practice in reporting scientific observations, due acknowledgement has been made whenever the work described is based on the findings of other investigators.

Koushik Pal

CERTIFICATE

I hereby certify that the matter embodied in this thesis entitled "**First-principles Theoretical Prediction and Analysis of Materials with Nontrivial Electronic Topology**" has been carried out by Mr. Koushik Pal at the Chemistry and Physics of Materials Unit, Jawaharlal Nehru Centre for Advanced Scientific Research, Bangalore, India under my supervision and that it has not been submitted elsewhere for the award of any degree or diploma.

Prof. Umesh V. Waghmare
(Research Supervisor)

Acknowledgements

I would like to take this opportunity to express my heartfelt thanks to my thesis advisor Professor Umesh V. Waghmare to whom I owe deepest gratitude for his constant support and excellent guidance during my graduate study at JNCASR. It was an extreme pleasure working with him who has boundless energy and intense curiosity in uncovering the mysteries in materials physics. Apart from being an excellent scientist, he is a good teacher from whom I have learnt how to ask the right questions for a given problem. I have always enjoyed intense scientific discussions with him at Chandriah canteen or IISc, which often used to continue for long time with the accompaniment of refreshments. Thank you sir for innumerable cups of cappuccino and sugarcane juice! His passion and enthusiasm for science have always motivated and influenced me. He is a person who always welcomes new scientific ideas, gets involved into it actively and helps to solve it efficiently. Many thanks to you Professor Waghmare for giving me enormous academic freedom during my candidacy.

I am truly indebted to my experimental collaborators Prof. CNR Rao, Prof. Ajay K. Sood, Prof. C. Narayana, Prof. PS Anil Kumar, Dr. Kanishka Biswas, Dr. P. Chithaiah, Achintya, Gyan, Kunjalata, Manoj, Rajaji for fruitful collaborations. I thank them for engaging me in fascinating, exciting and rigorous scientific interactions and meetings. Working with experimentalists has taught me how to think of a problem from a practical point of view and solve it.

I thank all the TSU, CPMU, NCU faculty particularly Professors S. Narasimhan, U. V. Waghmare, S. K. Pati, S. K. Das, G. U. Kulkarni, S. Balasubramanian, T. K. Maji, M. Eswaramoorthy, R. Ganapathy, C. Narayana, K. S. Narayan, Ranjan Dutta, S. M. Shivaprasad, S. Rajaram, H. Ila and A. Chakraborty (IISc) for their excellent course works.

I am very thankful to my past and present lab members Sharmila, Summayya, Abhishek-ji, Jayashree, Arghya, Anjali, Meha, Vinay, Arpita, Suchitra, Pawan, Krishnamohan, Shashwat, Anupam, Sandhya, Harish, Ayesha, Himanshu, Henu, Sweta, Aseem, Aviral,

Megha, Rafeeq, Sunil, Shambhawi, Simran, Archana, Anuja, Bhupalee for many academic, non-academic and fun interactions and lessons. I also thank Aruna madam and Kruti for their warm hospitality and good company during our group treats!

I am very grateful to my Int. PhD batch mates Anirban, Arkamita, Ankush, Ram, Chandan K, Chandan D, Rajasekhar, Sisir for their help and company in all these years. We really had some tough as well as fun times during our course works and assignments. I will cherish those memories forever!

I thank Pralok, Dibyajyoti, Sudeshna, Arkamita, Monoj, Debdipto, Rajib for making me realize the importance of learning cooking when we are away from home and making my stay in the hostel a lively and joyful one. These guys made me feel I was not too far from home. I sincerely thank my other friends in CPMU, TSU, NCU, MBGU particularly Ritesh da, Suman da, Debu da for all the fun and happy moments that we shared together in JNC!

Thanks to my teachers in schools and in Jadavpur University, who always motivated me to pursue research as a career. I thank particularly my childhood home tutor Mr. Ajit Thakur for bearing my troubles and guiding me in the right direction whenever I was going wrong! He taught me that hard work, discipline and perseverance never go in vain.

Thanks to Amit, Vijay and Anand from TUE-CMS for always giving a helping hand whenever any problem had arisen while making use of the supercomputing resources of Thematic Unit of Excellence-Computational Materials Science (TUE-CMS) of JNC. I also thank the complab, Academic, Admin staffs for quick help in any official issues. I thank Dhanvantari staffs, Hostel mess staffs, Utility store and Chandriah canteen for keeping and feeding me well.

Last but not the least, I thank my parents, my brother and Mousumi-di for always believing in me, providing me endless freedom and unconditional support at all stages of my life.

Synopsis

Quantum theory of solids predicts myriad quantum states of matter e.g., superconductivity, charge density waves, ferro-magnetism, etc. Each of these phases arises as a result of spontaneously broken symmetries in a material. Hence, each phase can be associated with an order parameter with consequences to observables that acquire finite values in those states of matter. Discovery of quantum Hall effect in 1980 revealed a fascinating quantum state of matter that does not require any explicit symmetry breaking and yet exhibits some new fundamental properties like quantized Hall conductance that is insensitive to small perturbations. It was shown that there exists a topological order in quantum mechanical many-body wave functions of its ground state that protects and is responsible for the quantized conductance.

Though the concept of topological order have been existing in condensed matter physics for a long time, research in this area has revived significantly after the recent discovery of quantum spin Hall (QSH) effect in HgTe/CdTe quantum wells in 2006. QSH systems are 2D topological insulators which host robust conducting edge states that remain protected by time-reversal symmetry, and physics of such systems can be adequately described in terms of single-particle quantum mechanics. Discovery of robust topological phases in non-interacting and real materials gave an immense boost to the research in topological physics.

The work in my Ph.D. dissertation is focused on the prediction of new materials with nontrivial electronic topology using first-principles calculations based on density functional theory (DFT), which have proven to be very useful and effective in studying electronic topology of materials. In addition to first-principles analysis, we have developed model Hamiltonians using group theoretical analysis and provided qualitative mechanism of the vibrational anomalies observed at electronic topological transition (ETT), which would otherwise be difficult to obtain within DFT. Model Hamiltonian based analysis also allowed us to go beyond the adiabatic Born-Oppenheimer approximations in order to capture the dynamical corrections due to electron-phonon coupling at the ETT. During my

thesis, we have actively collaborated with experimentalists in India and have successfully explained their experiments.

As many good thermoelectric materials are shown to possess non-trivial electronic topology (e.g., Bi_2Te_3), another important aspect of my thesis involves determination and analysis of thermoelectric properties of topologically non-trivial and related materials. We have attempted to understand the link between thermoelectricity and topology. Based on the information obtained from this analysis, we suggest ways to improve thermoelectric efficiency of materials.

The work in the thesis is broadly divided into four parts dealing with materials belonging to different symmetry and topological classes. First part (Chapter 3-4) of the thesis deals with strong Z_2 topological insulators in three dimensions. In Chapter 3, we investigated pressure/strain induced electronic topological transition (ETT) in rhombohedral Sb_2Se_3, β-As_2Te_3 and Bi_2Se_3 in the low pressure regime (< 8 GPa). In Chapter 4, we have uncovered the mechanism that explains the origin of anomalous temperature dependence of electronic and vibrational properties of strong topological insulator Sb_2Te_3.

Learning from the physics and the concurrent transient Dirac semimetallic state at an ETT in Chapter 3, we have provided detail theoretical recipes to achieve topological Dirac semimetallic state in *non-centrosymmetric* ternary half-Heuslers (e.g., LiMgBi) as well as centrosymmetric Zintl family of compounds Bi_2Mg_2X (X=Mg, Ca, Sr, Ba) in the second part of the thesis (Chapter 5-6).

Like strong Z_2 topological insulator, weak topological insulator is also a fascinating quantum states of matter that exhibits exotic quantum phenomena e.g., one dimensional helical modes along dislocation lines, half quantum spin Hall effect. In the third part (Chapter 7), we have predicted emergence of weak topological insulating phase in BiSe, whose crystal structure consists of a Bi bilayer sandwiched between two Bi_2Se_3 quintuple layers.

In the fourth and final part of my thesis, we have calculated the electronic (Chapter 8) and vibrational (Chapter 9) contributions to thermoelectric properties of topologically non-trivial and related materials. Based on our calculations, we predicted that TaAs, a Weyl semimetal, would be a good thermoelectric material. Our calculations also uncovered that rattling vibrations of the In^+ atoms in InTe and Tl^+ atoms in $TlInTe_2$ are mainly responsible for reducing their lattice thermal conductivity to an ultralow value.

List of Publications

(1) Achintya Bera, **Koushik Pal**, D. V. S. Muthu, Somaditya Sen, Prasenjit Guptasarma, Umesh V. Waghmare and Ajay K. Sood, "Sharp Raman anomalies and broken adiabaticity at a pressure induced transition from band to topological insulator in Sb_2Se_3", Phys. Rev. Lett. **110**, 107401 (2013).

(2) **Koushik Pal**, and Umesh V. Waghmare, "Strain induced Z_2 topological insulating state of β-As_2Te_3", App. Phys. Lett. **105**, 062105 (2014).

(3) Achintya Bera, **Koushik Pal**, DVS Muthu, Umesh V. Waghmare, Ajay K Sood, "Pressure-induced phase transition in Bi_2Se_3 at 3 GPa: electronic topological transition or not?", Journal of Physics: Condensed Matter **28**, 105401 (2016).

(4) Gyan Prakash, **Koushik Pal**, Manish Jain, Umesh V. Waghmare, and Ajay K. Sood, "Anomalous temperature dependence of electronic and vibrational Properties in topological insulator Sb_2Te_3: ultrafast time resolved pump probe experiment and theory", (accepted for publication in Phys. Rev. B).

(5) **Koushik Pal** and Umesh V. Waghmare, "Prediction of robust non-centrosymmetric topological Dirac semi-metallic state in ternary half-Heusler compounds", *under review.*

(6) **Koushik Pal**, Umesh V. Waghmare, "Theoretical prediction of topologically nontrivial semi-metallic states in Zintl family of Bi_2Mg_2X (X=Mg, Ca, Sr) compounds", (preprint available).

(7) **Koushik Pal**, Shashwat Anand and Umesh V. Waghmare, "Thermoelectric properties of materials with nontrivial electronic topology", Journal Mat. Chem. C, **3**, 12130 (2015).

(8) Kunjalata Majhi*, **Koushik Pal***, Himanshu Lohani, Abhishek Banerjee, Pramita Mishra, Anil K Yadav, R Ganesan, BR Sekhar, Umesh V. Waghmare, P.S. Anil Kumar, "Emergence of a weak topological insulator from the Bi_xSe_y family", App. Phys. Lett. **110**, 162102 (2017). *Equal contributions.

(9) Manoj K. Jana, **Koushik Pal**, Umesh V. Waghmare, Kanishka Biswas, "The origin of ultralow thermal conductivity in InTe: lone pair induced anharmonic rattling", Angew. Chem. Int. Ed. **55**, 7792 (2015).

(10) Manoj K. Jana, **Koushik Pal**, Avinash Warankar, Pankaj Mandal, Umesh V. Waghmare and Kanishka Biswas, "Intrinsic rattler-induced low thermal conductivity in Zintl type $TlInTe_2$" J. Am. Chem. Soc. **139**, 4350–4353 (2017).

List of Figures

2.1 Flow chart of a typical DFT calculation. 25
2.2 Schematic representation of a pseudopotential 28
2.3 Schematic representation of a LAPW basis set. The unit cell is divided into atom centered region (red color) and interstitial region (blue color). . . 30

3.1 Raman spectra of Sb_2Se_3. FWHM of the M1 mode and electronic bands near the Fermi level as a function of pressure. 45
3.2 Conventional and primitive unit cells, Brillouin zone and phonon frequencies vs pressure graph at Γ of Sb_2Se_3. 46
3.3 Band inversion of Sb_2Se_3 across the critical pressure (P_c=2 GPa). 47
3.4 Evolution of electronic structure and the bulk band gap around the critical pressure P_c (= 2 GPa). 49
3.5 Effect of electron-phonon coupling on the electronic structure of Sb_2Se_3 as obtained from first-principles calculations. 51
3.6 Dynamical corrections to phonon frequencies. 54
3.7 Electronic structure of β-As_2Te_3 (space group: $R\bar{3}m$) at vanishing strain. . 60
3.8 Evolution of electronic bands and bulk band gap of β-As_2Te_3 as a function of uniaxial strain (ϵ_{zz}). 62
3.9 Electronic structure and density of states of β-As_2Te_3 at ϵ_{zz}=-0.06. 64
3.10 Phonon dispersion of β-As_2Te_3 at ϵ_{zz}= -0.06 calculated within a non-relativistic description. 65
3.11 Experimental Raman shift of Bi_2Se_3 as function of pressure and hexagonal crystal structure of Bi_2Se_3. 68
3.12 Enthalpy differences between the three different structures of Bi_2Se_3. . . . 71
3.13 Anomalies in the structural parameters of Bi_2Se_3 near P $\sim$ 3 GPa as determined from first-principles calculations. 72
3.14 Calculated electronic structure of Bi_2Se_3 as a function of pressure. 73

3.15 Electronic structure of the (001) surface of Bi_2Se_3. 73
3.16 Calculated Raman and IR active modes as a function of pressure. 75

4.1 Experimentally obtained temperature dependence of refractive index, extinction coefficient, sound velocity and Young's modulus of of Sb_2Te_3. . . . 79
4.2 Hexagonal unit cell of the pristine and faulted structures of Sb_2Te_3. 80
4.3 Free energy difference between the pristine and faulted structure of Sb_2Te_3. 82
4.4 Calculated Young's modulus and refractive index for different structures of Sb_2Te_3. 84
4.5 Electronic structure and band gap for different structures of Sb_2Te_3. 85

5.1 Crystal, electronic structures, phonon dispersion and Brillouin zone of LiMgBi. 89
5.2 Phonon dispersion for the unstable structure of LiMgBi. 90
5.3 Primitive unit cells of LiMgBi crystal structures distorted with ϵ_c and ϵ_a, Brillouin zone and electronic topological phase diagram. 93
5.4 Electronic structures of the different topological phases of LiMgBi and generic topological phase diagrams. 94
5.5 Evolution of the frontier bands ($\Gamma_{4*}^{(C_{3v})}$, $\Gamma_4^{(C_{3v})}$, and $\Gamma_5^{(C_{3v})}$) with strains. . . 96
5.6 Visualizations of 3D-Dirac cone, Fermi surfaces and non-zero Berry curvature at the Dirac point of LiMgBi. 98
5.7 Electronic structure of NaGaSn for different strains. 100
5.8 Electronic structure of RbGaSi for different strains. 101
5.9 Electronic structure of YAuPb for different strains. 102
5.10 Electronic structure of YPtBi for different strains. 103
5.11 Electronic structures of LiMgAs and LiMgSb showing their band insulating phases at ambient conditions. 103

6.1 Crystal structure and bonding environment in Zintl family of Bi_2Mg_2X (X = Mg, Ca, Sr, Ba) compounds. 108
6.2 Band inversion in Bi_2Mg_3 at Γ point. 110
6.3 Electronic structure of Bi_2Mg_2X (X=Mg, Ca, Sr, Ba) compounds calculated with spin-orbit coupling. 111
6.4 Electronic structures of the (001) surface of Bi_2Mg_2X (X = Mg, Ca, Sr, Ba) compounds. 114
6.5 Tunable topological states of Bi_2Mg_2Ca with strain. 116
6.6 Electronic structure of Bi_2Mg_2Ba determined in its native Dirac semimetallic (DSM) state using first-principles calculations and model Hamiltonian. . 117

6.7 Atom projected phonon spectra of Bi_2Mg_2X (X = Mg, Ca, Sr, Ba) compounds. 120
6.8 Seebeck coefficient and power factor as a function of temperature. 123

7.1 Total electronic charge density plot and different unit cells of BiSe for electronic structure calculations of the bulk and (001) surface. 129
7.2 Time reversal invariant momenta (TRIM) in the hexagonal Brillouin zone (BZ), unit cell and corresponding BZ for side surface states calculation. . . 131
7.3 Electronic structure and phonon dispersion of BiSe. 133
7.4 Layer projected electronic density of states along high symmetry directions in Brillouin zone. 134
7.5 Electronic structure on (001) surface of BiSe for different surface terminations and thicknesses. 136
7.6 Unit cell and surface electronic structure of a free standing bismuth bilayer. 138

8.1 Crystal structures and symmetries of the topologically nontrivial materials considered here. 144
8.2 Dependences of density of state, electrical conductivity, Seebeck coefficient, power factor on Fermi levels at different temperatures. 149
8.3 Electronic structure of the bulk of the materials under consideration, calculated with spin-orbit coupling. 151
8.4 Electronic structure, density of states and transport properties (S, σ, P) for unstrained β-As_2Te_3 and strained PbTe. 155
8.5 Electronic structure and transport properties of strained PbTe. 156
8.6 Schematic picture of band inversion between the valence band maximum (VBM) and conduction band minimum (CBM). 158

9.1 Crystal structure, Brillouin zone, charge density and electron localization function of InTe. 162
9.2 Phonon dispersions of InTe at 0 GPa and 3 GPa. 165
9.3 Potential energy wells for the constituent atoms of InTe. 166
9.4 Crystal structure, Brillouin zone, charge density and electron localization function of $TlInTe_2$. 169
9.5 Electronic structure and orbital projected density of states of $TlInTe_2$. . . . 171
9.6 Full and atom projected phonon dispersions of $TlInTe_2$. 173
9.7 Atom projected phonon density of states and Grüneisen parameters (γ_i) for the lowest three phonon branches of $TlInTe_2$. 175

9.8 Atomic displacements patterns of a few low frequency optical phonons of $TlInTe_2$ are shown in the primitive unit cell. 176

10.1 A schematic summarizing the ideas and work presented in this thesis. . . . 182

List of Tables

3.1 Table showing nominal frequencies of the phonon modes for Bi_2Se_3 family of compounds. 50
3.2 Parity of the occupied bands and calculation of Z_2 invariant. 60
3.3 Parities of the fourteen occupied bands and the lowest energy unoccupied band of Bi_2Se_3 at pressures in the range of 0-8 GPa. 76

8.1 Structural parameters and cutoffs defining basis sets used in WIEN2k density functional theory (DFT) calculations. 148
8.2 Table summarizing different types of peaks in the power factor (P) of the materials with nontrivial electronic topology. 150

9.1 Sound velocities corresponding to the three acoustic branches of InTe and their associated Grüneisen parameters. 164
9.2 Sound velocities corresponding to the three acoustic branches of $TlInTe_2$. . . 172

Contents

Acknowledgements v

Synopsis vii

List of Publications ix

List of Figures xi

List of Tables xv

1 Introduction 1

1.1 Distinct topological phases of matter 5

1.1.1 Quantum Hall effects 7

1.1.2 Z_2 topological insulators 9

1.1.3 Topologically nontrivial semimetals 10

1.2 Elements of topological band theory 11

1.2.1 Bulk-boundary correspondence principle 11

1.2.2 Berry curvature and Berry phase 12

1.2.3 Chern number 12

1.2.4 Z_2 invariants 13

1.3 Spin-orbit coupling 14

1.4 Overview of the thesis 16

2 Methods and Formalism 19

2.1 Electronic structure 20

2.1.1 Born-Oppenheimer approximation 20

2.1.2 Classical nuclei approximation 21

2.2 Density functional theory . . . 23
2.2.1 Thomas-Fermi model . . . 23
2.2.2 Hohenberg-Kohn theorems . . . 24
2.2.3 Kohn-Sham approach to DFT . . . 26
2.2.4 Pseudopotential-based calculations . . . 27
2.2.5 All-electron method . . . 30
2.3 Exchange & correlation energy functional . . . 31
2.4 Inclusion of spin-orbit coupling . . . 32
2.5 Phonons . . . 33
2.5.1 Density functional perturbation theory . . . 33
2.6 Wannier function . . . 35
2.6.1 Maximally localized Wannier function (MLWF) . . . 36
2.6.2 Calculation of Z_2 invariants via WCC . . . 38
2.7 Semi-classical Boltzmann transport equation . . . 40

I Strong Topological Insulators

3 Electronic Topological Transition in Binary Chalcogenides 42
3.1 Pressure Induced Electronic Topological Transition in Sb_2Se_3 . . . 42
3.1.1 Introduction . . . 42
3.1.2 Experimental observations . . . 45
3.1.3 Crystal structure and computational details . . . 47
3.1.4 Electronic structure and phonons . . . 48
3.1.5 Going beyond the adiabatic approximation . . . 50
3.1.6 Conclusions . . . 56
3.2 Strain Induced Z_2 Topological Insulating Phase in β-As_2Te_3 . . . 57
3.2.1 Introduction . . . 57
3.2.2 Computational details . . . 58
3.2.3 Results and discussion . . . 59
3.2.4 Conclusions . . . 65
3.3 Pressure Induced Phase Transition in Bi_2Se_3 at 3 GPa: Electronic Topological or Not? . . . 66
3.3.1 Introduction . . . 66
3.3.2 Experimental observations . . . 68
3.3.3 Crystal structure and computational details . . . 69
3.3.4 Theoretical analysis . . . 70
3.3.5 Conclusions . . . 76

4 Anomalous Temperature Dependence of Electronic and Vibrational Properties of Sb_2Te_3 77
4.1 Introduction . . . 77
4.2 Experimental observations . . . 78
4.3 Crystal structure . . . 78
4.4 Computational details . . . 80
4.5 Possibility of iso-structural transition . . . 81
4.6 Origin of anomalous temperature dependence . . . 82
4.7 Summary . . . 85

II Dirac Semi-metals

5 Prediction of Robust Non-centrosymmetric Topological Dirac Semi-metallic State in Ternary Half-Heusler Compounds 87
5.1 Introduction . . . 87
5.2 Crystal structure and stability of LiMgBi . . . 89
5.3 Computational methods . . . 91
5.4 Electronic topological phase diagram of LiMgBi . . . 92
5.5 Generic topological phase diagrams . . . 99
5.6 Experimental signature of nontrivial topology . . . 100
5.7 Heterostructures . . . 101
5.8 Summary . . . 102

6 Theoretical Prediction of Topologically Nontrivial States in Zintl Family of Bi_2Mg_2X (X=Mg, Ca, Sr, Ba) Compounds 104
6.1 Introduction . . . 104
6.2 Crystal structure and computational methods . . . 107
6.3 Electronic structure and topology . . . 110
6.3.1 Electronic structure of the bulk . . . 110
6.3.2 Z_2 invariant and surface states . . . 113
6.4 Tunability of electronic topology . . . 115
6.4.1 Effects of strain . . . 115
6.4.2 Model Hamiltonian to capture tunability with strain . . . 116
6.5 Vibrational properties . . . 119
6.6 Potential applications . . . 121
6.6.1 Electronic thermoelectric properties . . . 121
6.6.2 Heterostructures and devices . . . 122
6.7 Conclusions . . . 124

III Weak Topological Insulator

7 Emergence of Weak Topological Insulating Phase in BiSe 126
7.1 Introduction . . . 126
7.2 Crystal structure and Brillouin zone . . . 128
7.3 Computational details . . . 129
7.4 Theoretical analysis . . . 132
7.4.1 Projected electronic structure of the bulk . . . 133
7.4.2 Calculation of Z_2 invariants . . . 135
7.4.3 Surface electronic structure . . . 137
7.5 Conclusions . . . 138

IV Thermoelectric Properties of Topologically Nontrivial and Related Materials

8 Thermoelectric Properties of Materials with Nontrivial Electronic Topology 140
8.1 Introduction . . . 140
8.2 Materials with nontrivial electronic topology . . . 143
8.3 Computational methods . . . 146
8.4 Results . . . 147
8.4.1 Band and topological insulators . . . 150
8.4.2 Topological, Dirac and Weyl semimetals . . . 153
8.5 Discussion . . . 154
8.5.1 Multiple band extrema and sub-band structure . . . 154
8.5.2 Tunability with strain: ETT and convergence of bands . . . 156
8.6 Summary . . . 158

9 Ultralow Lattice Thermal Conductivity in Group III Tellurides 160
9.1 Lone-pair Induced Rattling and Ultralow Lattice Thermal Conductivity in InTe . . . 160
9.1.1 Introduction . . . 160
9.1.2 Crystal structure . . . 162
9.1.3 Computational details . . . 163
9.1.4 Theoretical analysis . . . 164
9.1.5 Conclusions . . . 167
9.2 Intrinsic Rattler-induced Low Lattice Thermal Conductivity in $TlInTe_2$ . . . 167
9.2.1 Introduction . . . 167

9.2.2 Crystal structure 169
9.2.3 Computational details 170
9.2.4 Theoretical analysis 171
9.2.5 Conclusions 175

10 Summary **177**

Bibliography **183**

Chapter 1

Introduction

Science is the belief in the ignorance of experts.

Richard P. Feynman

Electronic structure calculations based on Kohn-Sham density functional theory (DFT) are thus far proved to be a widely popular and highly successful theory in condensed matter physics and materials science. DFT has shown unprecedented accuracy in predicting and explaining the macroscopic as well as microscopic properties of materials in the bulk form, surfaces and interfaces, which are quantitatively comparable to the experimental measurements. With the predictive capability of DFT along with advances in supercomputing resources, a large number materials can be screened to find the required properties, thereby reducing the efforts of experimentalists and making research and scientific exploration of materials *cost-effective*. Novel materials and their exotic properties can be predicted within DFT. While some of the predictions can be readily realized within the laboratory, some of them may not be feasible in immediate experimental realization within the existing experimental capabilities. This confidence, flexibility and success of DFT stem from its ability to compute properties of materials with no adjustable parameters. Properties of condensed phases of matters are characterized by arrangements of the electrons, their interaction among themselves and with ions. Theoretically, the behavior

of electrons and ions can be described exactly by the many body quantum mechanics. However, due to interactions between electrons and ions, the many body Schrödinger equation practically becomes impossible to solve. In order to circumvent this problem, and solve the electronic structure of the condensed phase of a material, Kohn-Sham DFT uses (a) classical nuclei and (b) Born-Oppenheimer approximations, where the many body Schrödinger equation is mapped onto a set of self-consistent one-electron equations assuming that the non-interacting electrons move in an effective field generated by electrons and ions. Such one-particle Hamiltonian is known as the Kohn-Sham Hamiltonian (KSH). All many body effects (*e.g.*, electron-electron interactions) are lumped into the exchange-correlation energy term which is a universal functional of the electronic density and included in the non-interacting Kohn-Sham Hamiltonian. The KS-DFT works quite well for describing electronic and vibrational properties of those systems which have weak electronic correlations.

One of the main tasks in condensed matter physics has been to classify phases of matter. For example, quantum theory of solids predicts different quantum states of matter like ferro-magnetism, superconductivity, charge density waves etc. Each of these phases arises as a result of spontaneously broken symmetry in a material [1, 2]. For example, a ferromagnetic material breaks the time reversal symmetry, a superconductor breaks subtle gauge symmetry, and a crystalline solid breaks continuous translational symmetry. In each of these states, we can define an order parameter which acquires a nonzero value in that ordered phase with consequences to observables. The physics of such phases near the phase transition can be adequately captured using an effective mean field theory namely the Landau theory [3], which expresses the free energy of a system in terms of its order parameter taking into account the dimensionality and symmetry. Thus, Landau theory provides universal and phenomenological explanation of these quantum phases of matter arising from broken symmetries, though it is appropriate close to the phase transition, where fluctuations are strong.

Discovery of certain quantum states of matter in the last few decades *e.g.*, the fractional quantum Hall effect (FQHE) [4,5] has challenged the existing classification scheme of states of matter based on spontaneously broken symmetry. In FQHE, we observe fundamental properties like robust quantized conductivity even when no explicit symmetry is broken. It was shown that FQHE is associated with a robust topological order parameter which is highly non-local in nature, and such a quantum state can not be phenomenologically described by Landau's theory. Generally, states of materials that possess robust order parameters are called topologically ordered materials and the phases associated with them are called topological phases whose low energy effective physics can be described by topological field theory. Although, the concept of topologically ordered phases of matter existed in condensed matter physics for many years, most examples involve somewhat complicated states of matter like FQHE, which have strong electron-electron correlations and hence description of its physics requires an inherently many-body treatment.

After the discovery of integer quantum Hall (IQH) effect [6] in 1980, it was realized for the first time that a non-interacting system can also host robust topologically nontrivial electronic phase. The IQH state possesses robust edge states and exhibits quantized Hall conductivity which are insensitive to the smooth adiabatic changes in the material parameters and hence can not be destroyed without a quantum phase transition. The IQH effect requires an external magnetic field, which explicitly breaks time reversal (TR) symmetry. Later, TR invariant systems with robust edge/surface states were proposed *e.g.*, in Haldane model [7] and quantum spin Hall (QSH) insulator [8] which possess nontrivial band topology. It was realized that the strong spin-orbit interaction in non-interacting fermionic systems can give rise to topologically nontrivial phases in the electronic structure. The term 'topology' is attached to any electronic state of matter which ensures the existence of bulk topological invariants that are used to distinguish trivial and nontrivial phases of a material with same symmetry.

The extended branch of band theory of solids that describes the topological physics of non-interacting electronic systems is known as the topological band theory. The crucial

elements of topological band theory are Berry connection, Berry phase, Chern number which can be easily formulated and computed within single particle quantum mechanics. For these reasons, DFT proves to be a very useful theoretical tool in dealing with materials with nontrivial electronic topology as it can accurately treat a material within single particle approximation and include the effect of spin-orbit coupling (SOC) in the KS Hamiltonian, which is one of the most crucial ingredients in known nontrivial topological material.

The first remarkable success of DFT in the area of topological physics came when Bi_2Se_3, Bi_2Te_3 and Sb_2Te_3 were predicted to be the strong Z_2 topological insulators in three dimensions with only a single Dirac cone in the electronic structure of their (001) surfaces [9]. These predictions were subsequently confirmed by experiments [10]. Thallium based ternary chalcogenides ($TlBiSe_2$, $TlBiTe_2$, $TlSbSe_2$) were also first predicted theoretically [11] to be strong topological insulators, and their topological properties verified by angle resolved photoemission spectroscopy (ARPES) experiments [12]. After the discovery of insulating phases in materials with Z_2 topological order, materials belonging to the different symmetry and topological classes have been predicted mostly by first-principles calculations based on DFT, and some of which have even verified experimentally.

For decades, electronic structure and properties of semiconductors are being investigated by **k.p** or tight binding model Hamiltonians which accurately describe the electronic dispersions around the Fermi energy with the same level of accuracy as of first-principles DFT calculations. These model Hamiltonians have been important theoretical tools to understand and analyze the topological nature of the electronic structure of a material. Linearly dispersed gapless surface or edge states are one of the unique features in identifying the nontrivial topology of a topological insulators. Calculation of these nontrivial surface or edge states with model Hamiltonian can be a bit tricky as the complex interaction on the surface of a material (*e.g.*, polarity of the surface, dangling bonds, surface reconstruction etc.) are not included in a model Hamiltonian. For these reasons and also for the fact that DFT can accurately calculate the electronic structure and properties of

materials of large sizes with any structural and chemical complexities, it has gained huge popularity and success in dealing with specific materials with nontrivial electronic topology. Moreover, DFT offers numerous possibilities like checking the stability of a topologically nontrivial material with respect to a substrate, its interaction with other materials, behavior under extreme conditions like high pressures, external electric, magnetic field, etc. Using DFT calculated results, we can construct tight binding model Hamiltonian using maximally localized Wannier functions (MLWFs) [13] which are molecular orbital analogue of a crystal, and thus are easy to use in analysis of electronic structure and bonding. Using this MLWFs, Chern number, topological Z_2 invariants can be calculated with ease [14].

The foundations of modern topological phenomena in physics were laid by David J. Thouless, F. Duncan M. Haldane and J. Michael Kosterlitz, who in the early 1970s and 1980s theoretically [7, 15, 16] explained the physics associated with quantum Hall effect [17], superfluid phase transition [18] using the mathematical tools of topology. Their theory not only unraveled new exotic and unusual quantum states of matter but also sparked a flurry of research activity in topological materials that could be used in future fault-tolerant fast electronics, superconductors or even quantum computers. For these pioneering works, David J. Thouless, F. Duncan M. Haldane and J. Michael Kosterlitz were awarded the Nobel prize in physics in 2016 *"for theoretical discoveries of topological phase transitions and topological phases of matter*"*. Now recognized as fundamental mechanism in condensed matter physics, topological nontrivial phases have been discovered in materials ranging from systems in 1D [19] to 2D materials to even materials in three dimensions.

1.1 Distinct topological phases of matter

A unifying concept of these novel and exotic quantum states of matter is the existence of *bulk-boundary correspondence principle* which relates the nontrivial electronic topology

*citation from https://www.nobelprize.org/nobel_prizes/physics/laureates/2016/

of the bulk to the presence of robust conducting surface or edge states. Although most of the materials having nontrivial topology host gapless surface/edge states, it has been theoretically shown that nontrivial topological phase may exist even without exhibiting gapless edge modes [20].

Initially, it was thought that the topological band theory can only be applied to gapped phases *e.g.*, to insulators and semiconductors, as smooth adiabatic deformation can not change the topology of the bulk of a system as long as the ground state and the excited states are separated by a band gap [21]. In order to change a topological insulator into a band insulator, a quantum phase transition must take place and the system must pass through a *gapless* electronic state. However, recent advances in topological research have altered this concept and the existence of topologically nontrivial phases are theoretically predicted and experimentally observed in semimetals with vanishing band gaps. Moreover, topological phase transition is shown to occur without passing through a gapless state [22]. Examples of semimetals with nontrivial electronic topology are topological semimetal [23, 24], Dirac semimetal [25], Weyl semimetal [26]. Most of these topologically nontrivial semimetals are more exciting than their insulating counterparts as they exhibit exotic phenomena like open Fermi arcs in the surface states, giant negative magneto-resistance [27], ultrahigh mobility [28], chiral anomaly [29].

Study of topologically exotic phases in the context of real materials is expanding enormously because of their rich physics and potential for applications in electronic devices. For example, Majorana fermions are shown to exist at the edge of a topological superconductor [30], which are the heart of quantum computers. Highly spin-polarized and robust conducting surface states or edge channels in topological insulators can be used in spintronics which are fault tolerant and thus can minimize loss of informations. After the discovery of quantum Hall effects [7, 31, 32], an array of research activity in this area has spurred that has uncovered different topological phases of matter. A list of such systems exhibiting electronic topology is given below.

1.1.1 Quantum Hall effects

Quantum Hall effect

The modern research in the field of topological phases of matter kick-started with the discovery of quantum Hall (QH) effect [31] in 1980, which was observed in a two-dimensional electron gas system subjected to a strong magnetic field at low temperature. A quantum Hall system exhibits quantized hall conductance ($\sigma_{xy}=\nu\frac{e^2}{h}$), which originates from the Berry curvature of the filled magnetic Blöch bands (or Landau level). The integration of the Berry curvature associated with these bands in the Brillouin zone gives rise to a topological invariant quantity (ν) known as the Thouless-Khomoto-Nightingle-den Nijs (TKNN) number [33]. The conducting edge states in a QH system are robust and their conduction is dissipation-less. Hence, they can be used in fault-tolerant high speed electronic devices.

Quantum anomalous Hall effect

Since QH effect requires strong magnetic field and generation of strong magnetic field at low temperature is quite unfeasible for widespread application of QH effect in devices, it is highly desirable to realize QH effect in materials without applying the external magnetic field. In 1982, Haldane proposed an analogous model (known as the Haldane mode [7]) to realize the quantum Hall effect in a 2D honeycomb lattice which does not require an external magnetic field and yet exhibits quantized conductance ($\sigma_{xy}=\nu\frac{e^2}{h}$, with ν=1). In this model, the time-reversal (TR) symmetry of the honeycomb lattice is broken by applying a periodic magnetic field in such a way that the net magnetic flux in a unit cell becomes zero. The broken TR symmetry lifts the degeneracy of Dirac cone in the electronic structure of the honeycomb lattice and opens up a gap at the Dirac point. In this gapped state, the Chern number of the system is unity. This type of Hall effect, which does not require any net magnetic field, is known as quantum anomalous Hall effect (QAHE), and an insulating material exhibiting such property is called quantum

anomalous Hall insulator or Chern insulator. Although Haldane provided a simple route to realize the QH effect without applying any magnetic field, no real material system was proposed for its experimental verification. For this reason, after the prediction of QAHE, it was not initially accepted unanimously within the scientific community partly because (a) 2D systems were considered to be unstable and (b) Haldane's proposal of applying alternating magnetic flux in a single unit cell was not feasible in experiments. But after the discovery of graphene [34], the wonder material in two dimensions, the work by Haldane renewed the attention and increased the significance of the Quantum anomalous Hall effect. Experimentally QAHE was realized both in the context of graphene [35] and ferromagnetic topological insulator [36].

Quantum spin Hall effect

As the quantized Hall conductivity in QH effect or QAHE is odd under time-reversal symmetry, the robust conducting edge channels (which are topologically nontrivial because of their non-zero Chern number) in them can only be realized in systems where time reversal symmetry is broken either by external magnetic field or by magnetic order. However, the presence of spin-orbit coupling (SOC) in a material allows a different topological classification of insulators which are invariant under time-reversal symmetry and exhibit robust gapless topologically nontrivial edge/surface states. These insulators where TR symmetry is preserved are called Z_2 topological insulators [37], and their associated topological invariants are characterized by Z_2 indices.

The possibility of having a time-reversal invariant topological insulator in two-dimension was first proposed in the Kane-Mele model [32] which is considered to be composed of two copies of the Haldane model with both up and down spin electrons. Addition of spin-orbit interaction term in the Kane-Mele model gives rise to topological insulating state in it. This 2D topological insulator is also known as quantum spin Hall (QSH) insulator that exhibits quantized spin Hall conductance, but with a vanishing charge Hall conductance. After the theoretical prediction of the QSH effect, it was experimentally

realized in HgTe/CdTe quantum well heterostructure [38].

1.1.2 Z_2 topological insulators

Strong topological insulator

The concept of topological insulating phase in 2D systems (or QSH insulators) can be extended to three dimensions. In a 3D topological insulator, the electronic structure of a material remains gapped in the bulk but on its surface it hosts gapless robust conducting states which are protected by time-reversal symmetry (in Z_2 topological class). In three dimensions, topological insulators are divided into two classes (a) strong topological insulator (STI) and (b) weak topological insulator (WTI). In a seminal work, Zhang et al. theoretically predicted the first three dimensional STI in Bi_2Se_3 materials class [9], which hosts a single Dirac cone in the electronic structure of (001) surface. These states are robust and show spin-momentum locking. Their theoretical prediction was experimentally verified with angle resolved photo-emission spectroscopy (ARPES) experiments [10]. In three-dimension, there are four Z_2 invariants $(\nu_0; \nu_1, \nu_2, \nu_3)$ for a time-reversal invariant system. For a STI, ν_0 must be 1 and the rest of the indices may or may not take non-zero values.

Weak topological insulator

On the other hand, if ν_0 is zero, but at least one of the other three indices (ν_1, ν_2, ν_3) becomes 1, then the TR-invariant material belongs to weak topological insulating phase. For a weak topological insulator (WTI), the appearance of the topological surface states depend on surface termination. A WTI consists of stacked layers of 2D topological insulators and topological surface sates only appear on its side surfaces [39]. Nevertheless, WTIs are very interesting as they exhibit several intriguing quantum phenomena like one dimensional helical modes along dislocation lines [40], weak anti-localization effect [41] and half quantum spin Hall effect [42].

Topological crystalline insulator

Topological crystalline insulators (TCIs) are novel states of quantum matter where the topologically nontrivial phase in their electronic structure is induced by the crystalline symmetry of the materials [43]. Presence of topologically nontrivial crystalline insulating phase was first theoretically predicted in SnTe family of materials [44]. These TCIs were shown to possess non-zero mirror Chern number (a topological invariant quantity) in the bulk, and exhibit gapless metallic surface states with even number of Dirac cones on their high symmetry crystal surfaces [44]. Soon after its theoretical prediction, TCI phase was experimentally verified in $Pb_{1-x}Sn_xSe$ using ARPES experiments [45].

1.1.3 Topologically nontrivial semimetals

Topological semimetal

Studies of topologically nontrivial electronic states in metallic and semi-metallic systems have revealed many exotic topological phenomena like giant magneto-resistance, ultrahigh mobility [28], chiral magnetic effect [29]. Two pioneering theoretical studies [23, 24] predicting the existence of topologically nontrivial semi-metallic state in ternary half-Heusler (HH) compounds added a new dimension to the research in topological phases of matter. These HH compounds are shown to possess nontrivial Z_2 order in their bulk form and can be driven into distinct topological phases under mechanical strain. One characteristic feature of this TSM phase is that, the valence and conduction bands touch each other quadratically at Γ near the Fermi level [23, 24].

Dirac semimetal

Dirac semimetal (DSM) is a novel quantum state of matter where doubly degenerate bands cross linearly near the Fermi level. The crossing point is called Dirac point which is quadruply-degenerate. The low energy physics of a Dirac semiemtal is described by the Dirac Hamiltonian. BiO_2 is the first theoretically Dirac semimetal in three dimensions,

where the Dirac points in its electronic structure appear due to the non-symmorphic symmetry or space group of the crystal lattice [46]. Wang et al. [25] predicted topological Dirac semi-metallic (TDSM) state in A_3Bi (A=Na, Rb, Cs) class of compounds which are both inversion symmetric and invariant under time-reversal symmetry. These TDSMs host a pair of Dirac points in their bulk Brillouin zone. This theoretical prediction of TDSM state in Na_3Bi has been experimentally verified by ARPES measurements [47].

Weyl semimetal

In a Weyl semimetal (WSM), non-degenerate bands cross linearly near the Fermi level and give rise to a Weyl point which is doubly degenerate. The low energy physics of a WSM can be effectively described with the Weyl Hamiltonian $H(\mathbf{k}) = \pm v\mathbf{k}.\sigma$, where $\mathbf{k}$ is the wavevector, v is electron's velocity and σ are the Pauli matrices. By breaking either the spatial inversion symmetry or time reversal symmetry, we can turn a DSM into a WSM. The WSM state was first theoretically predicted in $A_2Ir_2O_7$ (A=Y or Ln) pyrochlore iridates [48]. The most prominent examples of WSMs are transition-metal monopnictides (TaAs, TaP, NbAs, NbP) which were first theoretically predicted [49] using first-principles calculations based on DFT. Later, these compounds were experimentally verified to be WSMs using ARPES technique [26, 50–52].

1.2 Elements of topological band theory

1.2.1 Bulk-boundary correspondence principle

According to the bulk-boundary correspondence principle, at the interface between two materials belonging to same symmetry but different topological classes, topological edge or surface states appear. For example, if the two materials have bulk topological invariants n and m, then at their interface there will be precisely |n-m| number of edge states [53]. Basically, this principle establishes the relation between edge/surface states to topological properties of the bulk wave functions. This principle in general holds true

for non-interacting fermionic systems [20].

1.2.2 Berry curvature and Berry phase

When an electronic state undergoes a cyclic adiabatic evolution in a closed path in the Brillouin zone, it may acquire a phase which is known as the Berry's phase (γ). If there are M non-degenerate bands present in a material, then for each band n, Berry's phase is given by $\gamma_n = \oint_c d\mathbf{k}.A_n(\mathbf{k})$, where $\mathrm{A}_n(\mathbf{k})$ is the Berry connection of the n-th band and is analogous to magnetic vector potential in the reciprocal space. Berry connection is given by $A_n(\mathbf{k}) = i \langle u_n(\mathbf{k})| \frac{\partial}{\partial \mathbf{k}} |u_n(\mathbf{k})\rangle$. Berry curvature is defined as the field associated with the Berry potential $\mathrm{A}_n(\mathbf{k})$ and can be obtained as: $\Omega_n(\mathbf{k}) = \nabla_{\mathbf{k}} \times A_n(\mathbf{k})$. In the case of non-degenerate bands, Berry curvature is Abelian. But when degeneracy is present within the band manifold of interest, the conventional adiabatic theorem needs to be generalized, and Berry curvature becomes non-Abelian which is represented by a tensor. This extension of the Berry curvature to the tensor framework was done in analogy with the non-Abelian gauge theories by Wilczek and Zee [54] in 1984. In the case of degenerate bands, the Berry connection is given by, $A_{mn}(\mathbf{k}) = i \langle u_m(\mathbf{k})| \frac{\partial}{\partial \mathbf{k}} |u_n(\mathbf{k})\rangle$, where m, n indicate the band indices ($m, n \in \sum$) within the degenerate subspace ($\sum = 1, ..., N$). In this case, the non-Abelian Berry curvature is given by [55],

$$\Omega_{mn}(\mathbf{k}) = i \langle \frac{\partial u_m(\mathbf{k})}{\partial \mathbf{k}}| \times |\frac{\partial u_n(\mathbf{k})}{\partial \mathbf{k}}\rangle + i \sum_{l \in \sum} \langle u_m(\mathbf{k})|\frac{\partial u_l(\mathbf{k})}{\partial \mathbf{k}}\rangle \times \langle u_l(\mathbf{k})|\frac{\partial u_n(\mathbf{k})}{\partial \mathbf{k}}\rangle \tag{1.1}$$

1.2.3 Chern number

Chern number is a topological invariant quantity which is obtained as an integration of the Berry curvature in a closed surface in the Brillouin zone. Using the definition of Berry curvature for the non-degenerate case above, the Chern number for the n-th band is given by,

$$C_n = \frac{1}{2\pi} \int \Omega_n(\mathbf{k}) d^2k, \tag{1.2}$$

where the integration is taken over the two-dimensional Brillouin zone.

1.2.4 Z_2 invariants

Presence of robust edge states in two-dimensional topological insulator or quantum Spin Hall (QSH) insulator suggests that there must exist a topological distinction between quantum spin Hall insulator and ordinary insulator for which there are no topological edge states present. For a time reversal invariant system, Z_2 topological invariants differentiate a QSH phase form an ordinary insulating phase, In two dimensions, there is a single Z_2 invariant ν (which can be either 0 and 1). In three dimensions, there are four Z_2 topological indices $(\nu_0; \nu_1, \nu_2, \nu_3)$ [56], where ν_0 is the strong topological index and the rest (ν_1, ν_2, ν_3) are called weak topological indices. According to Fu & Kane, a Z_2 invariant quantity can be described as an obstruction to finding a smooth gauge for the Blöch wavefunction in the half-Brillouin zone (BZ) and is given by [57, 58],

$$\Delta = \frac{1}{2\pi}\left(\oint_{\partial\tau_{\frac{1}{2}}} \mathbf{a}.d\mathbf{l} - \int \Omega_{xy} d^2k\right) \; mod \; 2, \tag{1.3}$$

where $\tau_{\frac{1}{2}}$ and $\partial\tau_{\frac{1}{2}}$ denote half-BZ and its boundary respectively. $a_j = i\sum_n \langle u_n(\mathbf{k})| \frac{\partial}{\partial \mathbf{k}_j} |u_n(\mathbf{k})\rangle$ is the the Berry connection and Ω_{xy} is the Berry curvature.

In a centrosymmetric material, the Z_2 topological invariants can be computed straightforwardly using the parity of the wave functions of the occupied bands at the time-reversal invariant momenta (TRIM) in the Brillouin zone [56]. In three dimensions, there are eight TRIM which form a parallelepiped in the BZ, which are given by $\Gamma_i = \frac{1}{2}(n_1\mathbf{b}_1 + n_2\mathbf{b}_2 + n_3\mathbf{b}_3)$, where $\mathbf{b}_1, \mathbf{b}_2, \mathbf{b}_3$ are primitive reciprocal lattice vectors and n_1, n_2, n_3 can take values of 1 and 0. In this method, the strong topological index is given by, $(-1)^{\nu_0} = \prod_{i=1}^{8} \sigma_i$, where $\sigma_i = \prod_m \xi_{2m}^{(i)}$ is the product of parity of the occupied bands at i-th time reversal invariant momentum, and m indicates a band from each doubly degenerate Kramer's pairs. The other three weak topological indices $(\nu_k, k = 1, 2, 3)$ are determined based on the parity of the occupied states at four different combinations of

TRIM in the BZ which form a surface of the parallelepiped excluding the Γ point (in the k_xk_y-, k_yk_z- and k_xk_z- planes) through the relation [59] $(-1)^{\nu_k} = \prod_{i=1}^{4} \sigma_i$.

1.3 Spin-orbit coupling

Spin-orbit coupling (SOC) is one of the most important relativistic effects of electrons in a solid which arises from the interaction of angular momentum of electrons with the internal magnetic field originating from the spin-angular momentum. Strength of SOC is also a crucial ingredient for a material to be topologically nontrivial. In general, relativistic effects in a solid can be quite spectacular which can affect its electronic, vibrational, spectroscopic properties. From elementary quantum mechanics we know that velocity of an electron is proportional to Z (atomic number) of an atom. Thus, the relativistic effects (particularly SOC) become more prominent for heavy elements (i.e. high Z value).

One of the greatest triumphs of the twentieth century's physics was to successfully combine special theory relativity and quantum mechanics to unravel many mysteries in physics. After the initial efforts of Gordon & Klein, it was the British physicist P. A. M. Dirac who was able to give a successful and elegant theory of relativistic quantum mechanics. Here, we show how spin-orbit coupling term naturally arises in the relativistic equation of Dirac. The relativistic Dirac Hamiltonian for a free particle is given by, $H = c\boldsymbol{\alpha}.\mathbf{p} + \beta mc^2$, where $\mathbf{p} = -i\hbar\nabla$ is the momentum operator and c is the speed of light in vacuum. It was shown that the minimum dimension of $\boldsymbol{\alpha}$ and β matrices in the solution of the Dirac Hamiltonian is four [60]. Among many number of possible choices, the standard form of $\boldsymbol{\alpha}$ and β are

$$\boldsymbol{\alpha} = \begin{pmatrix} 0 & \boldsymbol{\sigma} \\ \boldsymbol{\sigma} & 0 \end{pmatrix} \qquad \beta = \begin{pmatrix} I_{2\times2} & 0 \\ 0 & -I_{2\times2} \end{pmatrix} \tag{1.4}$$

where $\boldsymbol{\sigma}$ are the Pauli spin matrices and I is identity matrix of order 2. The Pauli spin

matrices $\boldsymbol{\sigma}$ are given by,

$$\boldsymbol{\sigma}_1 = \begin{pmatrix} 0 & 1 \\ 1 & 0 \end{pmatrix} \qquad \boldsymbol{\sigma}_2 = \begin{pmatrix} 0 & -i \\ i & 0 \end{pmatrix} \qquad \boldsymbol{\sigma}_3 = \begin{pmatrix} 1 & 0 \\ 0 & -1 \end{pmatrix} \tag{1.5}$$

The Dirac Hamiltonian for a particle with charge q in the presence of electromagnetic field $(\mathbf{A}, \phi)$ is [61], $H = c\boldsymbol{\alpha}.(\mathbf{p} - q\mathbf{A}) + q\phi + \beta mc^2$, where $\mathbf{A}$ is the magnetic vector potential and ϕ is the scalar electrostatic potential. This equation can be put into the form as,

$$[(E - q\phi) - c\boldsymbol{\alpha}.(\mathbf{p} - q\mathbf{A}) - \beta mc^2]\psi(\mathbf{r}) = 0, \tag{1.6}$$

where $\psi(\mathbf{r})$ is a four component spinor wave function of the Dirac equation. The four component spinor wave function can be written in terms of two component spinors $\phi(\mathbf{r})$ and $\eta(\mathbf{r})$ as follows,

$$\psi(\mathbf{r}) = \begin{pmatrix} \phi(\mathbf{r}) \\ \eta(\mathbf{r}) \end{pmatrix} \tag{1.7}$$

In the above equation (i.e. Eq. (1.7)), $\phi(\mathbf{r})$ and $\eta(\mathbf{r})$ are called large and small component spinor wave functions, respectively.

For a central field (Coulomb potential near the nucleus), $\mathbf{A} = 0$ and $q\phi = -e\phi = V(\mathbf{r})$. Substituting Eq. (1.7) in Eq. (1.6) we get,

$$\begin{aligned} E\phi(\mathbf{r}) &= c(-i\hbar\boldsymbol{\nabla} - q\mathbf{A}).\boldsymbol{\sigma}\eta(\mathbf{r}) + (q\phi + mc^2)\phi(\mathbf{r}) \\ E\eta(\mathbf{r}) &= c(-i\hbar\boldsymbol{\nabla} - q\mathbf{A}).\boldsymbol{\sigma}\phi(\mathbf{r}) + (q\phi - mc^2)\eta(\mathbf{r}). \end{aligned} \tag{1.8}$$

In the Coulomb field of a nucleus and in the non-relativistic limit of the Dirac equation, from Eq. (1.8), we can write,

$$\eta(\mathbf{r}) = \frac{1}{E' + 2mc^2 - V(r)} c(-i\hbar\boldsymbol{\sigma}.\boldsymbol{\nabla})\phi(\mathbf{r}), \tag{1.9}$$

where $E = E' + mc^2$. In the above Eq. (1.9), $|E'|$ and $|q\phi| = V(\mathbf{r})$ are much smaller than

mc^2 term.

We solve for $\phi(\mathbf{r})$ by substituting Eq. (1.9) in the first equation of Eq. (1.8). Expanding $[E' + 2mc^2 - V(r)]^{-1}$ to lowest order we get,

$$E'\phi(\mathbf{r}) = \Bigg[-\frac{\hbar^2}{2m}\boldsymbol{\nabla}^2 + V(r) + \frac{\hbar^2}{2m}\frac{E' - V(r)}{2mc^2}\boldsymbol{\nabla}^2 + \frac{1}{2m^2c^2}\frac{1}{r}\frac{dV}{dr}\mathbf{L}.\mathbf{S} - \frac{\hbar^2}{4m^2c^2}\frac{dV}{dr}\frac{\partial}{\partial r}\Bigg]\phi(\mathbf{r}), \tag{1.10}$$

where the fourth term represents the spin-orbit coupling Hamiltonian, commonly denoted by H_{SO}.

$$H_{SO} = \frac{1}{2m^2c^2}\frac{1}{r}\frac{dV}{dr}\mathbf{L}.\mathbf{S}. \tag{1.11}$$

While arriving at Eq. (1.10), we have used the following approximations and relations,

$$\begin{cases} [E' + 2mc^2 - V(r)]^{-1} \simeq \frac{1}{2mc^2}[1 - \frac{E' - V(\mathbf{r})}{2mc^2}] \\ \mathbf{L} = \mathbf{r} \times \mathbf{p} = \mathbf{r} \times (-i\hbar\boldsymbol{\nabla}) \\ \mathbf{S} = i\hbar\boldsymbol{\sigma}/2 \end{cases} \tag{1.12}$$

Here, $\mathbf{L}$ and $\mathbf{S}$ represent total orbital angular momentum and spin angular momentum of an atom respectively. The strength of spin-orbit interaction is roughly proportional to Z^4. The physical reasoning behind this is that as Z increases, the number of electrons increase. Therefore, the electrons experience stronger internal magnetic field, and the interaction energy also becomes larger. In crystalline solids, the spin-orbit interaction is $\mathbf{k}$-dependent. For example, at L-point in the Brillouin zone of a cubic material, the spin-orbit splitting is typically 2/3 order of magnitude smaller than at Γ-point [62].

1.4 Overview of the thesis

The work in this thesis involves first-principles theoretical prediction and analysis of topologically nontrivial materials belonging to different symmetry classes (Chapter 3-7)

and investigations of the electronic (Chapter 8) and vibrational (Chapter 9) contributions to thermoelectric properties of topologically nontrivial and related materials. After a brief introduction to the work here, I give an overview of the computational methods in Chapter 2, and summarize the thesis in Chapter 10.

The content of the thesis has been broadly divided into four parts. In the first part (Chapter 3 & Chapter 4), we focus on Sb_2Se_3, β-As_2Te_3, Bi_2Se_3, materials belonging to the same crystal family and topological class (strong topological insulators) at ambient or perturbed conditions. In Chapter 3, we describe the physics of binary chalcogenides (Sb_2Se_3, β-As_2Te_3, Bi_2Se_3) at the electronic topological transition as a function of pressure or strain. In Chapter 4, we investigate the microscopic mechanism responsible for the anomalous temperature dependence of electronic and vibrational properties of Sb_2Te_3 in 200-250 K temperature range. This is relevant to other layered chalcogenides (*e.g.*, Bi_2Se_3, Bi_2Te_3) as well.

The second part (Chapter 5 & Chapter 6) of the thesis is related to the materials that are Dirac semi-metals (DSMs). DSM is a quantum state of matter that exhibits exotic chiral, transport and superconducting properties and also acts as a parent state to other topological states (*e.g.*, topological insulator). In Chapter 5, we predict the existence of topological Dirac semi-metallic state in the strained structure of *non-centrosymmetric* ternary half-Heusler (HH) compounds, where a pair of Dirac points is protected by the three-fold crystal symmetry. Taking LiMgBi as a model system, we determine its topological phase diagram, and discover that topological insulating, Dirac semi-metallic and band insulating states are common to the strained structure of the HH compounds. We also uncover a gapped band insulator to topological insulator transition in LiMgBi, and explain it with symmetry arguments. In Chapter 6, we predict nontrivial topological states in a Zintl family of Bi_2Mg_2X (X=Mg, Ca, Sr, Ba) compounds. While Bi_2Mg_2Ba exhibits a Dirac semi-metallic state at ambient conditions, Bi_2Mg_2Ca and Bi_2Mg_2Sr are narrow band gap topological semiconductors in their native states that can be driven into DSM phase by applying three-fold symmetry preserving strains.

In the third part of my thesis (Chapter 7), we predict yet another exotic quantum state of matter known as weak topological insulator (WTI) in BiSe. The unit cell of BiSe consists of a Bi_2 layer, sandwiched between two Bi_2Se_3 quintuple layers along the c-direction (layered direction of the crystal). We showed that even number of band inversions in its Brillouin zone make this material a WTI. We established its WTI states by calculating the Z_2 topological invariants, which are (0;001). Through calculation of its surface electronic structure, we show that there exists an even number of gapless Dirac cones on its side surface, further confirming the WTI phase.

In the fourth part (Chapter 8 & Chapter 9) of my thesis, we present thermoelectric (TE) properties of topologically nontrivial (Chapter 8) and related chalcogenide materials (Chapter 9). In Chapter 8, we present our work on the electronic contributions to thermoelectric properties of materials belonging to different symmetry and topological classes. We find that multiple sub-band structure, small band gap of topological insulators, and their vicinity to a metallic state associated with an ETT are responsible for their superior TE performance. In Chapter 9, we focus on vibrational properties relevant to thermoelectric performance of InTe ($In^{1+}In^{3+}Te_2^{2-}$) and $TlInTe_2$ compounds, both of which are shown to exhibit ultralow lattice thermal conductivity (κ_l). These compounds share similar crystal structures consisting of a rigid anionic and loosely bound cationic sub-structures showing the characteristics of part-crystalline part-liquid-like materials. With the help of first-principles calculations based on density functional theory, we show that the ultralow κ_l of these compounds arises from (a) very low sound velocities, and (b) the rattling vibrations of In^{1+} and Tl atoms along z-directions in InTe and $TlInTe_2$ respectively, which scatter the heat carrying acoustic phonons through strong anharmonic phonon-phonon interactions. The lattice anharmonicity in these compounds is evident in their anomalously high Grüneisen parameters.

Chapter 2

Methods and Formalism

In this chapter, we briefly discuss the theoretical background and the computational methods that we employed in our calculations within the framework of density functional theory.

First, we show in section 2.1 how calculation of electronic structure of a material can be carried out within certain approximations *e.g.*, Born-Oppenheimer [63] and classical nuclei approximations. Using these, many body Schrödinger equation can be reduced to a set of coupled one electron equations of Kohn-Sham, which then can be practically solved (see section 2.2). The total energy obtained after solving the Kohn-Sham Hamiltonians can be used further to calculate many physical quantities. For example, first order derivatives of total energy with respect to the electric, magnetic field, atomic displacement give polarization, magnetization and forces, respectively. Similarly, dielectric constant, magnetic susceptibility, elastic moduli can be obtained by taking the second order derivatives of the total energy with respect to electric, magnetic fields and strain, respectively.

Phonons are quanta of lattice vibrations in a material. In section 2.5, we have discussed the theoretical approach within the adiabatic density functional perturbation theory (DFPT) [64] used to calculate the phonon frequencies and related properties. In section 2.6, we describe how maximally localized Wannier function (MLWF) [13] can be used efficiently to calculate Berry phase, Berry curvature, Chern number of a material.

Using MLWF and employing the idea of time reversal polarization [14,65], we review how Z_2 topological invariants can be obtained. In the final section (2.7) of this chapter, we have presented a semi-classical Boltzmann transport equation which is used to calculate electronic contributions to thermoelectric properties *e.g.*, electrical conductivity, Seebeck coefficients, thermoelectric power factor.

2.1 Electronic structure

The total quantum mechanical Hamiltonian of a material consisting of electrons and ions is written as,

$$\mathcal{H} = \sum_I \frac{\mathbf{P}_I^2}{2M_I} + V(\mathbf{R}_I) + \sum_i \frac{\mathbf{p}_i^2}{2m} + \sum_{i,I} u(\mathbf{r}_i, \mathbf{R}_I) + \frac{1}{2}\sum_{i\neq j} \frac{e^2}{|\mathbf{r}_i - \mathbf{r}_j|}, \tag{2.1}$$

where $\mathbf{P}_I$ and M_I are the momentum and mass of I-th ion. $\mathbf{p}_i$ and m are the momentum and mass of the i-th electron. $V(\mathbf{R}_I) = \frac{e^2}{2}\sum_I \sum_{J\neq I} \frac{Z_I Z_J}{|\mathbf{R}_I - \mathbf{R}_J|}$ and $\frac{e^2}{|\mathbf{r}_i - \mathbf{r}_j|}$ are inter-nuclear and inter-electronic Coulomb interactions, respectively. $u(\mathbf{r}_i, \mathbf{R}_I) = -e^2 \sum_{I=1} \sum_{i=1} \frac{Z_I}{|\mathbf{R}_I - \mathbf{r}_i|}$ is the electron-ion interaction potential. Here Z_I is the atomic number of the I-th ion.

Many properties of a material can in principle be derived from the above Hamiltonian, if we can solve Eq. (2.1). As a material consists of large number electrons and ions and their degree of freedoms are coupled to each other, this is a rather hard problem, which is almost impossible to solve. Hence, we need to use some reasonably good approximations in order to make the solution of Eq. (2.1) practically feasible.

2.1.1 Born-Oppenheimer approximation

The adiabatic or Born-Oppenheimer approximation [63] is one of the most commonly used approximations involved in the calculation of electronic structure of a material. This assumption has been made observing the fact that time-scales associated with the motion of the nuclei (ions) are much slower than those associated with electronic motion. Therefore,

electrons instantaneously follow the motion of the ions, remaining in the same stationary (adiabatic) state (ground or excited) without causing non-radiative transition by the nuclear dynamics. If this condition is satisfied in a material, then dynamics of the electrons is said to be adiabatic. Non-adiabatic effects in a system are inversely proportional to energy difference between the adiabatic electronic eigenstates (*i.e.* band gap) and hence can be safely ignored if the energy gap of a material is large. Hence, Born-Oppenheimer approximation holds good in semiconductors and insulators. But in materials with zero band gaps (*e.g.*, metals, semimetals), the Born-Oppenheimer approximation may break down. One example of such systems is graphene [66] which has a zero band gap. We will show interesting consequences of broken adiabaticity on the vibrational properties of rhombohedral Sb_2Se_3 in the third chapter of this thesis.

Within the Born-Oppenheimer approximation, we can decouple the electronic and ionic degrees of freedom, and hence Eq. (2.1) can be written as,

$$\mathcal{H}\Xi(\mathbf{R}_I, \mathbf{r}_i) = E\Xi(\mathbf{R}_I, \mathbf{r}_i), \tag{2.2}$$

where $\Xi(\mathbf{R}_I, \mathbf{r}_i) = \Psi(\mathbf{R}_I)\Phi_{\mathbf{R}_I}(\mathbf{r}_i)$ is the total wave function of a material constituting the electronic part ($\Phi_{\mathbf{R}_I}(\mathbf{r}_i)$) and the ionic part ($\Psi(\mathbf{R}_I)$). The total energy of the electrons thus can be obtained through solving

$$H_e\Psi(\mathbf{R}_I) = E_e(\mathbf{R}_I)\Psi(\mathbf{R}_I), \tag{2.3}$$

where $H_e = T_e + U_{ee} + u(\mathbf{r}_i, \mathbf{R}_I)$ is the electronic Hamiltonian. T_e is the kinetic energy of the electrons. $U_{ee} = \frac{1}{2}\sum_{i\neq j}\frac{e^2}{|\mathbf{r}_i - \mathbf{r}_j|}$ is inter-electron interaction potential and $u(\mathbf{r}_i, \mathbf{R}_I)$ is the electron-ion interaction potential between the electrons and ions.

2.1.2 Classical nuclei approximation

The masses of the ions (nuclei) are much larger than the electronic mass. Therefore one can safely assume that quantum phase coherence of the nuclear wave functions is very less

or doest not exist at all and hence, we can safely treat nuclei as classical particles. This is known as *classical nuclei approximation* which is the second most important assumption made in simplifying the electronic structure of a matter. Within this approximation, we can write the total nuclear wave function as the product of all individual nuclear wave function and therefore we can neglect the exchange and correlation energy arising from their interactions.

The dynamics of the mean values of position and momentum operators can be obtained through Ehrenfest's theorem

$$i\hbar\frac{d\langle\mathbf{R}\rangle}{dt} = \langle[\mathcal{H},\mathbf{R}]\rangle = i\hbar\frac{\langle\mathbf{P}\rangle}{M} \Rightarrow M\frac{d\langle\mathbf{R}\rangle}{dt} = \langle\mathbf{P}\rangle \tag{2.4}$$

$$i\hbar\frac{d\langle\mathbf{P}\rangle}{dt} = \langle[\mathcal{H},\mathbf{P}]\rangle = -i\hbar\langle\nabla E_e(\mathbf{R})\rangle, \tag{2.5}$$

where $\mathbf{R}$ and $\mathbf{P}$ are position and momentum operators respectively. E_e is the total energy corresponding to the electronic Hamiltonian of Eq. (2.3). Combining Eq. (2.4) and Eq. (2.5), we can arrive at the very familiar Newton's equation of motion,

$$M\frac{d^2\langle\mathbf{R}\rangle}{dt^2} = -\langle\nabla E_e(\mathbf{R})\rangle \tag{2.6}$$

From the Hellmann-Feynman theorem [67], we know that the variation of the electronic energy with respect to any external parameter, λ, coupled to the electrons, can be obtained as,

$$\frac{\partial E_e(\lambda)}{\partial\lambda} = \left\langle \phi_{\mathbf{R}_I}(\mathbf{r}) \middle| \frac{\partial H_e(\lambda)}{\partial\lambda} \middle| \phi_{\mathbf{R}_I}(\mathbf{r}) \right\rangle, \tag{2.7}$$

where $\phi_{\mathbf{R}_I}(\mathbf{r})$ is the electronic wave function for the nuclear configuration $\{\mathbf{R}_I\}$. If $E_{PES}(\mathbf{R}_I) = E_e(\mathbf{R}_I) + V(\mathbf{R}_I)$ can be defined as the potential energy surface (PES) of any system for some ionic configurations $\{\mathbf{R}_I\}$, then together with the help of Eq. (2.6) and Eq. (2.7), we can write for $\lambda = \mathbf{R}_I$,

$$M_I\frac{d^2\langle\mathbf{R}_I\rangle}{dt^2} = -\left\langle \phi_{\mathbf{R}_I}(\mathbf{r}) \middle| \frac{\partial H_e(\lambda)}{\partial\lambda} \middle| \phi_{\mathbf{R}_I}(\mathbf{r}) \right\rangle - \frac{\partial V(\mathbf{R}_I)}{\partial\mathbf{R}_I}. \tag{2.8}$$

The solution of the stationary problem *i.e.* $\nabla E_{PES}(\mathbf{R}_I) = 0$ to find the minimum force on each ion through Eq. (2.7) is known as *geometry optimization* of a material. In order to achieve this, we have to first determine the total electronic energy $E_e(\mathbf{R}_I)$ of the system. Solving the time independent Schrödinger equation Eq. (2.3) to get $E_e(\mathbf{R}_I)$ is known by the name of *electronic structure calculation* [68].

2.2 Density functional theory

Among all the existing methods which can calculate the electronic structure and properties of materials, density functional theory (DFT) is the most popular and widely used by physicists, chemists as well as materials scientists. The main idea behind density functional theory is that it casts the interacting many-body problem into a set of single particle problems via the charge density of the electrons, where many-body effects are included through the exchange-correlation energy functional. The foundation of DFT lies on the basis of two powerful theorems given by Hohenberg & Kohn [69] in 1964, followed by their practical implementation by Kohn & Sham [70] in 1965.

The modern electronic structure calculation began with the idea of L. H. Thomas [71] and E. Fermi [72], who around the same time of Hartree, thought that the full electronic density can be used as a fundamental variable in many body problems rather than the complicated many-body wave function itself. Their approximation is known as *Thomas-Fermi* approximation.

2.2.1 Thomas-Fermi model

Thomas and Fermi wrote the total electronic energy of an inhomogeneous system as a functional of electron density ρ as given below,

$$E_\alpha[\rho] = \int \rho(\mathbf{r})\epsilon_\alpha[\rho(\mathbf{r})]d\mathbf{r}, \tag{2.9}$$

where $\epsilon_\alpha[\rho(\mathbf{r})]$ is the energy density which consists of the contributions coming from the kinetic, exchange and correlation energies of a homogeneous electron gas for which good approximations already exist. This energy density is calculated locally in terms of $\rho(\mathbf{r})$ at every point and integrated over whole space to get the total energy. This is known as *local density approximation* (LDA). The above expression in the square bracket of Eq. (2.9) is called a functional as it is a function of another function (*i.e.* electron density $\rho(\mathbf{r})$).

The exchange and correlation effects were introduced in the same *local* spirit by Dirac [73] and Wigner [74] respectively and are given by,

$$E_X[\rho] = -C_X \int \rho(\mathbf{r})^{4/3} d\mathbf{r} \tag{2.10}$$

$$E_C[\rho] = -a \int \frac{\rho(\mathbf{r})^{4/3} d\mathbf{r}}{b + \rho(\mathbf{r})^{1/3}}, \tag{2.11}$$

where $C_X = \frac{3}{4}(3/\pi)^{1/3}$. a, b are numerical constants. When exchange interaction is included, the theory is called *Thomas-Fermi-Dirac* approximation. Finally the total electronic energy according to the Thomas-Fermi-Dirac theory as a functional of electron density can be written as,

$$\begin{aligned} E_{TFD}[\rho] &= C_k \int \rho(\mathbf{r})^{5/3} d\mathbf{r} + \int \rho(\mathbf{r}) \nu_{ext}(\mathbf{r}) d\mathbf{r} \\ &+ \frac{1}{2} \iint \frac{\rho(\mathbf{r})\rho(\mathbf{r'})}{|\mathbf{r} - \mathbf{r'}|} - C_X \int \rho(\mathbf{r})^{4/3} d\mathbf{r} + E_C[\rho], \end{aligned} \tag{2.12}$$

where $\int \rho(\mathbf{r}) \nu_{ext}(\mathbf{r}) d\mathbf{r} = V_{ext}$ is the external field arising from the electron-ion interactions and $C_k = \frac{3}{10}(3\pi^2)^{2/3}$.

2.2.2 Hohenberg-Kohn theorems

The modern density functional theory stands upon two powerful theorems given by Hohenberg & Kohn [69] who formulated DFT as an exact ground state theory of a many-electron system. This formulation of DFT applies to any interacting system where electrons are assumed to move in an external potential $V_{ext}(\mathbf{r})$. The Hamiltonian of such systems can

be written as,

$$H_e = T_e + V_{ext}(\mathbf{r}) + U_{ee}(\mathbf{r}) \tag{2.13}$$

- 1st Hohenberg-Kohn theorem - For any system of interacting particles in an external potential $V_{ext}(\mathbf{r})$, the potential $V_{ext}(\mathbf{r})$ is uniquely determined by the ground state electronic density $\rho_0(\mathbf{r})$ of the system within the ambiguity of an additive constant.

- 2nd Hohenberg-Kohn theorem - A universal functional of energy $E[\rho]$ can be defined for any external potential $V_{ext}(\mathbf{r})$. The ground state energy of a system is the global minimum of this functional. The electronic density $\rho(\mathbf{r})$ which minimizes the functional is called ground state density $\rho_0(\mathbf{r})$ of the system.

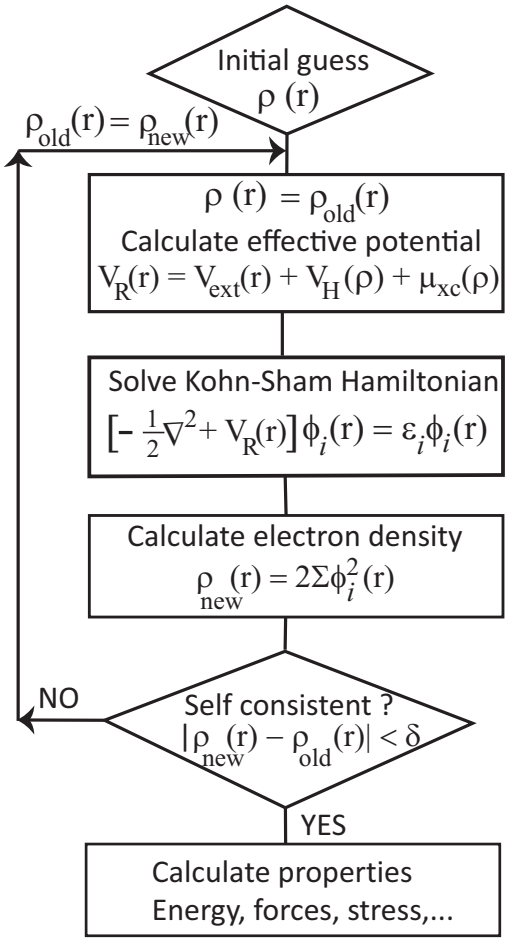

Figure 2.1: Flow chart of a typical DFT calculation.

2.2.3 Kohn-Sham approach to DFT

Having established the basic formulas, the problem arises in casting the many-body theory in a tractable scheme based on the Hohenberg-Kohn theorems where the total energy as a functional of electron density is not known. The problem, however, was made easy by Kohn & Sham [70] who described systems consisting of non-interacting electrons having same $\rho(\mathbf{r})$ moving in a mean filed of external potential arising from the complex electron-ion and electron-electron interactions. This is the central theme of Kohn-Sham approach to density functional theory. The idea of Kohn-Sham is that if one can find any non-interacting electronic system that produces the same electronic density as that of the interacting system, then the kinetic energy of the electrons can be approximated through one electron orbitals. The kinetic energy calculated in this way is not exactly the same as that of the kinetic energy obtained from the many-body wave functions. The missing fraction in the energy comes due to the *correlation* among the electrons which can be included in correlation effects in the exchange-correlation energy functional. The ground state density matrix can be written as (in terms one electron orbitals),

$$\rho(\mathbf{r}, \mathbf{r'}) = \sum_i f_i \phi_i(\mathbf{r}) \phi_i^*(\mathbf{r'}), \tag{2.14}$$

where f_i are the occupations of the one electron orbitals $\phi_i(\mathbf{r})$. The kinetic energy of a non-interacting is

$$T = -\frac{\hbar^2}{2m} \sum_i f_i \left\langle \phi_i \right| \nabla^2 \left| \phi_i \right\rangle \tag{2.15}$$

Let us assume that the reference potential for a non-interacting system be $\nu_R(\mathbf{r})$. The electron density of this system becomes $\rho(\mathbf{r}) = \sum_i f_i |\phi_i(\mathbf{r})|^2$, while the kinetic energy is

$$T_R[\rho] = -\frac{\hbar^2}{2m} \sum_i \left\langle \phi_i \right| \nabla^2 \left| \phi_i \right\rangle, \tag{2.16}$$

where $\phi_i(\mathbf{r})$'s are the solutions of the one electron Kohn-Sham (KS) Hamiltonian,

$$H_e = -\frac{\hbar^2}{2m}\nabla^2 + \nu_R(\mathbf{r}). \tag{2.17}$$

$\nu_R(\mathbf{r})$ is the potential for the reference system and will be defined shortly. With the above equations for the non-interacting reference system, the *Kohn-Sham* energy functional can be written as,

$$E_{KS}[\rho] = T_R[\rho] + \int \rho(\mathbf{r})\nu_{ext}(\mathbf{r})d\mathbf{r} + \frac{1}{2}\iint \frac{\rho(\mathbf{r})\rho(\mathbf{r'})}{|\mathbf{r}-\mathbf{r'}|}d\mathbf{r}d\mathbf{r'} + E_{XC}[\rho], \tag{2.18}$$

where $T_R[\rho]$ is the kinetic energy of the electrons in the non-interacting reference system. The minimization of the Eq. (2.18) with respect to density ρ, subject to the constraint that electron density integrates out to the total number of electrons in the system, will lead to ground state energy of the system.

The reference potential energy can be written as,

$$\begin{aligned} \nu_R(\mathbf{r}) &= \nu_{ext}(\mathbf{r}) + \iint \frac{\rho(\mathbf{r'})}{|\mathbf{r}-\mathbf{r'}|}d\mathbf{r'} + \mu_{XC}[\rho(\mathbf{r})] \\ \text{with,} \qquad \mu_{XC}[\rho(\mathbf{r})] &= \frac{dE_{XC}[\rho]}{d\rho(\mathbf{r})} \end{aligned} \tag{2.19}$$

This equation has to be solved self-consistently making sure that the density used to construct the reference potential matches (*i.e.* self-consistent) that obtained from $\phi_i(\mathbf{r})$'s that are solutions of Kohn-Sham Hamiltonian Eq. (2.17) via $\rho(\mathbf{r}) = \sum_i f_i|\phi_i(\mathbf{r})|^2$.

2.2.4 Pseudopotential-based calculations

Wave functions of the free electrons can be written in terms of plane waves. These plane waves are the exact solutions to the Schrödinger equation. But the situation in a real crystal is far from the case of free electrons. Due to presence of nuclear potential, wave functions of the electrons in an atom show oscillatory behavior in their core regions. Due to orthogonality between core and the valence states, the valence wave function

in the core region become more oscillatory with many number of nodes. To represent the electronic wave functions of a real material with plane waves, one needs in principle an infinite number of plane waves in the expansion. This makes the diagonalization of the KS Hamiltonian quite demanding. To overcome this problem, a number of recipes were proposed like *augmented plane wave* (APW) [75] method where the plane wave expansion was augmented with the solutions of the atomic problem in a spherical core region around the atoms and the potential outside this sphere is assumed to be zero. Another approach, called *orthogonalized plane wave* (OPW) method was proposed by Herring [76] who expanded the valence states as a linear combination of plane waves and choose the expansion coefficients so as to make the resultant wave function orthogonal to the core states.

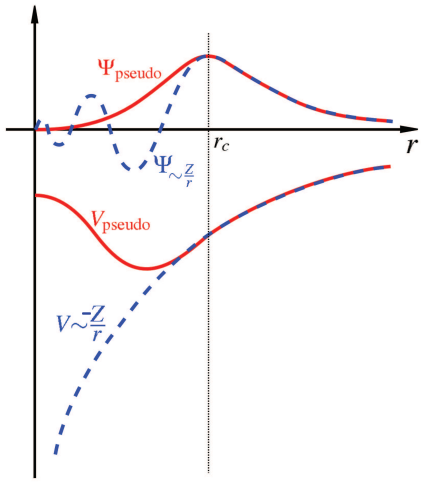

Figure 2.2: Schematic representation of a pseudopotential. r_c is the cut-off radius above which the pseudo wave function matches the all-electron wave function. This figure is taken from https://en.wikipedia.org/wiki/Pseudopotential.

Pseudopotential approximation derives its idea from the OPW method. Noting the fact that it is the valence electrons which take part in bonding and other chemical activity and core electrons mostly are inert in a material, one can replace the interaction between the core region (which consists of nuclei and core electrons) and the valence electrons with a smooth effective potential which has the same scattering properties as those of the true potential. With this smooth potential, one can construct a node-less wave function

(pseudo wave function), which needs a small number of plane waves in its expansion and thus rendering the diagonalization of the Hamiltonian feasible in practical calculation.

The original pseudopotential theory is due to Philips & Kleinman [77], who showed that one can construct a smooth valence wave function $\tilde{\phi}_v$ which is not orthogonal to the core wave states (ϕ_c) by combining the core and true valence wave function (ϕ_v) in the following way,

$$|\tilde{\phi}_v\rangle = |\phi_v\rangle + \sum_c \alpha_{cv} |\phi_c\rangle \,, \tag{2.20}$$

where $\alpha_{cv} = \langle\phi_c|\tilde{\phi}_v\rangle \neq 0$. This pseudo wave function satisfies the following pseudo Hamiltonian which has same eigenvalue as the original Hamiltonian.

$$\left[\mathcal{H} + \sum_c (\epsilon_v - \epsilon_c) |\phi_c\rangle \langle\phi_c|\right] |\tilde{\phi}_v\rangle = \epsilon_v |\tilde{\phi}_v\rangle \,, \tag{2.21}$$

where $\mathcal{H} = T + V$, $V = (-Z_C/\mathbf{r})$ is the bare Coulomb potential. Now we can define the pseudopotential as,

$$V_{PS} = -\frac{Z_c}{\mathbf{r}} + \sum_c (\epsilon_v - \epsilon_c) |\phi_c\rangle \langle\phi_c| \tag{2.22}$$

This pseudopotential acts differently on quantum states of different angular momentum. The most general form of a pseudopotential is thus given by,

$$V_{PS}(\mathbf{r}) = \sum_{l=0}^{\infty} \sum_{m=-l}^{l} v_{PS}^{l}(r) |lm\rangle \langle lm| \,, \tag{2.23}$$

where $\langle\mathbf{r}|lm\rangle = Y_{lm}(\theta, \phi)$ are spherical harmonics and v_{PS}^{l} is the pseudopotential corresponding to the angular momentum l.

Traditionally, a pseudopotential is divided into *local* and *non-local* parts, where the former is long-ranged and the later is typically short-ranged. In the Eq. (2.22), the first and the second terms are *local* and *non-local* parts of a pseudopotential, respectively. Using the notation of spherical harmonics, the non-local part of a pseudopotential can be

written as,

$$V_{NL}(\mathbf{r}) = \sum_{lm} v^{l}_{PS}(r)\delta(r - r')Y_{lm}(\hat{r})Y^{*}_{lm}(\hat{r}') \tag{2.24}$$

2.2.5 All-electron method

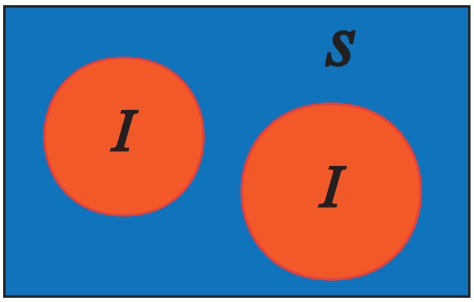

Figure 2.3: Schematic representation of a LAPW basis set. The unit cell is divided into atom centered region (red color) and interstitial region (blue color).

Results of all-electron (core and valence electrons are treated explicitly) calculations have higher accuracy but are computationally more expensive than pseudopotential-based (valence electrons only) electronic structure calculations. In addition to pseudopotential-based methods, we have used here an all-electron linearized augmented plane wave (LAPW) method to calculate electronic structure and related properties of some of the materials studied in this thesis. LAPW method [78] derives its idea from Slater's augmented plane wave (APW) [75, 79] method which includes core electronic states and does not need a pseudpotential. To obtain total energies and eigenvalues of the electrons in a solid using the LAPW method, we use a basis set achieved by dividing the unit cell into non-overlapping spherical regions centered at each atom and the interstitial region. Two different types of basis sets are used in these two regions: plane wave basis set is used in expansion of the electronic wave functions inside the interstitial region, and it is augmented by atomic like wave functions (linear combination of the solutions of the radial Schrödinger equation and spherical harmonics) in the space inside every atomic sphere. These atomic-like wave functions form the basis set inside each non-overlapping atomic

sphere. In the LAPW formalism, the basis wave function thus can be written as,

$$\phi(\mathbf{r}) = \begin{cases} \Omega^{-\frac{1}{2}} \sum_G C_G e^{i(\mathbf{k}+G).\mathbf{r}} & for \quad r \in S, \\ \sum_{lm} (A_{lm} u_{lm}(\mathbf{r}) + B_{lm} u'_l(\mathbf{r})) Y_{lm}(\mathbf{r}) & for \quad r \in I \end{cases} \tag{2.25}$$

Here Ω, I and S denote the unit cell volume, atom centered and interstitial regions, respectively. $u'_l(\mathbf{r}) = \frac{\partial u_l}{\partial E}$, and $u_l(\mathbf{r})$ are the radial solution of the Schrödinger equation for an atom. C_G, A_{lm} and B_{lm} are expansion coefficients, and the subscripts l and m denote angular and magnetic quantum numbers, respectively. Y_{lm} are spherical harmonics.

2.3 Exchange & correlation energy functional

The main approximation in density functional theory is in the formulation of a correct exchange-correlation energy functional. Among all the existing functionals, local density approximation (LDA) and generalized gradient approximation (GGA) are the most commonly and widely used, due to their simplicity and reasonable accuracy.

In LDA, the effect of exchange and correlation functionals are considered to be local in nature as it was assumed by Kohn & Sham in their seminal paper [70]. In this approach, the inhomogeneous electronic system is thought to be locally homogeneous and exchange-correlation energy is obtained simply by integrating the exchange-correlation energy density at each point in the space. This energy density is known accurately for homogeneous electron gas [73] as a function of density, which is used in the LDA exchange-correlation energy functional:

$$E_{xc}^{LDA}[\rho] = \int d^3\mathbf{r} \rho(\mathbf{r}) \epsilon_{xc}^{homo}[\rho(\mathbf{r})] \tag{2.26}$$

The LDA approximation has been quite successful for many systems especially for those whose electron density is relatively uniform such, as bulk metals, ionic crystals etc. But, it is somewhat limited in certain properties of semiconductors, strongly correlated systems

due to fact that the excitation spectrum of homogeneous electron gas is gap-less and exchange-correlation energy is regular [68]. LDA also fails to capture weak inter-molecular bonds, hydrogen bonds etc.

The improvement over LDA leads to the development of generalized gradient approximation (GGA). In general, the exchange-correlation energy in GGA is written as [80],

$$E_{xc}^{GGA}[\rho] = \int d^3\mathbf{r}\rho(\mathbf{r})\epsilon_{xc}[\rho(\mathbf{r}), |\nabla\rho|] \tag{2.27}$$

The GGA method turns out to be better than LDA in the sense that it improves binding energies and sometimes bond lengths. For these reasons, we have used GGA exchange-correlation functional in all the *ab-initio* calculations described in this thesis.

2.4 Inclusion of spin-orbit coupling

The effects of spin-orbit coupling (SOC) are quite significant for materials consisting of heavy elements. Most importantly, while dealing with materials with non-trivial electronic topology, inclusion of SOC in calculations of electronic structure becomes inevitable. Here, we briefly discuss how the effect of SOC is included in pseudopotential-based calculations as well as all-electron LAPW method.

To include the effect of SOC, we need to construct the pseudopotentials from the large components of the spinor solution of the Dirac equation, which give projectors ($\beta_{l,j}$) and pseudopotential coefficients for each value of l, j, the orbital and total angular momentum ($j = l + s$, with s being the spin angular momentum). The non-local part of a pseudopotential includes both scalar relativistic effects and spin-orbit coupling [81],

$$V_{NL} = \sum_I \sum_{l,j,m_j} E_{l,j}^I \left|\beta_{l,j}^I Y_{l,\frac{1}{2}}^{I,j,m_j}\right\rangle \left\langle\beta_{l,j}^I Y_{l,\frac{1}{2}}^{I,j,m_j}\right|, \tag{2.28}$$

where $Y_{l,\frac{1}{2}}^{I,j,m_j}$ are the two-components spin-angle functions which appear in the solution of the Dirac equation in a spherically symmetric potential.

In an all-electron electronic structure calculation (*e.g.*, LAPW method), the effect of SOC is taken into account through a second variational procedure [82, 83].

$$H\psi(\mathbf{r}) = \varepsilon\psi(\mathbf{r}) + H_{SO}\psi(\mathbf{r}), \tag{2.29}$$

where ψ is the four-component spinor of the Dirac equation as given in Eq. (1.7), and H_{SO} is the spin-orbit coupling Hamiltonian as given in Eq. (1.11), which operates on the large component of the four-component spinor wave functions.

2.5 Phonons

In condensed matter physics, properties of a material typically arise from collective excitations. For example, to explain the electrical conductivity of a material we describe a material consisting of Fermi liquid or an electron gas. The thermal conductivity of a material is explained through collective excitations of lattice vibrations and so on. In fact, to explain any physical phenomena occurring over a time scale, we need to consider collective behavior arising from all particles inside a matter instead dealing with individual particle.

Phonons are quanta of lattice vibrations in a crystal. To calculate any property of a material arising from the lattice vibrations, we have to treat the collective oscillations of all the atoms. Phonon dispersion of a crystal reveals very interesting physics and insightful dynamical information of a system. Now-a-days, with availability of powerful computers, efficient and optimized algorithms, phonon dispersion of a material is routinely calculated and used for further post-processing analysis *e.g.*, calculation of the vibrational contribution to free energy at finite temperature.

2.5.1 Density functional perturbation theory

Lattice-dynamical properties of a system are not only related to the lattice vibrations, but also it has some profound electronic connections. A combination of density functional

theory and linear response theory gives rise to what is known as the density functional perturbation theory [84, 85]. Now we will discuss the basic mathematical formulation of this theory. Born-Oppenheimer approximation helps in decoupling the electronic degrees of freedom from that of the vibrational one. The equation of ions which arises from this approximation can be written following Eq. (2.1) as,

$$\Big[-\sum_I \frac{\hbar^2}{2M_I}\frac{\partial^2}{\partial \mathbf{R}_I^2} + V(\mathbf{R}_I) + E_{e\mathbf{R}_I}\Big]\Psi(\mathbf{R}_I) = E\Psi(\mathbf{R}_I), \tag{2.30}$$

The lattice-dynamical properties of any system is given by the eigenvalue E and eigenfunction $\Psi(\mathbf{R}_I)$ of this equation. Thus, the energy $E_{e\mathbf{R}_I}$ is the ground state energy of the interacting electrons moving in the field of nuclei fixed at $\mathbf{R}_I$. The equilibrium geometry of the system or *geometry optimization* is given by the condition that force acting on each atom should be minimum and this is written mathematically as,

$$F_I = -\frac{\partial E_{e\mathbf{R}_I}}{\partial \mathbf{R}_I} - \frac{\partial V(\mathbf{R}_I)}{\partial \mathbf{R}_I} \tag{2.31}$$

The vibrational frequencies (ω) of a system is obtained from the Hessian of E after being scaled properly by the nuclear masses by solving the following equation.

$$det\left|\frac{1}{\sqrt{M_I M_J}}\frac{\partial^2 E}{\partial \mathbf{R}_I \partial \mathbf{R}_J} - \omega^2\right| = 0 \tag{2.32}$$

The forces on the atoms or the first order derivative of energy can be obtained accurately using Hellman-Feynman theorem with the help of Eq. (2.7) and Eq. (2.8). The electronic Hamiltonian depends on the nuclear coordinates through the electron-nuclear interaction and it couples to the electrons through electronic charge density. In terms of electronic charge density, Eq. (2.31) can be written as,

$$F_I = -\int \rho_{\mathbf{R}_I}(\mathbf{r})\frac{\partial u(\mathbf{r}_i, \mathbf{R}_I)}{\partial \mathbf{R}_I} d\mathbf{r} - \frac{\partial V(\mathbf{R}_I)}{\partial \mathbf{R}_I}, \tag{2.33}$$

where $\rho_{\mathbf{R}_I}(\mathbf{r})$ is the ground state electronic density corresponding to nuclear configuration $\{\mathbf{R}_I\}$. The second derivative of E yields,

$$\begin{aligned}\frac{\partial^2 E}{\partial \mathbf{R}_I \partial \mathbf{R}_J} &= -\frac{\partial F_I}{\partial \mathbf{R}_J} \\ &= \int \frac{\partial \rho_{\mathbf{R}_I}(\mathbf{r})}{\partial \mathbf{R}_J} \frac{\partial u(\mathbf{r}_i, \mathbf{R}_I)}{\partial \mathbf{R}_I} d\mathbf{r} + \int \rho_{\mathbf{R}_I}(\mathbf{r}) \frac{\partial^2 u(\mathbf{r}_i, \mathbf{R}_I)}{\partial \mathbf{R}_I \partial \mathbf{R}_J} d\mathbf{r} + \frac{\partial^2 V(\mathbf{R}_I)}{\partial \mathbf{R}_I \partial \mathbf{R}_J},\end{aligned} \tag{2.34}$$

where $u(\mathbf{r}_i, \mathbf{R}_I)$ and $V(\mathbf{R}_I)$ are the electron-ions and ion-ions interaction potentials, respectively. From Eq. (2.34) it can be seen that the Hessian matrix or the force constant matrix requires ground state electronic charge density $\rho_{\mathbf{R}_I}(\mathbf{r})$ as well the *linear response* of it under the perturbation of nuclear geometry. Hence the name *density functional perturbation theory*.

2.6 Wannier function

Wannier function (WF) is a localized wavefunction, obtained through a unitary transformation of the extended Blöch functions [86–88]. Given an isolated set of J Blöch bands which are the eigenstates of a Hamiltonian, it is always possible to find another set of J bands through a unitary transformation, that might not be the Hamiltonian eigenstates but span the same Hilbert space as the original set of Blöch bands. Thus, one trades off localization in energy for localization in space [13]. Although the concept of Wannier function has been prevalent in solid state theory for a long time, practical calculations involving WFs were rarely performed due to (a) the phase indeterminacy (*i.e.* arbitrary gauge freedom) of the Blöch functions ($\psi_{n\mathbf{k}}$) at each wave vector ($\mathbf{k}$), which imposes non-uniqueness in carrying out arbitrary unitary transformation to a set of occupied Blöch function and (b) presence of degeneracy in the electronic band structure at certain high symmetric points in the Brillouin zone (BZ), which makes it difficult to separate the bands and apply "wannierization". Therefore, it is important to choose first a proper subset of bands in a given material before determining its WFs.

One of the most important developments in this regard came from the work of Marzari

and Vanderbilt [89], who introduced a "maximal localization" criterion for identifying a unique set of WFs in a given crystalline insulating material. The procedure of the maximal localization was later extended to the case of metals in which some of the bands have partial occupations.

The WF centered in the **R**-th unit cell and corresponding to n-th band is given by [89],

$$|\mathbf{R}n\rangle = \frac{V}{(2\pi)^3}\int d\mathbf{k} e^{-\mathbf{k}.\mathbf{R}} |\psi_{n\mathbf{k}}\rangle \,, \tag{2.35}$$

where **R** is the real space lattice vector and V is the volume of the unit cell.

Wannier functions are useful for a number of reasons. For example, WFs can provide better insight into the nature of chemical bonding, otherwise missing from the calculation based on an extended Blöch functions. Using WF basis, accurate model Hamiltonian can be constructed which can be used to analyze the physics and chemistry of a particular group of bands in the electronic structure. Thus, WFs have become an established tool to post-processing electronic structure calculation based on modern state-of-the-art density functional theory, to obtain useful information. More interestingly, the evolution of the charge centres of the WFs are formally linked to the Berry phase of the Blöch function. This is clarified in the context of modern theory polarization [90, 91] and more recently it has gained significant attention in the research of topological physics as Berry curvature, Chern number, and topological invariants [14] can be computed easily in the framework of maximally localized Wannier function (MLWF). In the following we will discuss how to calculate Z_2 topological invariants using MLWFs.

2.6.1 Maximally localized Wannier function (MLWF)

The above formula of the Wannier function involves only a single Blöch band, n. In general, we can consider a manifold of J Blöch bands which are separated from any higher or lower bands outside the manifold. Within this manifold, these bands may cross each other as a function of **k** and degeneracies may be present. In the multi-band case

the above formula is generalized to

$$|\mathbf{R}n\rangle = \frac{V}{(2\pi)^3}\int d\mathbf{k}e^{-\mathbf{k}.\mathbf{R}}\sum_{m=1}^{J}U_{nm}^{(\mathbf{k})}|\psi_{m\mathbf{k}}\rangle\,, \tag{2.36}$$

where $U_{nm}^{(\mathbf{k})}$ is the unitary transformation or gauge transformation that performs a rotation of the original Blöch functions which are the eigenstates of the Hamiltonian *i.e.*

$$|\tilde{\psi}_{n\mathbf{k}}\rangle = \sum_{m=1}^{J}U_{nm}^{(\mathbf{k})}|\psi_{m\mathbf{k}}\rangle \tag{2.37}$$

In general, the eigenstates of a Hamiltonian may not be smooth functions of $\mathbf{k}$. So, to get the well-localized WFs in the real space, we need to cancel out the discontinuity of the Blöch bands using this unitary transformation and restore the smooth-ness. Even if this unitary gauge transformation might not be necessary in the wannierization procedure if the bands in the manifold do not touch each other within the BZ, this unitary rotation becomes necessary [89] to get well-localized WFs.

A very general and widely used procedure to generate maximally localized Wannier functions was given by Marzari and Vanderbilt [89], who enforce localization by introducing a *localization criterion* and refining the unitary transformation $U_{nm}^{(\mathbf{k})}$ that minimizes the localization function defined by,

$$\Omega = \sum_{n}^{J}[\langle 0n|\,r^2\,|0n\rangle - \langle 0n|\,\mathbf{r}\,|0n\rangle^2] = \sum_{n}[\langle r^2\rangle - \mathbf{r}_n^2], \tag{2.38}$$

which measures the sum of the quadratic spreads of the J WFs in the home unit cell. To minimize this function with respect to $U_{nm}^{(\mathbf{k})}$, the above expression is cast as function of $\mathbf{k}$. There are many finite difference formulas available in literature which give the above expression as a function of $\mathbf{k}$. The form given by Marzari and Vanderbilt is:

$$\begin{cases}\mathbf{r}_n = -\frac{1}{N}\sum_{\mathbf{k},\mathbf{b}}w_b\mathbf{b}\mathrm{Im}\,\ln M_{nn}^{(\mathbf{k},\mathbf{b})}\\ \langle r^2\rangle = \frac{1}{N}w_b[1-|M_{nn}^{(\mathbf{k},\mathbf{b})}|^2] + [\mathrm{Im}\,\ln M_{nn}^{(\mathbf{k},\mathbf{b})}]^2\end{cases} \tag{2.39}$$

In the above expressions, $M_{nn}^{(\mathbf{k},\mathbf{b})} = \langle u_{m\mathbf{k}} | u_{n,\mathbf{k}+\mathbf{b}} \rangle$ is the overlap matrix element between Blöch functions at two neighboring $\mathbf{k}$ points in the mesh of k-points considered for the evaluation of Eq. (2.39). $\mathbf{b}$ is a vector that connects a $\mathbf{k}$ point to one of its neighbors and w_b is an appropriate weight factor that depends on number of k-points in the shells in the k-mesh and its geometry [89]. N is the number of k-points in the mesh. Thus, procedure of obtaining MLWF gives us the expectation values $\langle r^2 \rangle$ and $\mathbf{r}_n$; the latter, known as the Wannier charge centres (WCCs), in particular are the primary ingredients needed to determine Chern number and Z_2 topological invariants [14].

2.6.2 Calculation of Z_2 invariants via WCC

Wannier charge centre (WCC) is the average position of the charge of Wannier function in the home unit cell *i.e.*,

$$\mathbf{r}_n = \langle 0n | \, \mathbf{r} \, | 0n \rangle \tag{2.40}$$

Due to ambiguity in choosing the home unit cell, WCCs are only defined modulo a lattice vector. Moreover, when there are multiple bands present in the chosen band manifold, the individual WCC is not gauge-invariant, only the sum of all the WCCs is gauge-invariant modulo a lattice vector.

As the unitary transformation *i.e.* the gauge choice is not unique, the resultant WFs will show change in shape and their localization in real space if different gauge choices are taken in the "wannierization". To have an exponentially localized WF, we need a smooth gauge, which is hard to find. Mathematically it was proven that it is always possible to find a smooth gauge in 1D [87], ensuring the maximal localization of 1D Wannier function. Moreover, 1D maximally localized Wannier function satisfy the required gauge criteria needed to define Z_2 topological invariants *i.e.* the gauge be time-reversal invariant and continuous in the half-torus (*i.e.* half of the Brillouin zone) [14].

In 1D, the Wannier charge centre can be written in terms of Berry connection as,

$$\begin{cases} \bar{x}_n = \frac{i}{2\pi} \int_{-\pi}^{\pi} \langle u_{n\mathbf{k}} | \, \partial_k \, | u_{n\mathbf{k}} \rangle \\ = \frac{1}{2\pi} \int_{-\pi}^{\pi} A_n(\mathbf{k}).dk, \end{cases} \tag{2.41}$$

where $A_n(\mathbf{k}) = i \langle u_{n\mathbf{k}} | \, \partial_k \, | u_{n\mathbf{k}} \rangle$ is the Berry connection which was already introduced in subsection (1.2.2). of the first chapter.

Z_2 topological invariants can be defined using the notion of time reversal polarization [14, 65] derived in terms of 1D Wannier charge centres (WCCs). In a time-reversal invariant system, electronic bands always come in time-reversed pairs (let's assume I & II denote two bands within such a time-reversed pair). Then, the Z_2 invariant in a time-reversal invariant plane is given by [14],

$$(\sum_n [\bar{x}_n^I(T/2) - \bar{x}_n^{II}(T/2)] - \sum_n [\bar{x}_n^I(0) - \bar{x}_n^{II}(0)]) \text{ mod } 2, \tag{2.42}$$

where $\bar{x}_n^{I(II)} = \frac{i}{2\pi} \int_{-\pi}^{\pi} dk \, \langle u_{nk}^{I(II)} | \, \frac{\partial}{\partial_k} \, | u_{nk}^{I(II)} \rangle$ is the Wannier charge centres calculated at t=0 and t=T/2 planes which are invariant under time reversal (TR) symmetry, and T represents the period of a full cyclic adiabatic evolution. In the Brillouin zone of a periodic crystal, T is equivalent to a reciprocal lattice vector which defines the periodicity in the reciprocal space. The topological invariant of a TR-invariant plane is non-zero if the WCCs switch pairs under a cyclic adiabatic evolution which can be easily tracked by seeing evolution of the mid-point of the largest gap between two adjacent WCCs at any t $\in$ [0, T/2] in the half-cycle [14]. In this case, the largest gap in WCCs exhibits abrupt jumps in their cyclic evolution [14] with $\mathbf{k}$. We have calculated the strong topological index (ν_0) by taking the sum (modulo 2) of the topological invariants calculated at k_z=0 and k_z=0.5 planes (positions are in crystal coordinate and the chosen planes are TR-invariant) in the Brillouin zone. At each of these planes, WCCs, calculated along k_x direction, evolve along the k_y direction which is parameterized with time, t.

2.7 Semi-classical Boltzmann transport equation

We use the density functional theory based electronic structure within a semi-classical Boltzmann theory under a constant scattering time approximation to calculate electrical conductivity, Seebeck coefficient and thermoelectric power factor of materials as a function of Fermi energy (E_F) and temperature (T). Electrical conductivity ($\sigma_{\alpha\beta}$) and Seebeck coefficient ($S_{\alpha\beta}$) which are tensor quantities are obtained using [92, 93] the following equations,

$$\sigma_{\alpha\beta}(T, E_F) = \frac{1}{\Omega}\int \Sigma_{\alpha\beta}(\varepsilon)[-\frac{\partial f_0(T, \varepsilon, E_F)}{\partial \varepsilon}]d\varepsilon \tag{2.43}$$

and

$$S_{\alpha\beta}(T, E_F) = \frac{1}{eT\sigma_{\alpha\beta}(T, E_F)}\int (\varepsilon - E_F)\Sigma_{\alpha\beta}(\varepsilon)[-\frac{\partial f_0(T, \varepsilon, E_F)}{\partial \varepsilon}]d\varepsilon, \tag{2.44}$$

where α, β are Cartesian indices, Ω, f_0 are volume of unit cell, and Fermi-Dirac distribution function of the carriers respectively. Central to these relations is the transport distribution function ($\Sigma_{\alpha\beta}$),

$$\Sigma_{\alpha\beta}(\varepsilon) = \frac{e^2}{N}\sum_{i,\mathbf{k}} \tau v_\alpha(i, \mathbf{k}) v_\beta(i, \mathbf{k})\delta(\varepsilon - \varepsilon_{i,\mathbf{k}}), \tag{2.45}$$

where $\mathbf{k}$ and i are wave vector and band index, and N in the total number of k-points used in sampling the Brillouin zone, τ is the relaxation time, and $v_\alpha(i, \mathbf{k}) = \frac{1}{\hbar}\frac{\partial \varepsilon_{i,\mathbf{k}}}{\partial \mathbf{k}_\alpha}$ is the group velocity. The derivative of the energy $\varepsilon_{i,\mathbf{k}}$ is determined through Fourier expansion of band energies ($\bar{\varepsilon}_{i,\mathbf{k}}$) using the star functions of the space group symmetry [94]: $\bar{\varepsilon}_i(\mathbf{k}) = \sum_{\mathbf{R}} c_{\mathbf{R}i} S_{\mathbf{R}}(\mathbf{k})$ and $S_{\mathbf{R}}(\mathbf{k}) = \frac{1}{n}\sum_{\{\wedge\}} e^{i\mathbf{k}.\wedge\mathbf{R}}$, where $\mathbf{R}$ is a direct lattice vector, $\{\wedge\}$ are the n point group symmetry operations, and $c_{\mathbf{R}i}$ are the expansion coefficients. Σ is determined typically using a fine mesh of k-points (*i.e.* large N).

Part I

Strong Topological Insulators

Chapter 3

Electronic Topological Transition in Binary Chalcogenides

3.1 Pressure Induced Electronic Topological Transition in Sb_2Se_3 *

3.1.1 Introduction

Topological insulators (TIs) are a new class of quantum materials which exhibit an electronic band gap and a topologically nontrivial electronic structure in their bulk form [9, 96, 97]. The nontrivial topology of the bulk electronic wave function gives rise to exotic electronic states on the surface as a consequence of *bulk-boundary correspondence principle*, for example, one-dimensional edge spin states in two-dimensional quantum spin Hall systems. A three-dimensional TI with time-reversal symmetry [9, 56] exhibits gapless surface states. While the transport properties of a TI are theoretically predicted to be influenced by the topology of its electronic structure [98], much of its experimental confirmation comes from studies of the surface electronic structure [97], specifically from the linearly dispersing Dirac cones on its surface. The nontrivial topology of electronic

*This work has been published in Phys. Rev. Lett. **110**, 107401 (2013) [95]. Reproduced with permission from the American Physical Society.

structure of a topological insulator results in magneto-electric coupling [99,100], yet to be explored experimentally. Although the signatures of the electronic topology in the bulk properties may be subtle, they are expected to be more readily detectable when there is a sharp change in the electronic topology, *i.e.*, at an electronic topological transition from a band insulator to topological insulator.

The electronic structure of a TI is characterized by topological invariants [56, 101], which are determined from geometric properties of electronic states as a function of the Blöch vector. Similar ideas are involved in the theory of electric polarization [90], which is determined as a geometric phase of Blöch states. An integer quantum of change in polarization has been shown to arise from a cyclic evolution (adiabatic pumping) of the insulator along a path that encloses a metallic state [102]. Similarly, a bulk state with vanishing electronic gap in the vicinity of a TI influences the geometric properties of electronic states and is relevant to an electronic topological transition (ETT). Hence, It will be interesting to probe effects of the resulting slow dynamics of electrons at the ETT, particularly on phonons which would require going beyond the adiabatic approximation.

An occurrence of broken adiabaticity has been seen in graphene, also characterized by a vanishing band gap due to the presence of gapless Dirac cones at K and K' points. Explanation of vibrational signatures of doping in graphene probed by Raman spectroscopy required going beyond the Born-Oppenheimer (adiabatic) approximation [66, 103]. Similar nonadiabatic effects arising from the vicinity of a TI to a metallic state prompt us to carefully look for subtle reflections in Raman spectra of materials undergoing an ETT.

Since the discovery [9,104] of time-reversal invariant TI in three dimensions in Bi_2Se_3, Bi_2Te_3 and Sb_2Te_3, these materials have been extensively studied [105–107] both theoretically and experimentally. In this family of compounds, the spin-orbit coupling (SOC) competes with crystal-field splitting and chemical bonding (hybridization) between cation and chalcogen, and is strong enough to give rise to band inversion of the valence band maximum (VBM) and conduction band minimum (CBM). This inversion of bands of opposite parity leads to ETT making a ordinary band insulator to a topological insulator

characterized by an overall odd parity of the valence band manifold [9]. Vilaplana et al. [107] examined an ETT in Bi_2Se_3 as a function of pressure using Raman spectroscopy and calculations, though the nature of changes in electronic structure or topology needs further clarification. Interestingly, a close cousin of these compounds, Sb_2Se_3 having the same [9, 108] crystal symmetry (*i.e.* rhombohedral) as that of Bi_2Se_3, is a band insulator at ambient conditions with an overall even parity of the valence band manifold, in contrast to an overall odd parity exhibited by the TIs (*e.g.*, Bi_2Te_3) [9]. Under uniaxial strain, rhombohedral Sb_2Se_3 was shown theoretically to undergo a transition to a TI state [109]. Thus, Sb_2Se_3 is an ideal host system for exploration of a possible ETT and its reflections in bulk properties. Competition between the spin-orbit coupling and hybridization can be tuned to introduce an ETT either by substitution of Bi at the Sb site or by application of pressure. While the former would alter the spin-orbit coupling, the latter would tune the crystal field splitting and hybridization between Sb and Se.

In this work, using first-principles calculations based on density functional theory, we predict a pressure induced electronic topological transition in the rhombohedral crystal structure of Sb_2Se_3 at P_c= 2 GPa. We establish the nontrivial topology of its bulk electronic structure by calculating the Z_2 topological invariant across P_c. The ETT is accompanied with reversal of bands of opposite parity at the Γ point and passes through a gapless metallic state with linear dispersion of bands (*i.e.* a Dirac semi-metallic state) at Γ. As our calculations do not capture the phonon anomalies as observed in Raman spectroscopy experiment [95] at the ETT, we derive symmetry-invariant forms of electron-phonon coupling, and go beyond the adiabatic approximation using a model Hamiltonian in our analysis, uncovering mechanisms responsible for the anomalies in Raman spectra of Sb_2Se_3 signifying the change in electronic topology at its ETT. In particular, the asymmetry in observed phonon anomalies at the ETT arises from reversal of parities of electronic states across the gap.

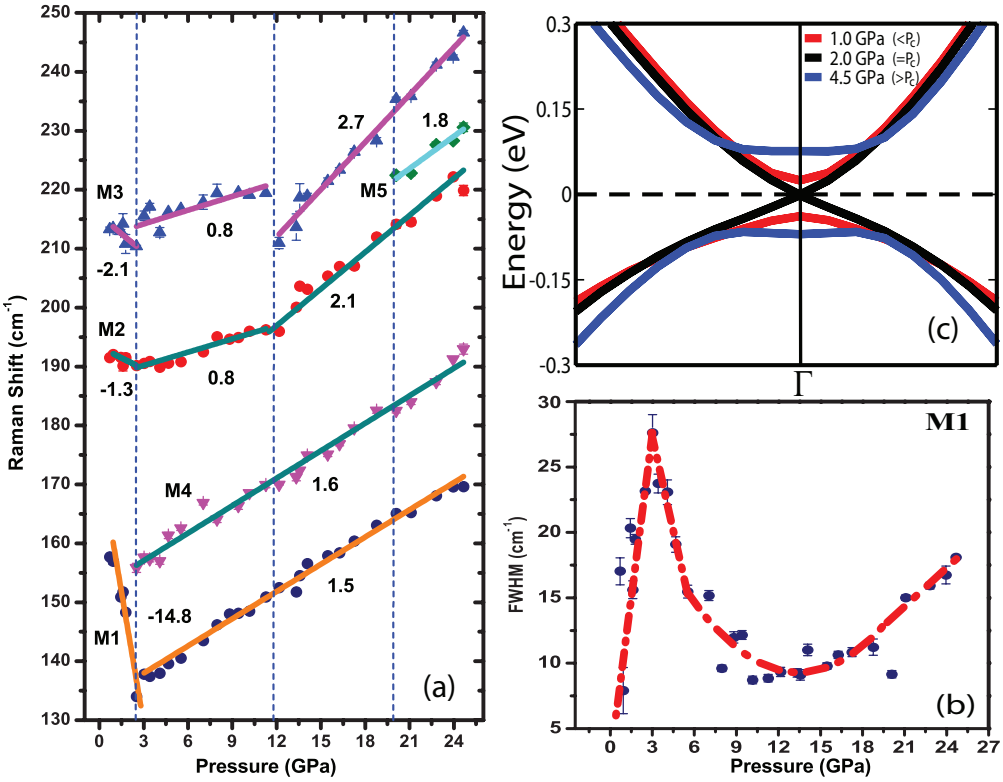

Figure 3.1: Experimental Raman spectra of Sb_2Se_3, FWHM of the M1 mode and calculated electronic bands near the Fermi level as a function of pressure. (a) Raman shift versus pressure plot. Solids lines are linear fit to the observed frequencies. The numbers next to the solids are slopes of each fitted straight lines. The errors bar, if not seen, are less than the size of the symbol. (b) FWHM of the M1 mode (solid points) as a function of pressure and dashed line is drawn as guide to the eyes. (c) First-principles calculations of electronic structure near the gap as a function of pressure in the neighborhood of transition (P_c= 2 GPa).

3.1.2 Experimental observations

High pressure Raman experiments on the rhombohedral crystal of Sb_2Se_3 were carried out at room temperature by Achintya Bera from Prof. A. K. Sood's group [95] at the Indian Institute of Science, Bangalore. Group theoretical analysis for the centrosymmetric rhombohedral structure of Sb_2Se_3 (point group: D^5_{3d}) predicts 12 optical phonons at the Γ point in the Brillouin zone: $2A_{1g} + 2E_g + 2A_{2u} + 2E_u$, where g and u refer to Raman and infrared active modes, respectively [107]. Raman spectroscopy has been used to study electronic transition in Bi_2Te_3 [106], Bi_2Se_3 [107], and Sb_2Te_3 [110] compounds at high

pressure. As this transition involves reconstruction of Fermi surface topology, it is often called as electronic topological transition. Probing of ETT with pressure has been done either by observing changes in slope and FWHM (full width at half maximum) of the Raman active modes.

Raman spectra on the single crystal of Sb_2Se_3 was studied up to 24.6 GPa, which shows an ETT at P_c=2.5 GPa marked by (a) a large softening $\sim$ 25 cm^{-1} of the low frequency Raman mode (M1) and together with an anomalous increase of its linewidth by 200% within a narrow pressure range of 0 to 2.5 GPa and relatively less softening by two other (M2 and M3) modes and (b) change in sign of slope of the M1 Raman active mode above 2.5 GPa (see Fig. 3.1). The nominal frequencies of the modes (*e.g.*, at 0.7 GPa) are: M1 (166 cm−1), M2 (192 cm^{-1}), and M3 (214 cm^{-1}) The mode M1 is assigned as E_{2g}, M2 as A_{21g}, and M3 as a combination mode.

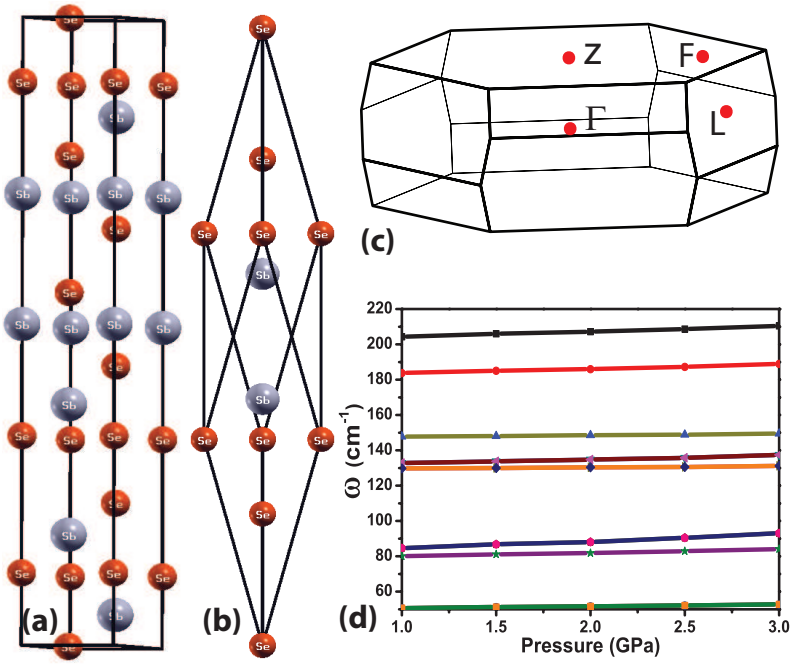

Figure 3.2: (a) Conventional hexagonal and (b) primitive rhombohedral unit cells of the Sb_2Se_3 and (c) its Brillouin zone with high symmetry points. In the hexagonal crystal structure of Sb_2Se_3, the atomic planes arrange themselves in A(Se1)-B(Sb)-C(Se2)-A(Sb)-B(Se1)-C(Se1)... order along the z-direction, where, Se2 atom acts as the inversion center in the lattice. Grey and orange colors represent Sb and Se atoms, respectively. (d) Phonon frequencies at Γ point as a function of pressure, calculated within the adiabatic density functional perturbation theory. Phonon frequencies of all the modes vary linearly with pressure near P_c(=2 GPa) showing no anomaly.

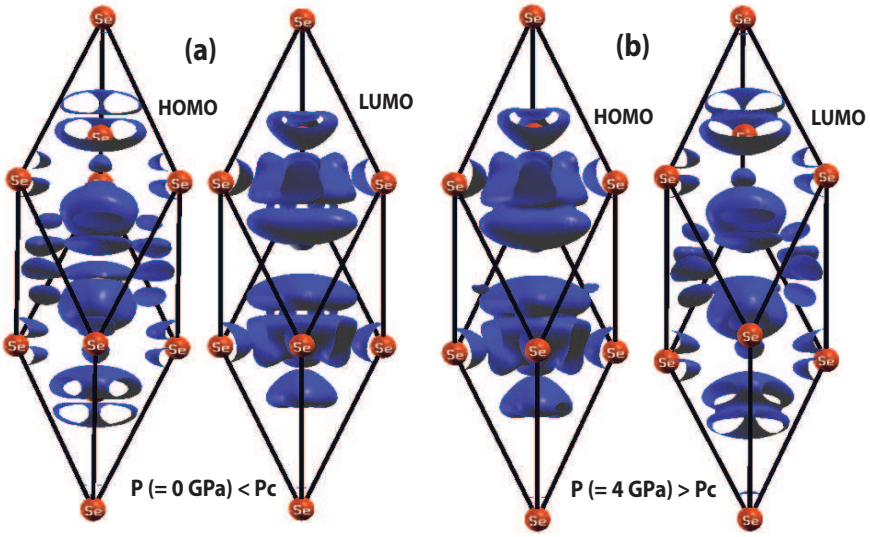

Figure 3.3: Band inversion of Sb_2Se_3 across the critical pressure (P_c=2 GPa). Iso-surfaces of charge densities associated with the top of the valence (HOMO) and bottom of the conduction (LUMO) band at a pressure (a) before (P=0 GPa) and (b) after(P=4 GPa) the critical pressure P_c.

It is worth mentioning that a low pressure transition around 3 GPa was reported in Bi_2Te_3 [106], Bi_2Se_3 [107] and Sb_2Te_3 [110], which manifest change in slope and FWHM of their Raman active modes. But these changes are not as drastic and anomalous as the case of Sb_2Se_3. This transition was later verified to be an iso-structural transition [111]. The large softening of phonons up to 2.5 GPa and anomalous linewidth maximum of the M_1 mode as seen in the Raman spectra (Fig. 3.1) is unique to Sb_2Se_3 which involves ETT, characterized by change in Z_2 topological invariant of Sb_2Se_3 across P_c.

3.1.3 Crystal structure and computational details

Materials belonging to the A_2B_3 (A = Sb, Bi; B = Se, Te) crystal family have layered crystal structures in their bulk with space group $R\bar{3}m$ (No. 166) [9,108,109]. The primitive unit cell has a rhombohedral crystal structure with five atoms, whereas the conventional hexagonal unit cell has 15 atomic planes in which quintuple layers of the formula units are stacked along the c-direction (see Fig. 3.2).

We use first-principles calculations based on density functional theory as implemented in the QUANTUM ESPRESSO (QE) code [112] to calculate electronic structure of Sb_2Se_3.

We adopt fully relativistic norm-conserving pseudopotentials to represent the interaction between the frozen core and the valence electrons of an atom facilitating the inclusion of spin-orbit coupling in the calculations. We use generalized-gradient approximation (GGA) [113] to the exchange-correlation energy functional as parametrized by Perdew, Burke and Ernzerhof (PBE) [114] while constructing the pseudopotentials within fully relativistic analysis. Expansion of the electronic wave functions and charge density in plane wave basis were truncated with cut-off values of 45 Ry and 180 Ry, respectively. The integrations over the the Brillouin zone are sampled in a dense grid of $9 \times 9 \times 9$ k-points. The discontinuity in the occupation numbers of the electrons are smeared with a broadening of 0.003 Ry across the gap of the Fermi level. At each value of the applied hydrostatic pressure, the bulk unit cell is fully relaxed while keeping the c/a ratio fixed at the experimental value and varying the lattice constant a. Phonon frequencies are determined using density functional perturbation theory as implemented in PH [64] code of the QE distribution.

3.1.4 Electronic structure and phonons

We now present results of first-principles density functional theory-based calculations of electronic structure and phonons for the rhombohedral structure of Sb_2Se_3 as a function of pressure. Our theoretical estimate of the lattice constant is a= 4.09 Å, at which a direct energy gap at the Γ point separates valence band states with odd parity from the conduction band states with even parity (see Fig. 3.4(a)), as was shown by Zhang et al. for a band insulator [9]. The odd parity of the state at the top of the valence band is evident in the involvement of the p orbitals of Se atoms present at the inversion center. A strong hybridization between p states of Sb and Se is evident in the electronic eigenstates across the gap (Fig. 3.3). Band gap vanishes precisely at P_c= 2 GPa passing through a Dirac metallic state and opens up for $P > P_c$ (see Fig. 3.1(c)). This involves inversion of valence band maximum (VBM) and conduction band minimum (CBM) at Γ point (see Fig. 3.3) and reversal of their parity across P_c marking a transition from a band insulator

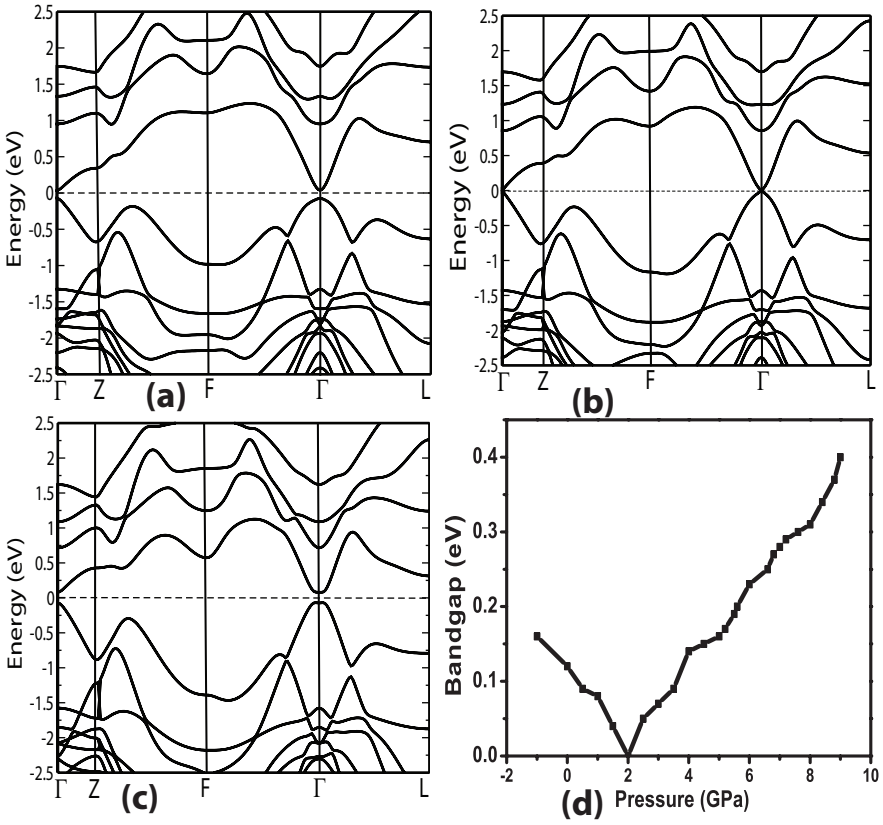

Figure 3.4: Evolution of electronic structure and the bulk band gap around the critical pressure P_c (= 2 GPa). Electronic band structure of Sb_2Se_3 at (a) P (= 0 GPa) < P_c (b) P = P_c and (c) P (= 4 GPa) > P_c. (d) Closing and reopening of bulk band gap across the critical pressure causing the inversion of bands across P_c.

to a topological insulator.

Frequencies of all phonons at the Γ point, calculated within the adiabatic density functional perturbation theory, vary linearly with pressure, and exhibit no anomaly at the transition at P_c (Fig. 3.2(d)), leaving us puzzled about the mechanism of the sharp Raman anomalies as seen in experiment (Fig. 3.1(a)). The Nominal frequencies of Sb_2Se_3 are given and compared with other topological insulators in Table 3.1. From this table, we can see that the frequencies for Sb_2Se_3 are higher than other compounds because of the lighter masses of Sb and Se atoms as compared to Bi and Te atomic masses.

	A_{1g}^2	A_{1g}^1	E_g^2	E_g^1	A_{2u}^2	A_{2u}^1	E_u^2	E_u^1
[a]Sb_2Se_3	211.5	78	138.3	53.2	190.9	149.8	131.4	94.6
[18],[b]Sb_2Te_3	169	67	117	49	146	109	100	77
[19],[c]Sb_2Te_3	165	69	112					67
[20],[b]Bi_2Se_3	166.3	63.8	123.9	38.8	155.4	136.7	126.8	64.7
[21],[c]Bi_2Se_3	175.3	73.3	132.6	39.9	159.9	128.9	124.9	67.9
[20],[b]Bi_2Te_3	127.2	53.8	95.9	35.4	118.6	95	91.2	48.4
[22],[c]Bi_2Te_3	134.1	62.0	101.7	34.3				

[a] this work, [b] theoretical calculation and [c] experiment.

Table 3.1: Vibrational frequencies of twelve optical modes $2(A_{1g} + E_g + A_{2u} + E_u)$ of topological insulator materials having D_{3d}^5 point group symmetry. All frequencies are in the unit of cm^{-1}. The vibrational frequencies of Sb_2Se_3 are given here at P = 3.5 GPa *i.e.* in its topological insulating phase. For other materials which are already TIs at ambient pressure, the above frequencies are at equilibrium lattice constant *i.e.* at zero pressure. g and u denote Raman (R) and Infrared (IR) active modes respectively.

3.1.5 Going beyond the adiabatic approximation

We now present theoretical analysis beyond the adiabatic approximation and determine dynamical corrections [66, 103] to phonon frequencies. We use the universal four-band model developed by Zhang and co-workers [9,115] written in terms of Dirac matrices and note that states at the top of the valence and bottom of the conduction bands are doubly degenerate, and their energies are given by $C_0 \pm M_0$, where C_0 and M_0 are the parameters of the model Hamiltonian [115], and $M_0 < 0$ for a topological insulator. Treating $M_0 = -\kappa (P - P_c)$ with a positive κ, we reproduce the electronic structure near the Γ point close to the transition from a band insulator to a topological insulator as reflected in the reversal of bands of opposite parity.

Electron-phonon coupling is needed to estimate dynamical corrections to vibrational frequencies, and we now derive their form at the lowest order within the four-band model, expressing them in terms of Dirac matrices. Symmetry properties of the Dirac matrices [irreducible representations (irreps) for the symmetry group of Sb_2Se_3] have been derived by Liu et al. [115]. We note that Raman-active and IR-active modes have even and odd parity, all of them are invariant under time reversal symmetry. An electron-phonon

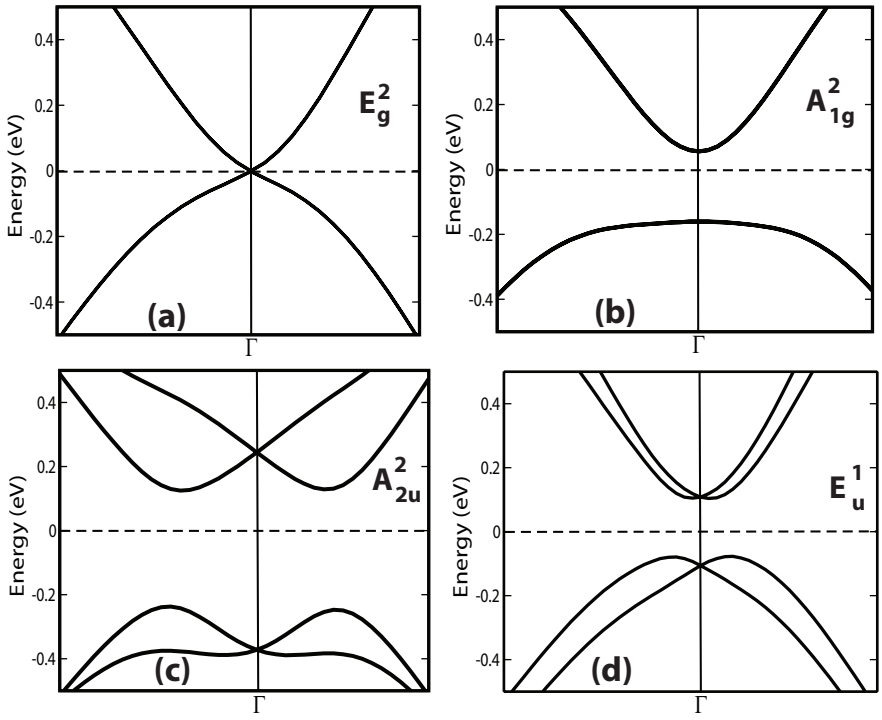

Figure 3.5: Electronic bands of Sb_2Se_3 at P_c near the Γ point for the undistorted crystal structure. First-principles evidence of electron-phonon coupling obtained by distorting the crystal structure along the direction of displacement of atoms for (a) E_g^2 (b) A_{1g}^2, (c) A_{2u}^2 and (d) E_u^1 modes. The form of electron phonon coupling for A_{2u} mode (see text) yields splitting of bands near the gap obtained within the 4-band model, which has been verified using first-principles calculations.

coupling term in the Hamiltonian can be expressed as a product of phonon degree of freedom and a Dirac matrix (or its commutator).

To derive symmetry invariant form of electron-phonon coupling (EPC) Hamiltonian for each of the phonon modes, we introduce the projection operator ($\hat{\mathbf{P}}_{\tilde{\Gamma}_n^{\pm}}$) [62],

$$\hat{\mathbf{P}}_{\tilde{\Gamma}_n^{\pm}} = \frac{1}{g}\sum_{\mathcal{R}} A_{\tilde{\Gamma}_n^{\pm}}(\mathcal{R})\hat{P}_{\mathcal{R}}, \tag{3.1}$$

where $\hat{P}_{\mathcal{R}}$ is the symmetry operator corresponding to symmetry operation $\mathcal{R}$ and $A_{\tilde{\Gamma}_n^{\pm}}(\mathcal{R})$ is the character of $\tilde{\Gamma}_n^{\pm}$ irreducible representation (irrep) of the symmetry group. The summation in Eq. (3.1) is over all the symmetry operations of the group (D_{3d}^5) and g is its order. ± sign represent even and odd parity respectively of the irreps. The phonon eigenmodes A_{1g}, A_{2u} and E_g have the symmetries of the irreducible representations given

by $\tilde{\Gamma}_1^+, \tilde{\Gamma}_2^-$ and $\tilde{\Gamma}_3^+$ [62], respectively. We first considered direct product representation obtained from a multiplication of an irrep of a phonon mode and each irrep of D_{3d}^5. From these, we pick the ones that contain identity representation of D_{3d}^5. We write the electron-phonon coupling term by projecting the product of the suitable Dirac matrix and u mode displacement onto identity representations [116].

For A_{1g} mode, picking only the leading terms which give significant change in the electronic structure, the EPC Hamiltonian can be written as,

$$H_{A_{1g}} = \hat{\mathbf{P}}_{(\tilde{\Gamma}_1^+ \equiv A_{1g})}.[u_{A_{1g}}\Gamma_5] \simeq A_{A_{1g}} u_{A_{1g}}\Gamma_5 \tag{3.2}$$

Similarly for A_{2u} mode the EPC Hamiltonian is given by the following expression,

$$H_{A_{2u}} = \hat{\mathbf{P}}_{(\tilde{\Gamma}_2^- \equiv A_{2u})}.[u_{A_{2u}}\Gamma_5] \simeq A_{A_{2u}} u_{A_{2u}}\Gamma_{45}, \tag{3.3}$$

where we note that each of $u_{A_{2u}}$ and Γ_{45} belongs to $\tilde{\Gamma}_2^-$ irrep. Here Γ_m is a Dirac matrix and $u_{A_{1g}}$, $u_{A_{2u}}$ are the displacements of the A_{1g} and A_{2u} phonon modes respectively. Γ_{ij} is a Dirac matrix commutator $[\Gamma_i, \Gamma_j]/2i$.

For E_g mode,

$$\hat{\mathbf{P}}_{(\tilde{\Gamma}_1^+)}.[\{u_{E_g}^x, u_{E_g}^y\} \otimes \{\Gamma_{15}, \Gamma_{25}\}].\Gamma_{35} \simeq A_{E_g}(u_{E_g}^x\Gamma_{15} + u_{E_g}^y\Gamma_{25})\Gamma_{35} \tag{3.4}$$

$u_{E_g}^x$ and $u_{E_g}^y$ are the x and y component of the displacement of the doubly E_g phonon mode. In this equation, each of matrix Γ_{35} and $(u_{E_g}^x\Gamma_{15} + u_{E_g}^y\Gamma_{25})$ transforms according to Γ_1^- irrep and is even under time-reversal, hence their product is symmetry invariant. Since the product of two noncommuting Hermitian operators is not Hermitian, we construct a symmetry-invariant Hermitian form as,

$$H_{E_g} \simeq A_{E_g}\frac{(u_{E_g}^x\Gamma_{15} + u_{E_g}^y\Gamma_{25})\Gamma_{35} - H.c.}{2i}, \tag{3.5}$$

where $H.c.$ means Hermitian conjugation.

Similarly other symmetry allowed lowest order terms for EPC Hamiltonian of H_{E_g} mode are,

$$B_{E_g}\frac{(u^x_{E_g}\Gamma_{24}-u^y_{E_g}\Gamma_{14})\Gamma_{34}-H.c.}{2i}+B'_{E_g}\frac{(u^x_{E_g}\Gamma_{24}-u^y_{E_g}\Gamma_{14})\Gamma_{12}-H.c.}{2i}$$
$$+C_{E_g}(k_x u^x_{E_g}-k_y u^y_{E_g})\Gamma_4 \tag{3.6}$$

We validate the form of electron-phonon coupling by comparing the electronic structure of the model with that obtained from first-principles calculations for the lattice distorted with each mode of Sb_2Se_3 (see Fig. 3.5). For a frozen A^2_{1g} mode at $P = P_c$, the band gap opens up in a way similar to how it opens up at infinitesimally small deviation in pressure or strain. For a frozen A^2_{2u} mode, band splitting is more interesting: each of the doubly degenerate valence and conduction bands of definite parity split up as this mode breaks the parity symmetry. The minima or maxima of bands shift away from the Γ point. However, the splitting or changes in the model band structure associated with the electron-phonon coupling of the E^2_g mode are not captured within first-principles calculations, suggesting that the physics of this coupling is beyond the formal mean-field description of density functional theory used here. Thus, in the analysis below, we use the symmetry-invariant form with A coupling as a free parameter as the other terms are not needed to capture the essential aspects of the observed phonon anomalies.

We obtain the dynamical corrections to phonon frequencies as a function of pressure using these forms of electron-phonon couplings (keeping the strength of the coupling as free parameters) in first-order time dependent perturbation analysis [66] of the four-band model of Bi_2Se_3 derived by Zhang et al. [9] with pressure-dependent M_0 (see Fig. 3.6). To simplify our analysis, we make use of the layered nature of Sb_2Se_3 and carry out Brillouin zone integrations only in the xy-plane. It is evident that dynamical corrections to frequencies of Raman active modes change sharply below P_c and asymmetrically around P_c. Indeed, the sharp drop (Fig. 3.6) in frequencies of E^2_g and A^2_{1g} modes just below P_c , and a gradual increase in their frequencies for $P > P_c$, are consistent with the pressure

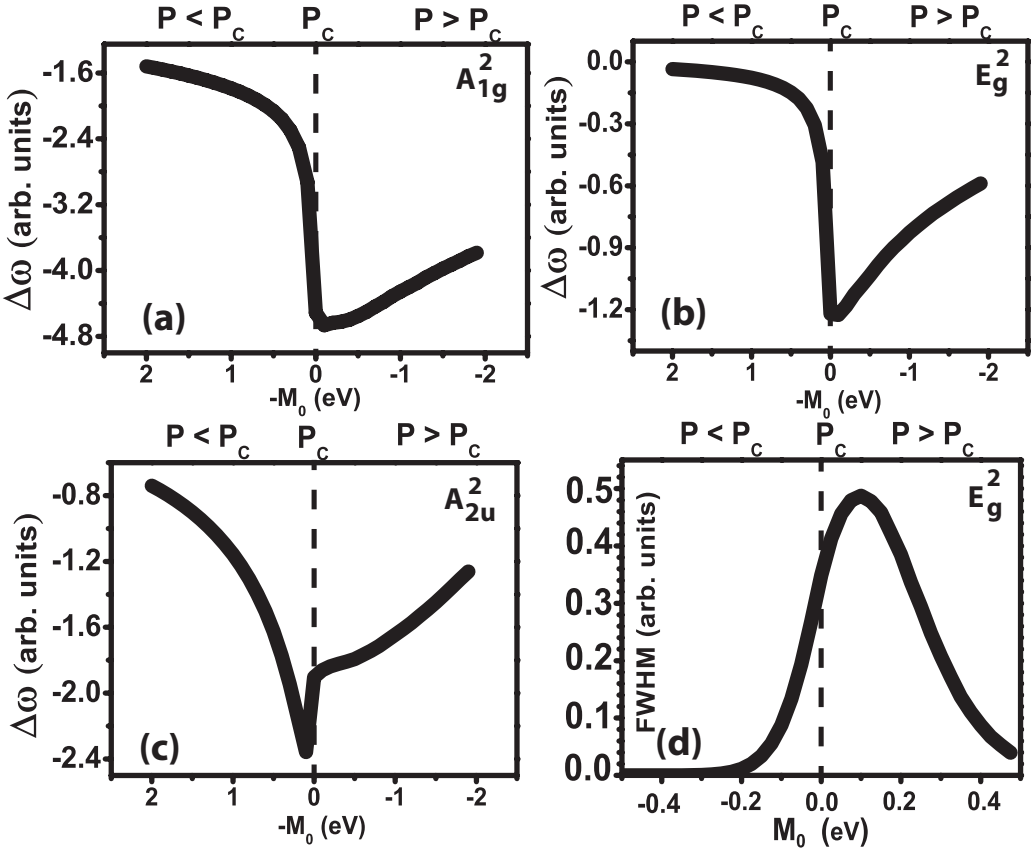

Figure 3.6: Dynamical corrections to frequencies of phonon modes (a) A^2_{1g}, (c) E^2_g and (c) A^2_{2u} as a function of -M_0 (*i.e.* $\propto$ (P-P_c)). The corrections are negative and make the modes softer near the transition; their asymmetry allows differentiation between the trivial and the nontrivial topology of electronic structure on the two sides of the transition. (d) The calculated linewidth (FWHM) of the mode E^2_g as a function of M_0 *i.e.* pressure.

dependent behavior of modes M1, M2, and M3 in the experimentally measured Raman spectra (see Fig. 3.1(a)). In contrast, dynamical corrections to the IR-active mode exhibit a sharp jump above P_c . Noting the calculated frequencies, we assign mode M1 to E^2_g and mode M2 to A^2_{1g} irreps. The mode M3 is the highest in frequency, and is most likely associated with the sum of two E^2_g modes (a second order Raman mode).

We now calculate the linewidth of the M1 Raman active mode. Following the procedure Lazzeri et al. [116] and Pisana et al. [66] used in their work on graphene, self energy of phonon with wavevector q and frequency ω_ν is given by,

$$\sum(q, \omega_\nu + i\delta) = \frac{2}{N_k} \sum_{kij} \frac{|g^\nu_{ki,(k+q)j}|^2 (f_{ki} - f_{(k+q)j})}{\epsilon_{ki} - \epsilon_{(k+q)j} - (\hbar\omega_\nu + i\delta)}, \tag{3.7}$$

where k is the Blöch wave vector of the electronic state, N_k is the total number of k vectors, f_{ki} is the Fermi-Dirac distribution function and i, j denote band indices. $g_{ki,(k+q)j}$ is the matrix element of electron-phonon coupling between states ψ_{ki} & $\psi_{(k+q)j}$ and δ is a small real number. At $q = 0$ the real part of the $\sum$ gives the dynamical correction to phonon frequency $\hbar\Delta\omega$ [66]. In our analysis, we treat a single layer of Sb_2Se_3 and carry out integration over k in the Brillouin Zone in 2-D plane. For a phonon ν at Γ point and four-band Hamiltonian, [117]

$$\Delta\omega_{\Gamma_\nu} = Re[\sum(0, \omega_\nu)] = \frac{2A}{(2\pi)^2}\mathcal{P}\int_{-\infty}^{\infty} d^2k \sum_{i,j=1}^{4} \frac{|g^\nu_{ki,kj}|^2(f_{ki} - f_{kj})}{\epsilon_{ki} - \epsilon_{kj} - \hbar\omega_\nu} \tag{3.8}$$

where $\mathcal{P}$ is the principle part of the integral.

Here, $g_{ki,kj}$ is given by $\langle ki| H_{A_{1g}} |kj\rangle$, $\langle ki| H_{A_{2u}} |kj\rangle$ and $\langle ki| H_{E_g} |kj\rangle$ respectively for A_{1g}, A_{2u} and E_g phonon modes. $|ki\rangle$ & $|kj\rangle$ are the eigenvectors of the effective four-band Hamiltonian $\mathcal{H}(\mathbf{k})$ with energies ϵ_{ki} and ϵ_{kj} respectively, as given by by Zhang et al. [9] .

At the Γ point the effective four-band Hamiltonian is given by the following expression,

$$\mathcal{H}_\Gamma = \begin{bmatrix} C_0 + M_0 & 0 & 0 & 0 \\ 0 & C_0 - M_0 & 0 & 0 \\ 0 & 0 & C_0 + M_0 & 0 \\ 0 & 0 & 0 & C_0 - M_0 \end{bmatrix} \tag{3.9}$$

To model the electronic structure across the electronic transition seen in the DFT calculations, we treat M_0 is function of pressure M_0 = -k(P-P_c), where k is a positive number and P_c is the critical pressure.

The linewidth of a phonon mode in a crystal having strong electron phonon interaction is mainly determined by electron-phonon coupling (EPC) term in the Hamiltonian. The EPC contribution to FWHM (γ_ν) of a phonon mode ν is given by the following expression [117],

$$\gamma_\nu = \frac{4\pi}{N_k}\sum_{k,i,j} |g^\nu_{ki,(k+q)j}|^2(f_{ki} - f_{(k+q)j}) \times \delta(\epsilon_{ki} - \epsilon_{(k+q)j} + \hbar\omega_\nu), \tag{3.10}$$

where δ is the Dirac delta function. Other terms in this expression have been explained in the previous sections.

The linewidth of the E_g^2 mode estimated from our analysis (see Fig. 3.6(d)) peaks asymmetrically near the transition pressure, quite consistent with the observed linewidth anomaly seen in Raman experiments (see Fig. 3.1(b)). This further corroborates our theoretical analysis, and allows us to determine the origin of asymmetry in phonon anomalies to the parity reversal of occupied and unoccupied bands in the immediate vicinity of the ETT. The similar analysis predicts the asymmetry in anomaly of the IR-active mode contrasting that in the Raman mode-with a jump in frequency above P_c.

3.1.6 Conclusions

In conclusion, we reveal a pressure-induced electronic topological transition (ETT) from band to topological insulating phase in the rhombohedral crystal structure of Sb_2Se_3. A combination of first-principles calculations and theoretical model-based analysis presented here show a breakdown of adiabatic approximation at the ETT. We established that electron-phonon coupling of nontrivial forms leads to anomalies as observed in the experimental Raman spectra [95]. These ideas are applicable to electronic transitions in other topological insulators too, and expected to stimulate experiments for exploring anomalies in Raman and IR vibrational spectra, and guide materials scientists in transforming a normal insulating material to a topological insulator.

3.2 Strain Induced Z_2 Topological Insulating Phase in β-As_2Te_3[†]

3.2.1 Introduction

Discovery of the nontrivial electronic topology in the layered semiconductors (Bi_2Se_3, Bi_2Te_3, Sb_2Te_3) [9, 119] with tetradymite crystal structure (space group: $R\bar{3}m$, No: 166) have stimulated enormous research activity in exploration of exotic states like superconductivity, anomalous quantum Hall, and magneto-electric effects that have been predicted theoretically [99, 100, 120]. These materials, commonly known as topological insulators (TIs), are insulators in their bulk form, but exhibit a metallic electronic spectrum at their surfaces. The nontrivial topology of the bulk electronic states of Bi_2Te_3 type TI's arises from strong spin-orbit interactions [9]. The metallic state of the surface of a topological insulator is protected by the time reversal symmetry, and is robust against any non-magnetic perturbations. Berry phases of electronic states at the surface of a strong topological insulator prevent back scattering of electrons from impurities resulting in a dissipation-less conduction of current on its surface [97].

Arsenic telluride has a monoclinic structure with space group C2/m (α-As_2Te_3) at the ambient pressure, and has been investigated as a thermoelectric material in earlier works [121–124] showing that it has a lower thermoelectric figure of merit than Bi_2Te_3. There is room for improving the thermoelectric performance of As_2Te_3 by applying pressure or with epitaxial strain. The high pressure study of α-As_2Te_3 by Scheidemantel et al. [124] revealed a pressure induced structural phase transition from monoclinic (α-As_2Te_3) to rhombohedral structure (β-As_2Te_3) near 7 GPa, leading to dramatic enhancement in its thermoelectric power. The β-As_2Te_3 phase can also be synthesized by rapid quenching from high temperature or by compressing monoclinic α-As_2Te_3 crystals [125].

The β-phase of As_2Te_3 is iso-structural to Bi_2Se_3 family of compounds with $R\bar{3}m$

[†]This work has been published in App. Phys. Lett. **105**, 062105 (2014) [118]. Reproduced with permission from the AIP Publishing.

symmetry (space group No:166) having 5 atoms in the bulk unit cell. Electronic structure of β-As_2Te_3 has been determined within a non-relativistic description *i.e.* without including the spin-orbit coupling (SOC) [126], and it is found to be similar to that of Bi_2Te_3 (also determined without SOC) [126] with a direct band gap of 0.12 eV at the Γ point. As_2Te_3 contains a relatively light element *As* and hence relatively weaker SOC, which can however be tuned with strain or pressure modifying its electronic properties. For example, a number of materials belonging to different crystal symmetries (at ambient conditions) have been predicted theoretically from the quantum materials repository by using a search model based on the strain-dependent electronic structure [127]. Motivated by this, we determine electronic structure of β-As_2Te_3 as a function of uniaxial strain along the c-axis including SOC, and show that it undergoes a quantum phase transition on application of a modest uniaxial stress of $\sigma_{zz} = 1.77$ GPa to an interesting topological insulating state with a small gap, a property which can be exploited to make devices.

3.2.2 Computational details

We use a combination of two different implementations of density functional theoretical (DFT) methods (a) the WIEN2K [128] code which is an all-electron full potential linearized augmented plane wave (FP-LAPW) based technique and (b) the Quantum ESPRESSO (QE) [112] code which treats only valence electrons replacing the potential of ionic core with a smooth pseudopotential. To obtain total energies and eigenvalues of the electrons in a solid using the FP-LAPW methods, we use a basis set achieved by dividing the unit cell into non-overlapping spherical regions centered at each atom and the interstitial region. Two different types of basis sets are used in these two regions. Plane wave basis set is used in the expansion of the electronic wave functions inside the interstitial region. It is augmented by atomic like wave functions (linear combination of the solutions of the radial Schrödinger equation and spherical harmonics) in the space inside every atomic sphere. These atomic-like wave functions form the basis set inside each non-overlapping atomic sphere. We use Perdew, Burke and Ernzerhof (PBE)

parametrization [114] of the exchange-correlation energy functional derived with a generalized gradient approximation (GGA) [113]. Spin-orbit interaction has been included through a second variational procedure [82, 83]. Truncation of the plane wave expansion of electronic wave functions inside the interstitial region is specified by a cut-off value of R_{mt}*K_{max} = 7 , where R_{mt} is the radius of the smallest atomic sphere (muffin-tin), K_{max} = 2.8 a.u^{-1} is the plane wave cut-off vector, and charge density is Fourier expanded up to by G_{max} = 12 Ry$^{1/2}$, where G_{max} represents the maximum value of G vector in the Fourier expansion. We adopt the tetrahedron method for sampling integrations over the Brillouin zone with a $9 \times 9 \times 9$ uniform mesh of k-vectors.

Lattice-dynamical properties are determined within the framework of self-consistent density functional perturbation theory (DFPT) as implemented within the QE code [64]. Since the effect of SOC is negligible on phonon frequencies and character of the vibrational modes is unchanged without the SOC, we determine vibrational frequencies of β-As_2Te_3 within a non-relativistic description. We use norm-conserving pseudopotentials and plane wave basis truncated with cut-off energies of 60 Ry and 240 Ry in representing of wave functions and charge density respectively. In order to calculate the phonon dispersion, force constant matrices are obtained on a 2×2×2 q-point mesh. The dynamical matrices at arbitrary wave vectors are then obtained using Fourier interpolations.

3.2.3 Results and discussion

Lattice parameters of β-As_2Te_3 are taken from the Materials Project repository [129] with a_{hex}=4.089 Å and c_{hex}= 30.306 Å. We keep a_{hex} fixed and apply uniaxial strain along the c-axis, relaxing the atomic positions at each value of the uniaxial strain until the forces on atoms become less than 1 mRy/bohr. In contrast to the earlier all-electron calculation [126], we include the SOC in determining electronic structure of β-As_2Te_3 as a function of ϵ_{zz}. From the electronic structure of β-As_2Te_3 (see Fig. 3.7) at vanishing strain, it is clear that the valence band maximum and the conduction band minimum are located at points along different directions in the Brillouin zone (*i.e.* band gap is indirect).

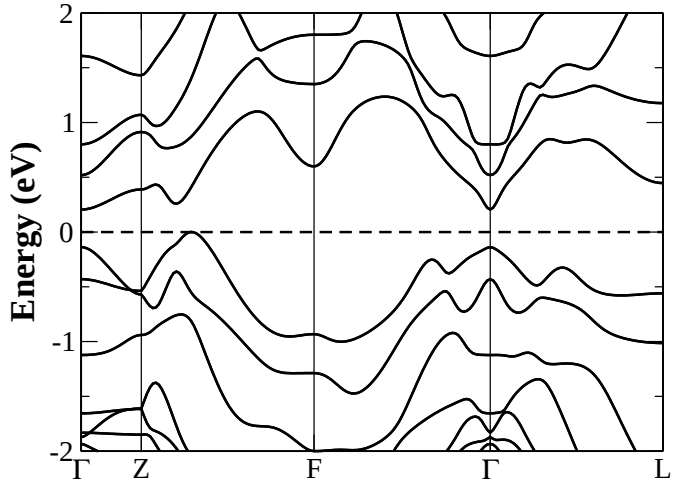

Figure 3.7: Electronic structure of β-As_2Te_3 (space group: $R\bar{3}m$) at vanishing strain. Spin-orbit coupling is included in the electronic structure calculation. The overall product of parities of the occupied bands is positive which signifies that it is a band insulator when $\epsilon_{zz} = 0$

However, the direct band gap at Γ point is 0.35 eV, higher than the earlier estimate (0.12 eV), obtained without the SOC [126].

ϵ_{zz} = -0.04	+	-	+	-	+	+	-	+	-	-	+	-	-	-	;	+	(+)
ϵ_{zz} = -0.06	+	-	+	-	+	+	-	+	-	-	+	-	-	+	;	-	(-)

Table 3.2: Parities of the fourteen occupied bands below the Fermi level and the lowest unoccupied band above the Fermi level across the transition point (ϵ_{zz} = -0.05) for β-As_2Te_3. The product of parities of the valence band manifold are given in the rightmost column and are indicated within the brackets. Positive and negative signs within the brackets mean that for $\epsilon_{zz} >$ -0.05, β-As_2Te_3 is a band insulator which undergoes a quantum phase transition and becomes a topological insulator upon increasing the strain beyond it.

Electronic states near the Fermi level of β-As_2Te_3 are contributed largely by the p-orbitals of As and Te atoms. In Bi_2Se_3-type layered materials, compressive strain (ϵ_{zz}) was found to tune the strength of the SOC by reducing the inter quintuple-layer distance [109, 130]. As β-As_2Te_3 shares similar layered crystal structure, ϵ_{zz} is expected to alter the strength of SOC and crystal field of β-As_2Te_3. At the compressive strain of ϵ_{zz} = -0.05, it exhibits a Dirac semi-metallic state (see Fig. 3.8(b)), where a Dirac cone with linear dispersion (in 3-D) of the electronic bands appears at the Γ point. Upon further

compression of the crystal along c-axis, repulsion between the electronic bands due to a strong SOC leads to reopening of the bulk band gap, accompanied by the inversion of the top of the valence and bottom of the conduction bands at the Γ point. Naturally, parities of the bands also change their sign through the band inversion. Band inversion and parity reversal of bulk electronic bands are characteristics of an electronic topological phase transition which has been observed in Bi_2Se_3 (a strong $\mathbb{Z}_2$ topological insulator) as a function of strain with $\epsilon_{zz} = 0.06$ being its critical value [109]. Here, we show that β-As_2Te_3 undergoes an electronic topological transition at the ϵ_{zz}= -0.05, with a uniaxial stress $\sigma_{zz} = 1.77$ GPa.

We now determine the $\mathbb{Z}_2$ topological invariant quantity ν_0 of β-As_2Te_3 below and above the critical value of the strain using the technique of Fu and Kane [56] that equates the product of parities of states in the valence band manifold (see Table 3.2) to $(-1)^{\nu_0}$. We find that the ν_0 is 0 and 1 for $\epsilon_{zz} >$ -0.05 and $\epsilon_{zz} <$ -0.05 (the critical strain ϵ_{zz}= -0.05) respectively, signifying that β-As_2Te_3 becomes a strong $\mathbb{Z}_2$ topological insulator for ϵ_{zz} $<$ -0.05. Similar to Bi_2Se_3, Bi_2Te_3 and Sb_2Te_3 which are strong $\mathbb{Z}_2$ topological insulators at the ambient pressure [9], the top of valence and the bottom of conduction bands of β-As_2Te_3 have even and odd parities respectively in its topological insulating phase.

As shown in Fig. 3.8(d), the band gap at the Γ point increases with strain beyond the transition point ($\epsilon_{zz} <$ -0.05), which is expected of a topological insulator, but with higher value of compressive strain (*e.g.* at $\epsilon_{zz} \sim$ -0.06), there is anti-crossing (see Fig. 3.8(c) & Fig. 3.9(a)) of these bands along the Γ-Z direction. This anti-crossing behavior can be explained with group theoretical analysis of their symmetries (see the next paragraphs). While the top-most valence band touches the Fermi level along Z-F direction, As_2Te_3 remains semiconducting at all $\epsilon_{zz} \neq$ -0.06, as evident in the electronic density of states (e-DOS) in Fig. 3.9(b).

β-As_2Te_3 has both spatial inversion and time reversal symmetries. Inversion centre in the crystal ensures the degeneracy of the electronic bands at **k** and **-k** *i.e.* $\varepsilon_{n\alpha}(\mathbf{k}) = \varepsilon_{n\alpha}(\mathbf{-k})$, where $\varepsilon_{n\alpha}(\mathbf{k})$ represents the electron energy for the n-th band with spin index α at

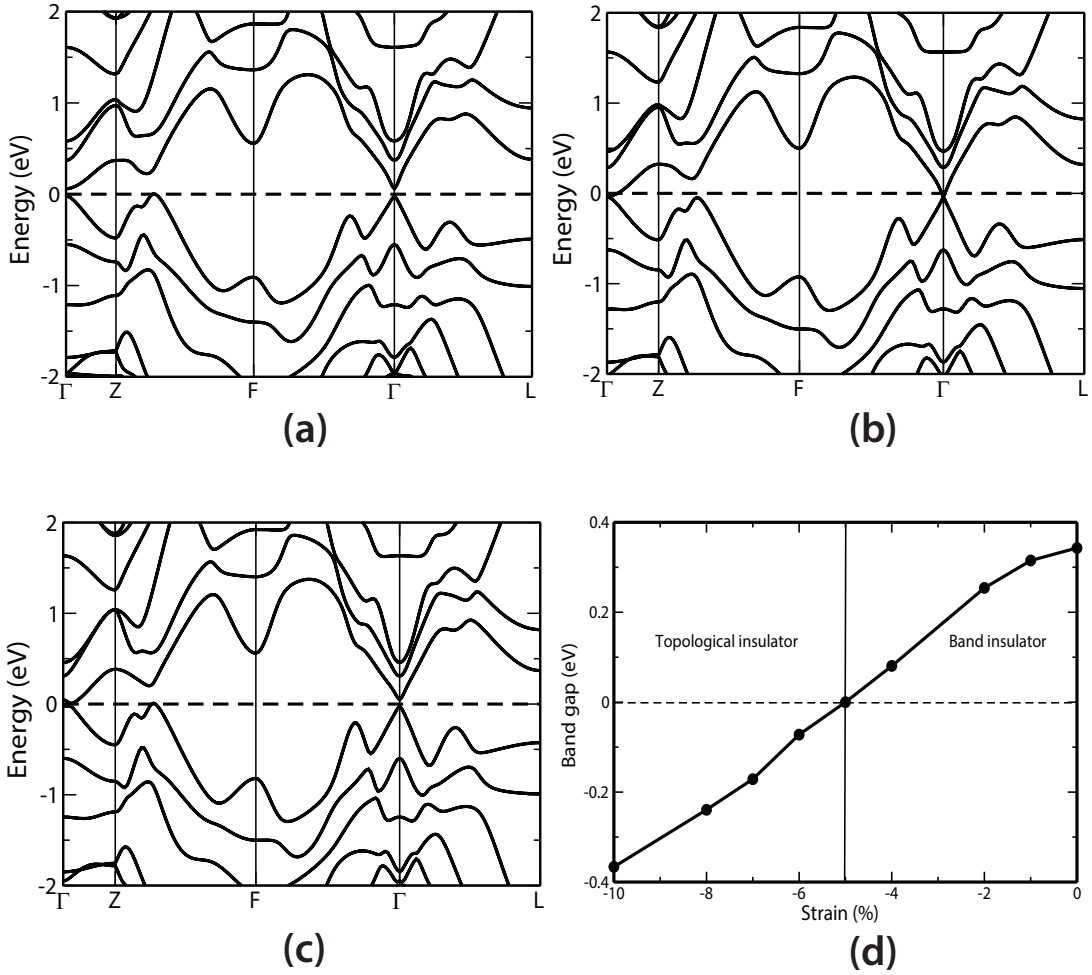

Figure 3.8: Evolution of electronic bands and bulk band gap of β-As_2Te_3 as a function of uniaxial strain (ϵ_{zz}). Electronic structure of bulk β-As_2Te_3 when the uniaxial strain are (a) ϵ_{zz}= -0.04, (b) ϵ_{zz}= -0.05, and (c) ϵ_{zz}= -0.06 showing the closing and reopening of the bulk band gap at the Γ point as a function of ϵ_{zz}. (d) Variation of the direct band gap at the Γ point as a function of uniaxial strain ϵ_{zz}. The electronic topological transition in β-As_2Te_3 passes through a metallic state at ϵ_{zz} = -0.05, where a linearly dispersing Dirac cone appears at the Γ point.

k wave vector in the Brillouin zone. On the other hand, the time reversal symmetry implies $\varepsilon_{n\alpha}(\mathbf{k}) = \varepsilon_{n\bar{\alpha}}(\mathbf{-k})$, where $\bar{\alpha}$ represents the spin opposite to α. When both symmetries are present, $\varepsilon_{n\alpha}(\mathbf{k}) = \varepsilon_{n\bar{\alpha}}(\mathbf{k})$, *i.e.* electronic bands acquire Kramers' double degeneracy at each **k** vector. As each electronic band in a $\mathbb{Z}_2$ topological insulator (having both time-reversal and inversion symmetries) is doubly degenerate, the irreducible representation for each band is two dimensional (*i.e.* E, according to Mulliken's symbol). In the Hamiltonian with SOC, the point group at any **k** vector is a double group due to inclusion of time

reversal symmetry. The irreducible representations of bands are hence determined by the character table of the corresponding double group of a spin-orbit coupled system [62]. At Γ point (*i.e.* null **k** vector) in the Brillouin zone, the group of the k-vector is D_{3d}, and electronic bands are labeled with representations (also known as small representations) of the double group of D_{3d}. The top of the valence and bottom of conduction bands in the topological insulating state have $E_{1/2g}(=\Gamma_{4+})$ and $E_{1/2u}(=\Gamma_{4-})$ symmetries respectively (see Fig. 3.9(a), where the scale of electronic structure has been zoomed along the Γ-Z direction) at Γ. For **k** along z-direction (Γ-Z), the group of **k** lacks the inversion symmetry, and therefore its subgroup is C_{3v}, and bands along Γ-Z direction are labeled with irreducible representations of the double group of C_{3v}.

When two bands belong to the same irreducible representation, a coupling between them is allowed by symmetry. As a result, they avoid crossing each other and lead to an "anti-crossing" [131]. Electronic bands just above and below the Fermi level along the Γ-Z direction anti-cross each other, because they belong to the same irreducible representation ($E_{1/2}=\Gamma_4$) of C_{3v}. This analysis establishes that there can be no band crossing and closure of gap along Γ-Z direction, and hence the electronic structure (see DOS in Fig. 3.9(b)) of β-As_2Te_3 remains semiconducting as a function of ϵ_{zz} (including ϵ_{zz}=-0.06).

As the bandgap vanishes at the electronic topological transition in β-As_2Te_3, we expect a breakdown of the adiabatic approximation in the vicinity of the critical point. This broken adiabaticity would lead to Raman anomalies in a narrow range of stress near P_c through a strong coupling between the electrons and phonons near the transition [95]. Thus, it is of fundamental importance to measure the electronic and vibrational spectra of β-As_2Te_3 as a function of uniaxial strain, and confirm the presence of electronic topological transition and associated spectroscopic anomalies in β-As_2Te_3.

Since topological insulators typically exhibit good thermoelectric properties [132,133], we expect β-As_2Te_3 to be a better thermoelectric than its ambient pressure monoclinic phase, consistent with the finding of Ref. [124]. Thin films of topological insulators like Bi_2Te_3, Bi_2Se_3 are better thermoelectric materials [132] than their bulk counterpart due to

the high mobility of the electrons on the metallic surface and low lattice thermal conductivity [133]. Strain engineering of thin films of Bi_2Se_3 was shown to be an effective way to optimize its thermoelectric figure of merit (zT) [134], given by $zT = \frac{\sigma S^2 T}{\kappa}$, where σ, S and, κ are electrical conductivity, Seebeck coefficient and thermal conductivity respectively.

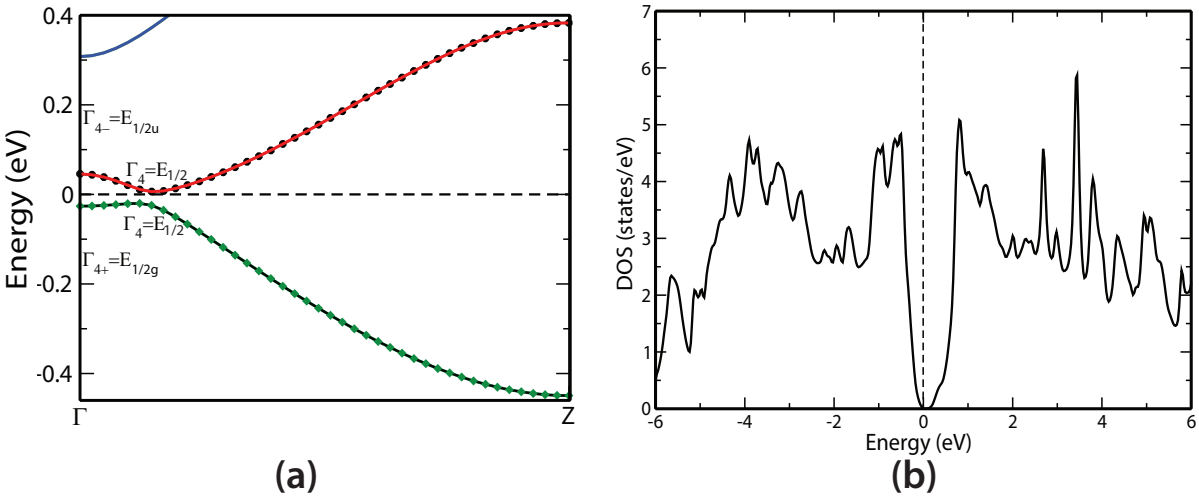

Figure 3.9: (a) Electronic structure of β-As_2Te_3 at ϵ_{zz}= -0.06 with spin-orbit coupling zoomed along the Γ-Z direction. The electronic states near the Fermi level having the same irreducible representations lead to an anti-crossing situation as discussed in the text. (b) The total electronic density of states (DOS) of β-As_2Te_3 at ϵ_{zz}= -0.06 show semiconducting nature of the material in its topological insulating state.

Low κ is key to thermoelectric performance of a material. As acoustic phonon bands of β-As_2Te_3 are limited to range of frequencies less than 50 cm^{-1} (see Fig. 3.10), and κ depends quadratically on slope of the acoustic band, we expect a rather low thermal conductivity of β-As_2Te_3 in all the three directions. The narrow gap of β-As_2Te_3 will facilitate high electrical conductivity at room temperature, and the asymmetry in its DOS (Fig. 3.9(b)) across the gap is expected to yield a high S (*e.g.* at ϵ_{zz} = -0.06, band gap is 0.06 eV). Since its narrow band-gap and the symmetry of its frontier states are sensitive to uniaxial stress, β-As_2Te_3 has the promise of a good thermoelectric whose properties are tunable with stress field. Thus, β phase of As_2Te_3 has the potential candidate for devices based on stressed thermoelectric.

With frequencies of all its phonons less than 200 cm^{-1}, vibrational entropy gives greater stability to β-As_2Te_3 with increasing temperature. As the quintuple layers of β-As_2Te_3

are held together by the weak van der Waals forces, it can be readily prepared in the form of an ultra-thin film. Surface of a topological insulator exhibits a robust two dimensional electron gas (2DEG) with a high carrier mobility, while that of a band insulator shows none. This property can be used to create a charge pump based on As_2Te_3 that is driven by mechanical stress field.

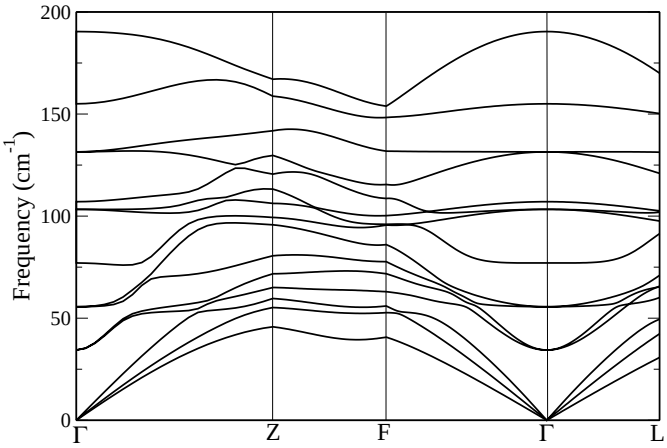

Figure 3.10: Phonon dispersion of β-As_2Te_3 at ϵ_{zz}= -0.06 calculated within a non-relativistic description.

3.2.4 Conclusions

In conclusion, we predict a uniaxial strain induced transition from band to topological insulating state in β-As_2Te_3 using first-principles density functional theory based calculations, highlighting the importance of spin-orbit coupling. It exhibits a direct band gap of 0.35 eV at the Γ point at ambient conditions, and passes through a Dirac semi-metallic state with linearly dispersing bands typical of a Dirac cone at ϵ_{zz} = -0.05 with non-zero gaps on the two sides of the transition. The ETT in the rhombohedral phase of As_2Te_3 has been demonstrated through the band inversion and parity reversal of the top of the valence and bottom of conduction bands across the critical strain, accompanied by a change in the $\mathbb{Z}_2$ topological invariant. Finally, uniaxial stress can be used to tune electronic gap and thermoelectric performance of thin films of β-As_2Te_3, which augurs well for its applications.

3.3 Pressure Induced Phase Transition in Bi_2Se_3 at 3 GPa: Electronic Topological or Not?[‡]

3.3.1 Introduction

Topological insulators (TIs) have gained immense attention [21, 97] due to the novel physics associated with their gapless surface states which are protected either by discrete (*e.g.*, time-reversal symmetry in Z_2 TI) or spatial (*e.g.*, point group symmetry in topological crystalline insulator [43]) symmetries of the crystal. Among all the materials that are shown to exhibit topological nontrivial electronic phases, Bi_2Se_3 is the first material to be discovered as Z_2 TI in three-dimensions which shows exotic properties like quantum magneto-resistance [135], highly spin-polarized currents [136].

Bi_2Se_3 belongs to the simplest topological class which hosts only a single Dirac cone in the electronic structure of its (001) surface [9]. But these topological surface states are not easy to probe experimentally, since it is masked by the bulk contributions due to impurities, high carrier density. Transport measurements have been performed on Bi_2Se_3 to explore the surface states [137, 138] by observing V-shaped conductance, ambipolar behavior and the enhancement in thermopower [139] due to Dirac electrons.

Spin-orbit coupling (SOC) plays an important role in inducing the nontrivial topology in the electronic structure of Bi_2Se_3, Bi_2Te_3 and Sb_2Te_3 compounds [104]. By calculating the parities of the occupied bands of Bi_2Se_3 class of materials from electronic structure calculations obtained within fully-relativistic analysis, Zhang et al. showed [9] how SOC leads to the inversion of valence and conduction bands of opposite parity and induces electronic topological phases in these compounds with Z_2 invariants (1;000) at ambient conditions. Mechanical strain was also shown to modify the strength of SOC relative to the crystal field strength and induce electronic topological transition in materials [109]. For example, it was shown in section 3.1 that how the application of hydrostatic pressure

[‡]This work has been published in Journal of Physics:Condensed Matter **28**, 105401 (2016) [111]. Reproduced with permission from the IOP Publishing.

turns the band insulating phase of rhombohedral Sb_2Se_3 into a topological insulator by modifying the relative strength of SOC [95].

Since the discovery of Bi_2Se_3 family of strong topological insulators, many theoretical and experimental works have been done on these compounds. For example, it was shown that Bi_2Te_3 undergoes a superconductivity transition [140, 141] with pressure around P = 4 GPa (at low temperature), making itself a platform to probe Majorana [142] fermions at the superconductor/TI interface [143]. The enhancement of thermoelectric power [144] of Bi_2Te_3, increase in resistivity [145] and monotonous decrease in mobility [145] for Bi_2Se_3 have also been reported in $\sim$ 3-5 GPa pressure range, which lies below the pressure ($\sim$ 8 GPa) at which the first structural transition occurs in this crystal family [106, 107]. A change in the elastic modulus parallel to the layered direction (and a minima of the c/a ratio) in the 3-5 GPa pressure range have also been observed for all three stoichiometric TIs Bi_2Se_3 [107], Bi_2Te_3 [106] and Sb_2Te_3 [110]. This low pressure transition is often termed as electronic topological transition (ETT) or Lifschitz transition [146].

Here, it is worth defining ETT which can have two implications: (a) the van Hove singularity associated with the band extrema passes through the Fermi level, and thereby the distribution of carriers and Fermi surface topology changes. This is also known as Lifshitz [146] transition assigned for all the aforementioned TIs in the range of 3-5 GPa; (b) another type of ETT is characterized by the Z_2 topological index, when the reversal of valence band and the conduction band with opposite parities occurs and as a result, odd number of surface Dirac cones appear. We revisit this low pressure transition of Bi_2Se_3 in this work and investigate the nature of this transition. We do not find any change in the electronic topology of both the types as mentioned above as a function of pressure (P $\leq$ 8 GPa) by examining the density of states at Fermi level, Z_2 invariants, and gapless Dirac cones in its surface electronic structure.

As presence of ETT (which involves change in Z_2 invariants) can be captured effectively by Raman spectroscopy experiments [95], our experimental collaborators (Achintya Bera and Prof. A. K. Sood, Indian Institute of Science, Bangalore) measured the Raman

spectra of Bi_2Se_3 as a function of hydrostatic pressure. Although, the pressure derivatives of Raman modes show a clear change at 2.4 GPa, no new modes appear at that pressure, ruling out any structural phase transition at 2.4 GPa. The angle of the rhombohedral unit cell increases sharply upto ∼3 GPa followed by a slow increase. We term this transition near 3 GPa as iso-structural transition (IST), instead of ETT, as there is no change in the Z_2 topological invariants of the bulk in 0-8 GPa range of pressure.

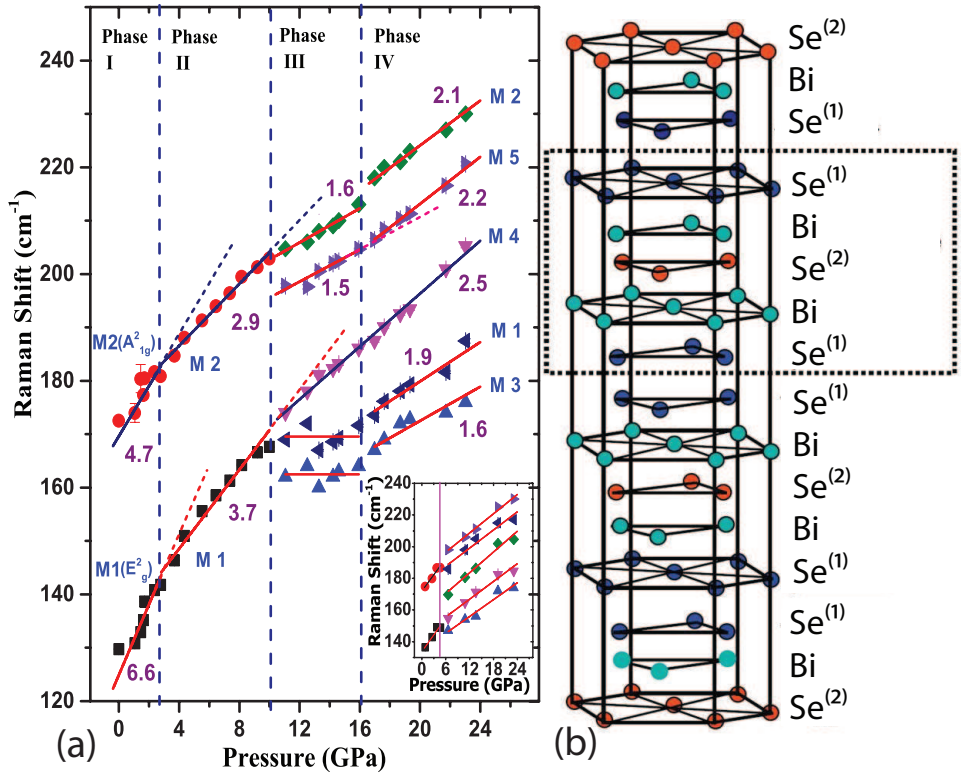

Figure 3.11: Experimental Raman shift of Bi_2Se_3 as function of pressure and hexagonal crystal structure of Bi_2Se_3. (a) Frequency as a function of pressure for various Raman active modes of Bi_2Se_3. The solid lines are linear fits to the observed frequencies (solid symbols). Error bars (obtained from the fitting procedure) are also shown. The inset represents the observed frequencies in the return pressure run. The vertical (dashed and solid) lines indicate the phase transition pressures. (b) Layered hexagonal crystal structure of Bi_2Se_3.

3.3.2 Experimental observations

The pressure dependence of various Raman active modes is shown in Fig. 3.11, from which the following observations can be made: (a) the decrease in pressure coefficient

(i.e. slope of the frequency vs pressure graph) of both E_g^2 and A_{1g}^2 modes occurs at 2.4 GPa; (b) from 2.4 GPa to around 8.2 GPa these two modes harden linearly; (c) above 8.2 GPa these two phonons soften slowly upto around 12.8 GPa; (d) a new mode assigned as N appears around 12.8 GPa which hardens with pressure and both E_g^2 and A_{1g}^2 modes show a change in the slope of pressure coefficient around 12.8 GPa. Here we focus only in the low pressure range (*i.e.* P $<$ 10 GPa) We associate the first transition at P$\sim$ 2.4 GPa to an iso-structural transition (IST) which is consistent with high pressure X-ray study on Bi_2Se_3 [107], where no jump in unit cell volume was observed. Our observations about change in the slope of high frequency mode A_{1g}^2 around IST is quite contrary to all earlier results of high pressure Raman investigations on Bi_2Te_3 [106], Bi_2Se_3 [107] and Sb_2Te_3 [147], where A_{1g}^2 showed no change. The change in pressure coefficient of E_g^2 mode at the IST (P$\sim$ 2.4 GPa) is larger than that of A_{1g}^2, which is in agreement with the studies of Vilaplana et al. on Bi_2Se_3 [107].

3.3.3 Crystal structure and computational details

Bi_2Se_3 has a rhombohedral crystal structure having space group R$\bar{3}$m (No. 166) with lattice parameters a_{hex}=4.143 Å and c_{hex}=28.636 Å [148]. The crystal structure of Bi_2Se_3 consists of quintuple layers (QLs) stacked along c-direction, where in one QL the atomic plane arrangement along c-axis becomes Se(1)-Bi-Se(2)-Bi-Se(1). Se(1) and Se(2) indicate the two different types of selenium atoms in the crystal (see Fig. 3.11(b)). Our calculated band gap (0.33 eV) is in good agreement with the experimentally reported [122] band gap of 0.35 eV. Group theoretical analysis for the centrosymmetric rhombohedral crystal structure of Bi_2Se_3 predicts 12 optical zone center phonons represented by $2A_{1g}+2E_g+2A_{2u}+2E_u$ [149, 150].

We employ the Quantum ESPRESSO (QE) code [112] for first-principles calculations based on density functional theory and both fully relativistic and scalar-relativistic pseudopotentials. While the spin-orbit coupling (SOC) has profound effect in modifying the electronic properties of a material containing heavy elements, it has only weak effects

on vibrational frequencies due to disparate energy scales associated with spin-orbit coupling and vibrational energy of the ions. As a consequence, the magnitude of the phonon frequencies does not change significantly and the character of the vibrational modes also remains unchanged with omission of the SOC. Effect of spin-orbit coupling is included in our first-principles calculations by constructing relativistic pseudopotential from the solution of the relativistic Dirac equation instead of non-relativistic Schrödinger equation. We have used relativistic pseudopotentials in determination of the electronic structure of Bi_2Se_3 and scalar-relativistic pseudopotentials for calculating its vibrational properties. We adopt the self-consistent density functional perturbation theory (DFPT) [64] available within the QE distribution in calculation of vibrational frequencies. We approximate the exchange-correlation energy functional with a generalized-gradient approximation (GGA) [113] as parametrized by Perdew, Burke and Ernzerhof (PBE) [114]. The kinetic energy cut-offs on the plane wave basis for the wave function and charge density are kept at be 60 Ry and 240 Ry respectively. Integrations over the Brillouin zone are performed with a dense mesh of $9 \times 9 \times 9$ k-points. Occupation numbers are treated according to the Fermi-Dirac distribution function with a broadening width of 0.04 Ry. We allowed the relaxation of the cell parameters as well as the atomic positions in the bulk unit cell at each target pressure (hydrostatic) until the magnitude of forces on atoms at each pressure are less than 1 mRy/bohr.

The surface electronic structure of Bi_2Se_3 is calculated with a $10\times10\times1$ mesh of k-points using a slab model whose unitcell has a hexagonal structure with QLs stacked along the z-direction. While constructing the slab for the surface calculations, we use the relaxed coordinates of the bulk with and use 6 QLs above which a vacuum of 15 Å was added to keep the electrostatic interaction between the periodic images low.

3.3.4 Theoretical analysis

Bi_2Se_3 exhibits several structural phase transitions as a function of pressure. At ambient condition it has rhombohedral crystal structure (α phase) and at higher pressures it

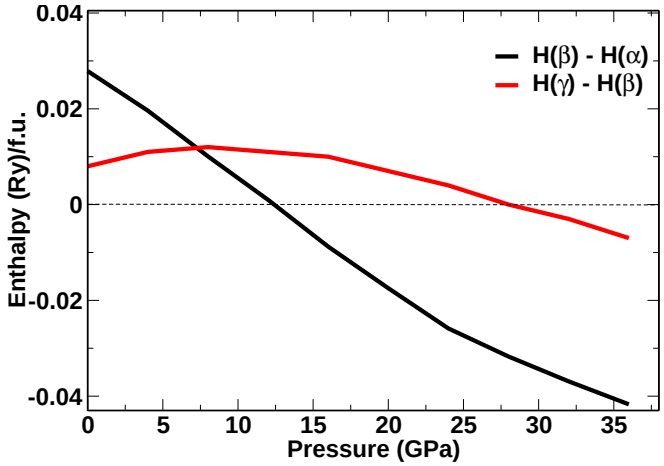

Figure 3.12: Enthalpy differences between the three different structures of Bi_2Se_3 which reveal the first structural phase transition from α to β phase at 12 GPa and second structural phase transition from β to γ at 28 GPa. H(α), H(β) and H(γ) are enthalpy of the α, β and γ phases of Bi_2Se_3 respectively. Here, f.u. stands for formula unit.

adopts two monoclinic structures with space group C2/m (β phase) and C2/c (γ phase). We have carried out total energy calculations for these three structures of Bi_2Se_3 (α, β and γ) as a function of pressure. Enthalpies H(P) of these structures reveal that α to β phase transition occurs at 12 GPa in agreement with the experimental results of our collaborators as well as others [107, 151, 152] and β to γ phase transition takes place at 28 GPa (see Fig. 3.12). The difference between the experimentally reported transition pressure from β to γ phase at 16 GPa and our calculated transition pressure of $\sim$ 28 GPa may be related to some non-hydrostatic component in the experiments, as also mentioned by Vilaplana et al. [106] while explaining their results.

We now analyze the nature of the phase transition at 2.4 GPa in details through first-principles calculations. Our calculations show an unusual change in the internal angle (α) of the rhombohedral unit cell near 3 GPa (see Fig. 3.13(a)). This anomalous change is also reflected in an anomaly in the c/a ratio of Bi_2Se_3 (see inset of Fig. 3.13(a)) near that pressure. To find the origin of this change in α (or c/a ratio) we examine the intra and inter QL distances between atomic planes (see Fig. 3.13(b)), and we find that it is the inter-quintuple layer (QL) distance (a_{QL}) which is responsible for the anomaly in the c/a ratio near 3 GPa. There is a distinct change in the da_{QL}/dP around 3 GPa (see Fig.

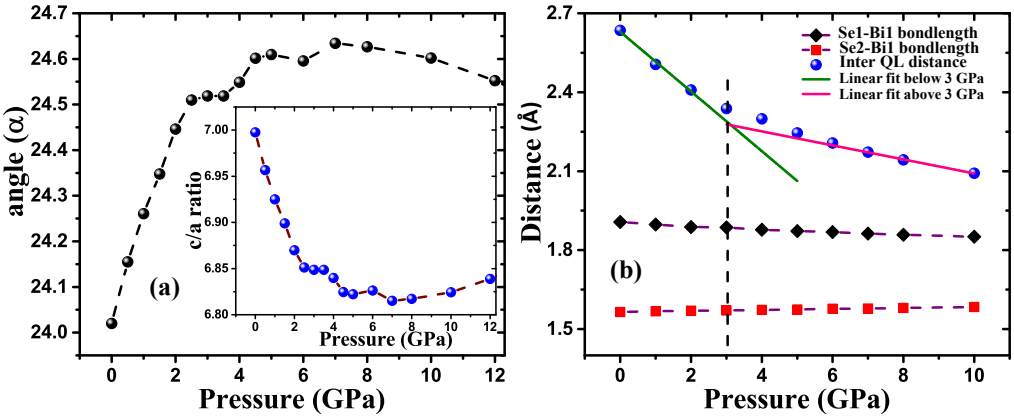

Figure 3.13: Anomaly in the structural parameters of Bi_2Se_3 near P $\sim$ 3 GPa as determined from first-principles calculations. (a) Angle (α) of the rhombohedral unit cell increases sharply upto 3 GPa and slowly above it, which is also reflected in the c/a ratio (inset figure). The unusual behavior of the α or c/a ratio appears due to the sharp decease of the inter quintuple layer (QL) distances below 3 GPa as evident in figure (b). Change in slope in the graph is marked with vertical dashed lines.

3.13(b)), which can be responsible for the observed changes in the slope of E_g^2 and A_{1g}^2 experimental Raman frequencies at this pressure (Fig. 3.11(a)).

It is clear from all the earlier experiments that anomalies in phonon spectrum are present around $\sim$ 3 GPa. To relate its relevance to ETT, we have performed detailed calculations on the bulk band gap as well as surface electronic structure below and above the transition region ($\sim$ 3 GPa). The direct band gap of the bulk of Bi_2Se_3 at Γ point increases with pressure and a change in the slope of the band gap appears near 3 GPa (see Fig. 3.14(a)). Though the direct band gap at Γ point increases monotonically with pressure, the smallest band gap of the bulk first increases upto 6 GPa and decreases above it (see Fig. 3.14(b)). With increasing pressure, the valence band maxima (VBM) and conduction band minima (CBM) change their positions in the momentum space making Bi_2Se_3 an indirect [9] to direct band gap material above P $>$ 4 GPa [153]. Electronic density of states (see Fig. 3.14(c)) reveal a small change in the band gap of Bi_2Se_3 as shown for a few typical pressures of 2 GPa, 4 GPa and 6 GPa. The electronic structure of the bulk calculated by including spin-orbit coupling shows a gap of 0.28 eV at ambient conditions.

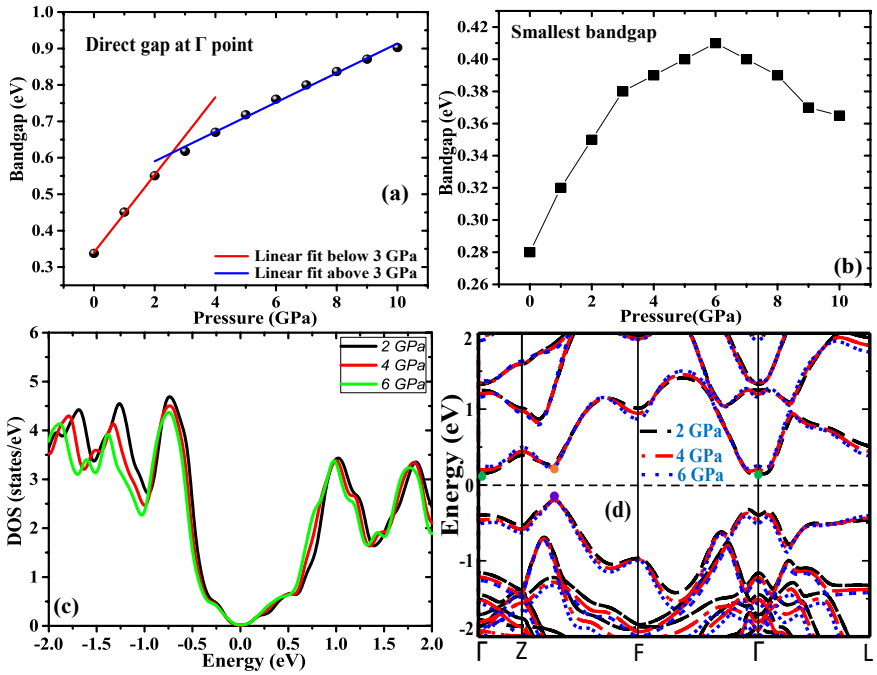

Figure 3.14: Calculated electronic structure as a function of pressure. (a) Change in the slope of direct band gap of Bi_2Se_3 at the Γ point near P $\sim$ 3 GPa, which is a consequence of the unusual change of c/a ratio near that pressure. (b) Smallest band gap as a function of pressure and (c) total electronic density of states at 2 GPa, 4 GPa and 6 GPa. (d) Though the band gap at Γ-point of Bi_2Se_3 increases with pressure, its electronic structure reveals small changes in the extrema in the bands around 4 GPa. Closer inspection of electronic structures reveals an indirect band gap of Bi_2Se_3 at 2 GPa, where VBM and CBM are marked with violet and green dots respectively, whereas at 6 GPa, Bi_2Se_3 exhibits a direct band gap where VBM and CBM are denoted with violet and orange dots respectively. We note that, with pressure the VBM remains fixed, but CBM changes its positions from Γ-point (green dot) to along Z-F line (orange dot).

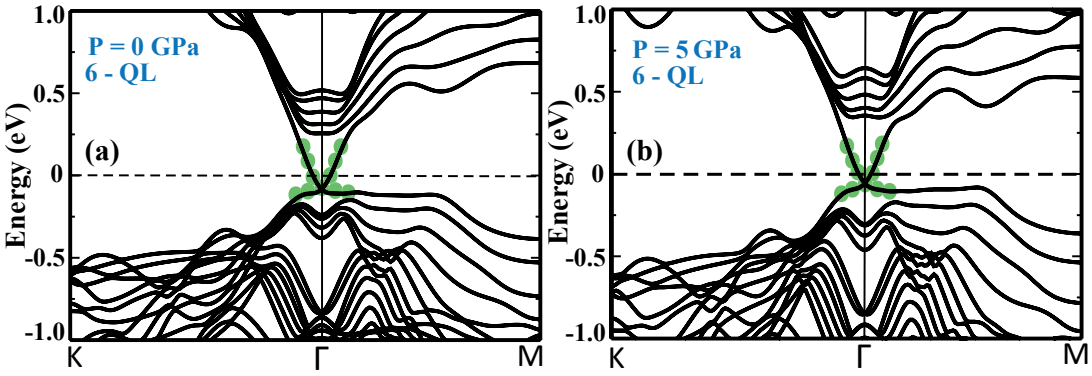

Figure 3.15: Electronic structure of the (001) surface of Bi_2Se_3 for (a) 0 GPa and (b) 5 GPa which reveal of a single Dirac cone (highlighted with green dots) at the Γ point showing no change in robust bulk electronic topology (which gives rise to gapless surface Dirac cone) as a function of pressure.

We compare the electronic structure of the bulk at different pressures near this transition (see Fig. 3.14(d)) and we do not find any significant changes in the electronic band dispersions. As Bi_2Se_3 is a strong $\mathbb{Z}_2$ topological insulator with topological invariant ν_0=1, we determined the $\mathbb{Z}_2$ invariant ν_0 of Bi_2Se_3 at pressures upto 8 GPa following the method developed by Fu and Kane [56] for a centrosymmetric material. In this method, we find the parity of the occupied bands at eight time reversal invariant momenta (TRIM), and use the relation $(-1)^{\nu_0} = \Pi_{i=1}^{8}\ \delta_i$, where i runs over eight TRIM and δ_i=$\Pi_m\ \xi_{2m}^i$, ξ_{2m} being the parity of the occupied bands indexed with 2m at each TRIM (i). We find that ν_0 remains 1 at all pressures upto 8 GPa (see Table 3.3). This signifies that there is no electronic topological transition occurring in the above pressure range and Bi_2Se_3 remains a topological insulator before it undergoes a structural transition to monoclinic structure at higher pressure.

As gapless Dirac cone in the surface electronic structure is characteristic of a strong topological insulator, we calculate the electronic structure of the (001) surface of Bi_2Se_3 as a function of pressure to see any topological change, as it is the nontrivial topology of the bulk electronic wave function which gives rise to symmetry protected Dirac cone on the surface. At ambient pressure, we find a gapless Dirac cone (Fig. 3.15(a)) as expected of a strong $\mathbb{Z}_2$ TI. Our first-principles calculation of the slab of Bi_2Se_3 reveals that, on the other side of the transition (*e.g.*, at P=5 GPa), band gap does not open up at Γ in its surface electronic spectrum maintaining its topological insulating nature intact (see Fig. 3.15(b)), in agreement with the observed angle-resolved photoemission spectroscopy (ARPES) [154]. Thus, there is clearly no change in the $\mathbb{Z}_2$ topological invariant of the electronic structure of Bi_2Se_3 through the transition at P$\sim$ 3 GPa.

In the light of recent results of Forster et al. [155], we note that we have determined the topological invariants of Bi_2Se_3 from calculations of its bulk form. Errors in the band gap in a density functional theoretical (DFT) calculations may result in some errors in the pressure of transition from band to topological insulating states. On the other hand, closure of a gap in the surface electronic structure is sensitive to the error in the DFT

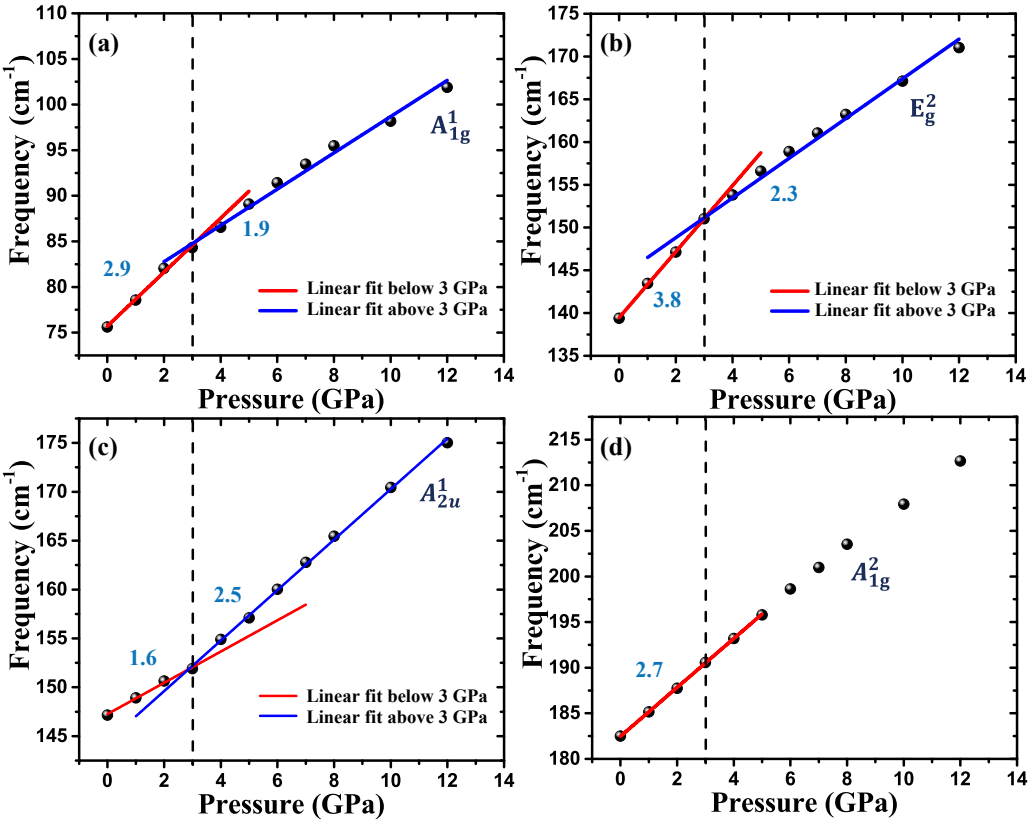

Figure 3.16: Calculated Raman and IR active modes as a function of pressure. The change of slope of the phonon modes as measured by the Raman experiment is also captured through our first-principles calculations. Change in slope (expressed in cm^{-1}/GPa) for Raman active modes A^1_{1g}, A^2_{1g}, E^2_g are shown in (a), (d) and (b) respectively. Infrared active mode A^1_{2u} also displays a change in slope near 3 GPa shown in (c). Vertical dashed lines are placed at the positions where the change in slope is observed.

band gap, but it is a finite size effect. Topological character can always be ascertained by using a thicker film or slab in the calculations.

Now, we discuss the calculated vibrational frequencies of Bi_2Se_3 as a function of pressure which, do reveal a change in their slopes (see Fig. 3.16) near the transition (*i.e.* in 2-5 GPa range of pressure) where the rhombohedral angle (α), c/a ratio and inter QL distance exhibit anomalous behavior (see Fig. 3.13). The most significant changes occur in the Raman active E^2_g and A^1_{1g} modes and also in the IR active A^1_{2u} mode. The change in slope of the A^2_{1g} mode is not captured in the calculation due to the anharmonic coupling between the A^2_{1g} and all other modes and hence pressure dependence of this mode originating from strong anharmonicity is not captured within the harmonic analysis presented

Bi_2Se_3	P (0 GPa)	+	-	+	-	+	-	+	+	-	+	-	-	-	+	;	-	(-1)
	P(4 GPa)	+	-	+	-	+	-	+	+	-	+	-	-	-	+	;	-	(-1)
	P (8 GPa)	+	-	+	-	+	-	+	+	-	+	-	-	-	+	;	-	(-1)

Table 3.3: Parities of the fourteen occupied bands and the lowest energy unoccupied band of Bi_2Se_3 at pressures in the range of 0-8 GPa. The product of parities of the valence band manifold are -1 as indicated within the brackets, which gives the value of $\mathbb{Z}_2$-invariant ν_0 to be 1.

here.

3.3.5 Conclusions

In conclusion, our calculations clearly show that the low pressure transition at ~ 3 GPa is *not* related to any change in the electronic topology, as there is no change in the $\mathbb{Z}_2$ index, and the gapless Dirac cone in the surface electronic structure remains intact below and above the transition. Hence, the lowest pressure transition should be better termed as an iso-structural transition, and not an ETT. While our theoretical calculations captured the change in slope of E_g^2 mode correctly, the change in slope of A_{1g}^2 mode at the iso-structural transition needs further understanding.

Chapter 4

Anomalous Temperature Dependence of Electronic and Vibrational Properties of Sb_2Te_3

4.1 Introduction

Sb_2Te_3 is a time-reversal invariant strong topological insulator in three dimensions belonging to same symmetry and topological class (characterized by Z_2 invariant) as that of Bi_2Se_3 and Bi_2Te_3, which hosts only a single Dirac in the electronic structure of (001) surface [9,104]. Topologically protected surface states of these insulators hold many promises for applications in spintronics [156], quantum computation [120]. These materials have layered structures where quintuple layers of the formula unit are stacked along c-axis which are held together by weak van der Waals forces.

While most experimental measurements on topological insulators have focused on investigations of their robust surface electronic structure [136, 157], measurements of the properties of their bulk have remained relatively scarce. Recent x-ray diffraction and dilatometry experiments have shown an intriguing anomaly in the thermal expansion coefficients of bulk Sb_2Te_3 [158] and Bi_2Se_3 [159], without any accompanying structural or

electronic phase transition. The coefficient of linear thermal expansion along the hexagonal c-axis of Sb_2Te_3 deviates significantly from the Debye law in the temperature region of 200-250 K. It decreases sharply within range showing a minimum at 225 K (even crosses zero and becomes negative) and then increases abruptly in the 225-236 K temperature region [158]. More importantly, the specific heat measurements of Sb_2Te_3 do not show any anomaly in this temperature range. Similar anomalous behavior of thermal expansion has also been seen for Bi_2Se_3 [157] and Bi_2Te_3 [160].

As no other physical property has been shown to display anomalous temperature dependence in the above temperature range (200-250 K) so far, the origin of the observed anomaly in thermal expansion coefficient is unclear. In this work, we seek to find an explanation of anomalous temperature dependence of electronic and vibrational properties of Sb_2Te_3 though first-principles theoretical analysis.

4.2 Experimental observations

Ultrafast time-resolved pump probe experiments were done by Gyan Prakash from Prof. A. K. Sood's group at the Indian Institute of Science on the single crystal of Sb_2Te_3 to investigate the dynamics of electrons and phonons in 3-300 K temperature range which includes the anomalous temperature regime as reported in earlier works [158]. Refractive index (n), extinction coefficient (k), longitudinal sound velocity ($v_{_{LA}} = \lambda\nu_{_{LA}}/2n$) and Young's modulus ($Y_{LA}$) related to LA modes along the c-axis as obtained from the experiments, are shown in Fig. 4.1. Near anomalous temperature (T_a=225 K), a significant decrease is observed in n and k, while the sound velocity ($v_{_{LA}}$) and Young's modulus $Y_{_{LA}}$ show a significant increase near T_a.

4.3 Crystal structure

Sb_2Te_3 has a layered crystal structure (space group $R\bar{3}m$, No 166), which consists of closed-packed atomic layers which are periodically stacked along the c-axis in units of five

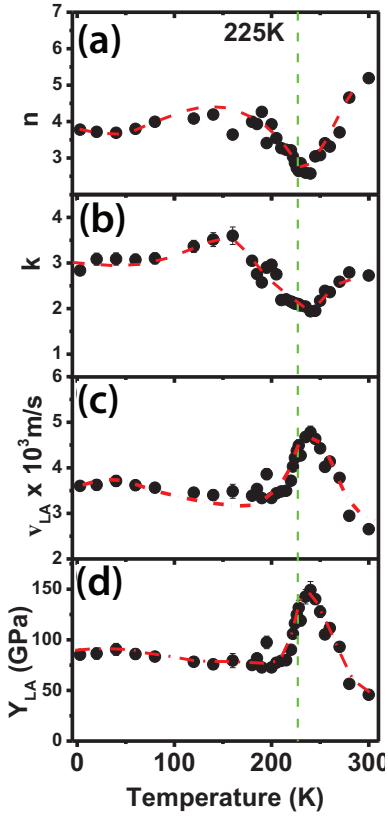

Figure 4.1: Experimentally measured temperature dependent (a) refractive index (n), (b) extinction coefficient (k), (c) sound velocity (v_{LA}) and (d) Young's modulus of (Y_{LA}) obtained using strain pulse propagation model. Dotted lines joining through data points are guide to eye. The dotted vertical line is drawn to match T_a=225 K.

atomic planes ($Te^{(1)}$-Sb-$Te^{(2)}$-Sb-$Te^{(1)}$) known as quintuple layer (QL). These QLs are bonded by weak van der Waals force [147,149]. There are five atoms in the rhombohedral unit cell, whereas the conventional hexagonal unit cell has 15 atoms [147, 149]. The hexagonal unit cell of Sb_2Te_3 is shown in Fig. 4.2. Group theoretical analysis of the symmetry point group (D^5_{3d}) of Sb_2Te_3 crystal predicts 12 optical phonons at the Γ point: $2A_{1g}$(R)+$2E_g$(R)+$2A_{2u}$(IR)+$2E_u$(IR) [147], where R and IR refer to Raman and infrared active modes, respectively.

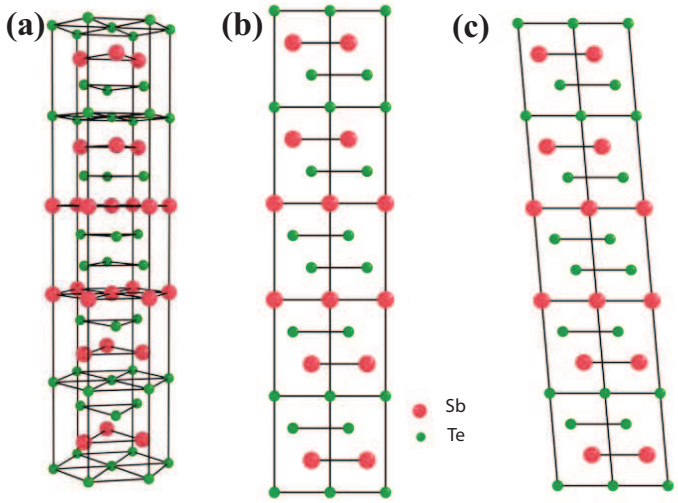

Figure 4.2: Hexagonal unit cell of the pristine and faulted structures of Sb_2Te_3. (a) Hexagonal crystal structure of pristine Sb_2Te_3, and (b) its side view. (c) Stacking faulted configuration of Sb_2Te_3 as seen from a side view.

4.4 Computational details

To uncover the origin of anomalous temperature dependence of the experimentally observed quantities *e.g.*, refractive index (n), Young modulus (Y_{LA}), we analyzed the structural, electronic and vibrational properties of Sb_2Te_3 as a function of temperature using first-principles calculations based on density functional theory (DFT). As Kohn-Sham DFT is a ground state theory and it can not directly (without molecular dynamics) take into account the effect of temperature, we incorporated temperature dependence in our calculations through using experimental lattice constants (a(T) and c(T)) measured as a function of temperature. We used the Quantum ESPRESSO (QE) [112] code which treats only the valence electrons, replacing the potential of ionic cores with smooth pseudopotentials. We used both fully relativistic (which includes spin-orbit coupling) and non-relativistic (which does not include spin-orbit coupling) norm-conserving pseudopotentials treating exchange-correlation energy functional with a generalized gradient approximation (GGA) [114]. Since a strong spin-orbit coupling (SOC) is responsible for nontrivial electronic topology [95,118], we have included SOC while calculating electronic structure of Sb_2Te_3. Our calculation of phonons at a fixed lattice constant both with and

without SOC reveals that change in frequencies is quite small ($\sim$ 1cm^{-1}). As calculations of phonons with SOC are computationally quite expensive, we calculated phonon frequencies of Sb_2Te_3 without including SOC *i.e.* using non-relativistic pseudopotentials. We truncated the plane wave basis used in expansion of the Kohn-Sham wave functions and the charge density with energy cut-offs of 60 Ry and 240 Ry, respectively. We used 9×9×9 and 12×12×2 uniform grids of k-points for sampling the Brillouin zone integrations of the rhombohedral and hexagonal unit cells, respectively, in self-consistent field (SCF) calculations along with the occupation number of electrons smeared with Fermi-Dirac distribution function. We used the DFT linear response with PH package [64], available within QE, to determine the phonon frequencies. High frequency dielectric constant (ϵ_∞) (and hence refractive index $n = \sqrt{\epsilon_\infty}$) is calculated first without SOC using the linear response theory keeping the occupation numbers of the electrons fixed, and was scissor-corrected to take into account the effect of SOC through the band gap using $n = n_{NSOC}\frac{E_g^{SOC}}{E_g^{NSOC}}$, where E_g is the band gap. SOC and NSOC indicate when the band gap is calculated with and without including SOC respectively. Young's modulus is calculated as the second derivative of total energy (calculated with SOC) with respect to uniaxial strain (ϵ_{zz}) in the hexagonal structures. We used nudged elastic band (NEB)-climbing image (CI) procedure without taking into account the effect of SOC to search for the occurrences of iso-structural phase transition in Sb_2Te_3.

4.5 Possibility of iso-structural transition

Taking temperature dependent experimental lattice constants of Sb_2Te_3 [158, 161], we fully relaxed atomic positions in the rhombohedral unit cell and determined its electronic structure and phonon frequencies as a function of temperature. We find that the electronic bands and the phonon frequencies show negligible change as function of temperature.

We next explored if the observed changes in the experiments can be associated with an iso-structural phase transition. In order to find the presence of another local minimum

of Sb_2Te_3 within the anomalous temperature range (200-250 K) of Sb_2Te_3, we picked the rhombohedral crystal structure of Sb_2Te_3 at a representative temperature of 215 K from the range of temperature (200-250 K) related to the anomaly and varied the position of one of the two Te layers (which sits at the point of centrosymmetry) within the unit cell keeping the symmetry of the crystal unchanged. We do find an iso-structural metastable state of Sb_2Te_3 which is 0.65 eV/f.u. higher in energy than the ground state minimum at 215 K, where f.u. stands for formula unit. The transition path connecting the stable and metastable structures of Sb_2Te_3 at 215 K determined with nudged elastic band climbing image (NEB-CI) method reveals that the barrier height for the transition path is too high (5.4 eV) for the phase transition to occur. Thus, the possibility of an iso-structural phase transition between the two local minima of Sb_2Te_3 as the origin of observed anomalies is ruled out.

4.6 Origin of anomalous temperature dependence

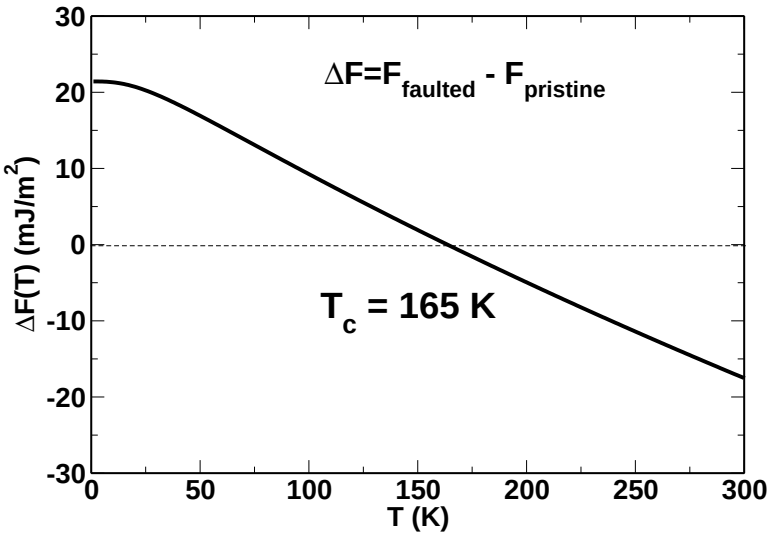

Figure 4.3: Free energy difference between the pristine and faulted structure of Sb_2Te_3. Free energy of both the structures are calculated taking into account their vibrational contributions as a function of temperature. The energy difference (ΔF) becomes negative at 165K which implies that a phase transition occurs from pristine to faulted structure at T = 165K.

As formation of stacking faults (SFs) are expected to be energetically inexpensive in

layered materials [162], we next explored formation of SFs as a possible mechanism of the anomalies in the physical properties of layered Sb_2Te_3. We introduce stacking faults in the basal plane of hexagonal structure (equivalent to rhombohedral one) of Sb_2Te_3 and constructed the pristine ($\vec{\mathbf{a}}_0$, $\vec{\mathbf{b}}_0$, $\vec{\mathbf{c}}_0$) and faulted configuration ($\vec{\mathbf{a}}_{\rm SF} = \vec{\mathbf{a}}_0, \vec{\mathbf{b}}_{\rm SF} = \vec{\mathbf{b}}_0, \vec{\mathbf{c}}_{\rm SF} = \vec{\mathbf{c}}_0 + \frac{1}{3}\vec{\mathbf{a}}_0 + \frac{2}{3}\vec{\mathbf{b}}_0$) of Sb_2Te_3, where $\vec{\mathbf{a}}, \vec{\mathbf{b}}$, and $\vec{\mathbf{c}}$ denote the lattice vectors of the hexagonal unit cell of Sb_2Te_3 (Fig. 4.2). We calculated the free energy $F = E_{\rm tot} + F_{\rm vib}$ of these structures as a function of temperature within harmonic approximation, where $E_{\rm tot}$ is the total energy at 0 K and $F_{\rm vib}$ is the vibrational contribution to the free energy at finite temperature given by $F_{\rm vib} = \frac{k_B T}{N_q} \sum_{iq} \log[2\sinh(\frac{\hbar\omega_{iq}}{2k_B T})]$. Here N_q is the total number of wave vectors q in the Brillouin zone, ω_{iq} is the frequency of i-th phonon with wave vector q obtained using DFT linear response calculations. After optimization of the cell parameters of pristine and faulted structures, we find that the free energy difference (ΔF) decreases with temperature and becomes negative at 165 K (see Fig. 4.3.). This means that a structure with infinitely extensive SF will stabilize above T_a =165 K.

Thus, our first-principles theoretical analysis shows that the observed anomalies in the experiment very likely arises from the formation of stacking faults in the layered structure of Sb_2Te_3 above T_a. Keeping in mind all the approximations, we do not expect the calculated T_a (Fig. 4.3) to match quantitatively the temperature of experimental anomaly ($\sim$225 K). To further examine the effects of formation of stacking faults on the properties of Sb_2Te_3, we considered intermediate deformed states along the path connecting the pristine (**P**) structure to the faulted (**F**) one. Such a path can be parameterized with λ to induce variation in $\mathbf{c}$ vector of the hexagonal cell $\mathbf{c} = \mathbf{c}_0 + \frac{1}{3}\lambda\mathbf{a}_0 + \frac{2}{3}\lambda\mathbf{b}_0$ with $0 < \lambda \leq 1$ ($\mathbf{c}_0$, $\mathbf{a}_0$ and $\mathbf{b}_0$ are pristine hexagonal unit cell lattice parameters). $\lambda = 0$ and $\lambda = 1$ correspond to pristine and faulted structures, respectively. We estimated the refractive index and the Young's modulus of each of the intermediate structures. The Young's modulus and refractive index (see Fig. 4.4) vary significantly along the path (as a function of λ). Refractive index (n), obtained as $\sqrt{\epsilon_\infty}$ exhibits a dip followed by a sharp rise along the path, qualitatively in agreement with experimental observation close to T=225 K. The

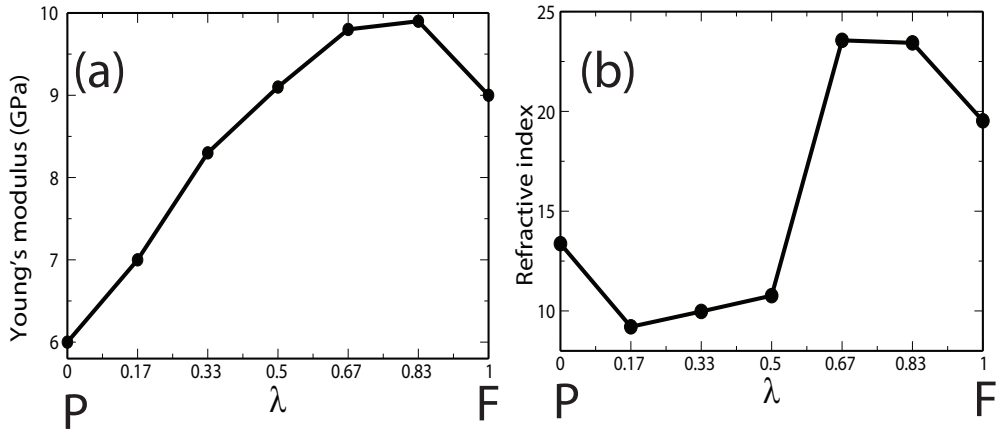

Figure 4.4: Calculated Young's modulus and refractive index for different structures of Sb_2Te_3. (a) Young's modulus (Y) is calculated for different structures of Sb_2Te_3 using the formula $Y=\frac{1}{V}\frac{\partial^2 E_{tot}}{\partial \epsilon_{zz}^2}|_{\epsilon_{zz}=0}$, where V is volume of the unit cell, E_{tot} is the total energy obtained with SOC and ϵ_{zz} is the uniaxial strain. (b) Refractive index, calculated for the pristine, faulted structures and their intermediate configurations, are scissor corrected with $n = n_{NSOC}\frac{E_g^{SOC}}{E_g^{NSOC}}$ where n is the refractive index, E_g is the band gap, SOC and NSOC indicate whether a quantity is calculated with (SOC) and without (NSOC) spin-orbit interaction respectively. (**P** and **F** represent the positions of pristine and faulted configurations respectively along the path parameterized by λ).

rise in n correlates with a minimum in band gap along the path (Fig. 4.5(b)). We note that the refractive index (n) was estimated using scissor correction based on the band gap obtained from a calculation performed with including SOC. Thus, the subtle changes in the electronic structure and the band gap arising from SOC during the formation of a SF appear responsible for the observed anomalies. Calculated Young's modulus along the path exhibits a peak (Fig. 4.4(a)) as the faulted structure forms, also consistent with the observed behavior (Fig. 4.1(d)). This interpretation assumes that stacking faults start forming in a narrow range of temperature below T_a.

To check whether the faulted structure of Sb_2Te_3 has the same electronic topology as that of its pristine structure, we examined the adiabatic continuity between the pristine and the faulted structures. For this, we calculated the electronic structures of configurations at the smoothly deformed intermediate states between the pristine and faulted structures (see Fig. 4.5(a)) to see any band gap closing and reopening. We found that

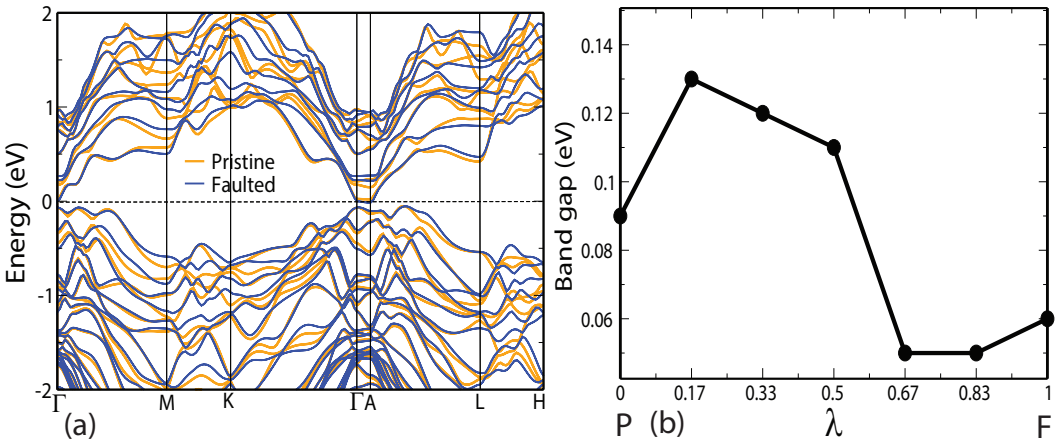

Figure 4.5: (a) Electronic structures of the pristine and faulted configurations of Sb_2Te_3, calculated with spin orbit coupling (SOC). (b) Band gap (determined with SOC) is plotted for the pristine, faulted and their intermediate configurations. (**P** and **F** represent the positions of pristine and faulted configurations respectively along the path parameterized by λ).

the band gap in intermediate configurations does not close (Fig. 4.5(b)), and hence we do not expect any electronic topological phase transition to occur. This implies that the electronic topology of the faulted structure remains the same as that of the pristine structure. Hence, a drop in the calculated band gap close to the faulted configuration is responsible for the observed anomalies in the refractive index, as well as Young's modulus.

4.7 Summary

In summary, our first-principles density functional theory calculations show that the temperature dependent anomalies in the electronic and vibrational properties of Sb_2Te_3 are associated with formation of stacking faults in the layered structure of Sb_2Te_3 above 200 K due to vibrational entropy. While electronic structure undergoes a non-monotonous change across the anomalous temperature T_a, using adiabatic equivalence principle we showed that electronic topology of Sb_2Te_3 remains unchanged before and after the formation of stacking faults.

Part II

Dirac Semi-metals

Chapter 5

Prediction of Robust Non-centrosymmetric Topological Dirac Semi-metallic State in Ternary Half-Heusler Compounds

5.1 Introduction

Dirac semi-metal (DSM) exhibits electronic structure with linearly dispersing conduction and valence bands crossing at quadrupole degeneracy at momenta or discrete points in reciprocal space [25]. This point, a Dirac node, is a combination of two doubly degenerate Weyl points of opposite chirality [29]. As a result, a DSM exhibits interesting chiral anomalies [29], ultrahigh mobility [28], giant magneto-resistance [163] and unconventional superconducting properties [164], and it is also a parent state to various electronic phases like topological insulator, Weyl semi-metal, topological metal and normal insulator [25]. While a DSM state does occur at a point of transition from a normal to topological insulator state (for example with pressure) [118], it is not easy to explore. Apart from the theoretical predictions of DSM states in BiO_2 [46], Cd_3As_2 and Na_3Bi are now established

as DSMs experimentally [47, 165]. We note that these DSMs are centrosymmetric, and metals lacking the centre of inversion are quite rare and fundamentally interesting. For example, there are contrasting views on the existence of a Weyl or Dirac semi-metallic state at a transition between *non-centrosymmetric* topological and normal insulators [166, 167].

Half-Heusler (HH) ternary compounds occur in a non-centrosymmetric structure [168], and a good number of them have been shown to exhibit electronic states with nontrivial topology that is tunable with structural distortion or strain [23, 24]. Many of them are topological semi-metals (TSMs), with quadratically dispersed conduction and valence bands touching at a single point in the Brillouin zone (BZ), and have been shown to become topological insulators with suitable strain [23, 24]. Thus, strained Heuslers are attractive for exploration of a non-centrosymmetric DSM state that is either robust or may occur accidentally at a transition between different topological states [23, 24], and resolve the controversy on adiabatic connectivity between normal and topological insulators lacking inversion symmetry [166, 167].

As the electronic spin-orbit coupling is large for heavy elements and relevant to electronic topology, search [23, 24] for topological insulators in ternary HHs has focused on the compounds containing Bi and other heavy elements such as Yb, Au, Pb, Pt. However, the bands associated with valence bands of heavy elements crowd up in a small energy window near the gap or Fermi level, and make engineering of Dirac nodes harder. We focus here on LiMgBi, an existing stable HH as a model system, because the bands constituted of valence electrons of its lighter elements (Li and Mg) are more dispersed and can be engineered with strain in a well-controlled manner.

To reduce the six-dimensional space of strains in the HH structure in our exploration, we use the design principles [169] and classification scheme [170] of Dirac semi-metals. For a Dirac node to occur in electronic structure, either a quadrupole degeneracy has to occur at a time reversal invariant momentum (wave vector), or two doubly degenerate bands of distinct symmetry should cross at a wave-vector along the axis of three, four or six-fold

structural symmetry [169, 170]. For a DSM based on HH compound with T_d point-group symmetry, we thus have a choice of only those structural distortions that preserve the three-fold rotational symmetry along ⟨111⟩ direction.

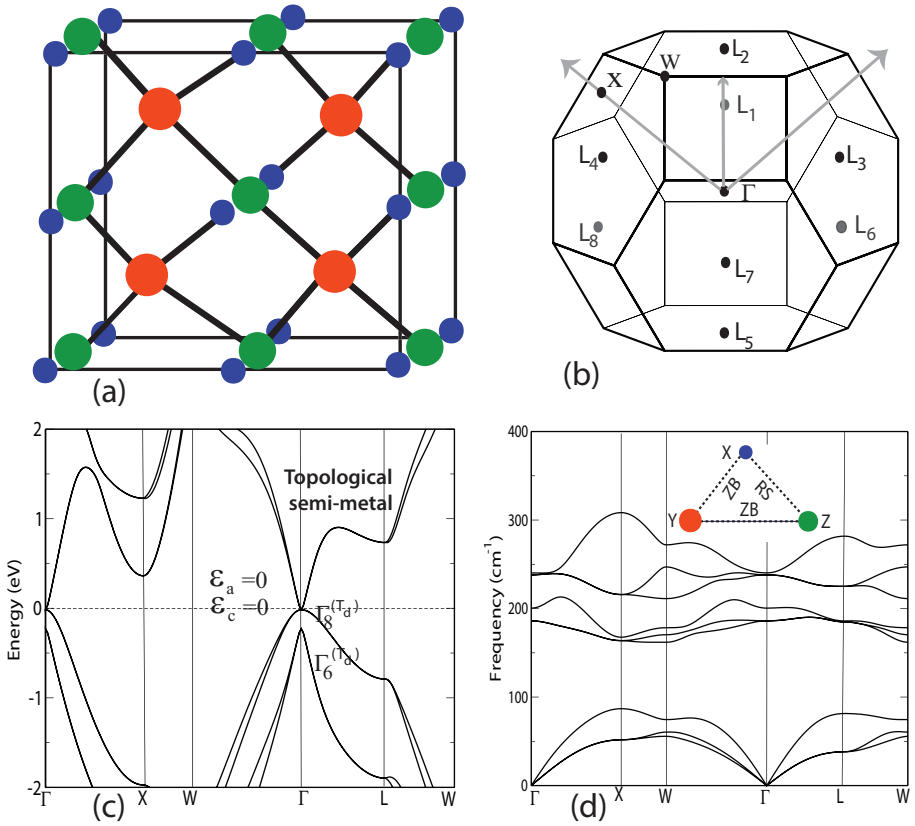

Figure 5.1: Crystal, electronic structures phonon dispersion and Brillouin zone of LiMgBi. (a) Conventional cubic unit cell of LiMgBi (space group: F$\bar{4}$3m), where Li (0,0,0), Mg ($\frac{1}{2}, \frac{1}{2}, \frac{1}{2}$) and Bi ($\frac{1}{4}, \frac{1}{4}, \frac{1}{4}$) atoms are represented with blue, green and orange spheres respectively and (b) Brillouin zone corresponding to its primitive unit cell. At the equilibrium lattice constant ($\epsilon_c = 0$ & $\epsilon_a = 0$), spin-orbit coupled electronic structure (c) reveals a topological semi-metallic state, and phonon dispersion (d) exhibits no lattice instabilities.

5.2 Crystal structure and stability of LiMgBi

While LiMgBi is a well-studied compound [171–174], its crystal and electronic structures both needed to be analysed with care. Its structure involves one formula unit in the primitive cell of the face centred cubic (FCC) Bravais lattice (Fig. 5.1(a)), in which sublattices of two of the atoms form a rocksalt structure, and the third atom occupies the sites of tetrahedral symmetry. In the inset of some of the figures, we have marked

the atomic positions with a triangle whose vertices denoted by X(0,0,0), Y($\frac{1}{4}, \frac{1}{4}, \frac{1}{4}$), and Z($\frac{1}{2}, \frac{1}{2}, \frac{1}{2}$) mark the position of the atoms (in crystal coordinates) in the unit cell. RS and ZB inside the triangle stand for rock-salt and zinc blende sub-lattices respectively. Our analysis shows that the experimental structure (ES) reported in the ICSD database [175] and Materials project [129] is the lowest energy stable structure of LiMgBi in which Bi occupies the tetrahedral sites (see Fig. 5.1(d)). The structure considered in a recent theoretical investigation [174], in which Mg occupies tetrahedral sites, is 0.45 eV/f.u. higher in energy than the ES, and exhibits lattice instabilities (see Fig. 5.2(a)). While LiMgBi was screened as a piezoelectric insulator in another theoretical report [172], we show that a nonzero gap (see Fig. 5.2 (b)) in this work is an artefact of neglect of spin-orbit coupling (SOC). We find that inclusion of SOC results in semi-metallic electronic structure of LiMgBi with inversion of its conduction and valence bands (see Fig. 5.1(c)). Based on this, and the fact that symmetry of its valence and conduction bands is identical to that of HgTe and topologically nontrivial half-Heuslers [23, 24, 176], we conclude that LiMgBi is a topological semi-metal (TSM) at ambient conditions. The local stability of the ES is established from the absence of any unstable modes in its complete phonon dispersion (Fig. 5.1(d)), and is understandable from the chemical argument that most electronegative atom Bi has the coordination of electropositive atoms Li and Mg.

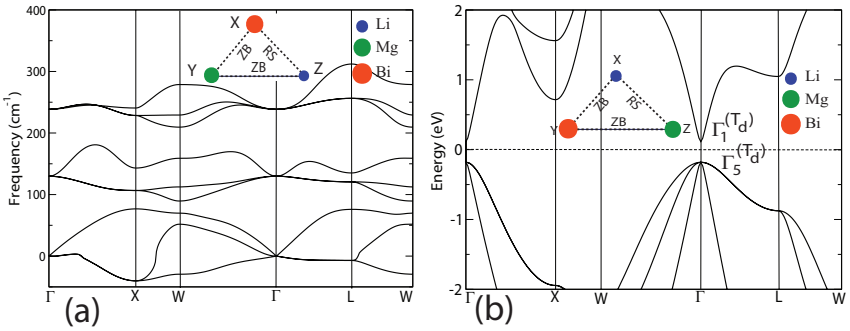

Figure 5.2: (a) Phonon dispersion for the unstable structure of LiMgBi, where Mg atoms occupy the tetrahedral site, showing imaginary frequency at X point in the Brillouin zone. (b) Electronic structure for the stable structure of LiMgBi, calculated without including the spin-orbit coupling (SOC), exhibits non-zero gap of 0.64 eV.

5.3 Computational methods

Our first-principles calculations are within the framework of density functional theory with the QUANTUM ESPRESSO (QE) code [112] in which the interaction between the ionic core and the valence electrons is replaced with a pseudopotential. To take into account the effect of spin-orbit coupling in the electronic structure calculations, we use ultrasoft pseudopotentials constructed from fully relativistic calculations. A generalized gradient approximation (GGA) is used to describe the exchange-correlation energy functional with parametrization of Perdew, Burke and Ernzerhof (PBE) [114]. The kinetic energy cut-offs for truncation of the basis sets used to represent the wave function and charge density are taken at 60 Ry and 480 Ry respectively. Integrations over the Brillouin zone are sampled with a uniform dense mesh of $9 \times 9 \times 9$ k-points. Discontinuity in occupation numbers is smeared with Fermi-Dirac distribution function with a broadening of 0.003 Ry. While calculating electronic structures for undistorted and strained crystal structures (distorted with different combination of ϵ_a and ϵ_c strains), we allowed the atomic positions of the atoms to relax for all values of ϵ_a and ϵ_c, until forces on each atom become less than 1 mRy/bohr. For electronic structure calculations of LiMgBi, LiMgSb, LiMgAs, NaGaSn, RbGaSi, YAuPb, and YPtBi, we use their primitive rhombohedral unit cells. Strains (ϵ_a and ϵ_c) are applied on LiMgBi with respect its optimized lattice constants a_{cubic} = 6.85 Å. Lattice dynamical properties are determined within the framework of density functional perturbation theory (DFPT) as implemented in the QE distribution [112]. Since effects of spin-orbit interaction on phonon frequencies are weak, we estimate vibrational frequencies within a non-relativistic description (*i.e.* without including SOC). We use norm conserving pseudopotentials with plane wave basis sets truncated with energy cut-offs of 60 Ry and 240 Ry respectively for representing wave functions and charge density. To determine phonon dispersion, we use Fourier interpolation of dynamical matirces calculated at wave vectors on 3×3×3 mesh of q-points. We determine the Z_2 invariants of these half-Heuslers in strained states represented with points on n×m mesh in (ϵ_c, ϵ_a) plane to confirm the nature of electronic topology of each of the distinct states

reported in this work using the *Z2*Pack code [177], which is based on the concept of time reversal polarization formulated in terms of Wannier charge centers [14]. We determine Berry curvature with the inclusion of SOC using the wannier90 code [178].

5.4 Electronic topological phase diagram of LiMgBi

Using first-principles quantum density functional theoretical calculations, we determine electronic topological phase diagram of LiMgBi as a function of two strains that maintain a three-fold symmetry of the structure, and establish (a) robust Dirac semi-metallic state over a wide domain of strains and (b) that a transition from normal to topological insulating state of LiMgBi is possible without closing its gap, and this is because another band of the same symmetry takes part in the band-inversion. We demonstrate the generality of the robust DSM state in other HH compounds (*e.g.*, YAuPb, YPtBi, NaGaSn and RbGaSi) [179, 180], and predict specific hetero topological structures that should be experimentally achievable with epitaxial growth.

For strained structures of LiMgBi, we use its rhombohedral unit cell (see Fig. 5.3(a)) as the reference, and introduce structural distortions that preserve the three-fold rotational symmetry of the structure: strain ϵ_c that changes the unit cell's size only along c-axis (diagonal of rhombohedral cell), and ϵ_a that changes the unit cell isotropically in the plane perpendicular to c-axis ($\langle 111 \rangle$ axis of the cubic structure). The Brillouin zone is distorted correspondingly, with direction Z_2-Γ-Z_1 being the only axis of its three-fold symmetry (Fig. 5.3(b)). In the $\epsilon_c - \epsilon_a$ plane spanning these distortions, electronic structure of LiMgBi exhibits a rich diversity in its topological character (Fig. 5.3(c)). Along the diagonal direction ($\epsilon_c = \epsilon_a$), the strain is isotropic and the tetrahedral symmetry is preserved. As a result, there is no splitting of any bands, but the energy gap between $\Gamma_8^{(\mathrm{T}_d)}$ and $\Gamma_6^{(\mathrm{T}_d)}$ bands reduces with increasing compressive strain and changes its sign (band inversion) at $\epsilon_c = \epsilon_a$=-0.011, making LiMgBi a trivial insulator (lower left quadrant of the phase diagram in Fig. 5.3(c)). Since its conduction band ($\Gamma_6^{(\mathrm{T}_d)}$) (see Fig. 5.4(c)) arises primarily

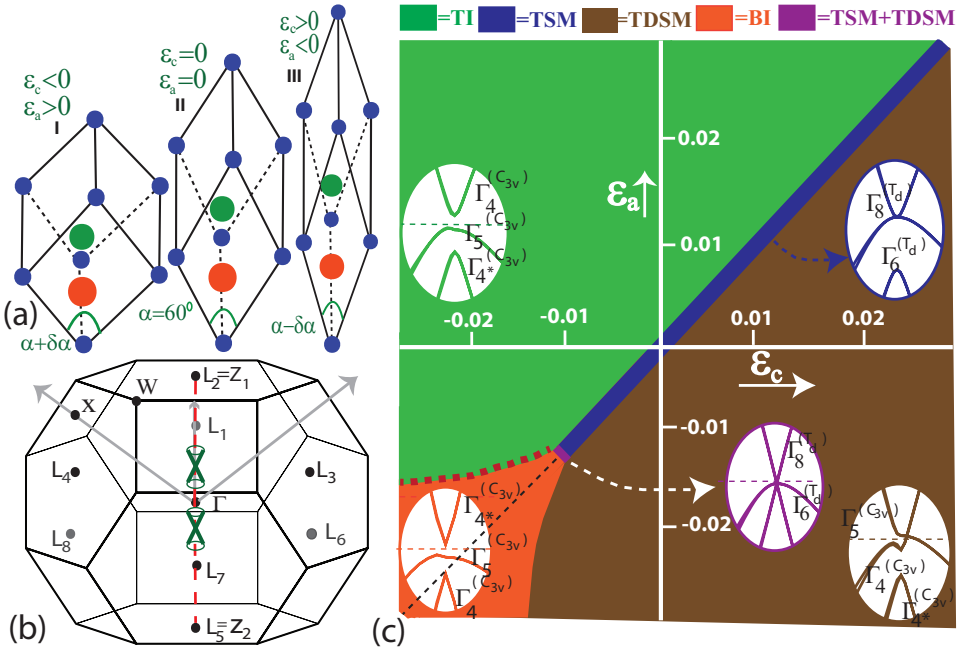

Figure 5.3: Primitive unit cells of structures distorted with ϵ_c and ϵ_a (a), Brillouin zone (b) and electronic topological phase diagram (TPD) of LiMgBi (c). A pair of Dirac cones (highlighted with green colors) appears along the three-fold rotational axis Z_2-Γ-Z_1 in the Brillouin zone of distorted structure. Distinct topological phases are marked with different colors, and electronic structure with symmetry labels for a particular phase is drawn with the corresponding color. TDSM, TSM, TI, BI stand for topological Dirac semi-metal, topological semi-metal, topological insulator and band insulator respectively. Red dotted line marks the boundary between BI and TI phases denoting a topological phase transition without closing the band gap.

from the *s*-orbitals of Mg, stronger cationic character of Mg evidently correlates with trivial topology, as expected from chemistry of an ionic insulator.

An anisotropic strain, corresponding to deviation from the diagonal line of the phase diagram, lowers the T_d symmetry of LiMgBi to C_{3v}, retaining only one axis of three-fold rotation. The compatibility relations of $\Gamma_6^{(T_d)}$ and $\Gamma_8^{(T_d)}$ irreducible representations (irreps) of T_d (double group) show that they decompose to $\Gamma_4^{(C_{3v})}$ and $\Gamma_5^{(C_{3v})}$ irreps of C_{3v} (double group) as follows: $\Gamma_6^{(T_d)} \rightarrow \Gamma_4^{(C_{3v})}$ (we label this as $\Gamma_{4*}^{(C_{3v})}$ here) and $\Gamma_8^{(T_d)} \rightarrow \Gamma_4^{(C_{3v})} + \Gamma_5^{(C_{3v})}$, where $\Gamma_4^{(C_{3v})}$ and $\Gamma_5^{(C_{3v})}$ have two dimensional irreducible representations. As a result, $\Gamma_8^{(T_d)}$ band splits into two doubly degenerate bands with $\Gamma_5^{(C_{3v})}$ ($6p_x$ and $6p_y$ orbitals of Bi) and $\Gamma_4^{(C_{3v})}$ ($6p_z$ orbital of Bi) representations of the double group of C_{3v}, while $\Gamma_6^{(T_d)}$ band of Mg *s*-orbitals remains doubly degenerate $\Gamma_{4*}^{(C_{3v})}$. At large tensile strains, Mg

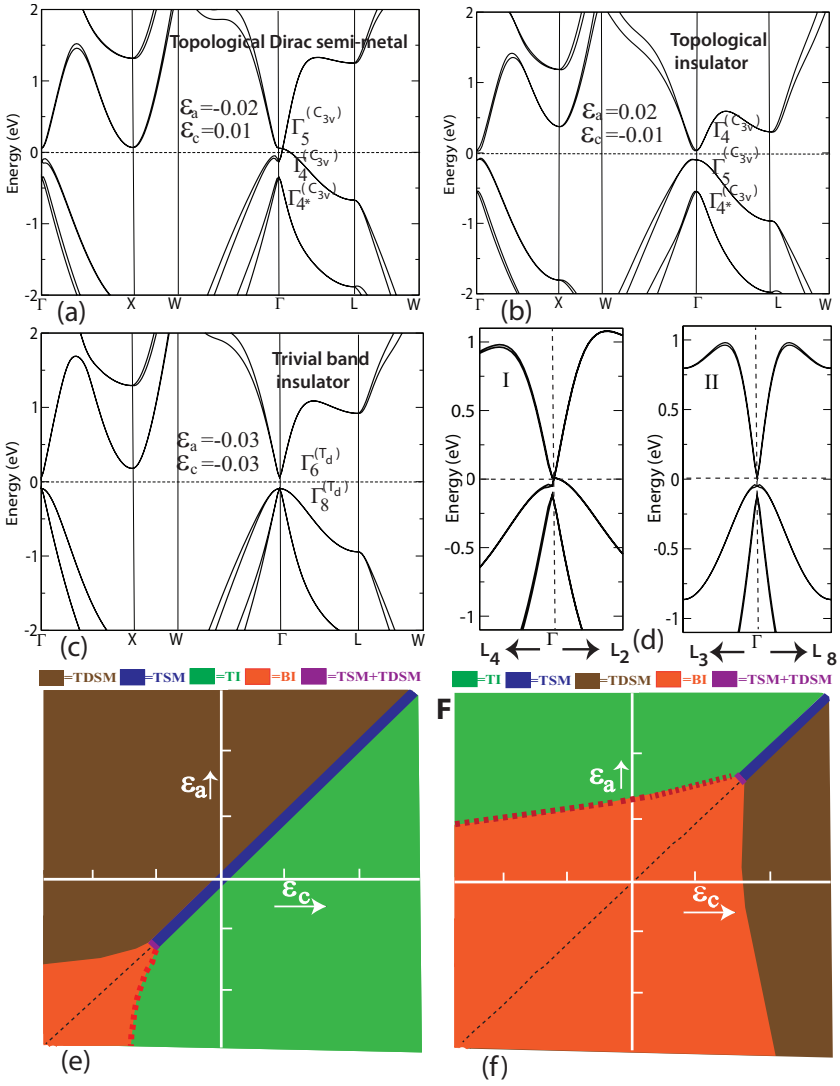

Figure 5.4: Electronic structures of the different topological phases ((a) Topological Dirac semi-metal (TDSM), (b) topological insulator (TI), (c) trivial band insulator (BI) and (d) TDSM) of LiMgBi and generic topological phase diagrams (e) & (f) of half-Heuslers. Two Dirac points in the TDSM appear along only Γ-L_2 (d) and Γ-L_5 directions (not shown here) and not in other Γ-L_i (i=1,3,4,6) directions. Topological phase diagrams (drawn using same color scheme of Fig. 5.3(c)) for the other two classes of half-Heusler compounds where for example (e) RbGaSi class and (f) LiMgSb class.

s-bands remain rather low in energy (the condition for *nontrivial* topology), and much of the interesting changes in electronic structure involve the splitting of $\Gamma_8^{(T_d)}$ band. For tensile strains $\epsilon_c < \epsilon_a$ (upper left of the diagonal $\epsilon_c = \epsilon_a$), $\Gamma_4^{(C_{3v})}$ band is higher in energy than $\Gamma_5^{(C_{3v})}$, and LiMgBi is a topological insulator (TI) with Z_2 invariant of 1, consistent with works of Felser and Hasan [23, 24], see its electronic structure in Fig. 5.4(b). On

the other hand, ordering of $\Gamma_4^{(C_{3v})}$ and $\Gamma_5^{(C_{3v})}$ bands is reversed for $\epsilon_c > \epsilon_a$ (upper right of the diagonal $\epsilon_c = \epsilon_a$), and LiMgBi becomes a topological Dirac semi-metal (TDSM), see its electronic structure in Fig. 5.4(a). While the TDSM is the stable phase over a large domain of $\epsilon_c - \epsilon_a$ plane, it was missed in earlier works [23, 24, 181].

In the TDSM state, electronic structure exhibits gap along three of the four cubic $\langle 111 \rangle$ directions (see Fig. 5.4(d)) because the symmetry of momenta ($\overrightarrow{\mathbf{k}}$) along these lines is significantly lowered resulting in avoided crossing of the iso-symmetric branches containing $\Gamma_4^{(C_{3v})}$ and $\Gamma_5^{(C_{3v})}$ states. Along the Z_2-Γ-Z_1 axis of three-fold symmetry however, these branches carry different representations of C_{3v} group, and their crossing is allowed. Since largely unoccupied s-orbitals of Mg contributing to band containing $\Gamma_4^{(C_{3v})}$ state are higher in energy at other $\overrightarrow{\mathbf{k}}$, dispersion of this band is upwards along Γ-Z_1 (or L_2) giving rise to its crossing with the $\Gamma_5^{(C_{3v})}$ band containing Bi-p states. This constitutes a Dirac point, though the degeneracy of bands splits along directions perpendicular to Γ-Z_1 due to lower symmetry of $\overrightarrow{\mathbf{k}}$. Thus, the TDSM state presented here arises from (a) the distinct symmetry of Mg-s and Bi-p_x bands at momenta with three-fold symmetry, and (b) opposite slopes of dispersion of these bands due to chemistry.

In the vicinity of the diagonal in lower left quadrant of the phase diagram (Fig. 5.3(c)) characterized by compressive strains, LiMgBi is a trivial insulator (see Fig. 5.4(c)) with a vanishing Z_2 invariant. Physics of this state is nevertheless quite rich because both $\Gamma_4^{(C_{3v})}$ and $\Gamma_{4*}^{(C_{3v})}$ bands (made of Bi-p_z and Mg-s orbitals respectively) are very close in energy. This is reflected in how this trivial insulating state transforms to TDSM and TI states with ϵ_c and ϵ_a respectively. To understand these transitions, we first examine evolution of these "frontier" bands with each of the strains ϵ_c and ϵ_a (see Fig. 5.5). Energies of $\Gamma_4^{(C_{3v})}$ and $\Gamma_{4*}^{(C_{3v})}$ bands vary monotonously and similarly (decrease) with strain ϵ_c, while they vary in a contrasting manner with ϵ_a (see Fig. 5.5 (a) and Fig. 5.5 (b)). Secondly, energies of $\Gamma_4^{(C_{3v})}$ and $\Gamma_5^{(C_{3v})}$ bands always vary in opposite manner and they cross at a point on the diagonal $\epsilon_c = \epsilon_a$, because both of them arise from splitting of the quadruply-degenerate $\Gamma_8^{(T_d)}$ state. This inversion of $\Gamma_4^{(C_{3v})}$ and $\Gamma_5^{(C_{3v})}$ bands nicely explains the transition from

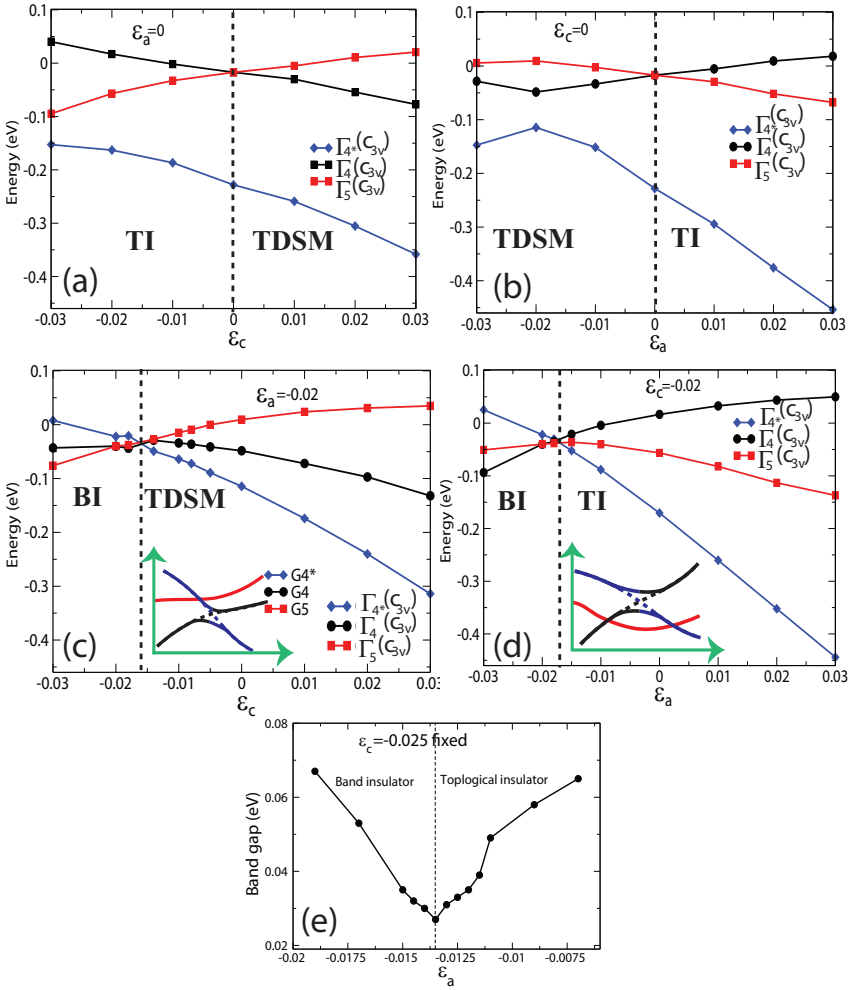

Figure 5.5: Evolution of the frontier bands ($\Gamma_{4*}^{(C_{3v})}$, $\Gamma_{4}^{(C_{3v})}$, and $\Gamma_{5}^{(C_{3v})}$) with strains (ϵ_c, ϵ_a) that illustrates band inversion in topological insulator (TI)-topological Dirac semi-metal (TDSM) (a), TDSM-TI (b), band insulator (BI)-TDSM (c) and BI-TI (d) transitions. A gap preserving transition is due to the deeper valence band with the same symmetry as of the conduction band, as evident in (c). Band crossings are shown schematically in the insets where blue, red and black lines denote $\Gamma_{4*}^{(C_{3v})}$, $\Gamma_{5}^{(C_{3v})}$ and $\Gamma_{4}^{(C_{3v})}$ states respectively and crossover of bands between the same symmetries (i.e. avoided crossing) is marked with dotted line. (e) Calculated band gap as a function of strain ϵ_a (keeping ϵ_c=-0.025 fixed) along a line in the topological phase diagram crossing the BI-TI boundary.

TDSM to TI states across the diagonal (see Fig. 5.5(a) and Fig. 5.5(b)). Similarly, a transition from the TDSM to trivial insulator involves inversion of $\Gamma_{4*}^{(C_{3v})}$ and $\Gamma_{5}^{(C_{3v})}$ bands, for example as a function of ϵ_c (see Fig. 5.5(c)), which is followed by a crossover between $\Gamma_{4}^{(C_{3v})}$ and $\Gamma_{4*}^{(C_{3v})}$ bands (see inset of Fig. 5.5(c)).

The transition from trivial insulator to topological insulator states of LiMgBi is a bit

intriguing. Normally, one expects closure of the band-gap through a Dirac or Weyl semi-metallic state at the transition. However, in non-centrosymmetric systems, this has been a point of argument [166, 167]. Symmetry labels of conduction band (CB), valence band (VB) and lower valence band (VB-1) of BI are $\Gamma_{4*}^{(C_{3v})}$, $\Gamma_5^{(C_{3v})}$ and $\Gamma_4^{(C_{3v})}$ respectively (*i.e.* $\Gamma_{4*}^{(C_{3v})}\Gamma_5^{(C_{3v})}\Gamma_4^{(C_{3v})}$). During transformation of the normal insulator to TI state as a function of ϵ_a, inversion of the two valence bands occurs first, resulting in ($\Gamma_{4*}^{(C_{3v})}\Gamma_4^{(C_{3v})}\Gamma_5^{(C_{3v})}$) configuration (see inset of Fig. 5.5(d)). In the second step, ordering of CB ($\Gamma_{4*}^{(C_{3v})}$) and VB ($\Gamma_4^{(C_{3v})}$) reverses *without closure of the gap* resulting in ($\Gamma_4^{(C_{3v})}\Gamma_{4*}^{(C_{3v})}\Gamma_5^{(C_{3v})}$) configuration (avoided crossing of the iso-symmetric bands with same symmetry). In the third step, inversion of the new valence bands occurs and ($\Gamma_4^{(C_{3v})}\Gamma_5^{(C_{3v})}\Gamma_{4*}^{(C_{3v})}$) configuration of the TI state emerges. In the overall transformation from BI to TI state, closure of gap occurs twice but *within* the valence bands, and the gap between valence and conduction bands is always nonzero (see inset of Fig. 5.5(d)). Analysis of Vanderbilt [166] and Nagaosa [167] is based on a model in the subspace of four bands, and we find that a gapped transition from BI to TI phase is possible provided there is another relevant valence band with the same symmetry as of the conduction band of BI (necessitating a suitable six band model).

In support of our claim of the *gapped* topological phase transition, we calculated electronic structure (and band gap) of LiMgBi as a function of strain ϵ_a (keeping ϵ_c=-0.025 fixed) in very small steps (i.e., $\Delta\epsilon_a$=0.0005) near the band to topological insulator phase transition. We find that the band gap remains nonzero (see Fig. 5.5(e)) along the path crossing the boundary between band insulator (BI) and topological insulator (TI) regions. To search for the occurrence of band crossings, if any, at a generic k-point, we calculated the electronic band energies on a 30×30×30 mesh of k-points. Our calculation reveals that the smallest gap (between valence band maximum and conduction band minimum) occurs at Γ point. We, thus, believe that the band gap does not close during the electronic topological transition from band to topological insulators in non-centrosymmetric LiMgBi. We note that finding more accurate value of band gap or band crossings, if any, may require higher level (e.g., hybrid functional) calculation at even

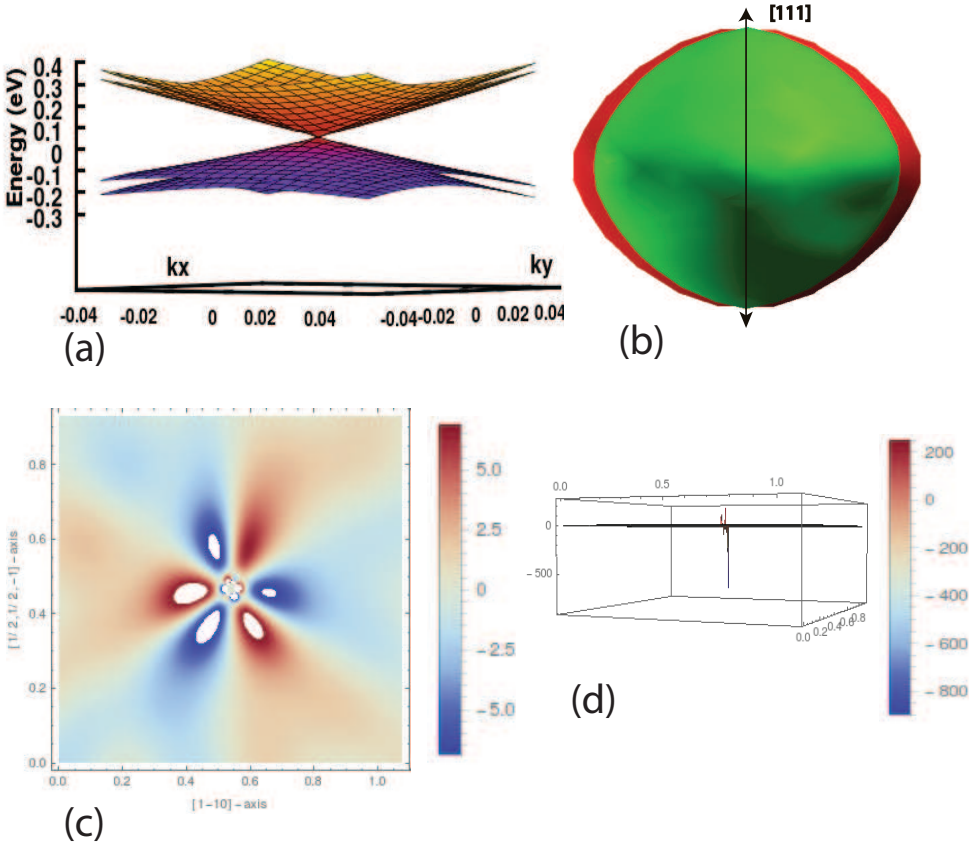

Figure 5.6: (a) Electronic bands making the Dirac cone are plotted in a plane perpendicular to [111] direction. It is clear that the bands are degenerate only along [111] axis and become non-degenerate elsewhere. (b) Fermi surfaces in the TDSM state of LiMgBi, visualized by shifting the Fermi level upward by 0.3 eV. (c) Density plot of the z-component of the Berry curvature ($\Omega^z(\mathbf{k})$) calculated in a plane perpendicular to [111] axis and passing through the Dirac point, that exhibits the three-fold crystal symmetry. (d) 3d plot of $\Omega^z(\mathbf{k})$ which shows a large nonzero value of $\Omega^z(\mathbf{k})$ at the Dirac point.

more dense k-point mesh. Hence, more detailed calculations of electronic structure are warranted in future investigations to look carefully into this subtle *gapped* topological transition in LiMgBi.

The Dirac cone in the TDSM state of LiMgBi is visualized (Fig. 5.6(a)) on a 2D plane perpendicular to [111] axis in the Brillouin zone. It is clear from Fig. 5.6(a), the valence and conduction bands making the Dirac cone split their degeneracy as they move away from the [111] direction because of the lack of centre of inversion in the crystal structure. As a consequence of this non-centrosymmetry, non zero Berry curvature with opposite signs appear at each of two Dirac points (see plot of Berry curvature for one

Dirac point in Fig. 5.6(d)). The symmetry of its crystal structure and non-zero Berry curvature allow a direct control valley Hall current with parallel electric field in LiMgBi. The color density plot of the z-component of the Berry curvature in Fig. 5.6(c) reveals the three-fold rotational symmetry of the LiMgBi crystal. The Fermi surface (Fig. 5.6(b)) in the TDSM state of LiMgBi is visualized for a n-doped LiMgBi (*i.e.* Fermi level of the undoped LiMgBi has been shifted upward by 0.3 eV), which reveals two ellipsoids (denoted by red and green colors) that touch each other along [111] axis but split away from it.

5.5 Generic topological phase diagrams

We now present a generic topological phase diagram of half-Heuslers based on extensive calculations of electronic structure of several compounds as a function of ϵ_c and ϵ_a. There are two key parameters that govern this phase diagram: (a) the sign of splitting of $\Gamma_8^{(\mathrm{T}_d)}$ band into $\Gamma_5^{(\mathrm{C}_{3v})}$ and $\Gamma_4^{(\mathrm{C}_{3v})}$ bands, and (b) the critical isotropic strain at which $\Gamma_8^{(\mathrm{T}_d)}$ and $\Gamma_6^{(\mathrm{T}_d)}$ bands cross marking a transition between band insulator and topological semi-metal. For LiMgBi, NaGaSn, YAuPb and YPtBi, tensile strain ϵ_c gives a splitting with higher energy $\Gamma_5^{(\mathrm{C}_{3v})}$ band, and TI and TDSM states are in the left and right of diagonal line of phase diagram (Fig. 5.3(c)), while this is reversed in RbGaSi (Fig. 5.4(e)). When the critical isotropic strain is large and positive, as we find in LiMgAs and LiMgSb, these materials are a band insulator for most part of the phase diagram (Fig. 5.4(f)), though it is indeed possible to access their TDSM and TI states with large enough tensile strains. Electronic structures of NaGaSn, RbGaSi, YAuPb and YPtBi for different combinations applied strains (ϵ_a, ϵ_c) are given in Fig. 5.7, Fig. 5.8, Fig. 5.9 and Fig. 5.10 respectively. Electronic structure of LiMgAs and LiMgSb are shown in Fig. 5.11, which show that these compounds are band insulators at ambient conditions as $E_{\Gamma_6^{(\mathrm{T}_d)}} > E_{\Gamma_8^{(\mathrm{T}_d)}}$ at Γ point. Please not that unlike the Γ_5 band of LiMgBi, NaGaSn and RbGaSi, the Γ_5 band of YPtBi and YAuPb splits along Γ-L direction (except at Γ and L TRIM points) in the

Brillouin zone. Thus, when Γ_5 band crosses the doubly degenerate Γ_4 band, two crossing points arise along Γ-L direction each with triple degeneracy. Hence, YPtBi and YAuPb should be better termed as triple point topological metals [182] instead of topological Dirac semimetals. We note that the small difference in energies of these triple points is much less than k_BT.

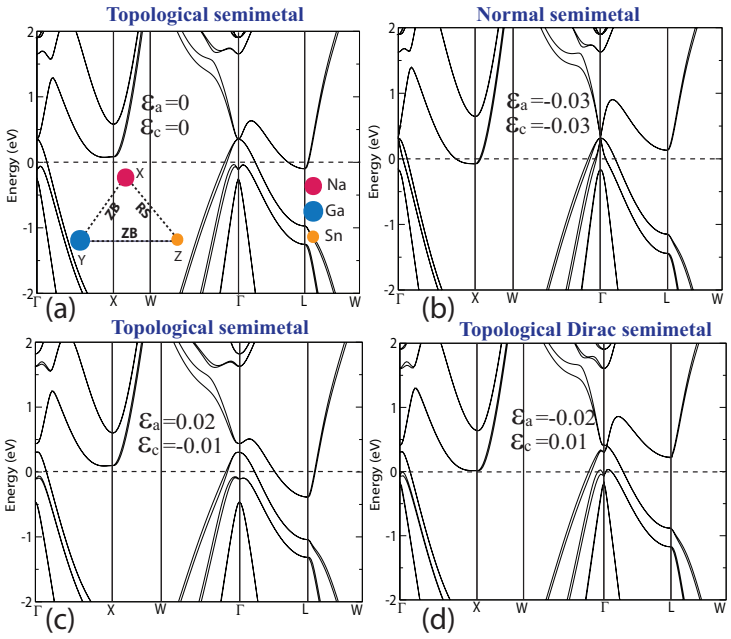

Figure 5.7: Electronic structure of NaGaSn for different strains. Electronic band structures of NaGaSn, calculated with spin-orbit coupling, reveal topological semimetallic state (a) for undistorted lattice, normal semimetallic (b), topological semimetallic (c) and topological Dirac semimetallic (d) states for strained lattices. Strains are applied with respect to its optimized lattice constant a_{cubic}= 6.4 Å.

5.6 Experimental signature of nontrivial topology

Signatures of trivial and nontrivial electronic topology of the half-Heusler compounds YPdBi and YPtBi have been identified in nuclear magnetic resonance (NMR) spectroscopy as the shifts in NMR peaks in opposite directions [183]: $p-$orbital character of the CB ($\Gamma_8^{(T_d)}$ state) in topologically nontrivial state of YPtBi gives a negative isotopic shift in its NMR peak, while $s-$orbital character of the CB ($\Gamma_6^{(T_d)}$) of YPdBi gives a positive shift [183]. A recent NMR experiment [173] on LiMgX (X=As, Sb, Bi) revealed a negative shift

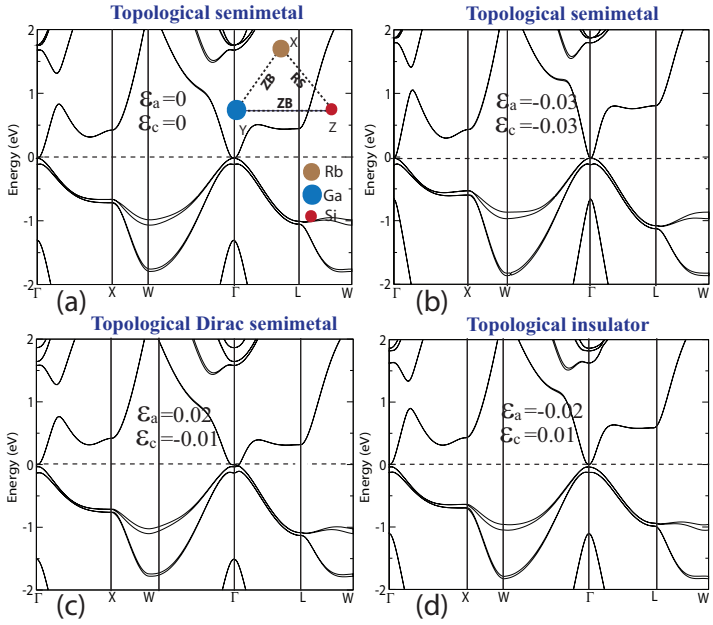

Figure 5.8: Electronic structure of RbGaSi for different strains. Electronic band structures of RbGaSi, calculated with spin-orbit coupling, reveal topological semi-metallic state (a) for unstrained lattice, topological semi-metallic state (b) under isotropic strain, topological Dirac semi-metallic (c) and topological insulating (d) states under strained conditions. Strains are applied with respect to its optimized lattice constant a_{cubic}= 6.7 Å.

of NMR peak of LiMgBi and a positive one of LiMg(As, Sb), consistent with our analysis that LiMgBi is a nontrivial topological semi-metal while LiMg(As, Sb) are topologically trivial band insulators (see Fig. 5.11).

5.7 Heterostructures

Various topological electronic states of the half-Heuslers can be achieved experimentally within epitaxial hetero-structures. For example, a TDSM state can be stabilized in LiMgBi grown epitaxially on a thick substrate of LiMgSb with 3.4 % smaller lattice constant. Conversely, a TI state can be stabilized in LiMgBi grown epitaxially on LiMgSb along ⟨111⟩ direction and applying a small compressive strain ϵ_c. Since these states are stable in a wide domain of the phase diagram of strained structures, they are robust and insensitive to (a) small structural changes arising extrinsically in experiments, or to (b) small errors in calculations.

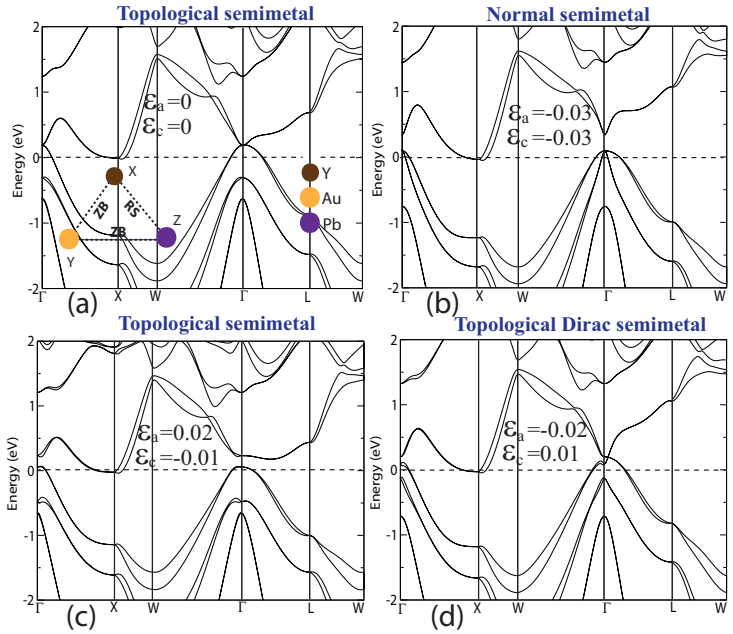

Figure 5.9: Electronic structure of YAuPb for different strains. Electronic band structures of YAuPb, calculated with including spin-orbit coupling, show topological semi-metallic state (a) in unstrained lattice, normal semi-metallic (b), topological semi-metallic (c) and topological Dirac semi-metallic (d) states under different strains. Strains are applied with respect to its experimental lattice constant a_{cubic}= 6.73 Å.

5.8 Summary

In summary, we have presented generic topological phase diagrams of strained half-Heusler compounds, and show that they exhibit a robust non-centrosymmetric topological Dirac semi-metallic state, that is stable in a large domain of strains preserving three-fold rotational symmetry. As a consequence of symmetry of their electronic states, we uncovered a gap-preserving topological phase transition between TI and BI phases of ternary half-Heuslers. This will stimulate fundamental studies of electronic topological transition in HHs. The possibilities of interfaces between TI, TSM, TDSM and normal insulating states, and associated room temperature phenomena involving chirality, polarity, correlations, will open up a route to exciting science within the platform of epitaxial heterostructures of ternary half-Heuslers grown in ⟨111⟩ direction. Adding to the diversity in their known properties and functionality, our discovery of their TDSM state and properties of their heterostructures should stimulate efforts in development of novel applications of

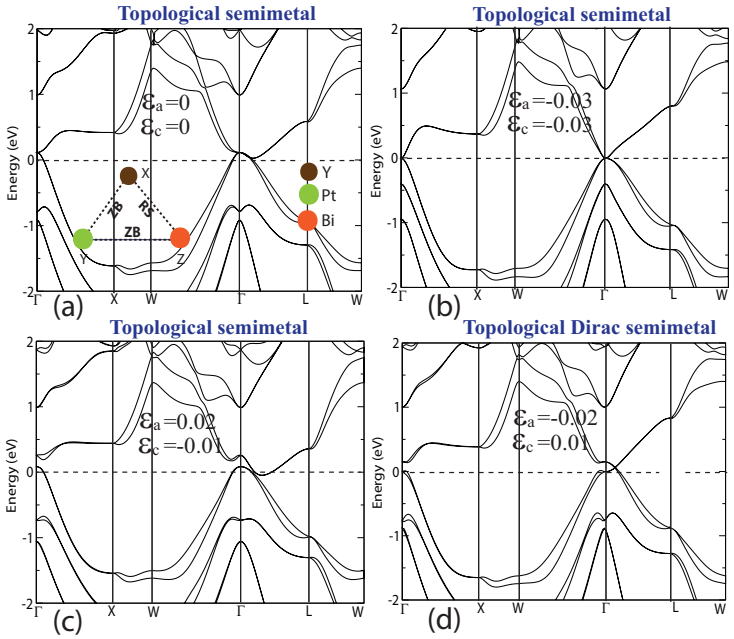

Figure 5.10: Electronic structure of YPtBi for different strains. Electronic band structures of YPtBi, calculated with including spin-orbit, exhibit topological semi-metallic state (a) in undistorted lattice, topological semi-metallic state under compressive isotropic strain (b), topological semi-metallic (c) and topological Dirac semi-metallic (d) states under mixed strain states. Strains are applied with respect to its experimental lattice constant a_{cubic}= 6.64 Å.

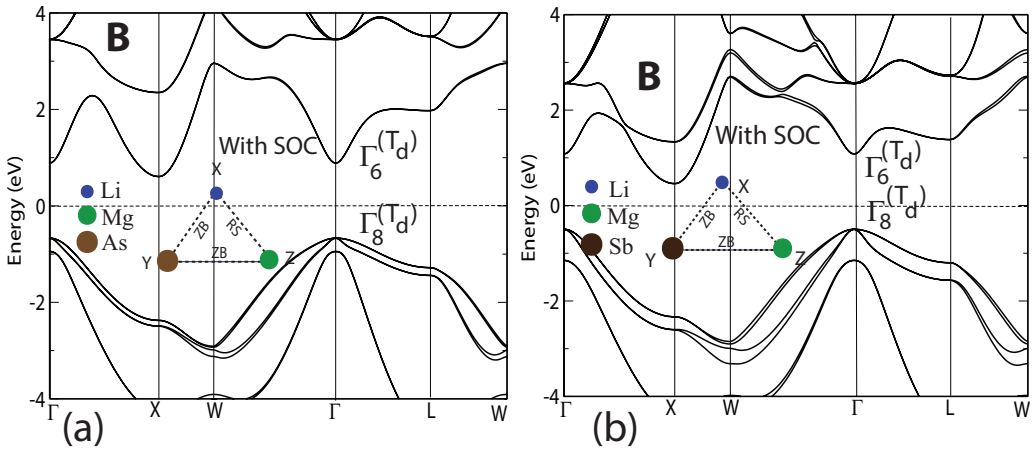

Figure 5.11: Electronic structures of LiMgAs and LiMgSb calculated at their optimized lattice constants with including spin-orbit coupling (SOC), show band gaps of 1.62 eV and 1.6 eV, respectively. At Γ point the ordering of the bands are $E_{\Gamma_6^{(T_d)}} > E_{\Gamma_8^{(T_d)}}$, signifying that both LiMgAs and LiMgSb are trivial band insulators at ambient conditions. The optimized lattice constants of LiMgAs and LiMgSb are a= 6.19 Å and a= 6.62 Å, respectively.

Heusler materials.

Chapter 6

Theoretical Prediction of Topologically Nontrivial States in Zintl Family of Bi_2Mg_2X (X=Mg, Ca, Sr, Ba) Compounds

6.1 Introduction

Discovery of topologically nontrivial electronic states of materials marked a paradigm shift in condensed matter physics [97]. Physics of such topological phases of matter is described by topological band theory [184] which allows classification of insulators into topologically trivial and nontrivial categories depending on whether they host gapless topological electronic states at the surface or not. Since the theoretical prediction [9] of the first three-dimensional strong topological insulator Bi_2Se_3 and its subsequent experimental verification [10], many insulators with topologically nontrivial phases have been theoretically predicted [104, 185, 186] and some of them have been verified experimentally [157, 184, 187]. Many of the materials which are known to show nontrivial electronic

topology have non-zero band gaps, and the occurrence of topologically nontrivial electronic phases in metallic and semimetallic systems has remained relatively rare. Recently, theoretical and experimental studies of topologically nontrivial metallic and semimetallic systems have revealed many exotic topological phenomena like giant magnetoresistance, ultrahigh mobility, chiral magnetic effect which have increased the research activity in finding topological materials with small band gap or no band gap at all [25, 28, 29, 47]. To this end, two pioneering theoretical studies [23, 24] predicting the existence of topological nontrivial semimetallic state in ternary half-Heusler (HH) compounds added a new dimension to the research in topological phases of matter. These HH compounds are shown to possess nontrivial Z_2 topological order [23] in their bulk form and can be driven into distinct topological states under mechanical strain [23, 24].

Wan et al. [48] predicted a new and distinct topological nontrivial semimetallic state of matter in pyrochlore iridates $A_2Ir_2O_7$ (A=Y or Ln) which exhibit several linear band crossing points (doubly degenerate) at the Fermi level in their bulk electronic structure. The linear dispersion near the crossing points is described by an effective Weyl Hamiltonian $H(\mathbf{k}) = \pm v\mathbf{k}.\sigma$, where $\mathbf{k}$ is the wave vector, v is the effective velocity of electron and σ's are the Pauli matrices. These materials are thus called Weyl semimetals [48] and the *doubly* degenerate crossing points are known as Weyl points. Weyl points always come in pairs and with opposite chiralities by virtue of the fermion doubling theorem [188]. Weyl semimetals are shown to exhibit intriguing quantum phenomena like chiral anomaly [29] and unusual transport properties [28].

In another work, Young et al. [46] predicted the existence of symmetry protected 3D Dirac points in the bulk electronic structure of BiO_2 which is a 3D analogue of graphene. A pair of doubly degenerate bands cross linearly at a quadruply degenerate point (Dirac point) at the Fermi energy. BiO_2 is the first example known from theoretical prediction of a Dirac semimetal in three dimensions. In BiO_2, the Dirac point is supported as a quadruply degenerate bands at the zone boundary [46]. Wang et al. [25] predicted topological Dirac semimetallic (TDSM) phases in A_3Bi (A=Na, K, Rb) compounds which host

a pair of Dirac points inside its Brillouin zone. As the low energy physics of the linearly crossing bands can be effectively described by four component Dirac Hamiltonian, this exotic quantum states of matter is known as the Dirac semi-metallic (DSM) state and the quadruply degenerate crossing point is known as the Dirac point, which consists of two superimposed Weyl points with opposite chiralities and are protected against annihilation by the three-fold crystal symmetry [170]. Soon after its prediction, angle resolved photo emission spectroscopy (ARPES) experiments confirmed the existence the 3D Dirac fermion in Na_3Bi [47]. Cd_3As_2 is another prototypical example of the TDSM which was first predicted theoretically [189] and was subsequently realized experimentally [165]. In Cd_3As_2 too, a pair of Dirac points appear symmetrically around Γ along $\pm$Z directions, and are protected by the C_4 rotational symmetry of the crystal. DSMs are shown to exhibit fascinating properties like ultrahigh mobility, giant magnetoresistance [25], chiral magnetic effect under magnetic field [29].

With only few compounds are known experimentally as the DSMs that are not easy to make, there is need to discover TDSM state possibly in the compounds that already exist. In our search of new class of materials with small band gaps and nontrivial electronic topology, we kept in mind the following facts: (a) Bismuth containing compounds are well known to host topological nontrivial phases of matter mainly due to strong spin-orbit coupling (SOC) at Bi site. For example, topological insulating state is found in binary Bi_2Se_3 family [9], ternary Bi_2Te_2Se family [190] of layered compounds in which atomic layers are stacked along c-direction. (b) In the Bi_2X_2Y (X=Te, Se, Y=Te, Se) class [190] of topological insulators, Bi has a formal valence charge of 3+ and Te or Se atoms have formal valence charges of 2-. To have more electrons influenced by SOC, we explore here the electronic topology of compounds where the valence charge of Bi atom is 3-.

With these criteria in mind, we came across an interesting family of alkaline earth based compounds: Bi_2Mg_2X (X = Mg, Ca, Sr, Ba), where Bi is more electronegative (hence it has formal valence charge of 3-) than X (X = Mg, Ca, Sr, Ba) atoms with

2+ valence charge. We have investigated the electronic topological properties of these compounds here and discovered the presence of topological nontrivial phases in them at ambient conditions. These compounds have coexisting ionic and covalent bonding and hence, they belong to a chemically very interesting class of Zintl compounds [191–194]. Nontrivial topological electronic states in Zintl compounds are relatively uncommon, and only a few compounds like Sr_2X (X = Pb, Sn) [195] and Ba_2X (X = Si, Ge) [196] in the Zintl family with orthorhombic structure (space group: Pnma, No. 62) [195, 196] are predicted to host either topological semimetallic or topological insulating phases.

We evaluate the topology of electronic states of Bi_2Mg_2X (X = Mg, Ca, Sr, Ba) from their electronic structure determined with fully relativistic calculations. We ascertain their nontrivial topological character by calculating the Z_2 topological invariants. We demonstrate that this is linked with band inversion at $\mathbf{k}$=(0,0,0), the Γ point in the Brillouin zone. Their surface electronic structure on (001) plane reveals gapless surface Dirac cones, further confirming the nontrivial electronic topology of these compounds.

As topologically nontrivial materials often exhibit good thermoelectric properties [197], we determine their phonon dispersion and analyze the electronic contribution to their thermoelectric properties within a semi-classical Boltzmann transport theory. In their phonon dispersion, we find low cut-off frequencies of the acoustic branches, that are expected to give low thermal conductivity in these compounds. While Bi_2Mg_3 exhibits low Seebeck coefficient (S), the other compounds have quite high S, relevant to better efficiency of thermoelectric energy conversion.

6.2 Crystal structure and computational methods

Bi_2Mg_2X (X = Mg, Ca, Sr, Ba) compounds crystallize in centrosymmetric hexagonal structure (space group: $P\bar{3}m1$, No. 164) with five atoms in the periodic unit cell. X atom occupies 1a Wyckoff site (0,0,0) whereas Bi and Mg atoms occupy 2d sites ($\pm\frac{1}{3}$, $\pm\frac{2}{3}$, $\pm$z) [194]. The bonding environment in this class of materials is described with

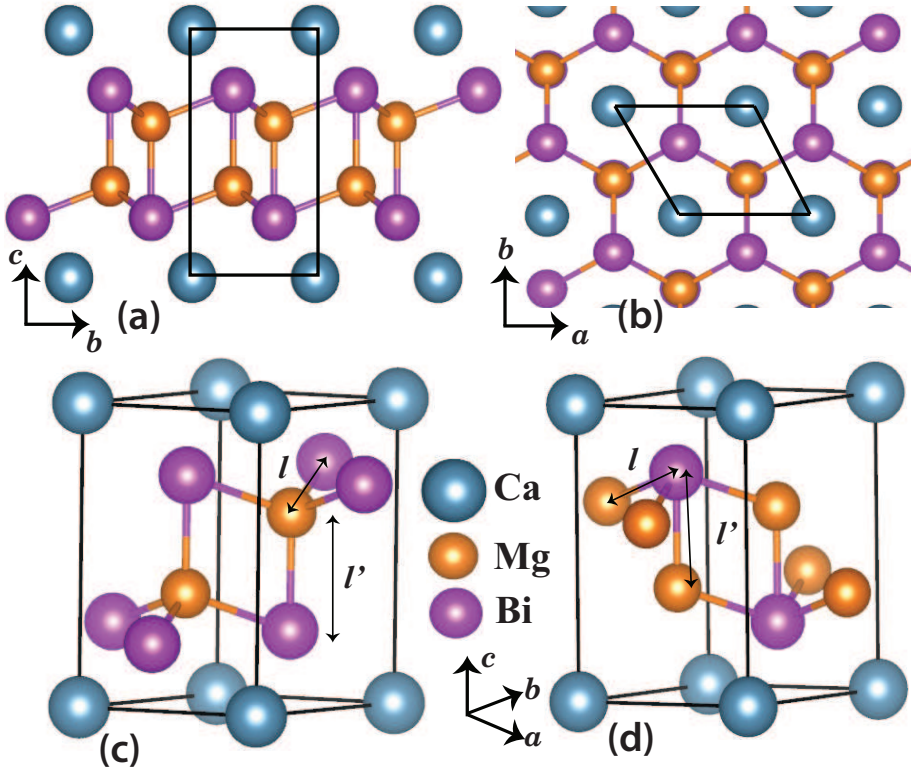

Figure 6.1: Crystal structure and bonding environment in Zintl family of Bi_2Mg_2X (X = Mg, Ca, Sr, Ba) compounds. (a) The hexagonal crystal structure consisting of a covalently bonded $[Bi_2Mg_2]^{2-}$ layers and intercalating cationic X^{2+} layers that bind weakly through a charge transfer mechanism. (b) A view of the crystal structure from the top (c-axis). $[Bi_2Mg_2]^{2-}$ layer basically consists of two buckled hexagonal layers stacked along c-direction. Within the $[Bi_2Mg_2]^{2-}$ layer each of the Mg and Bi atoms has four fold coordination numbers. Mg atoms (c) have slightly distorted tetrahedral coordination environment with $l' > l$ whereas the Bi atoms (d) have unusual flipped tetrahedral or "umbrella" coordination.

Zintl formalism where covalently bonded layer of $[Bi_2Mg_2]^{2-}$ is separated by relatively loosely bound layers of X^{2+} ions (see Fig. 6.1(a)). Within the covalent layers, Mg atom has a weakly distorted tetrahedral coordination (see Fig. 6.1(c)) whereas Bi atom has a rather unusual flipped tetrahedral environment or "umbrella" coordination [193] (see Fig. 6.1(d)). X atom occupying the 1a site in the crystal has a slightly distorted octahedral coordination [193]. Charge transfer between $[Bi_2Mg_2]^{2-}$ layer and intercalating X^{2+} layers stabilize the structure through ionic bonds [194].

Our first-principles calculations are based on density functional theory (DFT) as implemented in the Quantum ESPRESSO (QE) [112] code with a generalized gradient

approximation (GGA) [113] to the exchange-correlation energy functional as parametrized by Perdew, Burke and Ernzerhof (PBE) [114]. We replaced the ionic cores with smooth norm-conserving pseudopotentials derived within fully relativistic analysis [198] to take into account the effect spin-orbit coupling (SOC). We truncated the plane wave basis with cut-off energies of 60 Ry and 240 Ry in representations of Kohn-Sham wave functions and charge density respectively. The discontinuity in occupation numbers at the Fermi level or across the gap was smeared with a width of 0.003 Ry in the Fermi-Dirac smearing function. The Brillouin zone integrations were sampled on uniform meshes of 9×9×6 and 10×10×1 k-vectors respectively in the calculations of bulk and surface electronic structures.

We used experimental lattice constants of these compounds [175] and relaxed the atomic positions in their unit cell before determining the electronic structure. To determine electronic structure of (001) surfaces, we constructed free standing slabs and increased the number of layers along c-direction until the gapless surface Dirac states appear on the (001) surface (45 layers for Bi_2Mg_3 and Bi_2Mg_2Ca, 70 layers for Bi_2Mg_2Sr and 90 layers for Bi_2Mg_2Ba), keeping the atomic positions fixed to those in their bulk structures.

We obtained phonon dispersions of these compounds using calculations that include the spin-orbit interaction within the framework density functional perturbation theory (DFPT) as implemented within the QE code [64]. We determined the Z_2 invariants of Bi_2Mg_2X (X = Mg, Ca, Sr, Ba) Zintl compounds to ascertain their nontrivial electronic topology using the *Z2*Pack code [177], which is based on the concept of time reversal polarization formulated in terms of hybrid Wannier charge centers [14, 65]. We used input from electronic structure to analyze transport properties within a semi-classical Boltzmann theory under a constant scattering time approximation as implemented in the BoltzTrap code [94] and estimated electrical conductivity (σ), Seebeck coefficient (S) and power factor ($S^2\sigma$) as a function of temperature.

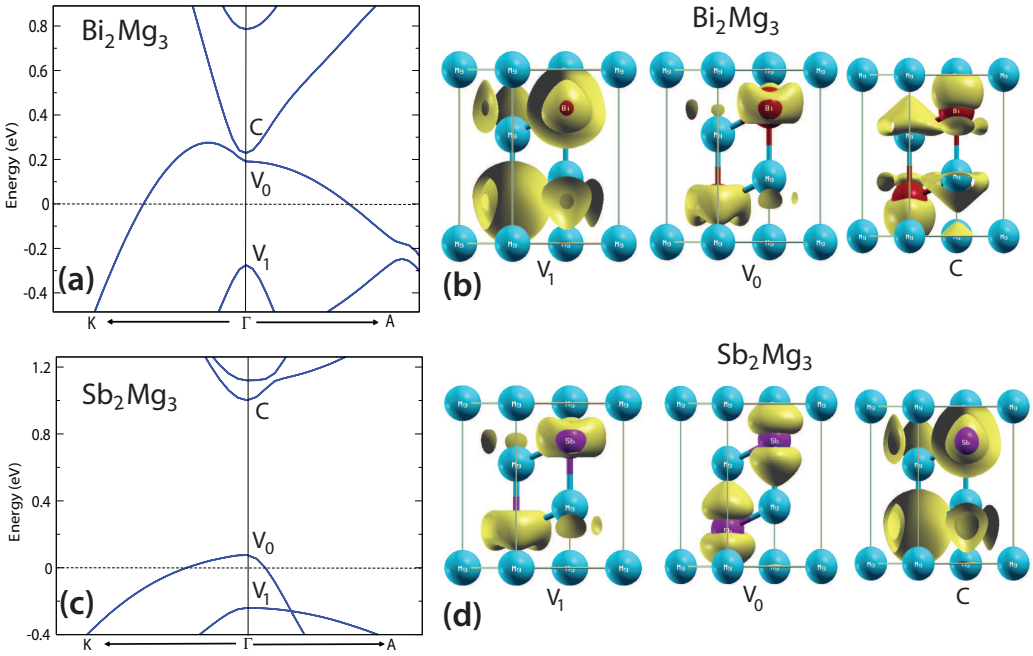

Figure 6.2: Band inversion in Bi_2Mg_3 at Γ point. Electronic bands of Bi_2Mg_3 (a) and Sb_2Mg_3 (c) at Γ are labeled with V_1, V_0, C and the corresponding charge densities are given in (b) and (d) for Bi_2Mg_3 and Sb_2Mg_3 respectively. It is clear that ordering of the bands are inverted in Bi_2Mg_3 compared to that of Sb_2Mg_3 (see *e.g.*, charge densities associated with V_1 and C in (b) and (d) respectively.

6.3 Electronic structure and topology

6.3.1 Electronic structure of the bulk

Among the four compounds studied here, the host compound Bi_2Mg_3 is more covalently bonded, as evident in the dispersion of its electronic bands (see Fig. 6.3(a)), and expected from the fact that Mg is less electropositive than the other alkaline earth elements. Nevertheless, electronic structure of Bi_2Mg_3 is quite interesting in the sense that it has inverted bands at the Γ point in the Brillouin zone compared to a closely related compound Sb_2Mg_3 having the same crystal structure as that of Bi_2Mg_3 (see Fig. 6.2). Due to heavier mass of Bi, the spin-orbit coupling (SOC) in Bi_2Mg_3 is relatively stronger than that in Sb_2Mg_3, and causes inversion of valence and conduction bands at Γ point in Bi_2Mg_3. As the inversion of bands of opposite parity is suggestive of topological phase transition in materials [9,95,118], we were prompted to explore which of Bi_2Mg_3 or Sb_2Mg_3 has a nontrivial electronic topology. As these compounds are invariant under the time-reversal symmetry,

we determined their Z_2 topological invariants [56], and find that Bi_2Mg_3 is topologically nontrivial with Z_2 invariant $\nu_0 = 1$, while Sb_2Mg_3 is topologically trivial with $\nu_0 = 0$.

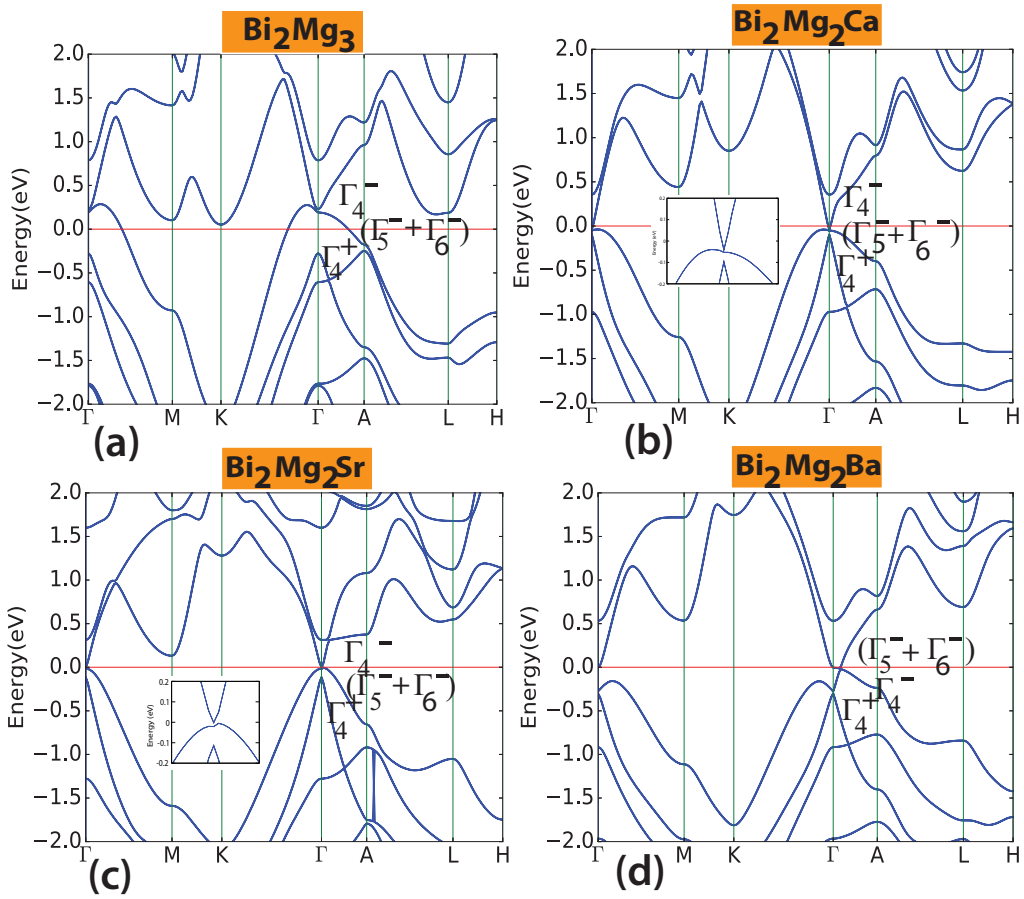

Figure 6.3: Electronic structure of Bi_2Mg_2X (X=Mg, Ca, Sr, Ba) compounds calculated with spin-orbit coupling. While Bi_2Mg_3 is a topological semimetal, Bi_2Mg_2X (X = Ca, Sr) are narrow band gap topological insulators in their native states (see insets of Fig. 6.3(b) & Fig. 6.3(c) for the small band gaps). Bi_2Mg_2Ba, on the other hand, exhibits topological Dirac semimetallic state due to its larger unit cell volume. While Bi_2Mg_2Ca and Bi_2Mg_2Sr with narrow gaps are at the boundary between topological and trivial states, Bi_2Mg_3 and Bi_2Mg_2Ba are quite robust in their respective electronic states. In the topologically nontrivial phase, the conduction band has either Γ_4^- (topological semimetal or topological insulator) or $\Gamma_5^- + \Gamma_6^-$ (Dirac semimetallic state) symmetries at the zone centre (Γ point).

We now analyze the symmetry of bands in the vicinity of Fermi level of Bi_2Mg_3 (Fig. 6.3(a)). As the point symmetry group of the lattice is D_{3d}, the symmetry of the electronic states at Γ (in the presence of spin-orbit interaction) can be labeled with irreducible representations of the double group of D_{3d} [199]. In the topological semimetallic state, its bands near the Fermi energy order as $E_{\Gamma_4^-} > E_{(\Gamma_5^- + \Gamma_6^-)} > E_{\Gamma_4^+}$ (marked in Fig. 6.3(a))

at the Γ point, where E is the energy of the band. These three bands are relevant to the topology of these materials and hence can be used as a basis to develop an effective six-band model Hamiltonian for analysis of topological physics in the long wavelength limit (near Γ). Unlike the topological semimetallic state in ternary half-Heusler compounds with point group T_d [23, 24], the conduction bands in Bi_2Mg_2X (X=Mg, Ca, Sr, Ba) are not four-fold degenerate due to lower symmetry of their crystal structure (point group D_{3d}). As a result, small gaps arise between the bands at Γ from such splitting. In Bi_2Mg_3, the highest occupied band dips below the Fermi level along Γ to K, M and A directions, making it a semimetal. As there exists a gap at all k-points that separate the conduction and valence bands, it is still possible to assign a topological invariant to the latter. There are no bands crossing the Fermi level in Bi_2Mg_2Ca and Bi_2Mg_2Sr, and they exhibit narrow band gaps with topologically nontrivial character of electronic structure. Bi_2Mg_2Ba, on the other hand, exhibits a pair of Dirac points (placed symmetrically around Γ point along [001] axis) in its electronic structure (see Fig. 6.3(d)). Thus, Bi_2Mg_2Ba is a topological Dirac semimetal similar to Na_3Bi [25]. We call this DSM state topological because its Z_2 invariant ν_0=1. This is understood by the fact that the topological insulating phase can be strained into the DSM state (see subsection 6.4.1) through inversion of bands of the same parity (*i.e.* Γ_4^- and $(\Gamma_5^- + \Gamma_6^-)$).

In Bi_2Mg_2X (X = Ca, Sr, Ba) compounds, X atom replaces the Mg atom at the 1a site which is the centre of inversion symmetry of the hexagonal unit cell. As Ca, Sr or Ba atoms are more electropositive than Mg, these compounds have varied degree of covalent and ionic bonding as explained earlier. In their native states (*i.e.* at the experimental lattice constants), Bi_2Mg_2Ca and Bi_2Mg_2Sr are in topologically insulating states with band gaps of 10 meV and 14 meV respectively (see Fig. 6.3(b) and Fig. 6.3(c)). The ordering of bands around the Fermi level is the same as that of Bi_2Mg_3. As the three bands Γ_4^-, $(\Gamma_5^- + \Gamma_6^-)$, Γ_4^+ lie in narrow window of energy, a slight compressive strain can induce band inversion in these compounds and drive the topological insulating state into band insulating phase (which is demonstrated in subsection 6.4.1). Hence, Bi_2Mg_2Ca and

Bi_2Mg_2Sr are in the critical region of this topological phase transition. Due to almost linearly dispersing conduction (Γ_4^-) and valence (Γ_4^+) bands (see inset of Fig. 6.3(b) & Fig. 6.3(c)), these materials have the characteristics of a gapped Dirac material.

The DSM state in Bi_2Mg_2Ba arises from (a) its larger unit cell volume than the other compounds here and (b) the presence of three-fold rotational symmetry. In the TDSM state, the ordering of the electronic bands around the Fermi level at Γ is: $E_{(\Gamma_5^- + \Gamma_6^-)} > E_{\Gamma_4^-} > E_{\Gamma_4^+}$, where Γ_4^- and $(\Gamma_5^- + \Gamma_6^-)$ bands with distinct symmetries cross to make the Dirac cone in this compound. Bi_2Mg_2Ba hosts a pair of Dirac points at $(0, 0, \pm k_z)$ (see Fig. 6.6(a)), which relate to each other by time-reversal symmetry operation. Please note that DFT calculations are performed here at the GGA level. Use of more accurate methods for electronic structure calculations (e.g., hybrid functional or GW approximation) may likely alter the nature of the band gap and the strength of band inversion. Hence, compounds with small band gaps, which lie in or close to the critical region of topological phase transition, may become topologically trivial. Nevertheless, topologically nontrivial phases can be induced in these compounds by applying suitable strain or pressure.

6.3.2 Z_2 invariant and surface states

To affirm the electronic topology of Bi_2Mg_2X (X=Mg, Ca, Sr, Ba) compounds, we determined their topological invariants and electronic structure of (001) surface. We used two methods to obtain Z_2 invariant: (a) parity criterion of Fu-Kane [56] and (b) k-dependent of Wannier charge centres using the ideas of time reversal polarization [14, 65]. Both the methods yield Z_2 invariant ν_0=1 for all these compounds (in their experimental lattice structures), establishing the nontrivial electronic topology in their native phases.

Electronic structure of (001) surfaces of Bi_2Mg_2X (X=Mg, Ca, Sr, Ba) were calculated using centrosymmetric slabs consisting of (001) atomic planes stacked along c-direction and a vacuum of 10 Å to keep the interaction between the periodic images low. We increased the number of layers in the slab of each of these compounds until we got gapless metallic Dirac surface states. The Dirac cone in the electronic structure of (001) surface

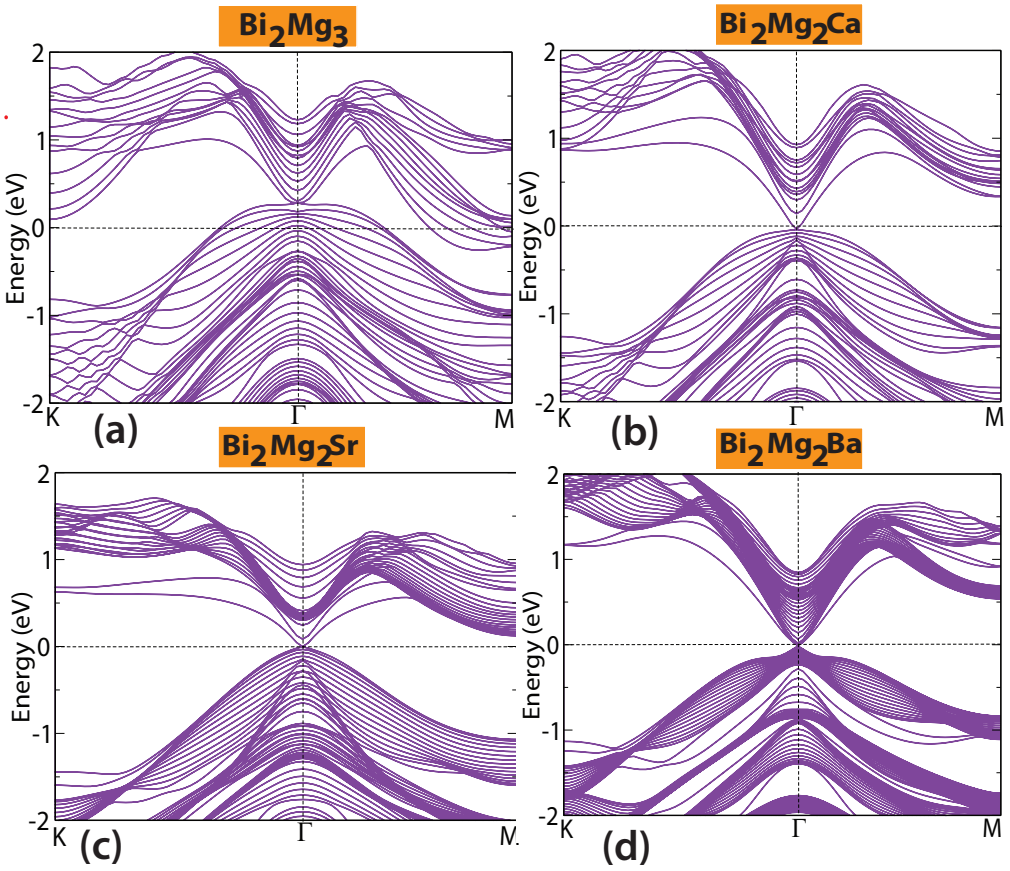

Figure 6.4: Electronic structures of the (001) surface of Bi_2Mg_2X (X = Mg, Ca, Sr, Ba) compounds, calculated within a slab model to show the existence of gap less Dirac surface states. Due to the topological semi-metallic and narrow band gap insulating natures of the bulk bands, the gap less Dirac surface states lie very close to the bulk bands. While the surface states making the Dirac cone in (a) Bi_2Mg_3 deviates from linearity away from Γ, they are quite linearly dispersing for (b) Bi_2Mg_2Ca and (c) Bi_2Mg_2Sr. (d) Bi_2Mg_2Ba being a Dirac semimetal in its native state also hosts linearly crossing gapless surface states which are mixed with the semimetallic bulk bands with similar energies.

lies in the midst of bulk bands: electronic structure of the (001) surface of Bi_2Mg_3 (Fig. 6.4(a)), Bi_2Mg_2Ca (Fig. 6.4(b)) and Bi_2Mg_2Sr (Fig. 6.4(c)) show gapless surface Dirac cones that lie in close proximity of the bulk bands. Bi_2Mg_2Ba, a Dirac semimetal in its native phase also exhibits gapless metallic surface states on (001) surface (Fig. 6.4(d)), for which the bulk band gap is zero. Appearance of the gapless Dirac surface states on (001) surfaces of Sr and Ca compounds further confirms the topologically nontrivial electronic structure of these alkaline earth based Zintl compounds.

6.4 Tunability of electronic topology

6.4.1 Effects of strain

Topological semimetallic phase in the ternary half-Heusler compounds is shown to be tunable with external strain or pressure [23, 24], and these alkaline earth metal based Zintl compounds are no exception. With the symmetry preserving strain, we can drive the native topological states of Bi_2Mg_2X (X=Ca, Sr, Ba) compounds either into topological Dirac semimetallic or band insulating states. Application of compressive strain on Bi_2Mg_3 induces a band inversion at Γ point between Γ_4^- and Γ_4^+ states making a topological phase transition to a normal semimetal, whereas application of compressive strain in Bi_2Mg_2Ca and Bi_2Mg_2Sr makes them band insulator with a band inversion of Γ_4^- & Γ_4^+ bands at Γ point. In trivial semimetallic or insulating phases, the ordering of frontier bands at Γ point is $E_{\Gamma_4^+} > E_{(\Gamma_5^- + \Gamma_6^-)} > E_{\Gamma_4^-}$.

Three-fold symmetry preserving strain is shown to induce topological Dirac semimetallic state in ternary half-Heusler compounds. Here too, DSM state arises with uniaxial strain along c-axis that preserves the three-fold rotational symmetry of the crystal (Fig. 6.5(b)). Learning from Bi_2Mg_2Ba with larger unit cell, isotropic expansion (which preserves all the symmetries of the crystal) gives rise to TDSM states in Bi_2Mg_2X (X = Mg, Ca, Sr) compounds.

Taking Bi_2Mg_2Ca as a model system, we demonstrate how strain induces distinct topological states in bulk of this compound. As Bi_2Mg_2Ca has a narrow band gap (10 meV), a small compressive strain inverts Γ_4^- and Γ_4^+ bands at Γ point inducing an electronic topological phase transitions and making Bi_2Mg_2Ca an ordinary band insulator with topological invariant ν_0=0 (see Fig. 6.5(a)). On the other hand, a small tensile uniaxial strain ($\sim 2\%$) which preserves three-fold symmetry inverts Γ_4^- and $(\Gamma_5^- + \Gamma_6^-)$ bands at Γ point leads to robust crossing of these bands with distinct symmetries along Γ-A direction, and thus induces a Dirac semimetallic state in Bi_2Mg_2Ca (see Fig. 6.5(b)).

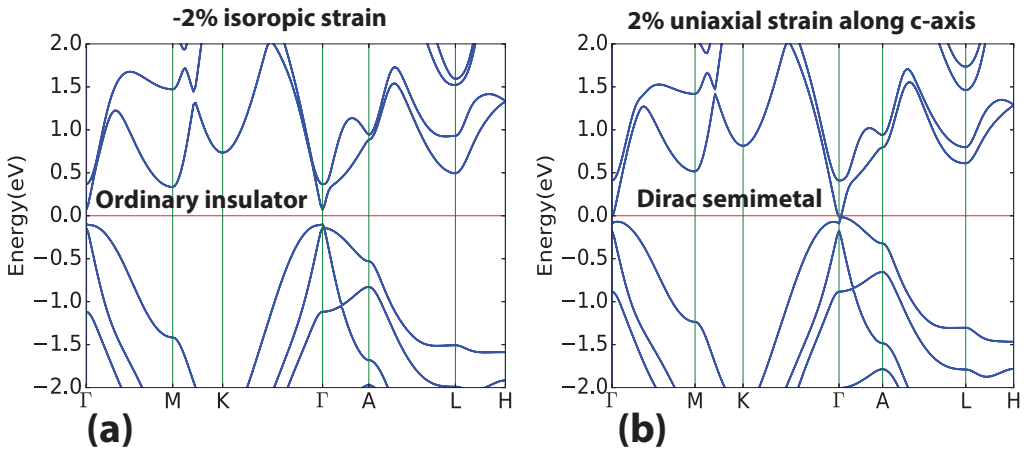

Figure 6.5: Tunable topological states of Bi_2Mg_2Ca with strain. (a) Normal band insulating state obtained after the application of an compressive isotropic strain of -2%, and (b) Dirac semimetallic state obtained with uniaxial strain (ϵ_c=0.02) along c-axis preserving the three-fold symmetry.

6.4.2 Model Hamiltonian to capture tunability with strain

To understand the effects of strain on the electronic structure of these Zintl compounds, we now present a simple **k.p** model Hamiltonian, which accurately captures the electronic structure in the neighborhood of Γ ($\mathbf{k} \to 0$). We start with the 8-band model Hamiltonian of Liu et al. [115,185], which was used in analysis of electronic structure in $\mathbf{k} \to 0$ limit of Bi_2Se_3 family of materials [115,185], which have the same point symmetry group as that of Bi_2Mg_2X (X = Mg, Ca, Sr, Ba) compounds *i.e.* D_{3d}. Noting that the frontier electronic states (Γ_4^-, Γ_4^+ and $\Gamma_5^- + \Gamma_6^-$) near E_F of bulk of Bi_2Mg_2X (X = Mg, Ca, Sr, Ba) are the most important states in description of their topologically nontrivial electronic phases, we construct an effective Hamiltonian by projecting this 8-band model Hamiltonian into the subspace of these six bands *i.e.* Γ_4^-, Γ_4^+ and $\Gamma_5^- + \Gamma_6^-$. The coupling between these and the remaining Γ_4^- band in the original model results in renormalization of the diagonal elements of the 6-band model Hamiltonian, given by,

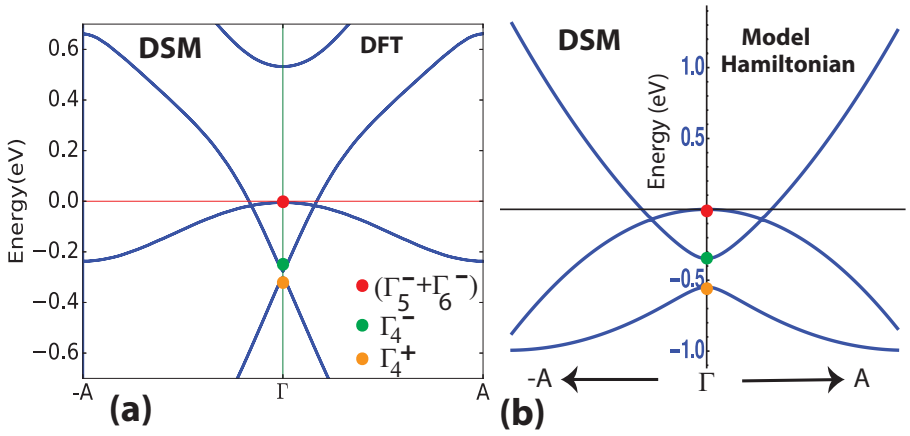

Figure 6.6: Electronic structure of Bi_2Mg_2Ba determined in its native Dirac semimetallic (DSM) state obtained within density functional theory (DFT) agrees qualitatively well with that obtained with the effective $\lambda \to \infty$ model Hamiltonian which includes the strain dependent terms. The symmetry labels of three bands are marked at Γ using red, green and yellow dots.

$$H_0 = \frac{\hbar^2}{2m_0} \begin{pmatrix} f_1(\mathbf{k}) - M_1 & 0 & \frac{2}{\hbar}k_z Q_1 & \frac{2}{\hbar}k_- P_1 & \frac{2}{\hbar}k_+ Q_2 & \frac{2}{\hbar}k_+ P_2 \\ & f_1(\mathbf{k}) - M_1 & \frac{2}{\hbar}k_+ P_1^* & -\frac{2}{\hbar}k_z Q_1^* & -\frac{2}{\hbar}P_2^* k_- & \frac{2}{\hbar}Q_2^* k_- \\ & & f_3(\mathbf{k}) + M_1 & 0 & g_{35}(\mathbf{k}) & g_{36}(\mathbf{k}) \\ & & & f_3(\mathbf{k}) + M_1 & g_{36}^*(\mathbf{-k}) & -g_{35}^*(\mathbf{-k}) \\ & & & & f_5(\mathbf{k}) + M_2 & 0 \\ & & H.c. & & & f_5(\mathbf{k}) + M_2 \end{pmatrix}$$

with $f_i(\mathbf{k}) = F_i k_z^2 + K_i k_\parallel^2$, $g_{ij}(\mathbf{k}) = U_{ij} k_z k_+ + V_{ij} k_-^2$, $k_\parallel^2 = (k_x^2 + k_y^2)$, $k_\pm = k_x \pm i k_y$. In the above model Hamiltonian, M_1, M_2 are constant terms which are added to the diagonal elements. In the expression of f_i, the sign and values of the parameters (effective

masses) F_5 and K_5 are changed from that of their values in Bi_2Se_3. We have kept the values of the other parameters in the model same as that of Bi_2Se_3 [115] *i.e.*, $F_1(eV\mathring{A}^2) = 3.73$, $K_1(eV\mathring{A}^2) = 6.52$, $F_3(eV\mathring{A}^2) = -1.12$, $K_3(eV\mathring{A}^2) = -14.0$, $P_1(eV\mathring{A}^2) = 3.33$, $Q_1(eV\mathring{A}^2) = 2.26$, $P_2(eV\mathring{A}^2) = 2.84$, $Q_2(eV\mathring{A}^2) = 2.84$, $U_{35} = U^*_{36}(eV\mathring{A}^2) = -2.31 - 7.45i$, $V_{35} = -V^*_{36}(eV\mathring{A}^2) = -1.05 - 5.98i$. We have added strain dependent terms in this model Hamiltonian using Bir & Pikus's approach [200] *i.e.* using $k_\alpha k_\beta \rightarrow \epsilon_{\alpha\beta}$, where $\epsilon_{\alpha\beta}$ is the component of strain tensor and α, β indicate Cartesian directions.

The form of the strain Hamiltonian, which is used to generate Fig. 6.6(b), is given by,

$$H_{strain}= \begin{pmatrix} -0.24 & 0 & 0 & 0 & 0 & 0 \\ 0 & -0.24 & 0 & 0 & 0 & 0 \\ 0 & 0 & -0.24 & 0 & 0 & 0 \\ 0 & 0 & 0 & -0.24 & 0 & 0 \\ 0 & 0 & 0 & 0 & 1.8 & 0 \\ 0 & 0 & 0 & 0 & 0 & 1.8 \end{pmatrix}$$

The total Hamiltonian is thus given by, $H_{tot} = H_0 + p * H_{strain}$, p is a scalar number. While generating Fig. 6.6(b), we have solved H_{tot} with $M_1 = 0.1$, M_2 =0.04, $p = 0.2$, F_5=-3.50 and K_5=3.11.

Analysis of the electronic states of Bi_2Mg_2X (X = Mg, Ca, Sr, Ba) reveals that Γ_4^- and $(\Gamma_5^- + \Gamma_6^-)$ states contain contributions from Bi 6s and 6p orbitals respectively, whereas Mg 3s orbitals contribute to Γ_4^+ state. Thus, stronger ionicity associated with unoccupied Γ_4^+ states in the conduction band gives rise to trivial topology. To get the correct ordering

of bands within this 6-band model Hamiltonian and reproduce the dispersion of the Dirac semimetallic state of Bi_2Mg_2Ba qualitatively correctly, we (a) used the parameters of Bi_2Se_3 [115] with slight modifications (renormalization of diagonal terms with M_i), (b) changed the effective masses (F_5 & K_5), and (c) added strain-dependent terms to the Hamiltonian. From Fig. 6.6, it is clear that the three bands (marked with red, green and yellow dots at Γ) in the electronic structure described by our model (Fig. 6.6(b)) agree qualitatively with the three bands obtained from the DFT calculations (see Fig. 6.6(a)). Thus, effects of large ionic radius of Ba can be captured with the strain-dependent terms. Effects of ionicity are captured with M_i parameters which influence the ordering of bands at Γ. The topology of electronic structure here is determined by the symmetry of occupied bands: if the band Γ_4^+ constitute conduction band, the topology is trivial. Our analysis of this model Hamiltonian helps in uncovering the roles of symmetry, ionicity and ionic size in determination of electronic topology.

6.5 Vibrational properties

As many of the Zintl phase compounds belonging to the family of Bi_2Mg_2X (X = Mg, Ca, Sr, Ba) crystals have been shown to be good thermoelectric materials [194], we determined their phonon dispersion to assess (a) the structural stability and (b) their thermoelectric performance.

Phonon dispersion of Bi_2Mg_3 reveals an imaginary phonon mode ($i15\text{cm}^{-1}$) at the L point (Fig. 6.7(a)) of the hexagonal Brillouin zone. This instability is associated with an optic phonon mode involving opposite displacements of two Bi atoms and two Mg atoms (at 2d site) along x-axis, and that of Mg atom (1a site) along -x direction. This phonon indicates a very weak local lattice instability in Bi_2Mg_3. In covalently bonded Bi_2Mg_3, the topmost valence band is partially occupied, and the associated energy-cost causes local lattice instability in Bi_2Mg_3. The other three Zintl compounds in this family are locally stable in their native states, with no unstable phonons in their phonon spectra

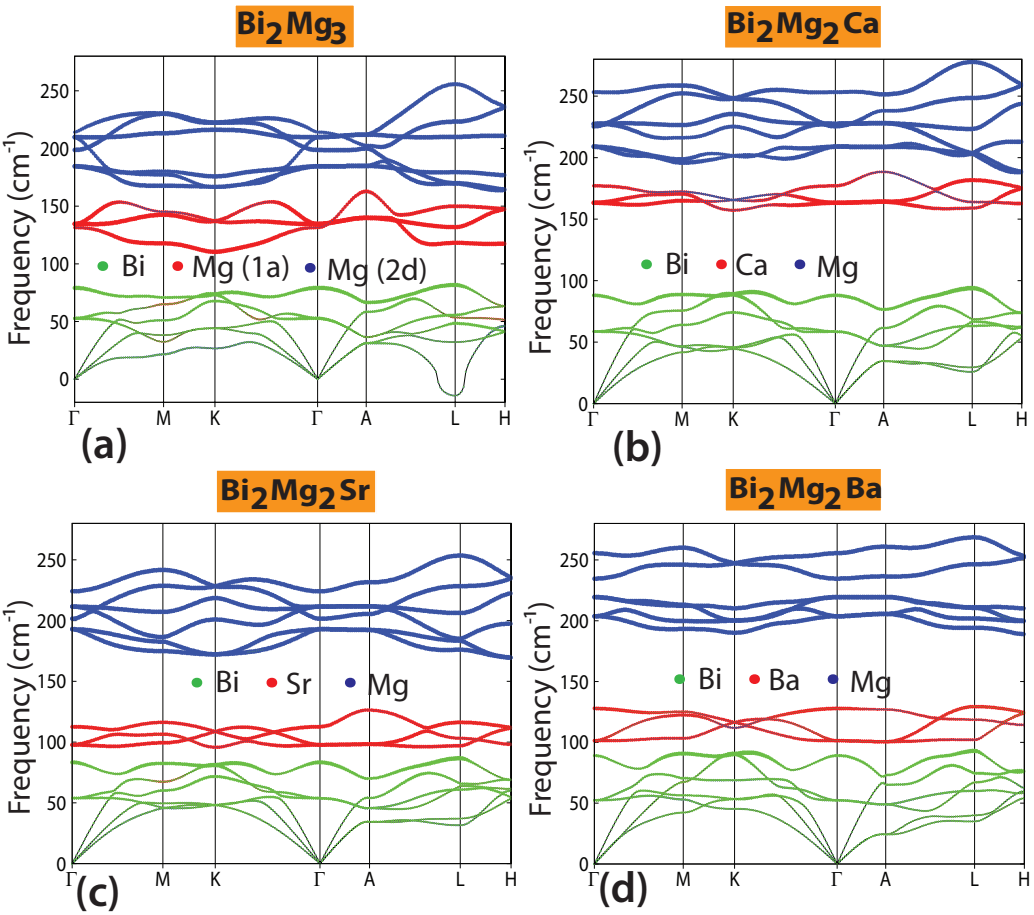

Figure 6.7: Atom projected phonon spectra of Bi_2Mg_2X (X = Mg, Ca, Sr, Ba) compounds. In each phonon spectrum, contributions of each inequivalent atom to the phonon branches are highlighted with separate colors and thickness of the lines denotes the extent of the contributions. (a) Bi_2Mg_3 exhibits an imaginary frequency ($i15\text{cm}^{-1}$) at L point in the Brillouin zone, whereas the rest of the compounds (b,c,d) do not exhibit any unstable phonons in their establishing their structural stability at the ambient conditions. Phonon branches are divided into three groups depending on the masses and the bonding environments of the constituent atoms. The three middle branches (highlighted with red color) originating from the vibrations of the X atom at 1a site, are mostly non-interacting and hence they are localized and flat.

(see Fig. 6.7). In Bi_2Mg_3, there are two symmetry inequivalent Mg sites in the crystal (occupying 1a and 2d sites), and their bond lengths with the surrounding Bi atoms are different. As a result, phonon branches (Fig. 6.7(a)) are distributed into three groups. The lowest six phonon branches are dominated by displacements of the heaviest bismuth atoms (highlighted with green color), the Mg at the 1a site contribute primarily to middle three branches (marked with red color), and the highest six phonon bands (marked with

blue color) arise from the Mg atoms occupying 2d sites with shorter Mg-Bi bond lengths.

Frequencies of the middle band in phonon dispersion drop from Bi_2Mg_2Ca to Bi_2Mg_2Sr to Bi_2Mg_2Ba, as expected from the increasing mass of the constituent atoms at 1a site. It is seen from the dispersion of these compounds (see Fig. 6.7) that the frequencies of acoustic branches are rather low, namely below 50 cm^{-1}. As thermal conductivity of a material depends quadratically on the slope of acoustic branches, we expect these compounds to exhibit ultra-low thermal conductivity [201] which is an important paradigm in design of efficient thermoelectric materials.

6.6 Potential applications

6.6.1 Electronic thermoelectric properties

Many alkaline and rare earth based Zintl compounds are known to be good thermoelectrics [194]. For example, Sb_2Zn_2A (A = Sr, Ca, Yb, Eu) are shown to exhibit good thermoelectric transport properties at high temperatures [202]. Solid solution of Sb_2Cd_2Yb and Sb_2Zn_2Yb *i.e.* $Sb_2Cd_{1.6}Zn_{0.4}Yb$ shows a thermoelectric figure of merit (zT) of 1.2 at 700 K [203]. Given the fact (a) Bi_2Mg_2X (X = Mg, Ca, Sr, Ba) compounds have nontrivial electronic topology which is relevant to electronic contribution to thermoelectric performance of materials [197] and (b) Zintl phase compounds are of general interest as thermoelectric materials [204, 205], we investigated the thermoelectric properties of Bi_2Mg_2X (X = Mg, Ca, Sr, Ba) compounds.

We estimated the electronic thermoelectric properties (Seebeck coefficient (S), and thermoelectric power factor(P)) of these compounds as a function of temperature under the conditions of electron (n-type) and hole (p-type) doping. We kept the carrier concentrations low and same for both types of doping to facilitate comparison of their thermoelectric efficiency. Among the four compounds, Bi_2Mg_2Ca and Bi_2Mg_2Sr (which are small band gap topological insulators) exhibit high Seebeck coefficients for both type of doping (see Fig. 6.8(a) & Fig. 6.8(b)) due to remarkable asymmetry in their density of

states. Bi_2Mg_2Ba which is a Dirac semimetal has a higher Seebeck coefficient with p-type doping than with n-type doping. On the other hand, the semimetallic phases of Bi_2Mg_3 has a relatively weaker Seebeck coefficients [197] (Fig. 6.8()a, and Fig. 6.8(b)), similar to what was seen in the Weyl semimetal TaAs [197]. Our calculations reveal that these materials generally exhibit better thermoelectric performance for n-type doping as the power factor of all these compounds are much larger compared to their p-doped counterparts (see Fig. 6.8(c) & Fig. 6.8(d)).

From the phonon spectra of these compounds (Fig. 6.7), it is clear that the cut-off frequencies for the acoustic modes are below 50 cm^{-1} which indicates ultralow sound velocities in these compounds. Our estimates of average sound velocities of Bi_2Mg_3, Bi_2Mg_2Ca, Bi_2Mg_2Sr and Bi_2Mg_2Ba are 2091 m/s, 2562 m/s, 2497 m/s and 2597 m/s, respectively, which are comparable to the sound velocities of Bi_2Te_3 based alloys (v_s = 2147 m/s), which exhibit very low lattice thermal conductivity (κ_l=1.5 $Wm^{-1}K^{-1}$) [206]. Moreover, the X^{2+} ions in these compounds at the 1a site bind only weakly. Hence, the phonon branches associated with the X^{2+} atoms are quite flat and localized. It is known that flat and localized phonon modes act as rattlers and are very active in reducing the lattice thermal conductivity of InTe (κ_l=0.4 $Wm^{-1}K^{-1}$) by scattering heat carrying acoustic phonons [201]. Thus, we expect that low sound velocities and flat localized vibrations of the X^{2+} atoms would induce ultralow lattice thermal conductivity in Bi_2Mg_2X (X=Mg, Ca, Sr, Ba) compounds, which further enhance their thermoelectric performance measured with zT.

6.6.2 Heterostructures and devices

Heterostructures consisting of ultra-thin layers of two or more compounds stacked together are playgrounds for exploiting the science of surface and interfacial states. They provide a platform for excellent control and tunability of these states with respect to strain and chemical doping. They naturally have the potential for use in devices. Epitaxially grown heterostructures of Bi_2Mg_2X (X=Mg, Ca, Sr, Ba) compounds are thus good candidates

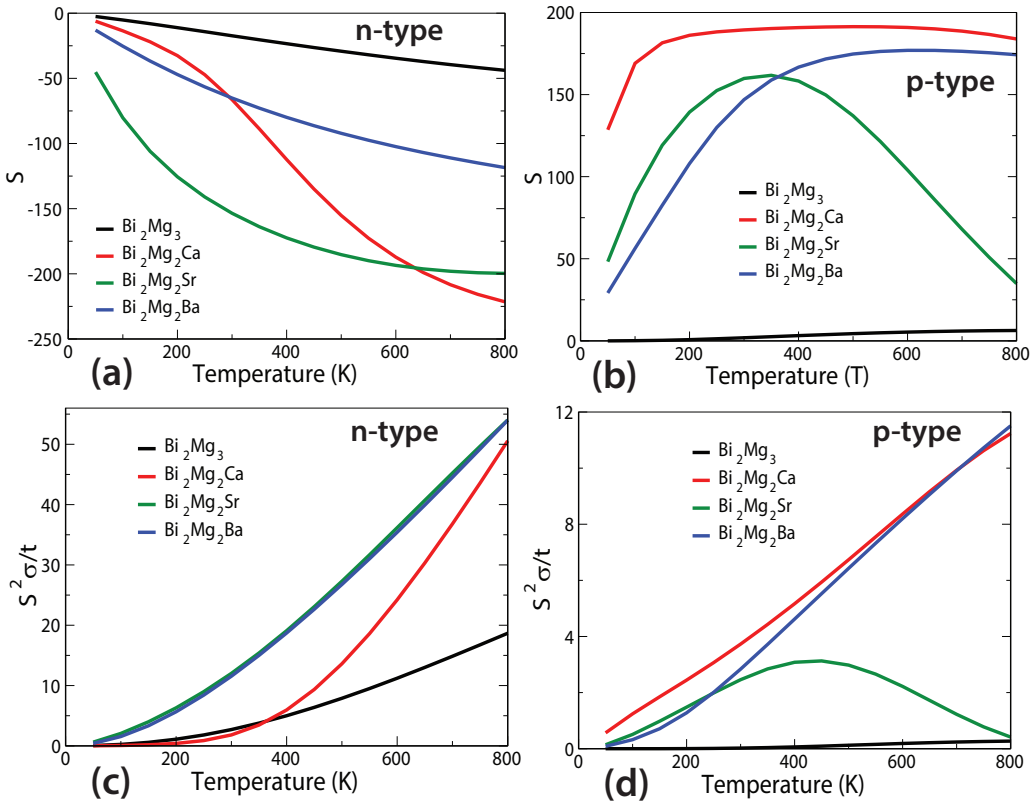

Figure 6.8: Seebeck coefficient (S) and power factor (P=$S^2\sigma$/t) as a function of temperature. While the Seebeck coefficient and power factor of both n-type (a,c) and p-type (b,d) Bi_2Mg_3 are quite small, S of Bi_2Mg_2Ca and Bi_2Mg_2Sr are quite large for the both types of doping. On the other hand, Bi_2Mg_2Ba, being a Dirac semimetal, shows quite high value of S for p-type doping than n-type doping. In contrast, power factor of all these compounds are high for n-type doping compared to p-type doping. The carrier concentrations are kept low and same for the both p and n-type doping. Units for Seebeck coefficient (S), and power factor ($S^2\sigma$/t) are μVK^{-1} and $10^{14}Wcm^{-1}K^{-2}s-1$ respectively.

for exploration of topologically nontrivial electronic states at the interfaces between their distinct topological states.

For example, there is a mismatch of 2.7% in the in-plane lattice constant of Bi_2Mg_3 and Bi_2Mg_2Sr. Thus, an ultra-thin film of Bi_2Mg_2Sr grown epitaxially on a Bi_2Mg_3 substrate along the layered direction (c-axis), will be a Dirac semi-metal due to in-plane epitaxial strain. Its interface with the substrate may host exotic interfacial states arising from the interaction between DSM and topological semimetal (TSM) phases. They can be utilized in high mobility electronics due to the presence of robust Dirac cones both in the bulk as well as at the interface. As a small compressive strain (isotropic or uniaxial)

makes Bi_2Mg_2X (X=Ca, Sr, Ba) compounds band insulators through a topological phase transition, the Dirac semimetallic state of Bi_2Mg_2Ba can be used as a resistive strain sensor.

6.7 Conclusions

Based on first-principles density functional theoretical analysis, we predict that alkaline earth based Zintl compounds Bi_2Mg_2X (X = Mg, Ca, Sr, Ba) host topologically nontrivial electronic states. Bi_2Mg_3, the most covalent compound among these, is a topological semimetal. Bi_2Mg_2Ca and Bi_2Mg_2Sr, on the other hand, are narrow band gap topological insulators. Interestingly, Bi_2Mg_2Ba with relatively larger X ion exhibits a topological Dirac semimetallic state. Our analysis of the electronic topology of these materials through determination of (a) Z_2 invariants and (b) surface electronic structures revealed the relevance of symmetry, ionic size and ionicity. With respect to electronic structure of related topologically trivial Sb_2Mg_3, conduction and valence bands of these compounds have opposite parity and character. We demonstrated that the strain preserving threefold rotational symmetry can transform these materials to normal insulating as well as Dirac semi-metallic states, uncovering the tunablity of electronic structure and topology of these compounds, that is accessible to experiments via epitaxial growth.

From their phonon dispersion, we surmise that these compounds would exhibit ultralow lattice thermal conductivity. Secondly, asymmetry in the density of states near the gap of Bi_2Mg_2Ca and Bi_2Mg_2Sr results in high Seebeck coefficients. This should stimulate experiments to measure thermoelectric properties of these compounds, as they are already known to exist. The relevance of symmetry, ionicity and ionic size identified here should guide in chemical design of centrosymmetric crystal with nontrivial electronic topology.

Part III

Weak Topological Insulator

Chapter 7

Emergence of Weak Topological Insulating Phase in BiSe

7.1 Introduction

The discovery of strong topological insulators (TIs) in three dimensions resulted in an enormous research activity in condensed matter physics leading to discovery of other topological phases of matter *e.g.*, topological crystalline insulator (TCI) [43], Dirac semimetals [25], Weyl semimetals [48]. Unlike an ordinary band insulator, the surface of a topological insulator hosts robust gapless metallic states that support high spin-polarization [96, 97]. These topological surface states arise from the nontrivial topology of the bulk electronic wave function that remain protected either by discrete (*e.g.*, time-reversal symmetry in a Z_2 TI) or spatial symmetry (e.g, crystalline symmetry in a TCI.)

Bisumth based chalcogenides (*e.g.*, Bi_2Se_3, Bi_2Te_2) [9, 104] are strong topological insulators in three dimensions that host an odd number of massless Dirac cones on their surfaces. A departure from this notion is the idea of a weak topological insulator, wherein only certain surface terminations host topologically nontrivial surface states characterized by an even number of Dirac nodes leading to exciting new physics.

Mathematically, TIs are differentiated from ordinary insulators based on global topological invariants [56,101,207]. In two dimensions, TIs are described by a single topological invariant (ν, which can be either 0 or 1), whereas in a three dimensional material, there are four Z_2 invariants $(\nu_0;\nu_1,\nu_2,\nu_3)$. Among these, ν_0 is known as strong topological index, whereas (ν_1,ν_2,ν_3) are known as weak topological indices. Three dimensional TIs are again classified into strong and weak classes. For a strong topological insulator (STI), ν_0 must be 1, rest of the indices may or may not take a non-zero value, whereas for a weak topological insulator (WTI), ν_0=0, and at least one of the three indices (ν_1,ν_2,ν_3) should be 1. Contrary to a STI which hosts robust surface states on all its surfaces, a WTI exhibits gapless topological surface states only on certain specific surface terminations. In this regard, topological surface states in a STI are always manifested, whereas it is either manifested or hidden in case of a WTI [39, 40, 208]. WTIs are topologically equivalent to a stack of 2D TI layers showing an even number of Dirac cones on their side surfaces [39]. The surface states of WTI were initially thought to be unstable towards non-magnetic disorder [39, 209], However, recently it has been shown that WTI surface states behave robustly under strong time-reversal invariant disorders, similar to those of STIs [39,41]. These states are further predicted to give rise to several novel topological quantum effects *e.g.*, one-dimensional helical modes along dislocation lines [40], weak-anti-localization (WAL) effect [41], half quantum spin Hall effect [42].

There are only few WTIs reported in literature. For example, KHgSb [59] and Bi_2Te_2I [210] were theoretically predicted to be WTIs, which are not experimentally verified yet. The only known experimental realization of a WTI is the bismuth-based layered compound $Bi_{14}Rh_3I_9$ [211]. The intuition for designing a WTI material comes from the idea that a stack of weakly coupled 2D topological insulators can emerge as a 3D WTI. In fact, $Bi_{14}Rh_3I_9$ is essentially a stacked graphene analogue [211], with each layer exhibiting large spin-orbit interaction generated by Bi. Another promising route is to stack alternating Bi bilayers, a 2D topological insulator, with a trivial insulator. Bi_2Te_2I follows this paradigm and was theoretically shown to be a WTI [210].

With the help of first-principles calculations based on density functional theory, we predict here the emergence of a weak topological insulating phase in BiSe which belongs to the Bi_xSe_y crystal family. We borrow the idea essentially from two observations. First, the fact that stacking of Bi bilayers is known to host a 3D WTI phase, therefore we intuit that stacking Bismuth bilayers sandwiched on either side by a topological insulator instead of a trivial insulator could also possibly host the WTI phase. Second, and more importantly, it is known that the Bismuth chalcogenides exhibit what is known as infinitely adaptive superlattice phase [212]. Essentially, the stoichiometry of Bi_xSe_y can be adjusted to a wide range of values by stacking of Bi_2Se_3 and Bi_2 in the correct ratio. For the simplest possible ratio with $x = 1$ and $y = 1$, one obtains a crystal structure as shown in Fig. 7.1(a) in which a repeating unit is formed by a Bi_2 bilayer sandwiched bwtween two Bi_2Se_3 quintuple layers on the top and bottom. The hallmark of this structure is that it consists of quantum spin hall insulators [213–215] that are coupled to 3D topological insulator. This work has been done in collaboration with experimentalists (Kunjalata Majhi and Prof. PS Anil Kumar, IISc) who measured magnetotransport properties of BiSe.

7.2 Crystal structure and Brillouin zone

BiSe has a hexagonal crystal structure with twelve atomic layers in the primitive unit cell (see Fig. 7.1(a)) with space group $P\bar{3}m1$ (No. 164) [175] where a bismuth bilayer is sandwiched between two quintuple layers (QLs) of Bi_2Se_3 in such a way such that it retains inversion symmetry. In the crystal structure of BiSe, all the layers are stacked along the c-direction and are held together by relatively weak bonding compared to the strong covalent bonding within the Bi_2Se_3 QLs and bismuth bilayer. This is clearly seen from Fig. 7.1(b), where electronic charge density clouds are highly localized within bismuth bilayer and Bi_2Se_3 QLs, but with very little or no contribution between the layers (see Fig. 7.1(b)). The Brillouin zone (BZ) of this hexagonal unit cell is shown in Fig. 7.2(a),

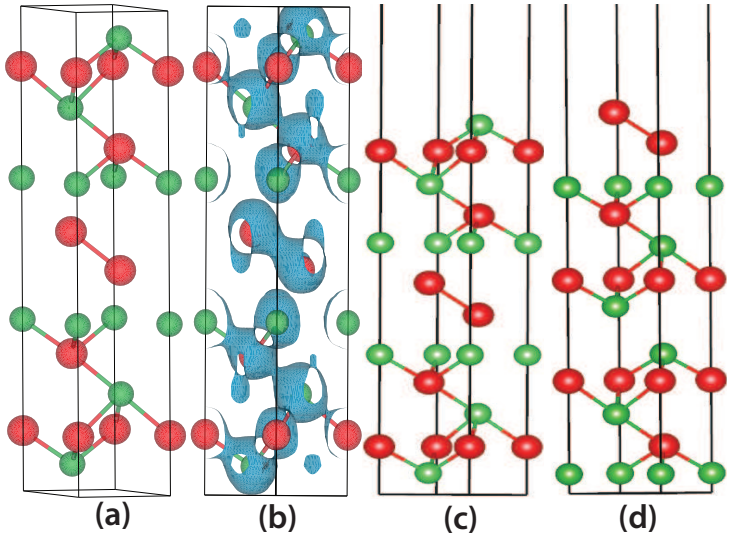

Figure 7.1: Total electronic charge density plot and different unit cells of BiSe for electronic structure calculations of the bulk and (001) surface. (a) Primitive hexagonal unit cell of BiSe consisting of a bismuth bilayer sandwiched between two Bi_2Se_3 quintuple layers stacked along c-direction. (b) Iso-surfaces of total electronic charge density (shown in blue color) shows strong covalent bonding within bismuth bilayer and Bi_2Se_3 QLs, but reveals weak interlayer interaction between them. (c) Se and (d) Bi bilayer terminated surfaces of BiSe used for (001) surface states calculation. Red and green spheres denote Bi and Se atoms respectively.

inside which a parallelepiped is drawn in red color whose vertices denote the eight time reversal invariant momenta (TRIM) ($\Gamma, M_{1,2,3}, L_{1,2,3}$, A) in that BZ.

7.3 Computational details

We have determined electronic structure of BiSe both without and with including spin-orbit coupling (SOC) in the calculations using the Quantum ESPRESSO (QE) [112] code which treats only valence electrons replacing the potential of ionic core with a smooth pseudopotential. The results from QE code were reproduced by another more accurate implementations of density functional theoretical (DFT) methods: the WIEN2K [128] code which is an all-electron full potential linearized augmented plane wave (FP-LAPW) based technique.

For simulations in QE, we have used both non-relativistic and fully relativistic (which includes SOC) norm-conserving pseudpotentials with kinetic energy cut-offs of 60 Ry and

240 Ry chosen respectively for wave function and charge density while truncating their representations in plane wave basis. Integrations over the Brillouin zone are performed with a dense mesh of 9×9×3 k-points. Occupation numbers are treated according to the Fermi-Dirac distribution function with a broadening width of 0.003 Ry. We allowed the relaxation of the atomic positions in the bulk unit cell until the magnitude of forces on atoms at each pressure are less than 1 mRy/bohr.

To obtain total energies and eigenvalues of the electrons in a solid using the FP-LAPW methods, we use a basis set achieved by dividing the unit cell into non-overlapping spherical regions centered at each atom and the interstitial region. Two different types of basis sets are used in these two regions. Plane wave basis set is used in the expansion of the electronic wave functions inside the interstitial region. It is augmented by atomic like wave functions (linear combination of the solutions of the radial Schrödinger equation and spherical harmonics) in the space inside every atomic sphere. These atomic-like wave functions form the basis set inside each non-overlapping atomic sphere. We use Perdew, Burke and Ernzerhof (PBE) parametrization [114] of the exchange-correlation energy functional derived with a generalized gradient approximation (GGA) [113]. Spin-orbit interaction has been included through a second variational procedure [82,83]. Truncation of the plane wave expansion of electronic wave functions inside the interstitial region is specified by a cut-off value of R_{mt}*$K_{max} = 7$, where R_{mt} is the radius of the smallest atomic sphere (muffin-tin), $K_{max} = 2.8$ a.u^{-1} is the plane wave cut-off vector, and charge density is Fourier expanded up to by $G_{max} = 12$ Ry$^{1/2}$, where G_{max} represents the maximum value of G vector in the Fourier expansion. We adopt the tetrahedron method for sampling integrations over the Brillouin zone with a 12×12×2 mesh of k-points.

Lattice-dynamical properties are determined within the framework of self-consistent density functional perturbation theory (DFPT) as implemented within the QE code [64]. Since the effect of SOC is negligible on phonon frequencies and character of the vibrational modes is unchanged without the SOC, we determine vibrational frequencies of BiSe within a non-relativistic description. In order to calculate the phonon dispersion, force constant

matrices are obtained on a 4×4×1 q-point mesh. The dynamical matrices at arbitrary wave vectors are then obtained using Fourier interpolations.

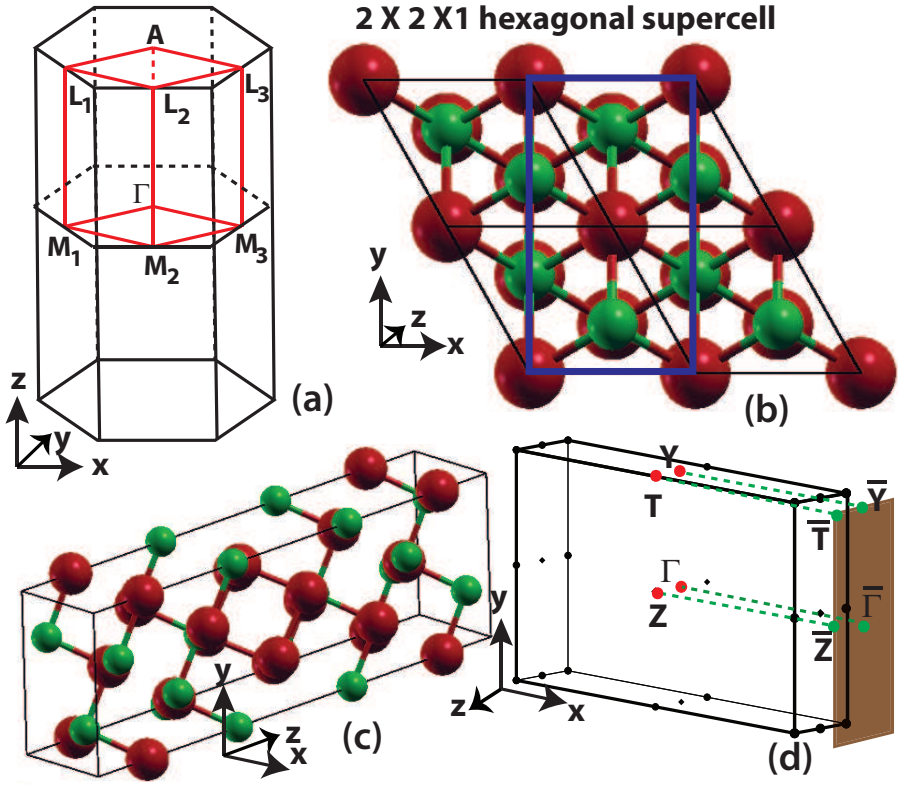

Figure 7.2: Time reversal invariant momenta (TRIM) in the hexagonal Brillouin zone (BZ), unit cell and corresponding BZ for side surface states calculation. (a) Vertices of the parallelepiped (drawn in red color within the hexagonal BZ) correspond to eight TRIM (Γ, $M_{1,2,3}$, $L_{1,2,3}$, A). (b) The rectangle marked with blue color in a 2×2×1 hexagonal supercell of BiSe form the basal (xy-plane) plane for the orthorhombic unit cell for side-surface calculations whose dimension is a×$\sqrt{3}$a×c (as shown in c), where a and c are the lattice constants of the bulk hexagonal unit cell of BiSe. (d) Brillouin zone of the orthorhombic side surface unit cell where red dots mark the high symmetry points in the bulk and green dots mark their projections on (100) surface on which the electronic structure for the (100) side surface of BiSe is calculated. Red and green spheres denote Bi and Se atoms respectively.

For the calculation of surface states on (001) surface of BiSe, we have taken the hexagonal unit cell with (a) Se and (b) bismuth bilayer terminations (see Fig. 7.1(c) & Fig. 7.1(d)) with three different thicknesses (12,24 and 36 layers) of BiSe along c-direction and used 9×9×1 mesh of k-points for BZ integrations. We have also calculated the surface electronic structure of a free standing bismuth bilayer for which we have adopted the same hexagonal unit cell as BiSe, except for a different value of lattice constant along c-axis

(see Fig. 7.6(a)).

For side surface states calculations, we have constructed an orthorhombic unit cell with dimension a×$\sqrt{3}$a×c from the hexagonal supercell of BiSe as shown in Fig. 7.2(b), where blue rectangle shows the basal plane of the orthorhombic unit cell with 24 atoms ($Bi_{12}Se_{12}$). a and c are the experimental lattice constants of the hexagonal unit cell of BiSe. The full orthorhombic unit cell and its BZ are shown in Fig. 7.2(c) and Fig. 7.2(d), respectively. The high symmetric points in the bulk of the orthorhombic BZ and their projections on the (100) side surface on which the surface electronic structure has been calculated are also shown in Fig. 7.2(d). For BZ integrations, we used 1×9×3 mesh of k-points. To obtain the surface electronic structure of Fig. 7.3(c), we have taken seven unit cell thick layers of the orthorhombic unit cell (as shown in Fig. 7.2(c)) along x-direction which is truncated with a vacuum of 15 Å to prevent electrostatic interactions between the periodic images of the slab along x-direction. On the side surface (yz-plane) of this semi-infinite slab, bismuth bilayer exhibits an armchair type termination on the boundary.

7.4 Theoretical analysis

Electronic structure of BiSe, calculated at the experimental lattice constant (a=4.212 Å and c=22.942 Å) [175] without including SOC (see Fig. 7.3(a)), reveals a metallic character with a flat conduction band along Γ-A line just above the Fermi level (E_F). The charge density of this band is highly localized and confined within the bismuth bilayer. Dispersion of this band near the E_F (along Γ-A) is similar to that of an unconventional superconductor MgB_2 [216], weak topological insulators like Bi_2TeI [210] and KHgSb [59]. This unoccupied conduction band is constituted primarily of σ-bonded p_x and p_y orbitals of Bi in the bismuth bilayer, and becomes dispersion-less due to relatively weaker interlayer interactions. Such empty covalent bonds cost energy, and this flat band pushes BiSe to the brink of lattice instability (with imaginary frequency of $\sim i15$ cm^{-1} appearing along

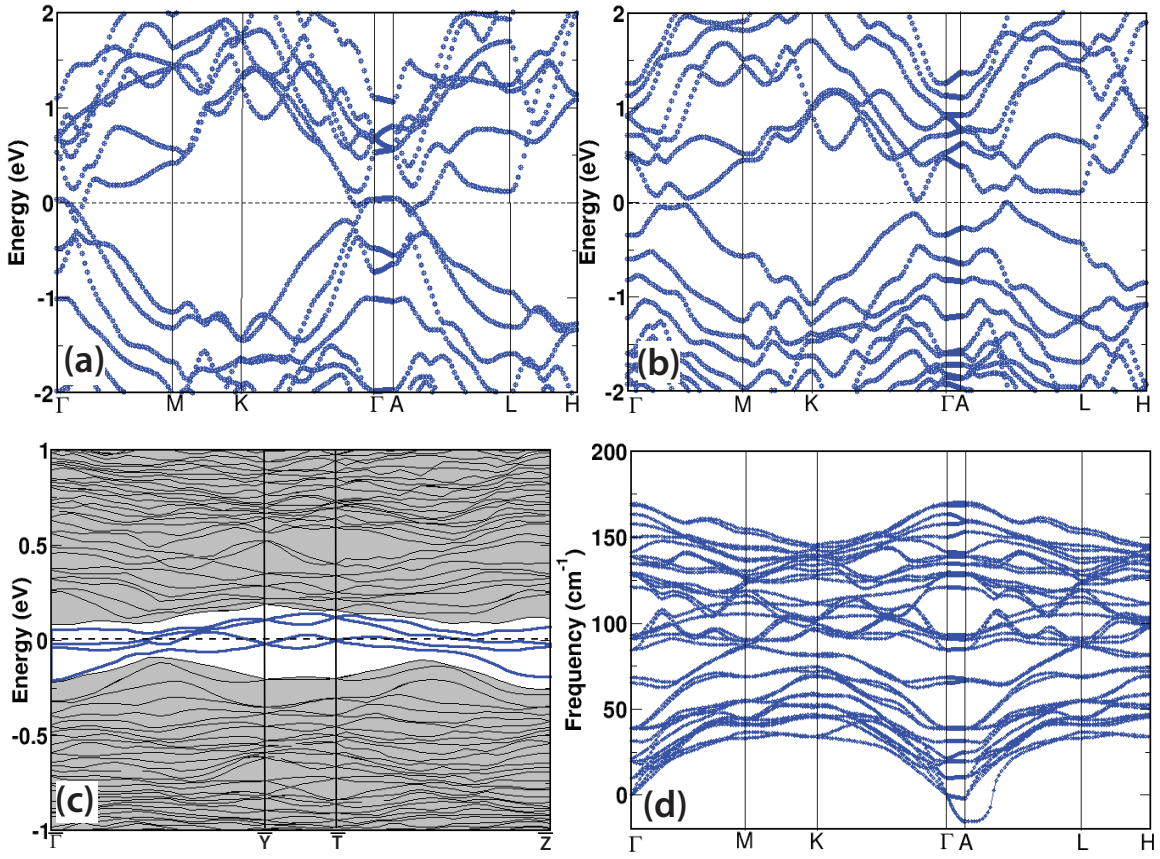

Figure 7.3: Electronic structure and phonon dispersion of BiSe. Electronic structure of BiSe calculated without spin-orbit interaction (a) reveals a metallic state. Spin-orbit interaction opens up a band gap throughout the Brillouin zone (BZ), making BiSe a small ($\sim$ 42 meV) indirect band gap semiconductor (b). Electronic structure of (100) surface of BiSe (c) calculated with SOC reveals two Dirac cones(highlighted with blue colors) at $\bar{Y}$ and $\bar{T}$ points in the surface BZ; here, grey shaded regions represent the bands arising from the bulk. The empty dispersion-less conduction band along Γ-A in (a) makes BiSe weakly unstable, as evident from its phonon dispersion (d) calculated without including spin-orbit coupling.

Γ-A direction, the crystallographic direction of stacking in BiSe, see Fig. 7.3 (d)).

7.4.1 Projected electronic structure of the bulk

Layer projected electronic structure (see Fig. 7.4(a) & Fig. 7.4(b)) reveals that the contributions to the valence band (VB) and conduction band (CB) around the Fermi level mainly come from the Bi bilayer and Bi_2Se_3 quintuple layers (QLs) respectively, except along the Γ-A line where this is reversed, indicating even number of band inversions at Γ and A points in the Brillouin zone. The inverted band structure together with even

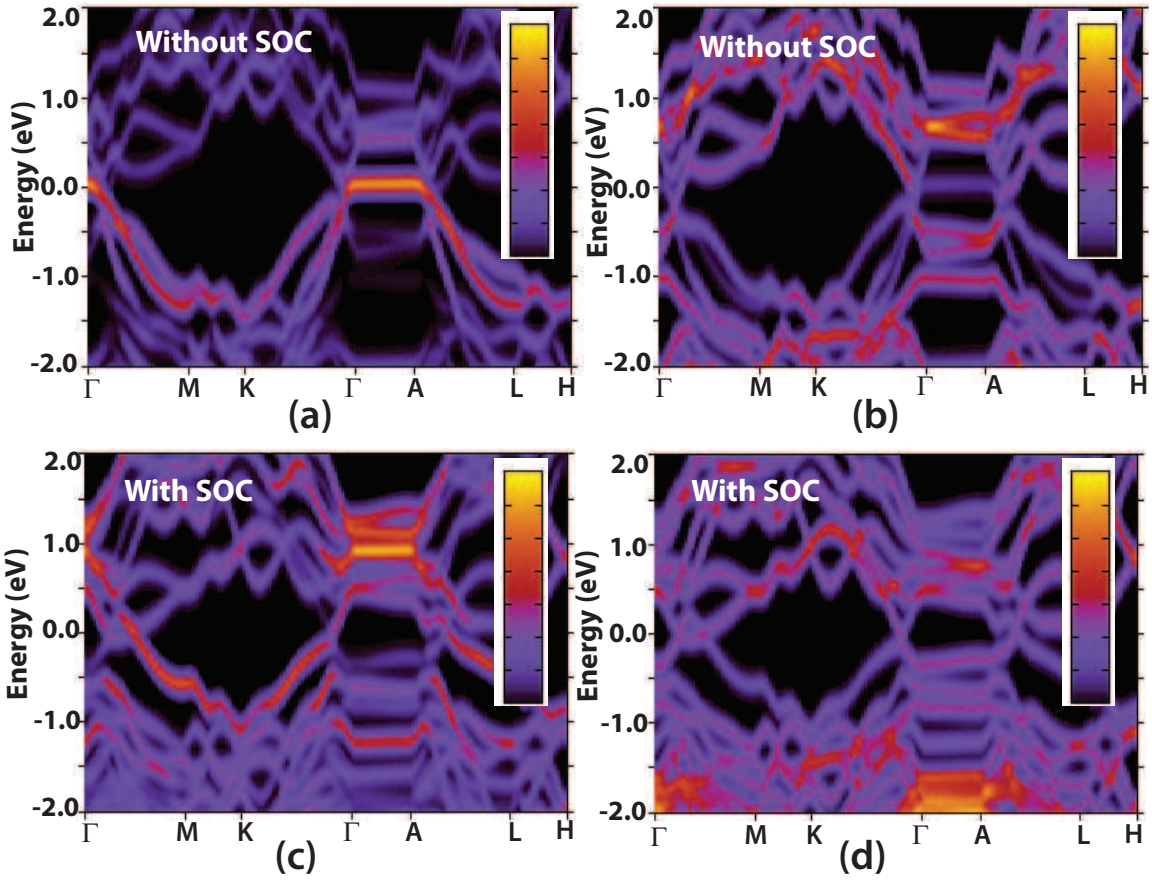

Figure 7.4: Bi bilayer (a,c) and Bi_2Se_3 quintuple layer (b,d) projected electronic density of states along high symmetry directions in Brillouin zone. Electronic density of states calculated without spin-orbit interaction shows the contribution coming from the bismuth bilayer (a) and Bi_2Se_3 quintuple layers (b). As can be seen in (a), the flat bands along Γ-A comes from the bismuth bilayer which gets split as a result of inclusion of spin-orbit interaction in (c), and opens up gap along Γ-A and elsewhere in the Brillouin zone. (d) Contribution coming from the Bi_2Se_3 QLs in presence of SOC. Hot (yellow) and cold (black) colors in the color scale signifies maximum and vanishing contributions, respectively.

number of band inversions hint towards the presence of a topological nontrivial (weak) phase in BiSe. Further analysis of the electronic structure reveals that the flat band comes from σ-bonded p_x and p_y orbitals of Bi atoms of the Bi_2 layer and is highly covalent in nature, which is evident from high localization of charge density within the bismuth bilayer (see Fig. 7.1(b)). Inclusion of SOC in the calculation splits the degeneracy of the flat conduction band along Γ-A (see Fig. 7.3(b) and also Fig. 7.4(c) & Fig. 7.4(d)) and opens up gaps at all k-points in the BZ which facilitates the calculation of Z_2 invariant, as the

occupied VB and unoccupied CB manifolds are separated by a local gap everywhere in the BZ [14]. Thus, SOC makes BiSe an indirect band gap semiconductor (band gap $\sim$ 42 meV) with its valence band maximum (VBM) and conduction band minimum (CBM) appearing respectively along A-L and Γ-K directions.

7.4.2 Calculation of Z_2 invariants

As SOC opens up a local gap at every k-point in the Brillouin zone, it facilitates the calculation of Z_2 invariants, which effectively determines the topological nature of any material. The calculation of Z_2 invariants are further simplified by the fact that BiSe possesses centre of inversion. We determined the four Z_2 invariants $(\nu_0, \nu_1, \nu_2, \nu_3)$ following Fu and Kane's parity criteria [56]. In this method, four Z_2 invariants in 3D space can be calculated from the product of the parity eigenvalues (σ_i, where i indicates a TRIM) of the occupied states at eight TRIM ($\Gamma, M_{1,2,3}, L_{1,2,3}$ and A, see Fig. 7.2(a)) in the BZ. Among the four topological indices, ν_0 is the strong topological index which can be calculated by taking the product of the parities at all eight TRIM through the relation $(-1)^{\nu_0} = \prod_{i=1}^{8} \sigma_i = \sigma_\Gamma \sigma_{M_1} \sigma_{M_2} \sigma_{M_3} \sigma_{L_1} \sigma_{L_2} \sigma_{L_3} \sigma_A$. The other three weak topological indices $(\nu_k, k = 1, 2, 3)$ are determined based on the parity of the occupied states at four TRIM points which form a surface of the parallelepiped (marked in red color in Fig. 7.2(a)) excluding Γ point through the relation [59] $(-1)^{\nu_k} = \prod_{i=1}^{4} \sigma_i$. To be more specific, we used the following relations [59] to get ν_1, ν_2, ν_3: $(-1)^{\nu_1} = \sigma_{M_1} \sigma_{M_2} \sigma_{L_1} \sigma_{L_2}$, $(-1)^{\nu_2} = \sigma_{M_2} \sigma_{M_3} \sigma_{L_2} \sigma_{L_3}$, $(-1)^{\nu_3} = \sigma_{L_1} \sigma_{L_2} \sigma_{L_3} \sigma_A$. At the experimental lattice constant of BiSe, the product of the parity eigenvalues of BiSe at eight TRIM are σ_Γ=1, σ_{M_1}=-1, σ_{M_2}=-1, σ_{M_3}=-1, σ_{L_1}=1, σ_{L_2}=1, σ_{L_3}=1 and σ_A = -1. Hence, calculation of Z_2 invariant using the above relations reveals that BiSe belongs to Z_2 (0;001) class of weak TIs which is same as the topological class of other weak TIs Bi_2TeI [210] and KHgSb [59].

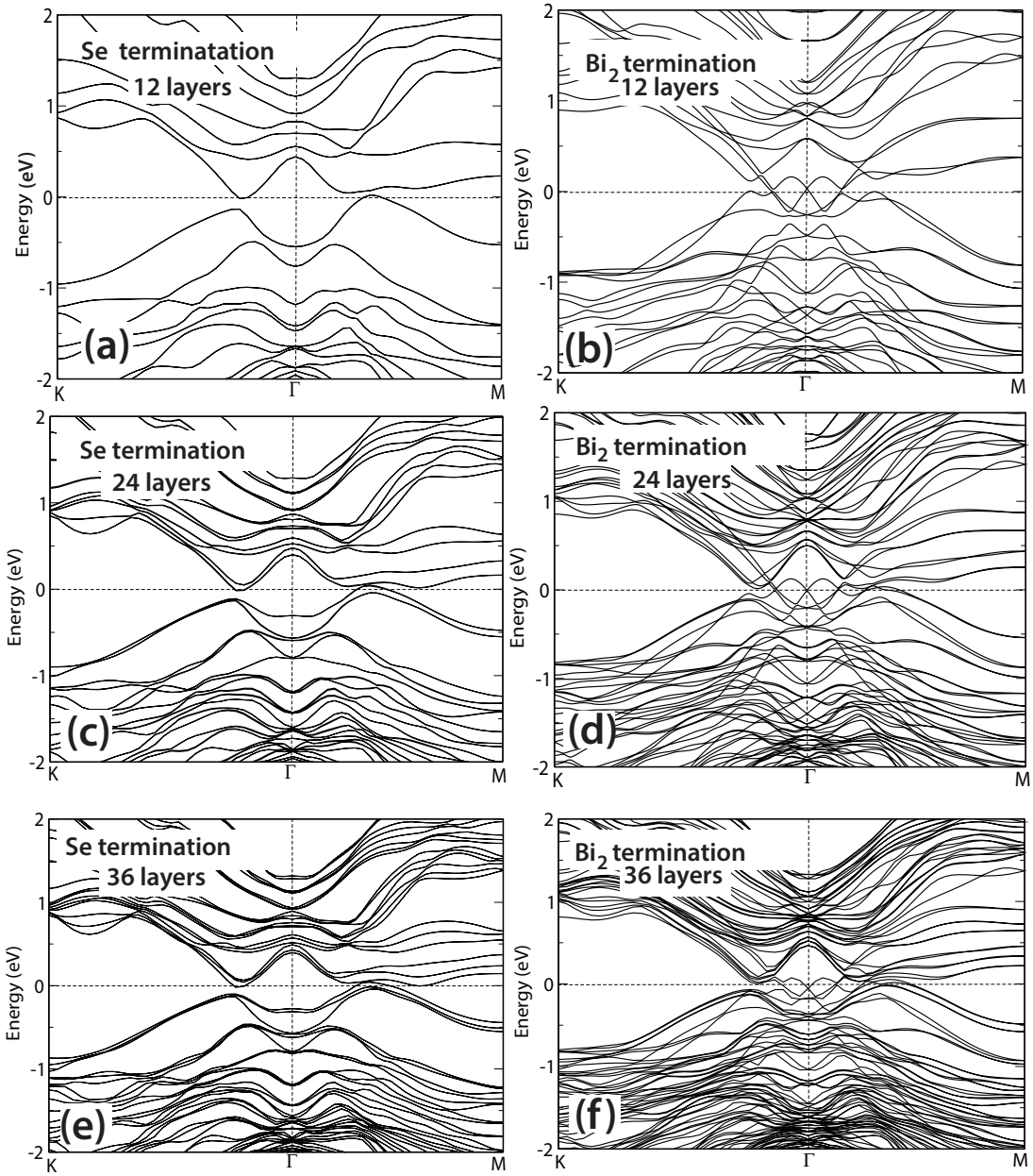

Figure 7.5: Electronic structure on (001) surface of BiSe for different surface terminations and thicknesses. (a,c,e) Se-terminated surface of BiSe shows absence of any linearly dispersing Dirac cone-like crossing, even when the the unit cell contains six quintuple layers of Bi_2Se_3. (b,d,f) Bismuth bilayer (Bi_2) terminated surface shows presence of a Dirac cone-like feature on their surface electronic structures, which are actually topologically trivial Rashba spin split states coming from the Bi_2 layers due to the presence of an internal electric field.

7.4.3 Surface electronic structure

Govaerts et al. [217] recently questioned the claim that bismuth bilayer terminated Bi_2Se_3 exhibits a single Dirac cone in the electronic structure of (001) surface [218]. They showed that the Dirac cone-like features on Bi_2 terminated surface actually corresponds to Rashba split states of the bismuth bilayer. These Rashba states arise from the presence of an internal electric field associated with polarity and charge transfer from Bi_2 layer to Bi_2Se_3 quintuple layers [217]. To verify their claim, we have calculated surface electronic structure of BiSe on both the (001) surface (*i.e.* perpendicular to the layer direction of BiSe) as well as on the side surface. As it was shown earlier that Bi or Se terminated surfaces of $(Bi_2)_m(Bi_2Se_3)_m$ systems are energetically equally preferable [217], for calculation on (001) surface, we used super cell of bulk hexagonal unit cell and considered both (a) Se and (b) Bi-bilayer terminations (see Fig. 7.1(c) & Fig. 7.1(d)). Se terminated surface electronic structures do not show any Dirac cone-like features (see Fig. 7.5(a), Fig. 7.5(c) and Fig. 7.5(e)) but Bi-bilayer terminated surface exhibits linearly crossing bands which resemble Dirac cones on the (001) surface (see Fig. 7.5(b), Fig. 7.5(d) and Fig. 7.5(f)). The Dirac cone-like feature on Bi bilayer terminated surface was misinterpreted as topological surface Dirac cone [218]. However, it was later found to be originating from the Bi_2 layer as a result of an internal electric field due to the charge transfer from the bismuth bilayer to the Bi_2Se_3 quintuple layers [217]. As Bi_2Se_3 requires minimum four QLs to exhibit nontrivial topological properties (*e.g.*, gapless topological surface Dirac cone) [217], we have gradually increased the thickness of the hexagonal super cell from 12 layers to 36 layers which accommodates 6 QLs of Bi_2Se_3 and 3 bismuth bilayers. Our systematic analysis of the surface electronic structures are given Fig. 7.5. Presence of linearly dispersing Dirac cone-like features on Bi_2 terminated surfaces electronic structures and absence of it on the Se terminated surfaces clearly prove that observed Dirac cones in Fig. 7.5(b), Fig. 7.5(d) and Fig. 7.5(f) are not topologically nontrivial, in agreement with the claim of Govaerts et al. [217]. In order to know, whether bismuth bilayer is giving rise to any Dirac cone on (001) surface, we have calculated surface electronic structure of a

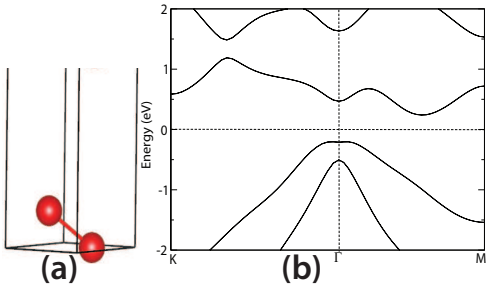

Figure 7.6: Unit cell and surface electronic structure of a free standing bismuth bilayer. (a) Hexagonal unit cell of a free standing Bi_2 layer and (b) its electronic structure on (001) surface reveals an insulating phase of the bismuth bilayer.

free standing bismuth bilayer in the same hexagonal unit cell (see Fig. 7.6(a)) as that of BiSe, which reveals an insulating surface electronic structure (see Fig. 7.6(b)). Thus, our analysis shows that the composite system BiSe neither shows strong topological properties of Bi_2Se_3 [9] nor these of bismuth bilayers [219], instead it exhibits a weak topological insulating state belonging to (0;001) weak Z_2 topological class. To further confirm the weak topological nature of BiSe, we determined surface electronic structure on the (100) surface (*i.e.* yz-plane of the surface unit cell of BiSe, which reveals the presence of an even (two) number of Dirac nodes at $\bar{Y}$ and $\bar{T}$ points of the Brillouin zone (Fig. 7.3(c)). Similar to the case of another weak TI, Bi_2TeI [210], these two Dirac nodes appear on points ($\bar{Y}$ and $\bar{T}$) in the surface BZ, that are not the projections of Γ and A points of the bulk BZ, where band inversions take place.

7.5 Conclusions

With first-principles calculations based on density functional theory, we predict that BiSe belonging to the richly explored bismuth chalcogenide family is a weak topological insulator. Our calculations reveal that BiSe exhibits a pair of band inversions at the Γ and A points in its 3D Brillouin zone. Calculations of the Z_2 topological invariants which are (0:001) confirms the WTI phase of BiSe with. We further confirm the WTI phase through calculation of electronic structure on the side surface, that reveals an even number of Dirac points.

Part IV

Thermoelectric Properties of Topologically Nontrivial and Related Materials

Chapter 8

Thermoelectric Properties of Materials with Nontrivial Electronic Topology *

8.1 Introduction

In recent years, thermoelectric (TE) materials have been a subject of significant research activity [220, 221], as they convert wasted energy in the form of heat into electricity, and provide an environment friendly all-solid state alternative to cooling technologies like refrigeration [222, 223]. Thermoelectric power generators have also been used for long in space missions. The Seebeck coefficient (S), a measure of the thermoelectric property, relates an electrical potential difference created from a temperature gradient in a TE material. Materials with large S can be versatile and robust for waste-heat recovery from various scenarios such as automobile exhaust systems, industrial furnaces, gas pipes etc. Recently, efficient conversion of solar energy to electrical energy has also been demonstrated using thermoelectric Seebeck effect [221].

The thermoelectric figure of merit (zT) is defined as, $zT = \sigma\ S^2\ T/\kappa = P\ T/\kappa$, where

*This work has been published in J. Mat. Chem. C **3**, 12130 (2015) [197]. Reproduced with permission from the Royal Society of Chemistry.

σ is the electrical conductivity, κ is the thermal conductivity and $P(= S^2\sigma)$ is the thermoelectric power factor. Unlike many other important functionalities like piezoelectricity, ferroelectricity and multiferroicity, thermoelectricity is not restricted by any symmetry of a material. However, materials with efficient thermoelectric conversion ability are hard to engineer due to conflicting requirements like low thermal conductivity (κ) and high electrical conductivity (σ), and also competing factors such as carrier concentration and effective mass [220], which are evident in the expressions of S and σ,

$$S = \frac{8\pi^2 k_B^2 T}{3eh^2} m^* \left(\frac{\pi}{3n}\right)^{\frac{2}{3}} \tag{8.1}$$

and

$$\sigma = \frac{ne^2\tau}{m^*}, \tag{8.2}$$

where k_B, T, m^*, n and τ are Boltzmann constant, temperature, effective mass, carrier concentration and relaxation time respectively. While both S and σ occur in the numerator of the expression for zT, they show opposite trends with effective mass and carrier concentration. Moreover, in metal the electronic contribution to thermal conductivity (κ_{ele}) is also linked to σ via the Wiedemann-Franz law [224] and effective mass of the charge carriers.

The dependences of S and σ on the density of states (DOS) at Fermi energy (E_F) are also, to a certain extent, conflicting. The dependence of S on local DOS at the Fermi level is captured by the Mott expression which, in general, holds for metals [225], but it is also applicable for semiconductors for which the Fermi level lies within a narrow region inside the density of states, where it increases locally [226].

$$\begin{aligned} S &= -\frac{\pi^2 k_B^2 T}{3e} \left\{ \frac{d[ln(\sigma(E))]}{dE} \right\}_{E=E_F} \\ &= -\frac{\pi^2 k_B^2 T}{3e} \left\{ \frac{1}{N}\frac{dN(E)}{dE} + \frac{1}{\mu(E)}\frac{d\mu(E)}{dE} \right\}_{E=E_F}, \end{aligned} \tag{8.3}$$

where energy dependent conductivity $\sigma(E)$, which is generally known as the transport

distribution function is given by,

$$\sigma(E) = D(E)f(E)e\mu(E) = N(E)e\mu(E), \tag{8.4}$$

where $D(E)$, $f(E)$, $\mu(E)$ denote energy dependent DOS, Fermi-Dirac distribution function and charge carrier mobility respectively, and $N(E) = D(E)f(E)$ denotes the carrier concentration. From Eq. (8.3), we see that a large S can be achieved by increasing $[\frac{dN(E)}{dE}]$, which in turn is caused by a local enhancement of $D(E)$ [92].

Recently, materials with good thermoelectric properties, such as Bi_2Te_3 and PbTe, have been discovered also to exhibit nontrivial electronic topology at ambient [9, 157] and/or applied pressures [227]. Materials with nontrivial electronic topology are novel quantum states of matter which exhibit exotic and robust conducting surface states as a consequence of nontrivial topology of the electronic structure in their bulk form. It appears that materials exhibiting a nontrivial electronic topology or high thermoelectric figure of merit often comprise of heavy elements and possess small band gaps [228]. Heavy atoms have low frequencies of vibration that result in low lattice thermal conductivity essential for a high thermoelectric figure of merit. They also exhibit large spin orbit coupling necessary for certain nontrivial topological materials. In addition, topological insulators (TIs) often have a small electronic band gap as they lie in the vicinity of a strain dependent electronic topological transition (ETT). This helps in tuning the intrinsic carrier concentration to optimize the thermoelectric power factor.

Other features of electronic dispersions of a topologically nontrivial material may also be used favorable to enhance thermoelectric efficiency [229, 230]. For example electronic structure of SnTe, which is a topological crystalline insulator (TCI), exhibits a heavy hole band near its light hole valence band maximum (VBM). Energy of the light and heavy hole bands can be brought closer (a phenomenon known as band convergence [231]) through alloying [230, 232], to optimize carrier mobility and enhance thermopower (S). Furthermore, zT of TIs is strongly size dependent [233], taking values greater than 1

in nanoscale regime where the metallic surface states become more relevant to electric conduction. Clearly, the electronic structure of topologically nontrivial materials seems to have a great potential for efficient thermoelectric transport, and they may possess a high P even in the semi-metallic or small band gap regime. Here, we focus on determination of P of materials belonging to different classes of nontrivial topology, and uncover the correlation between the two.

We use semi-classical Boltzmann transport theory within a constant scattering time approximation (see section 2.7) to calculate the transport properties S, σ and P. As E_F is tunable by doping, we calculate S, σ and P of the compounds over a wide energy window ($\sim$ 1.6 eV) straddling the undoped E_F. Our calculations suggest that a high zT in typical TE materials such as Bi_2Te_3 does not arise just from the strongly dispersing valence band (VB) and conduction band (CB) edges associated with the TI phase, but similar to ordinary band insulators (BIs), the TE properties of TIs too depend strongly on their density of states close (typically within $\sim$ 0.5 eV) to the Fermi level. With vicinity to strain-driven ETT, the TE properties of TIs (or corresponding BIs) are quite sensitive to strain. We demonstrate this for β-As_2Te_3, where applied strain not only closes the band gap but also aides in the band convergence to increase P by as a factor of 3. Our calculations reveal that PbTe exhibits better TE performance in its TCI phase than its BI phase. Contrary to naive expectation, our calculations also indicate that n-doped TaAs could be a promising thermoelectric with a high power factor.

8.2 Materials with nontrivial electronic topology

Nontrivial electronic topology of a material often arises from the spin-orbit coupling (SOC) that as strong relative to crystal field splitting (*e.g.*, Z_2 topological insulator [9]), which results in reordering or interchange of valence and conduction bands of distinct symmetries in a phenomenon known as band inversion. Certain crystallographic symmetries give rise to nontrivial topological phases in which symmetry protected linearly dispersing valence

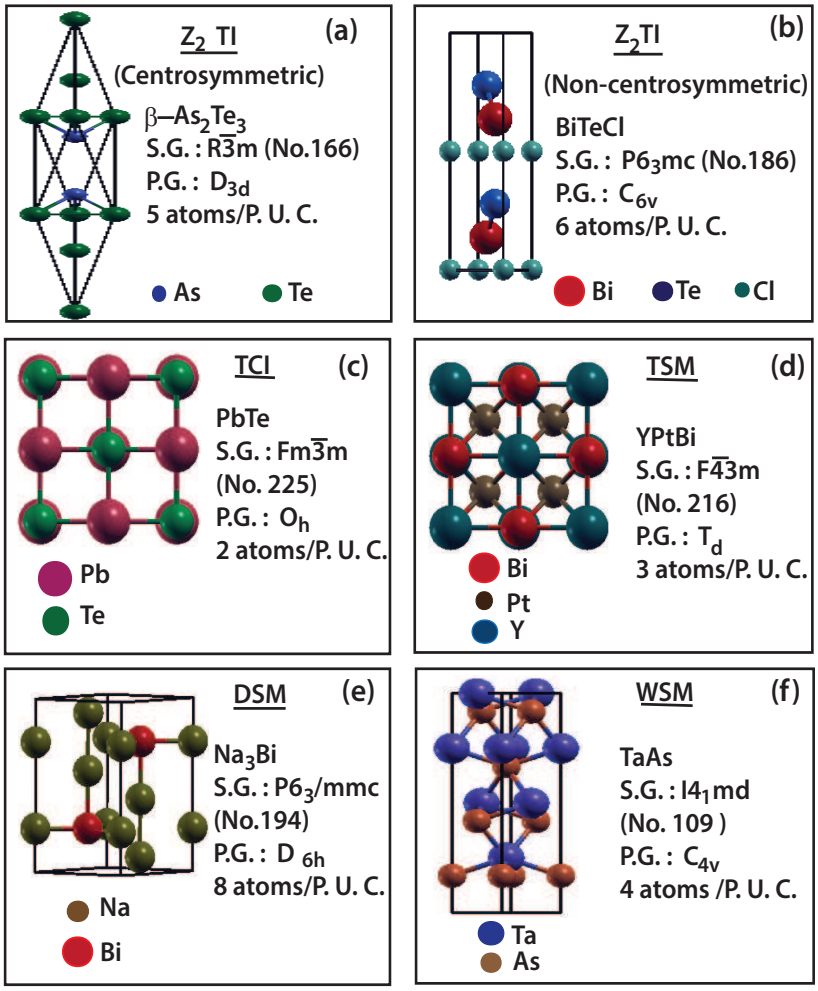

Figure 8.1: Crystal structures, space group (S.G.), point group (P.G.) symmetries of the six materials used in this work. The abbreviations TI, TCI, DSM, TSM, and WSM stand for topological insulator, topological crystalline insulator, Dirac semimetal, topological semimetal, and Weyl semimetal respectively. P.U.C stands for primitive unit cell.

and conduction bands cross in the electronic structure of a bulk material (*e.g.*, Dirac semimetal [47, 165], Weyl semimetal [52]), and gapless conducting states appear on its surface [43]. Depending on the dispersion of electronic bands near the Fermi level or gap of the bulk, surface states and their origin, we consider here six categories of topologically nontrivial materials: (a) Z_2 TI (centrosymmetric), (b) Z_2 TI (non-centrosymmetric), (c) TCI, (d) topological semimetal, (e) Dirac semimetal and (f) Weyl semimetal, and identify the correlation between their electronic topology and thermoelectric performance, if any.

A Z_2 TI exhibits a non-zero band gap in its bulk electronic structure, and gapless surface states with linearly dispersing bands forming a Dirac cone (or in odd numbers)

that typically falls in the bulk band gap, which are protected by time reversal symmetry. In the TCI class of materials, crystal symmetry and field play more significant role than time reversal symmetry and SOC [43]. For example, SnTe (a TCI) has a mirror symmetry in its crystal structure, due to which it exhibits even number of band inversions (as a function strain or pressure which modifies the relative strength of hybridization and crystal field splitting) in the electronic structure of its bulk. The robust surface states in this class of materials are protected by the mirror symmetry. In topological semimetals, VBM and CBM touch each other to give a semimetallic state, and the dispersion of bands is often quadratic at the touching point. In this class, the electronic structure possess an inverted band order (as in HgTe) of the VBM and CBM compared to their band insulator counterpart (as in CdTe) [234]. Materials with C_3 , C_4 or C_6 uniaxial rotational symmetries can host Dirac semimetallic states [169]. In a Dirac semimetal, a pair of doubly degenerate and linearly dispersing bands of different symmetries cross each other giving rise to a robust Dirac cone in their bulk electronic structure. In materials with broken spatial inversion or time reversal symmetries, the doubly degenerate bands become non degenerate due to SOC. Despite these broken symmetries, if the non-degenerate bands make robust linear crossing, the material is a Weyl semimetal in which the point of crossing is doubly degenerate and is called a Weyl node.

We choose six materials belonging to six different categories as mentioned earlier and summarize their structural features in Fig. 8.1. Amongst the materials studied here, β-As_2Te_3 has a rhomobohedral crystal structure with space group $R\bar{3}m$ (No. 166), which becomes a Z_2 TI at high pressure ($\sigma_{zz} > 1.77$ GPa) [118]. PbTe, which has a rocksalt structure with space group $Fm\bar{3}m$ (No. 225) undergoes electronic topologically transition with pressure and becomes a TCI (for P> 4 GPa) [227]. Na_3Bi, with space group $P6_3/mmc$ (No. 194), is a Dirac semimetal in its native state [165], BiTeCl with space group $P6_3mc$ (No. 186) is a large band gap non-centrosymmetric Z_2 TI [157], and YPtBi in Half-Heusler structure with space group $F\bar{4}3m$ (No. 216) is a topological semimetal with vanishing gap [179]. Non-centrosymmetric TaAs crystal with space group $I4_1md$

(No. 109) is a Weyl semimetal [52] at ambient pressure. Amongst these compounds, to the best of our knowledge, thermoelectric properties of only β-As_2Te_3 and PbTe have been investigated [226, 231, 235], albeit in their ambient pressure band insulating phases. Here, We determine the transport properties of β-As_2Te_3 and PbTe in both the BI and TI phases and other compounds in their topologically nontrivial phases. The thermoelectric performance of the electronically nontrivial topological phases of β-As_2Te_3, PbTe, BiTeCl, YPtBi, Na_3Bi and TaAs is assessed by comparing their power factors with that of band insulating PbTe which is an established high zT TE.

8.3 Computational methods

We employ a full potential linearized augmented plane wave (FPLAPW) based method as implemented in the WIEN2k code [128] to determine the electronic structure and properties of all the materials presented here. To obtain the total energy and eigenvalues of the electrons in a solid using FPLAPW method, we use a basis set achieved by dividing the unit cell into non overlapping spheres centered around each atom and the interstitial regions. Plane wave basis set is used to represent wave functions inside the interstitial region, which is augmented by the atomic-like wave function inside the spherical region around each atom. We use Perdew, Burke and Ernzerhof parametrization [114] of the exchange correlation energy functional derived within a gradient generalized approximation [113]. Truncation of the plane wave expansion of electronic wave functions inside the interstitial region is specified by R_{mt}*K_{max}, where R_{mt} is the radius of the smallest atomic sphere (muffin-tin), K_{max} is the plane wave cut-off vector. Charge density cut-off is specified by G_{max}. The cut-off values for the wave functions and charge density are summarized in Table 8.1. In all the calculations, we have included spin-orbit coupling through the second variational procedure [82, 83], and electronic structure (see Fig. 8.3) of the each of the materials is determined at the lattice constants (see Table 8.1) by including the SOC in the Kohn-Sham Hamiltonian. We use the density functional theory

(DFT)-based electronic structure within a semi-classical Boltzmann theory under a constant scattering time approximation as implemented in the BoltzTraP code [94], and calculate electrical conductivity ($\sigma_{\alpha\beta}$), Seebeck coefficient ($S_{\alpha\beta}$) and power factor of the six materials described earlier (also see Fig. 8.1) as a function of Fermi energy (E_F) and temperature (T). Band energies are determined on a dense mesh (40,000) of k-points for sampling the Brillouin zone for each of the materials. The actual calculation uses the symmetry and k-points only in the irreducible wedge of the corresponding Brillouin zone (see last column of Table 8.1). To achieve better fit between the Fourier interpolated energies($\bar{\varepsilon}_i(\mathbf{k})$) and DFT-calculated band energies ($\varepsilon_{i,k}$), the original grid of k-points was interpolated onto a k-mesh five times as dense. We calculate the transport properties using strained † lattice constants for β-As_2Te_3 and PbTe (at which they become TI and TCI respectively) and experimental lattice constants for Na_3Bi, BiTeCl, YPtBi and TaAs (see Table 8.1).

8.4 Results

We determined transport properties namely σ, S, and P (see Fig. 8.2) within a rigid band approximation (RBA) in which the electronic structure is assumed to be unchanged with doping. This approximation is reasonably good for low doping concentrations and is commonly used for theoretical study of TE materials [93, 94, 236–239]. Effects of doping concentration are thus determined essentially through the corresponding changes in the Fermi energy. To this end, we show the dependence of density of states on energy and of S, σ, $S^2\sigma$ on Fermi level (E_F), keeping E_F of the undoped compounds fixed at 0 eV. A positive E_F signifies n-type doping, while a negative E_F means p-type doping. The type of doping is also reflected in the sign of the Seebeck coefficient (S). Generally, S peaks at small doping levels and approaches values close to zero at large concentrations. Electrical conductivity (σ) depends directly on the DOS, thus behavior of $\sigma(E_F)$ and DOS ($D(E)$)

† β-As_2Te_3 and PbTe are band insulators at ambient conditions. Here, we calculate the transport properties at ϵ_{zz} = -0.07 and ϵ_h= -0.01 for β-As_2Te_3 and PbTe, respectively, where they are in topologically nontrivial states

Material	Lattice constants (Å)	E_g (eV)	R_{mt}(a.u.)	K_{max} (a.u.$^{-1}$)	G_{max} (Ry$^{\frac{1}{2}}$)	N_I
β-As_2Te_3	a=4.089 c=28.184*	0	2.5 for As & Te	2.8 for As & Te	12.0	1563
PbTe	a=6.374*	0.10	2.0 for Pb & Te	3.5 for Pb & Te	12.0	1059
Na_3Bi	a=5.459, c= 9.675	0	2.0 for Na & Bi	3.5 for Na & Bi	12.0	1936
BiTeCl	a=4.2426, c= 12.397	0.48	2.5 for Bi, Te, & Cl	2.8 for Bi, Te, & Cl	12.0	1944
YPtBi	a=6.64	0	2.5 for Y, Pt, & Bi	2.8 for Y, Pt, & Bi	12.0	1059
TaAs	a=3.437, c=11.646	0.032	2.48 for Ta 2.36 for As	2.82 for Ta 2.97 for As	12.0	2835

Table 8.1: Structural parameters and cutoffs defining basis sets used in WIEN2k density functional theory (DFT) calculations of six materials that exhibit electronic structure with nontrivial topology. We use experimental lattice constants of all the compounds except for β-As_2Te_3 and PbTe which are trivial insulators at ambient pressure (marked with $*$ in the table). We use lattice constants of β-As_2Te_3 and PbTe obtained with uniaxial strain ϵ_{zz} = -0.07 and isotropic strain (ϵ_h) = -0.01 respectively. E_g is the smallest band gap, values of R_{mt}, K_{max} and G_{max} are used in defining the basis sets, and N_I is the number of inequivalent k-points in irreducible wedge of the Brillouin zone (IBZ) of each of the materials when the full Brillouin zone is sampled with 40,000 k-points.

are very similar.

The TE power factor $P = S^2\sigma$ is noticeably large and exhibits multiple peaks in the energy window chosen. We classify these peaks into three categories (type-I, type-II and type-III) based on their origin and assess their relevance to applications by their proximity to the undoped Fermi level (see Table 8.2). The type-I peak occurs for doping concentrations where $D(E)$ (and correspondingly $\sigma(E)$) is large (see Eq. (8.3)). The maximum of the peaks in the power factor of the materials studied here is invariably (except for strained PbTe) in the type-I peak. In most cases, the type-II peak in P occurs in the vicinity of the peak in S which is caused by a sharp energy dependence of $D(E)$ (*i.e.* large $\frac{\partial D(E)}{\partial E}$), and occurs close to the undoped E_F (for example in YPtBi). Though these peaks are smaller in magnitude, they are more relevant to applications as they correspond to modest doping. The type-III peak in P as a function of Fermi energy appears when maxima in both $[\frac{\partial D(E)}{\partial E}]$ as well as S are close to each other, and arise as a convolution

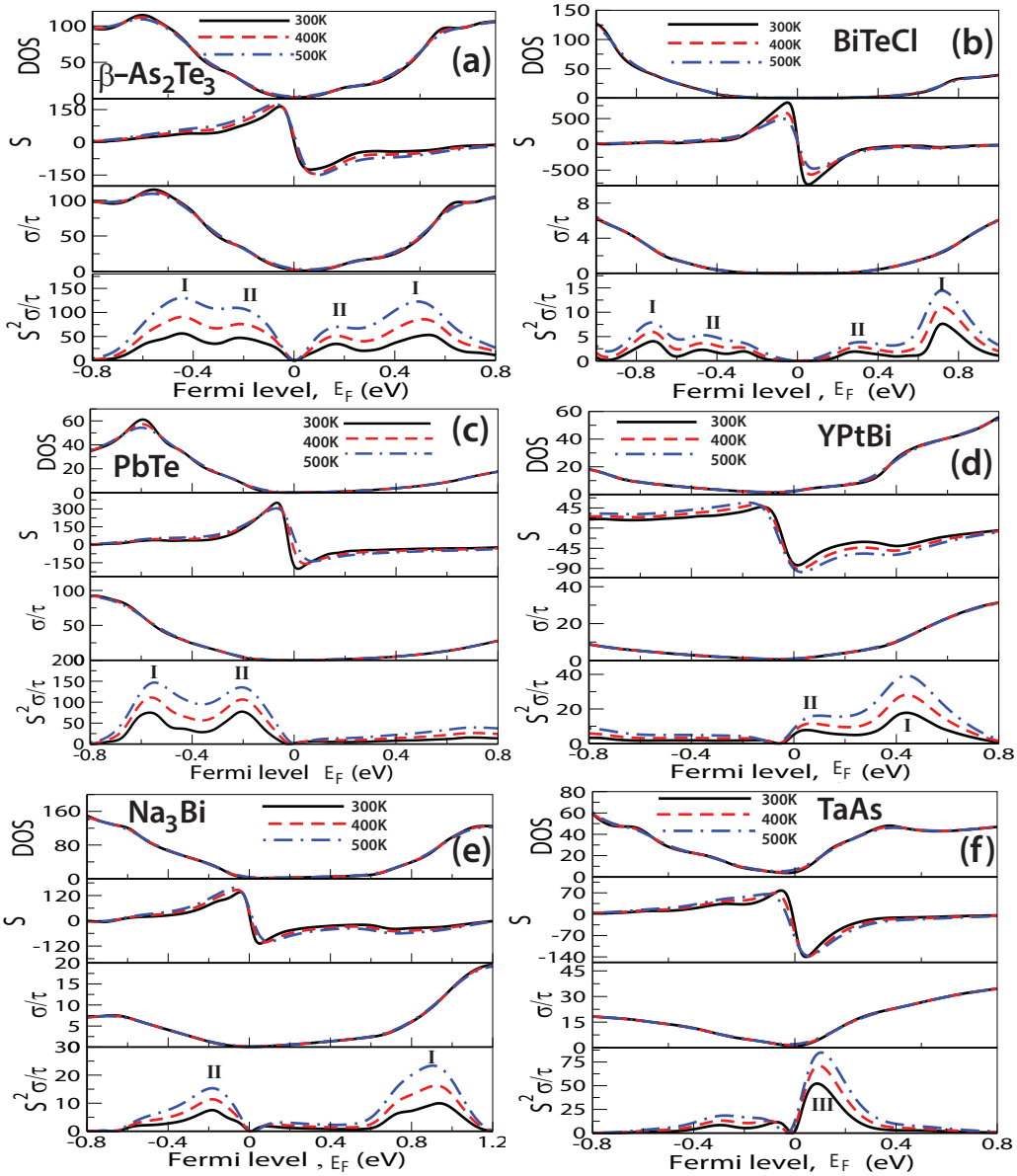

Figure 8.2: Dependences of density of state (DOS), electrical conductivity (σ/τ), Seebeck coefficient (S), power factor ($S^2\sigma/\tau$) on Fermi levels at different temperatures. Units for DOS, σ/τ, S, $S^2\sigma/\tau$ are number of states per eV per unit cell, $10^{17}\Omega^{-1}\text{cm}^{-1}\text{s}^{-1}$, μ V K^{-1} and $10^{14}\mu$ W cm^{-1}K^{-2}s^{-1} respectively. Type-I, type-II and type-III peaks are marked respectively with I, II and III either just above or below each peak in the power factor vs Fermi energy (E_F) graphs. Results for three different temperatures 300 K, 400 K and 500 K are indicated with black (solid line), blue (dashed line) and red (dash dotted line) colors respectively.

of type-I and type-II peaks. The power factors of all the compounds generally increase with temperature, though the required doping levels for maximal P depend only slightly on temperature. We now discuss the transport properties of each of the six compounds

in detail.

Material	Type of doping	Type of peak	E_{peak} (eV)	P_{max} at 300 K
β-As_2Te_3	p	I	-0.44	57
		II	-0.2	48
	n	I	0.54	53
		II	0.17	35
PbTe	p	I	-0.56	74
		II	-0.18	87
Na_3Bi	p	II	-0.18	7.5
	n	I	0.94	10
BiTeCl	p	I	-0.71	4
		II	-0.47	2.5
	n	I	0.72	8
		II	0.29	1.5
YPtBi	n	I	0.44	18
		II	0.05	8
TaAs	n	III	0.085	53

Table 8.2: This table summarizes different types of peaks which appear in the power factor (P) of the materials with their positions along the Fermi level (E_{peak}) marked with Roman numerals I, II, and III for type-I, type-II and type-III peaks respectively. Negative and positive values of the E_{peak} mean n and p-type doping. Local maximum in power factor (P_{max}) is given for each of the materials at 300 Kelvin in the unit of $10^{14}\mu W cm^{-1}K^{-2}s^{-1}$.

8.4.1 Band and topological insulators

Strained β-As_2Te_3 has an electronic structure with a vanishing band gap (see Fig. 8.3(a)). As a result, it has nonzero DOS throughout the energy window chosen (see Fig. 8.2(a)). Furthermore, its DOS is symmetric about the Fermi level. As a result, we find that its power factor is also roughly symmetrical, exhibiting two peaks (type-I and type-II) for the n-type doping and two peaks (type-I and type-II) for the p-type doping (see Fig. 8.2(a)). A maximum power factor of 57 $\times 10^{14}\mu W cm^{-1}K^{-2}s^{-1}$ is observed for p-type doping at E_F = -0.44 eV (see Table 8.2). In contrast, the maximum power factor of *unstrained* β-As_2Te_3 (see Fig. 8.4(b)) is relatively weaker ($\sim$ 40 $\times 10^{14}\mu W cm^{-1}K^{-2}s^{-1}$) occurring in the n-type region. The peaks in the p-doped region of unstrained β-As_2Te_3 are about 2.5

times weaker than those of strained β-As_2Te_3, showing the tunability of thermoelectric properties with strain, as is the tunability of electronic topology.

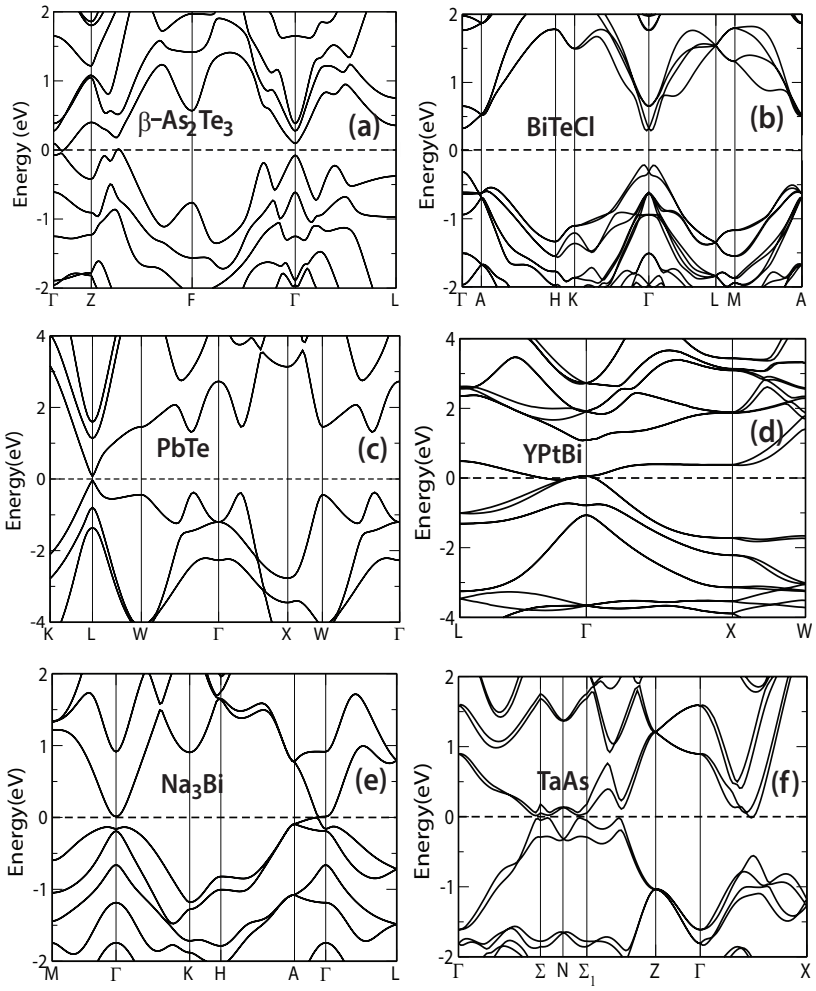

Figure 8.3: Electronic structure of the bulk of the six materials under consideration calculated with spin orbit coupling along the high symmetry directions of their Brillouin zones. Electronic structures for all these materials are calculated at their experimental lattice constants except for β-As_2Te_3 and PbTe for which their native states have trivial electronic topology (see Table 8.1).

Electronic structure of PbTe at the experimental lattice constant exhibits a zero band gap, which is far from its experimentally observed band gap of 0.3-0.4 eV. DFT calculations are known to generally underestimate electronic band gap (E_g), and this is further complicated here by the fact that gap depends on strain. An E_g is central to the TE properties of a material, we calculate the electronic structure of PbTe at applied isotropic strain $\epsilon_h = 0.02$ and ϵ_h = -0.01 (strain is applied with respect to the experimental lattice

constant, a_{exp}). At ϵ_h=0.02, PbTe is a band insulator (lattice constants; a_{BI}) with a band gap of 0.11 eV (see Fig. 8.4(c)) and at ϵ_h=-0.01, PbTe is in the TCI phase (lattice constant; a_{TCI}) with E_g=0.1 eV (see Fig. 8.3(c)). Remarkably, the dependence of power factor on doping concentrations is quite similar at both the lattice constants (see Fig. 8.2(c) and Fig. 8.4(d)). While P exhibits no peaks for n-type doping (see Fig. 8.2(c) and Fig. 8.4(d)), we find two peaks when the Fermi level enters the VB. As can be expected for PbTe, the peaks have high power factors with rather similar strengths (70-90 $\times 10^{14} \mu W cm^{-1} K^{-2} s^{-1}$) for both the band and topological insulating phases. We find that only type-II peak occurs around E_F= -0.18 eV (see Table 8.2), and therefore this is more relevant to achieving high performance TE experimentally. We also find that this peak is marginally stronger for topological insulating phase ($\sim$77 $\times 10^{14} \mu W cm^{-1} K^{-2} s^{-1}$) than for band insulating ($\sim$72 $\times 10^{14} \mu W cm^{-1} K^{-2} s^{-1}$), while their band gaps are similar. On applying larger compressive strains (ϵ_h = -0.014), band gap of PbTe widens further to 0.23 eV (see Fig. 8.5(a)) leading to enhancement in the type-II peak to $\sim$90 $\times 10^{14} \mu W cm^{-1} K^{-2} s^{-1}$ with large Seebeck coefficient, S (see Fig. 8.5(b)). This is rather interesting as the band gap of PbTe for ϵ_h= -0.014 is closer to the one observed experimentally, which is more appropriate to enhance zT of compounds with electronic structure similar to that of SnTe [230, 232].

BiTeCl is a large band gap (E_g = 0.5 eV) material (see Fig. 8.3(b)). Its conductivity is essentially zero for Fermi energy lying within the band gap (see Fig. 8.2(b)). Moreover, its DOS also grows very gradually on entering the VB and CB edges. It exhibits four peaks in its power factor, similar to β-As_2Te_3, with both n-type and p-type doping regions having both type-I and type-II peaks (see Fig. 8.2(b)). Among all the peaks, a maximum P (type-I) of 8 $\times 10^{14} \mu W cm^{-1} K^{-2} s^{-1}$ appears at E_F=0.72 eV in the n-doped region (see Table-II). Low value of P in BiTeCl practically rules it out from any thermoelectric applications.

8.4.2 Topological, Dirac and Weyl semimetals

Na_3Bi exhibits two types of peaks (type-I and type-II) in its power factor as a function of E_F. A maximum power factor (type-I peak) of 10 $\times 10^{14} \mu W cm^{-1} K^{-2} s^{-1}$ occurs at E_F=0.94 eV (see Table 8.2) for the n-doped region, while in the p-doped region it exhibits a type-II peak with a maximum power factor of 7.5 $\times 10^{14} \mu W cm^{-1} K^{-2} s^{-1}$ (see Table 8.2). Unlike strained β-As_2Te_3, the variation in its DOS with energy is rather weak, thereby leading to a relatively small S and P.

YPtBi is a zero band gap material and its DOS increases rather sharply at E_F= 0.44 eV due to the lowest conduction band which is flat (see Fig. 8.3(d)). However, due to its low S and σ, its thermoelectric power is rather small, with both type-I and type-II peaks in the n-doped region (see Fig. 8.2(d)). YPtBi belongs to the class of group IIIB-(Ni, Pd, Pt) type half-Heusler (HH) alloys [93], which, based on their n-type power factors, are expected to perform better as thermoelectric than the widely studied group IVB-Ni type HHs [240–243]. The maximum power factor (type-I peak) of YPtBi is 18 $\times 10^{14} \mu W cm^{-1} K^{-2} s^{-1}$, close to the maximum n-type power factors among HHs (LaPdBi with P of 25 $\times 10^{14} \mu W cm^{-1} K^{-2} s^{-1}$) [93]. Unlike other materials studied here, S of YPtBi increases with temperature, which could favor its use in high temperature thermoelectric transport applications.

TaAs has a very small band gap (0.032 eV), and it exhibits only a single type-III peak (maximum power factor of 53 $\times 10^{14} \mu W cm^{-1} K^{-2} s^{-1}$) in the power factor. This peak in P occurs at low concentration of n-type doping around E_F=0.085 eV. This single large peak arises from the coincidence of the maxima of S and $[\frac{\partial D(E)}{\partial E}]$. Maximum of P of this compound is similar in magnitude to the maximum P of β-As_2Te_3 (*i.e.* 57 $\times 10^{14} \mu W cm^{-1} K^{-2} s^{-1}$). Hence, we predict that that TaAs, whose TE properties is yet to explored experimentally, could be a high performance TE material.

8.5 Discussion

8.5.1 Multiple band extrema and sub-band structure

While bands associated with s and p-type orbitals are strongly dispersing, bands associated with d-orbitals are typically flat. Both types of dispersion play different roles in enhancing TE properties [244]. For example flat bands increase DOS and contain high effective mass charge carriers suitable for a large thermopower S (see Eq. (8.1)), whereas bands with a high curvature on the other hand contain light charge carriers favorable for electronic conductivity (see Eq. (8.2)). Amongst the compounds considered here, only YPtBi and TaAs contain transition metal (d-type valence electrons) atoms. Except for YPtBi however, bands of all other compounds are rather strongly dispersing (see Fig. 8.3). Despite this, we find a strong contrast in the TE properties of these compounds. For example, among Na_3Bi and strained β-As_2Te_3 with zero band gaps, Na_3Bi is a poor thermoelectric (see Fig. 8.2(e)), while strained β-As_2Te_3 (see Fig. 8.2(a)) exhibits a high P for both p and n type doping (see Table 8.2). To understand this, we compare the electronic structure of the two compounds (see Figs. 8.3(a) & 8.3(e)). We notice that the electronic structure of strained β-As_2Te_3 exhibits numerous extrema (peaks) in its electronic bands close to the Fermi level other than its VBM and CBM (see Fig. 8.3(a)). For example, it has valence band extrema (VBE) lying along the path Γ-Z-F-Γ-L paths. These VBE are within 0.3 eV below the Fermi level and enhance the DOS. These VBE also favor electronic conductivity as they contain light hole carriers, thereby enhancing P in both the ways. Undoped Na_3Bi does not exhibit VBE or conduction band extrema (CBE) (see Fig. 8.3(e)) around the Fermi level (within $\sim$ 1eV), and is relatively poorer TE.

Due to rather similar dispersion of electronic bands of most compounds studied here (except YPtBi), we identify the presence of these features of extrema in the electronic structure as the criterion for large power factor in topologically nontrivial materials. This is manifesting quite clearly in the electronic structure of PbTe and TaAs (see Fig. 8.3(c)

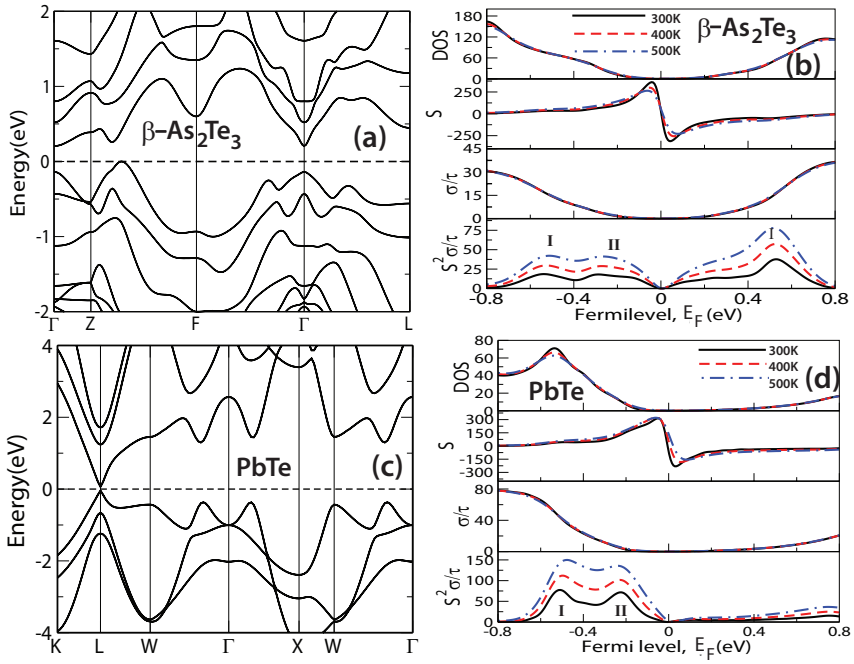

Figure 8.4: Electronic structure, density of states (DOS) and transport properties (S, σ, P) for unstrained β-As_2Te_3 (a, b) and strained (ϵ_h=0.02, a_{BI} = 6.567 Å, E_g = 0.11 eV) PbTe (c, d). a_{BI} is the lattice constant of the band insulating phase of PbTe. In (b) and (d) Type-I, type-II and type-III peaks in the power factors (P) are marked with Roman numerals I, II, and III, respectively. Results for three different temperatures 300 K, 400 K and 500 K are indicated with black (solid line), blue (dashed line) and red (dash dotted line) colors in (b) and (d), respectively.

and 8.3(f)) which exhibit significant P for only one type of doping (see Fig. 8.2(c) and 8.2(f)). This is due to the striking difference in DOS of VB and CB (see Fig. 8.2(c) and 8.2(f)) of these compounds. Similar to strained β-As_2Te_3 (see Fig. 8.3(a)), TaAs exhibits CBE along Σ_1-Z, Γ-X and VBE along N-Σ_1-Z, which enhance the DOS. Moreover, closely spaced peaks in the spin-split bands of TaAs along Σ-N-Σ_1 around the Fermi level could be controlled favorably towards band convergence, which can enhance TE performance. Similarly, PbTe exhibits VBE along W-Γ-X which gives rise to a sharp increase in its DOS (see Fig. 8.2(c)) of its VB. Power factor of YPtBi also exhibits moderate values only for n-type doping (see Table 8.2), due to large DOS of its CB however arising from a relatively flat d band just above the undoped Fermi level (see Fig. 8.3(d)). Thus, electronic bands of topologically nontrivial materials are usually strongly dispersing, and large values of P are observable mostly when the band structure has other VBE/CBE (or peaks) lying

close (within 0.5 eV) to the VBM/CBM.

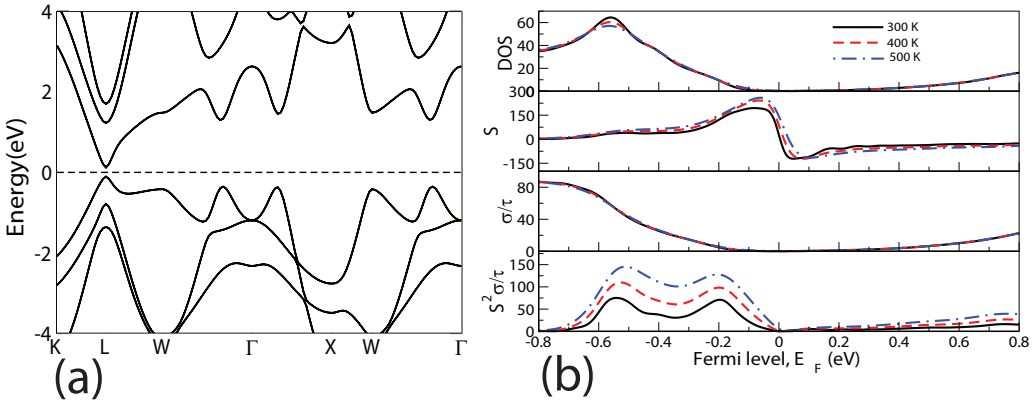

Figure 8.5: Calculated electronic structure and electronic transport quantities of PbTe with isotropic strain ϵ_h= -0.014 (a= 6.348 Å), applied with respect to the experimental lattice constant. At this value of the strain, PbTe is in the TCI state with band gap of 0.23 eV

8.5.2 Tunability with strain: ETT and convergence of bands

The thermoelectric power factors of TIs and TCIs are found to be quite sensitive to strain. Applying large enough compressive strains (ϵ_h=-0.014), thermoelectric power of PbTe increases from 72 $\rightarrow$ (see Fig. 8.4(d)) to 90 $\times 10^{14} \mu W cm^{-1} K^{-2} s^{-1}$ (see Fig. 8.5(b)) due to the widening the band gap (E_g) from 0.11 eV (see Fig. 8.4(c)) to 0.23 eV (see Fig. 8.5(a)). Our estimates of E_g at the experimental lattice constants of PbTe is 0 eV which is far from its experimental value, implying that the actual strains required to obtain larger band gaps in the TCI phase of PbTe might be a bit larger than the one estimated here (ϵ_h=-0.014). However, our results suggest a robust mechanism for enhancement of P in topologically nontrivial materials in general. Due to the phenomenon of band inversion, the CB and VB can be inverted and band gap of bulk TIs and TCIs can be closed and reopened with application of pressure or strain. This provides a unique way of controlling E_g of those materials which is central to their TE properties. E_g of a material undergoing an ETT can be increased upon application of appropriate compressive stresses, *irrespective* of whether they are in their BI or TI phases. Compressive stresses on TE modulators, which are typically flat devices, can be achieved readily by applying a mechanical load,

which is much more practical than application of shear or tensile stresses. Small E_g is a primary concern in materials such as SnTe (E_g = 0.18 eV at 300 K) which otherwise have suitable electronic structure for TE applications. As PbTe is in the vicinity of an ETT, its E_g can be tuned by applying external stresses. Thus, we argue that TE devices based on small E_g TIs/TCIs can operate more efficiently under mechanical loads.

Change in E_g of β-As_2Te_3 with strain (see Fig. 8.3(a) and Fig. 8.4(a)) results in considerable changes in its transport properties. While the maximum Seebeck coefficient (S_{max}) in strained β-As_2Te_3 (see Fig. 8.2(a)) decreases by 45% compared to S_{max} of unstrained β-As_2Te_3 (see Fig. 8.4(b)), its electrical conductivity (σ) increases by a factor of ~ 3. While P in the n-doped region remain similar, it increases by a factor of ~ 3 for p-type doping on application of uniaxial strain which shifts the maximum of the peaks in P from n-doped to p-doped region. This asymmetric increase in P is attributed to the stronger energy dependence of DOS of the VB of strained β-As_2Te_3. The origin of this enhanced DOS of strained β-As_2Te_3 lies in the convergence of valence bands induced by strain. The VBE like feature along Z-F-Γ paths of ambient β-As_2Te_3 converge into a smaller energy range on application of strain (ϵ_{zz} =-0.07), thereby increasing DOS near the VBM. As discussed above, strained β-As_2Te_3 also exhibits additional VBEs along Γ-Z-F-Γ-L, and exhibits superior thermoelectric properties. Experimentally synthesized β-As_2Te_3 doped with Sn, however, are intrinsically hole doped because of native defects and shows a maximum zT of 0.65 at 423K [235]. On the other hand, our calculations suggest that the asymmetric increase in P favoring p-type doping on application of uniaxial stress could increase zT of β-As_2Te_3 significantly.

Our analysis of TE performance of topologically nontrivial bulk phases of the materials does not include the effects of their conducting surface states. Secondly, the stress induced band convergence observed in β-As_2Te_3, may not be unique only to topological insulators. Thus, it would be interesting to identify conditions under which topological nontrivial phase of a material (*e.g.*, a TI) could outperform the corresponding trivial phase (*e.g.*, a BI) of the same compound. Based on our results, we believe that the TE performance of

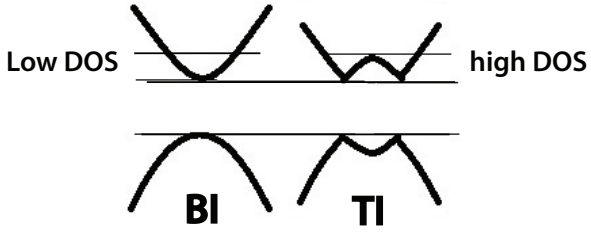

Figure 8.6: Schematic picture of band inversion between the valence band maximum (VBM) and conduction band minimum (CBM). Band insulator and topological insulator are denoted with BI and TI respectively. Due to band inversion, the density of states (DOS) near the Fermi level is higher in TI phase than that of band insulator.

a TI phases is better than its BI phase due to its electronic structure features associated with band inversion (see Fig. 8.6 for schematic of band edges associated with BI and TI phases). Band inversion in a TI phase lead to extra sharp edges in the DOS of its VB and CB, in addition to the VBM and CBM resulting in a higher DOS of the light carrier bands. Thus, this is one of the recipes for attaining a high power factors in bulk TIs.

Amongst the new materials investigated here, the maximum power factor of n-doped TaAs (see Fig. 8.2(f)) is similar (53 $\times 10^{14} \mu W cm^{-1} K^{-2} s^{-1}$) to that of good TE materials studied recently like β-As_2Te_3 [235] (which has a maximum power factor of 57 $\times 10^{14} \mu W cm^{-1} K^{-2} s^{-1}$, see Table 8.2). The electronic band gap of TaAs can be increased through suitable alloying which may enhance its TE power factor considerably. Furthermore, due to the heavy atomic masses of Ta and As and low frequencies of vibration, a low lattice conductivity is also expected, which would increase the zT of TaAs. Since the spin orbit coupling is often responsible for nontrivial electronic topology, many of the compounds with nontrivial topology involve heavy elements, and hence have low elastic moduli and thermal conductivity which add to their thermoelectric efficiency.

8.6 Summary

Our theoretical analysis of thermoelectric properties of topologically nontrivial materials reveals that (a) topological insulators with small band gaps are excellent TE, while Dirac

semimetals may not be quite so, (b) while topological semimetals exhibit relatively poorer TE power, a Weyl semimetal shows good TE power factor. We identify two mechanisms for the same: (i) due to band inversion occurring at an electronic topological transition of a topological nontrivial material, many local extrema appear in their valence and conduction bands, which enhance the density of electronic states and its asymmetry near the Fermi level resulting in enhanced conductivity and Seebeck coefficient, and (ii) energies of extrema in the VB and CB can be controlled with external strain leading to the phenomenon of band convergence, which is key to TE properties. Based on these mechanisms, the power factor exhibits multiple peaks (type-I, type-II and type-III) as a function of Fermi energy or doping, which can be tuned with strain. We demonstrated the phenomenon of band convergence in β-As_2Te_3 where compressive strains of about 7% result in enhancement of the power factor by a factor of 3 for p-type doping. Similar enhancement in the power factor of PbTe with compressive stresses suggests that TE modulators based on such TIs could operate more efficiently under small applied mechanical load. Among the topological and band insulating states of a compound with the same band gap, TE performance of the TI state is superior due to features in the electronic structure associated with band inversion. Finally, we predict that TaAs, a Weyl semimetal, is a promising TE and needs to be explored experimentally.

Chapter 9

Ultralow Lattice Thermal Conductivity in Group III Tellurides

9.1 Lone-pair Induced Rattling and Ultralow Lattice Thermal Conductivity in InTe*

9.1.1 Introduction

Thermoelectric materials have been a subject of intense research activity as they can convert wasted energy in the form of heat into useful electricity, providing environment friendly solutions to efficient energy management. The efficiency of a thermoelectric material is quantified by the dimensionless figure of merit, $zT = S^2\sigma T/(\kappa_l + \kappa_e)$, that depends on electrical conductivity (σ), Seebeck coefficient (S), lattice (κ_l) and electronic (κ_e) thermal conductivities, where T is the temperature. Due to the conflicting requirements of σ and S, one of the fundamental challenges in developing high-performance thermoelectric materials has been to achieve a simultaneous enhancement in thermoelectric power factor ($S^2\sigma$) and reduction in κ_l [245, 246]. Although significant reduction in κ_l can be achieved

*This work has been published in Angew. Chem Int. Ed. **55**, 7792 (2016) [201]. Reproduced with permission from the Wiley Online Library.

in a material through all-scale hierarchical architecture [206, 247] and endotaxial nanostructuring [246,248], finding materials with intrinsically low lattice thermal conductivity is of high practical interest due to their robustness against grain size and other structural variations. Intrinsically low κ_l are generally found in part-crystalline part-liquid-like materials [249], material having rattling modes [250, 251], and soft phonon modes [252].

Lattice anharmonicity and strong phonon-phonon interactions can induce intrinsically low κ_l in certain materials while preserving the carrier mobility [253, 254]. The origin of lattice anharmonicity and the ensuing ultralow κ_l in the I-V-VI2 chalcogenides such as $AgSbSe_2$ [255], $AgBiSe_2$ [256, 257], $AgBiS_2$ [258] has been traced to the electrostatic repulsion between the stereo-chemically active ns^2 lone-pair of group V cations and the valence p-orbital of group VI anions. Intrinsically low κ_l has also been observed in $Cu_{12}Sb_4S_{13}$ [259] and $PbCuSbS_3$ [260] arising from the bond anharmonicity caused by stereo-chemically active $5s^2$ lone-pair of Sb. The deformation of weak multicenter bonds in an electron-poor CdSb has been recently shown to cause lattice anharmonicity and thereby giving rise to a low lattice thermal conductivity [261]. Clathrates [262] and filled skutterudites [263] which bear the characteristics of phonon-glass-electron-crystal (PGEC) also exhibit very low κ_l. In these systems, a guest atom rattles within the over-sized host structural cages and scatters the heat-carrying acoustic phonons thereby significantly lowering κ_l. Hence, the exploration of new materials with intrinsically low lattice thermal conductivity along with a microscopic understanding of the underlying correlations among bonding, lattice dynamics and phonon transport is fundamentally important towards designing promising thermoelectric materials.

Our experimental collaborators, Manoj K. Jana and Dr. Kanishka Biswas from Jawaharlal Nehru Centre for Advanced Scientific Research, performed thermoelectric measurements [201] on high quality crystalline ingots of InTe, and they found ultralow lattice thermal conductivity ($\kappa_l \sim 0.4$ W/mK) in a temperature range of 300-650 K. Using first-principles calculations based on density functional theory, here, we showed that the presence of strongly anharmonic phonons originating from the rattling vibrations (along

the z-axis) of In^+ cations couple with the heat-carrying acoustic phonon modes and lead to an ultralow κ_l in InTe.

9.1.2 Crystal structure

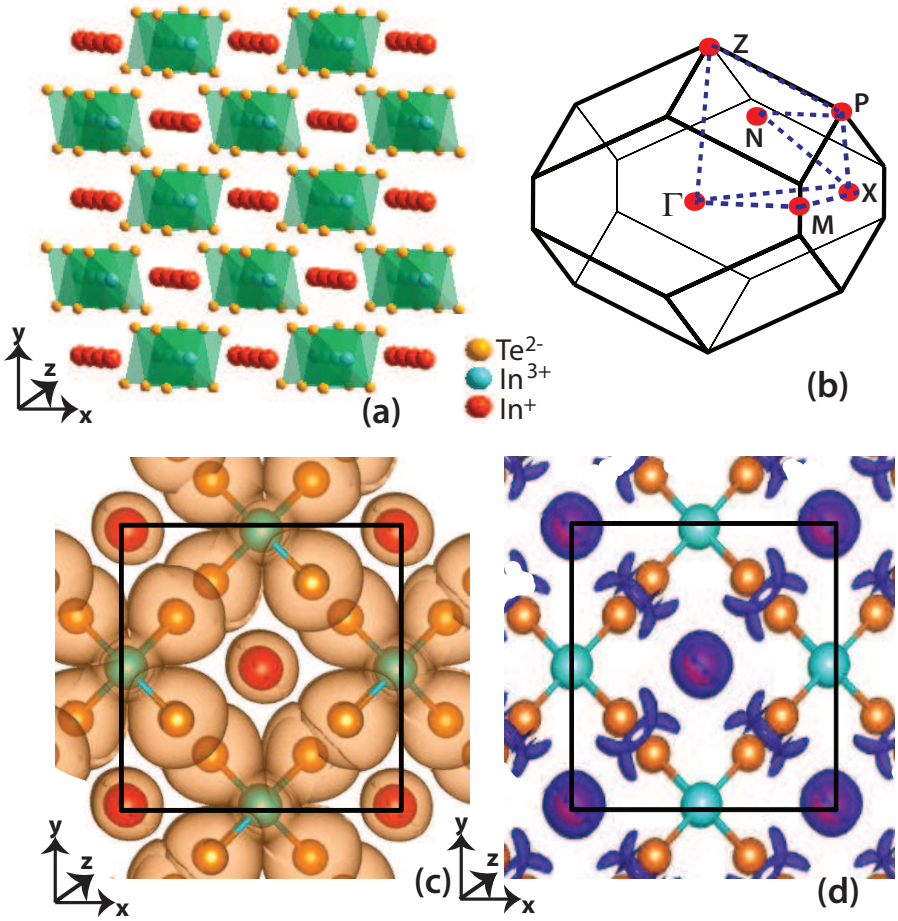

Figure 9.1: (a) Crystal structure of InTe showing chains of covalently bound, edge-sharing $In^{3+}Te_4^{2-}$ tetrahedra (green) alternating with chains of In^+ cations sitting at the centre of the hollow regions *i.e.* the Thompson cubes along z-axis. (b) Brillouin zone of the primitive unit cell and its high symmetry points. (c) Iso-surfaces of total charge density showing covalent bonding within the $In^{3+}Te_4^{2-}$ tetrahedron, and isolated In^+ cations at the body centre of the conventional tetragonal unit cell. (d) Electron localization function (ELF), plotted at an iso-value of 0.88, reveals a nearly spherical charge density around In^+ cation corresponding to its $5s^2$ electron lone-pair.

InTe, [*i.e.* $In^+In^{3+}Te_2^{2-}$], is a mixed valence compound belonging to tetragonal crystal family (space group: I4/mcm, No. 140) with a chain-like [264, 265] structure similar to TlSe [266]. The crystal of InTe has coexistent ionic and covalent substructures, where

In^{+} (4a Wyckoff site) and In^{3+} (4b Wyckoff site) cations occupy distinct crystallographic sites and possess different bonding environments. The trivalent In^{3+} cations form covalent (sp^3) In-Te bonds within the $In^{3+}Te_4^{2-}$ tetrahedra (see Fig. 9.1 (a)). These tetrahedra share their horizontal edges to form covalently bonded anionic substructure with a chain-like topology along the crystallographic z-axis. On the other hand, each monovalent In^{+} cation is surrounded by eight Te atoms in a distorted square antiprismatic arrangement which form skewed Thompson cubes [264, 265]. There are weak electrostatic interactions between the chains of In^{+} cations and the chains of $In^{3+}Te_4^{2-}$ tetrahedra.

9.1.3 Computational details

Our first-principles calculations are based on density functional theory (DFT) with Quantum espresso (QE) [112] implementation in which wave functions of the valence electrons are expanded in a plane wave basis, and their interaction with core electrons and nuclei is represented by pseudopotentials (we have employed norm-conserving type). We have treated electronic correlation energy with a generalized gradient approximated (GGA) [113] functional parameterized by Perdew, Burke and Ernzerhof [114]. We have truncated plane wave basis sets used in expansion of wave functions and charge density at energy cut offs of 60 Ry and 240 Ry, respectively. Integrations over the Brillouin zone are sampled on 9×9×9 uniform mesh of k-points with the occupation of electronic states smeared with Fermi-Dirac distribution function and a broadening of 0.003 Ry. We relaxed atomic positions in the unit cell at the experimental lattice constants (a=8.454 Å, c=7.152 Å) [175] of InTe, while we performed optimization with respect to lattice constants and atomic positions in simulations at 3 GPa. Lattice dynamical properties are calculated using a DFT linear response (density function perturbation theory [64]) as implemented in QE distribution. To determine the phonon dispersion, the force constant matrices are obtained on a 2×2×2 mesh of q-points, and are Fourier interpolated at an arbitrary q-vector. We use a primitive unit cell with eight atoms, and determine electronic structure and phonon dispersion along high symmetry lines in its Brillouin zone. We have

also calculated the Grüneisen parameters ($\gamma = -\frac{dln\omega}{dlnV}$ with ω and V being the phonon frequency and volume of the unit cell, respectively) that characterizes the relationship between phonon frequency and the volume change using a finite difference formula, giving an estimate of the strength of anharmonicity in the compound.

9.1.4 Theoretical analysis

Phonon dispersion of InTe calculated at its experimental lattice constant reveals a flat branch containing modes of imaginary frequencies (around -16 cm^{-1} at Γ point) along Γ-X-M-Γ directions of the Brillouin zone (Fig. 9.2(a)), which involve the displacement of only In^{+} cations along z-direction (see Fig. 9.2(d)). Another branch containing imaginary frequency (-28 cm^{1}) occurs at the Γ point, which involves anti-parallel displacements of In^{+} cations along the (±) z-directions and rotation of $In^{3+}Te_4^{2-}$ tetrahedra around zaxis through displacements of Te anions in the xy-plane (see Fig. 9.2(c)). These unstable modes necessarily involve collective rattling vibrations of In^{+} atoms (parallel to z-axis) within the columnar ionic substructure. The region of these instabilities in the Brillouin zone implies that (a) rattling motion involves displacement of about six In^{+} cations along the chain-direction, and (b) the In^{+} displacements in adjacent chains are random.

Directions	v_{TA1} (m/s)	v_{TA2} (m/s)	v_{LA} (m/s)	γ_{TA1}	γ_{TA2}	γ_{LA}
Γ-X	1671	1255	2187	5.2	1.64	1.74
Γ-Z	2111	911	3072	5.8	6	6
Γ-M	1533	1282	2167	0.41	1.7	2.1
Average	1771	1149	2475	3.47	3.11	3.28

Table 9.1: Sound velocities corresponding to the three acoustic branches of InTe along high symmetry directions in the Brillouin zone and their associated Grüneisen parameters. LA and TA denote longitudinal and transverse acoustic modes respectively.

The total charge density plot of InTe at the experimental lattice constant (see Fig. 9.1(c)) reveals strongly covalent In-Te bonds within the $In^{3+}Te_4^{2-}$ tetrahedron, as evident from its directionality between In^{3+} cation and the surrounding four Te^{2-} anions.

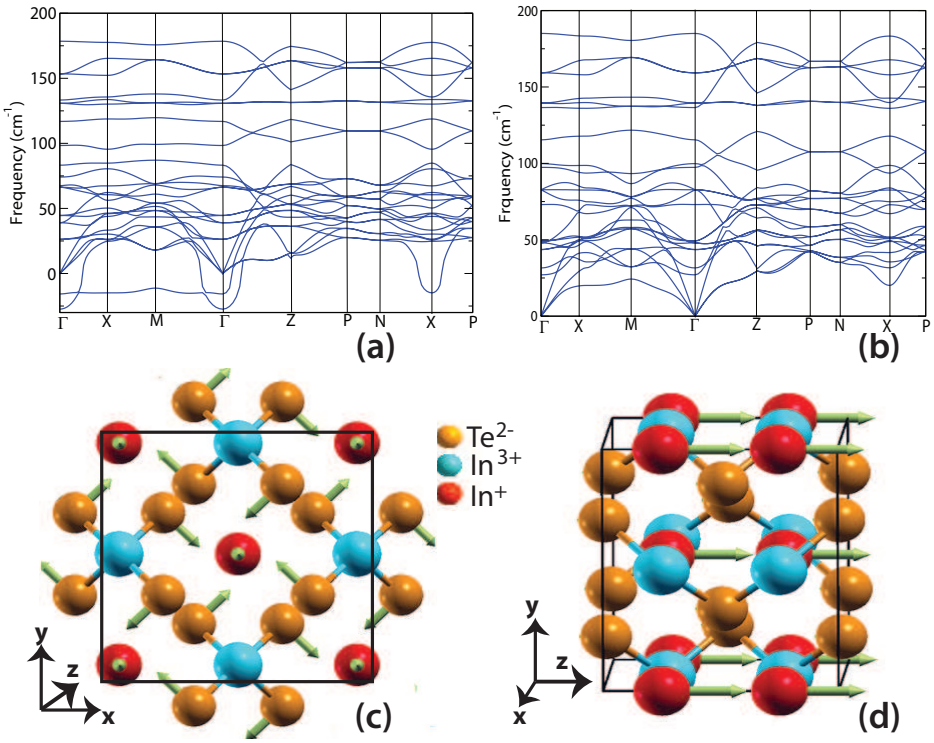

Figure 9.2: (a) Phonon dispersion of InTe at 0 GPa revealing two negative phonon branches with frequencies at -28 cm^1 and -16 cm^1 at Γ point; the associated atomic vibrations are shown in (c) and (d) respectively in the conventional tetragonal unit cell. (b) Phonon dispersion of InTe at 3 GPa showing no negative frequency modes.

Whereas, the In^+ cation at the centre of the hollow region (*i.e.* Thompson cube) remains chemically inactive and is surrounded by a uniform spherical charge density arising from the $5s^2$ lone-pair at the body centre of the conventional tetragonal cell. To confirm the presence of a lone-pair on In^+ cation, we calculated the electron localization function (ELF) of InTe (see Fig. 9.1(d)). ELF measures the degree of electron localization in a molecule or a solid with information of local influence of the Pauli repulsion. The ELF analysis shows a spherical electron localization around In^+ atoms, which is due to the $5s^2$ lone-pair of In^+, and a lobe-shaped asymmetrically localized electron cloud around Te^{2-}, which constitutes the $5s^2$ lone-pair of Te, hybridized partially as permitted by its site symmetry. The spherical shape of a lone-pair of an ion is known to cause its off-centering instability in a system [267]. Thus, the instabilities in the phonon spectrum originate from the $5s^2$ lone-pair around In^+ ions. On the other hand, the lobe-shaped lone-pair on

Te^{2-} ions causes their movement in the xy-plane (see Fig. 9.2(c)) giving the rotational instability. By shifting the atoms away from their equilibrium positions (along x- and z-directions), we find that the energy well of the In^{+} atom is very flat unlike In^{3+} and Te^{2-} atoms which sit in deep potential wells (see Fig. 9.3). The flatness of the potential well implies that In^{+} atoms are loosely bound to the lattice, resulting in large rattling vibrations along z-axis within the crystal structure, that scatters the heat carrying acoustic phonons.

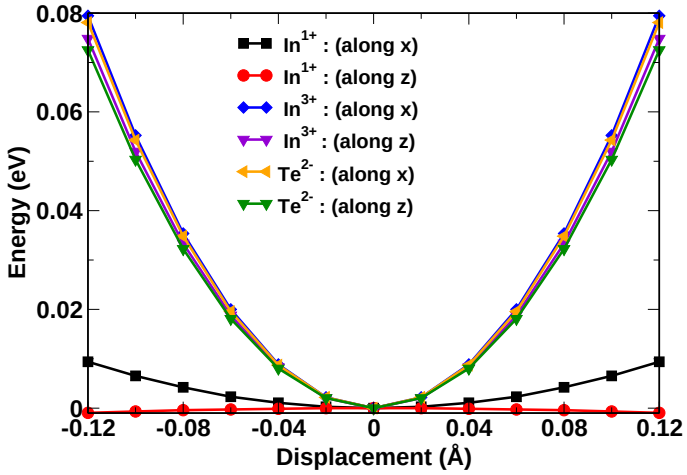

Figure 9.3: Calculated potential energy wells for all the atom types (In^{+}, In^{3+} and Te^{2-}) as a function of displacement about their equilibrium positions, along x- and z- directions.

The lattice thermal conductivity (κ_l) of a material depends on heat capacity (C_v), sound velocity (v) through the relation, $\kappa_l = \frac{1}{3}C_v v\tau$, where τ is the relaxation time. Our calculations of phonons show that the frequencies of acoustic modes are less than 50 cm^{-1} suggesting soft bonding and low sound velocities in InTe. Calculated sound velocities of InTe along Γ-X, Γ-Z and Γ-M directions are very low (see Table 9.1) , and hence their contribution to κ_l is weak. The ionic substructure with weakly bound In^{+} atoms results in large mode Grüneisen parameters (γ_i). As Umklapp (U) and normal (N) phonon scattering rates are proportional to γ^2, large values of γ_i reflect strong anharmonic phonon-phonon interactions [254] in InTe. Moreover the optical phonon instabilities ($\omega^2 < 0$) disappear in the phonon dispersion determined at a pressure of 3 GPa (see Fig. 9.2(b)), showing that the rattling optical modes are strongly anharmonic, and can scatter

the heat carrying acoustic phonons through phonon-phonon interactions to effectively reduce τ and κ_l of InTe.

9.1.5 Conclusions

In conclusion, we show that ultralow lattice thermal conductivity in InTe arises from the bonding asymmetry and lattice anharmonicity; In^{3+} cations covalently bond to Te atoms to form rigid substructure whereas weakly bound In^{+} cations rattle along the ionic substructure, resulting in large anisotropic atomic displacement parameters. The collective rattling vibrations of In^{+} cations manifest as weakly localized branches with imaginary frequencies in the phonon dispersion; they are strongly anharmonic and scatter the heat-carrying acoustic phonons to effectively lower κ_l.

9.2 Intrinsic Rattler-induced Low Lattice Thermal Conductivity in $TlInTe_2$

9.2.1 Introduction

Reduction of lattice thermal conduction in a crystalline solid without hampering its electrical conductivity by means of external doping is a difficult task in thermoelectric research. As materials exhibiting ultralow thermal conductivity are centric to the development of high performance thermoelectrics, which provide environment friendly solutions to cooling technologies [245] and hence, efficient energy-management. Thus, it is of paramount importance to design and discover materials with ultralow lattice thermal conductivity (κ_l). Although extrinsic strategies such as alloying and nanostructuring [247] have been shown to be very effective in suppressing the lattice thermal conductivity, sometimes they result in deterioration of electrical conductivity (σ) which is not desirable in designing materials with increasing thermoelectric efficiency. Hence, solids with intrinsically low lattice thermal conductivity are practically attractive being capable of offering nearly

independent control of κ_l over σ.

Lattice thermal transport in solids can be adequately described by theories based on scattering of phonons by grain boundaries, mass and strain fluctuations, and anharmonic phonon-phonon interactions (Umklapp processes). Recent investigations on minimal lattice thermal conductivity in certain thermoelectric solids have unveiled non-traditional phonon-scattering mechanisms *e.g.*, resonant phonon-scattering in filled-skutterudites [268], clathrates [269] with randomly rattling guest fillers, thermal damping due to liquid-like diffusive dynamics of a group of atoms in part-crystalline-part-liquid systems as exemplified by Cu_3SbSe_3 [249] and Cu_2Se [270]. A common characteristic of the above materials is the crystallographic heterogeneity with coexisting rigid and fluctuating sub-lattices. On the other hand, an intrinsically low κ_l in rock-salt I-V-VI chalcogenides [253–255] and $PbCuSbS_3$ [260] was ascribed to the strong lattice anharmonicity induced by ns^2 lone-pair of group V element. Other intrinsic phenomena leading to low κ_l include resonant bonding [271], rattling-modes [272], multicenter bonding [261, 273] and layered structure with significant anharnmonicity [274]. Hence, a thorough microscopic understanding of the underlying correlations amongst structure, chemical bonding and lattice dynamics together with their impact on phonon transport is highly desirable to explore and design materials with low lattice thermal conduction.

Learning from the results in section 9.1 that, in InTe (*i.e.* $In^{+}In^{3+}Te_2^{2-}$), it is the In^{+} atoms whose rattling motions along z-direction induce ultralow lattice thermal conductivity, we are intrigued to examine κ_l in an iso-structural compound $Tl^{+}In^{3+}Te_2^{2-}$ in which heavier Tl atoms replace the In^{+} atoms in the crystal structure. Experimental measurements of lattice thermal conductivity on $TlInTe_2$ by Manoj K. Jana from Dr. Kanishka Biswas's group at Jawaharlal Nehru for Advanced Scientific Research, reveals that like InTe, this compound too exhibit an ultralow κ_l (< 0.5 W/m.K) in the 300-673 K range, which remains close to the theoretical minimum limit. Using first-principles calculations based on density functional theory, we have investigated here the aspects of structure and lattice dynamics responsible for the low κ_l in $TlInTe_2$. Our calculations reveal that Tl^{+}

cations exhibit rattling dynamics driven by lone-pair repulsion and strong phonon-phonon interactions, which scatter the acoustic phonons, thereby causing low κ_l in $TlInTe_2$.

9.2.2 Crystal structure

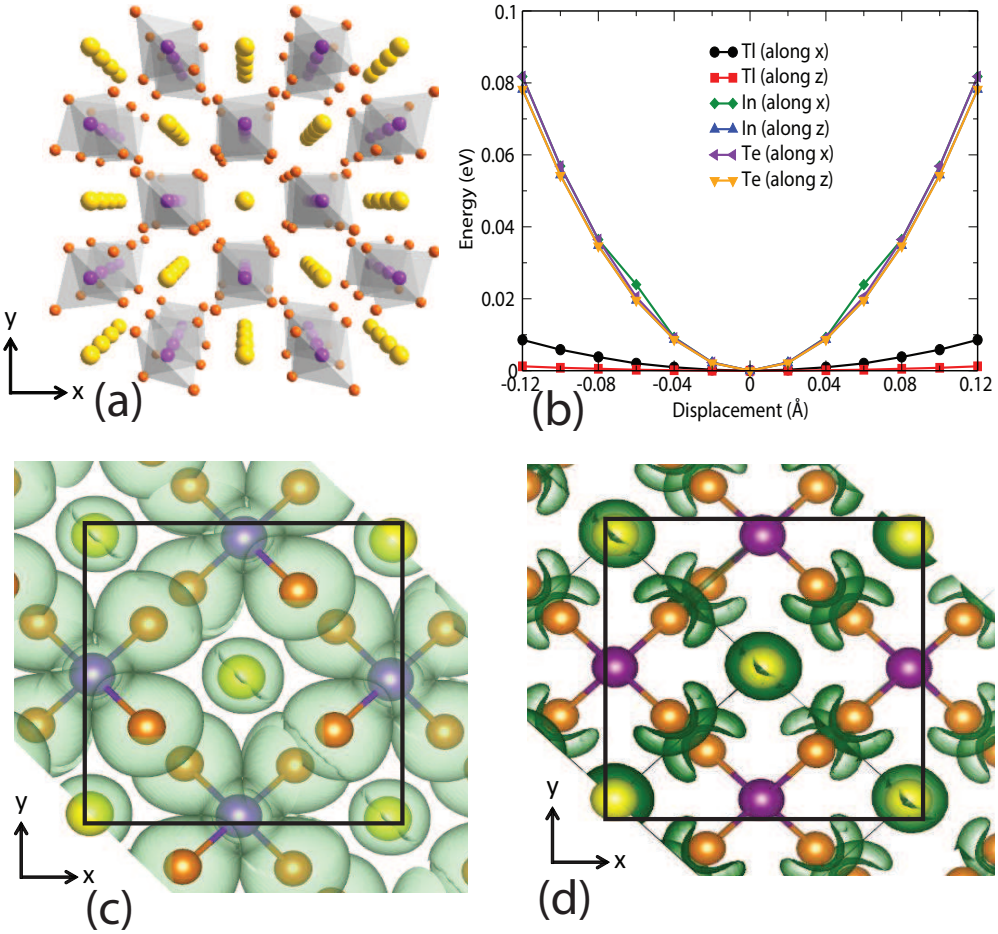

Figure 9.4: (a) Crystal structure of $TlInTe_2$ showing the anionic chains of covalently bound $(InTe_4)_n$ tetrahedra interlocked with cationic chains of Tl atoms. Yellow, violet and orange atoms denote Tl, In and Te atoms, respectively. (b) Calculated potential energy vs. displacements along crystallographic x- and z- directions of conventional tetragonal unit cell. (c) Total charge density and (d) electron localization function (ELF) of $TlInTe_2$.

$TlInTe_2$ has a tetragonal chain-like crystal structure (space group: I4/mcm, No. 140) (Fig. 9.4(a)) similar to that of InTe [201]. Its crystal structure constitutes anionic $(InTe_2)_n^{-n}$ chains alternating with chains of Tl^+ cations (Fig. 9.4(a)). Each In makes four covalent (sp^3) bonds with four Te atoms forming tetrahedrons; the latter share their horizontal edges to form anionic chains along the crystallographic c-axis. Each Tl is surrounded by

eight Te atoms (of the anionic substructure) in a distorted square antiprismatic arrangement forming skewed cages referred to as Thompson cubes. The latter share square-faces along the c-axis forming cationic chains. $TlInTe_2$ can be viewed structurally analogous to 1D Zintl compounds such as Ca_3AlSb_3, $Ca_5Al_2Sb_6$ and Sr_3GaSb_3 constituting 1D anionic chains. The latter exhibit low thermal conductivities owing to complex unit cells (26-56 atoms per unit cell). It is noted that $TlInTe_2$, with only 16 atoms in its conventional unit cell, is simple relative to the aforementioned 1D Zintl compounds yet exhibits low κ_l ($\sim$ 0.5 W/m.K at 300 K) owing to its distinct lattice dynamics.

9.2.3 Computational details

Our first-principles calculations are based on density functional theory (DFT) using Quantum ESPRESSO (QE) code [112]. It uses plane wave basis to represent wavefunctions and charge density, and pseudopotentials to capture the effect of potential arising from the nucleus and core electrons of an atom. We used norm-conserving pseudopotentials in our calculations. We treated the exchange and correlation energy of the electrons with a generalized gradient approximated (GGA) [113] functional as parametrized by Perdew, Burke and Ernzerhof [114]. The expansion of electronic wave function and charge density in plane wave basis was truncated with cut-off energies of 60 Ry and 240 Ry, respectively. Brillouin Zone (BZ) integrations were sampled on a uniform mesh of 8×8×8 k-points. The discontinuity in the occupations number of electronic states near the gap was smeared with Fermi-Dirac distribution functions with a broadening of k_BT = 0.003 Ry. Fully optimized lattice constants (a=8.44 Å, c=7.14 Å) of $TlInTe_2$ agree quite well with that of its experimental values (a=8.478 Å, c=7.185 Å). We determined electronic structure and lattice dynamical properties at the optimized crystal structure of $TlInTe_2$. We used QE implementation of density functional perturbation theory (DFPT) [64] to obtain phonon dispersion of $TlInTe_2$. In this, the interatomic force constant matrices were first obtained on a 2×2×2 mesh of q-points in the BZ, and were Fourier interpolated at an arbitrary q-vector. Gruneissen parameter (γ) measures the degree of anaharmonicity of phonons in

a material. We estimated γ of each of the phonon modes using finite difference formula and taking phonon dispersion calculated at two volumes (V_0 and $0.96V_0$, V_0 being the equilibrium volume at 0 GPa).

9.2.4 Theoretical analysis

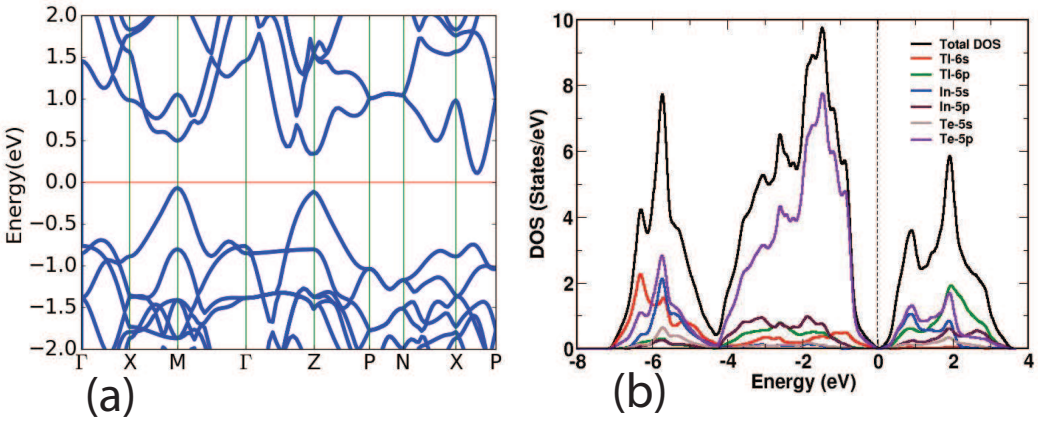

Figure 9.5: Electronic structure and orbital projected density of states of $TlInTe_2$.

Electronic structure of $TlInTe_2$ calculated at its optimized lattice constant reveals a direct band gap of 0.5 eV at the Z-point and an indirect band gap of 0.12 eV between the valence band maximum (VBM) and conduction band minimum (CBM) appearing at M point and along X-P lines respectively in the Brillouin zone (see Fig. 9.5(a)). As $TlInTe_2$ consists of rigid and weakly bound substructures, we expect the chemical bonding in $TlInTe_2$ to be different from solids with crystallographic homogeneity. We have examined the bonding environments in $TlInTe_2$ with the aid of real-space descriptors such as electronic charge density and electron localization function (ELF) calculated using the DFT. The calculated total charge density of $TlInTe_2$ reveals overlapping charge densities of In and Te atoms within the $InTe_4$ tetrahedra signifying a strong covalent bonding between them (Fig. 9.4(c)). On the other hand, the more electropositive Tl is surrounded by non-overlapping, nearly spherical charge density due to $6s^2$ electron lone-pair of Tl (Fig. 9.4(c)) implying the interaction between Tl and the surrounding Te atoms to be electrostatic in nature. ELF estimates the degree of electron localization in a molecule

or solid taking into account, the local influence of the Pauli repulsion. As seen from the ELF map shown in Fig. 9.4(d), a spherical electron localization around Tl is due to its $6s^2$ lone-pair, whereas a lobe-shaped asymmetrically distributed electron cloud around Te arises from the $5s^2$ lone-pair of Te, partially hybridized as permitted by its site symmetry. The calculated electronic density of states (DOS) shows the contribution of Tl-6s orbital to the valence band near the Fermi level (Fig. 9.5(b)). Besides, there is an overlap between Tl-6s and Te-5p orbitals indicating the interaction between respective electronic clouds. The hierarchical chemical bonds and lone-pairs in $TlInTe_2$ play an important role in causing low lattice thermal conductivity as discussed below.

Directions	v_{TA1} (m/s)	v_{TA2} (m/s)	v_{LA} (m/s)
Γ-X	1009	1042	2222
Γ-Z	1166	1166	2648
Γ-M	1105	1158	2195
Average	1093	1122	2355

Table 9.2: Sound velocities corresponding to the three acoustic branches of $TlInTe_2$ along different high symmetry directions in the Brillouin zone. TA and LA stand for transverse and longitudinal acoustic modes, respectively.

To get an insight into atomic-level dynamics, we have calculated the potential energy curves by displacing the atoms away from their static equilibrium positions along the x- and z-directions. It is clearly seen from Fig. 9.4(b) that In and Te atoms are confined in steep potential wells whereas Tl atom is located in a flat potential well suggesting that Tl atoms can easily vibrate within hollow Thompson cages with large amplitudes, especially along the z-axis. The flat potential well of Tl is consistent with its large atomic displacement parameters (ADPs) measured experimentally by our experimental collaborators. Hence, the low-energy optical modes associated with the Tl atoms can scatter the heat-carrying acoustic phonons, thereby reducing low κ_l. The electrostatic repulsion between the localized electron clouds on Tl and the surrounding Te-atoms plausibly drives large displacements of Tl and hence, large ADPs along the crystallographic z-axis.

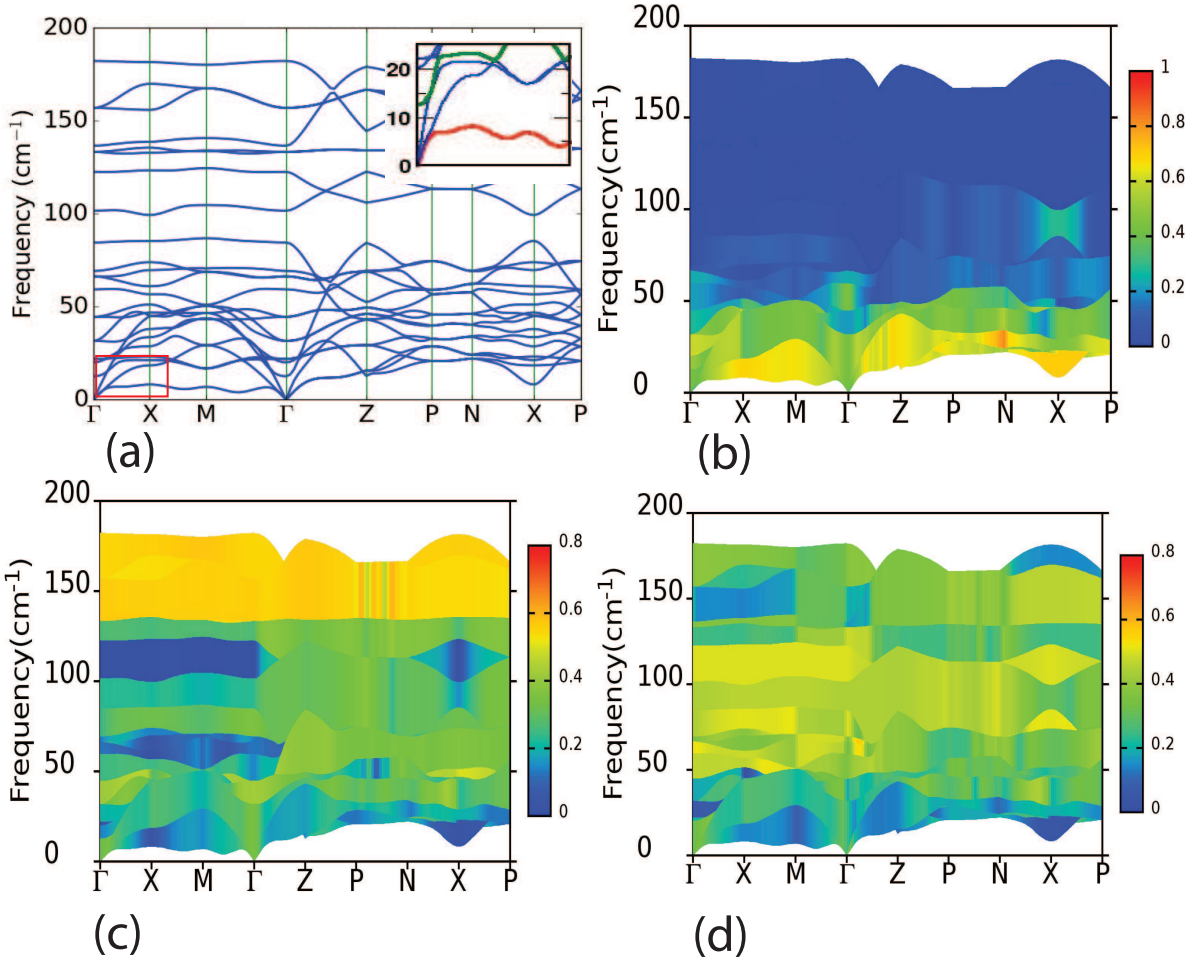

Figure 9.6: (a) Full phonon dispersion and (b) atom projected phonon dispersion of $TlInTe_2$ showing contributions coming from Tl atoms (b), In atoms (c) and Te atoms (d). Vibrations of Tl atoms govern the low frequency modes as well as the rattling motions of Tl atoms along z-direction. The region within the red box in (a) is zoomed in the inset, where a large avoided-crossing is clearly evident between the phonon branches highlighted with red and green colors.

The calculated phonon dispersion in Fig. 9.6(a) exhibits several low-frequency optical phonon modes starting from 12.4 cm^{-1} at the Γ-point and dispersing to higher frequencies along high symmetry directions in the Brillouin zone. A striking feature of the phonon dispersion of $TlInTe_2$ is the presence of a non-dispersive branch along Γ-X-M-Γ path (Fig. 9.6(a)). The corresponding atomic displacements viewed at the Γ, and along Γ-X, X-M and M-Γ directions essentially constitute large-amplitude coherent vibration of Tl atoms along the crystallographic z-axis (see Fig. 9.8). The abrupt shift in the slope of this branch beyond the Γ-point is a signature of optic-acoustic coupling which is evident from

the large avoided-crossing feature in the phonon dispersion (see inset of Fig. 9.6(a)). The cut-off frequencies of acoustic phonons lie below 25 cm^{-1}, hence the average sound velocities are quite low (see Table 9.2) which helps in inducing an ultralow κ_l in $TlInTe_2$. It is clearly seen from the atom-projected phonon DOS (see Fig. 9.6 and also Fig. 9.7(a)) that the dominant contribution to phonon DOS in the low-energy region (< 50 cm^{-1}) comes from Tl atom further indicating that the low-energy phonons are mainly dictated by Tl-vibrations. The lowest optical phonon at 12.4 cm^{-1} is in reasonable agreement with the lowest Einstein mode ($\theta_E = 24.8$ K) as measured by our experimental collaborators. It is also lower than the lowest optical phonon in low-κ_l α-MgAgSb (=0.6 W m^1K^1 at 300 K) [273]. In α-MgAgSb, the low-frequency optical phonons arise from weak multicenter bonding interactions and reduce the lattice thermal conductivity through resonant phonon scattering. Similar low-frequency optic modes and resonant phonon scattering mechanism have been shown to cause low lattice thermal conductivity in filled-skutterudites, clathrates and Cu-S based chalcogenides [250, 275]. In $TlInTe_2$, the low-frequency optical modes arising from the rattling vibrations of Tl atoms couple with heat-carrying acoustic phonons through symmetry-allowed anharmonic interactions as clearly evident from the avoided-crossing in the phonon dispersion (see inset of Fig. 9.6(a)). Secondly, the non-dispersive nature of optical branch along Γ-X-M-Γ suggests that the coupling exists over broad wavelength-range (see inset of Fig. 9.6(a)). It is thus clear from our first-principles analysis that low-energy optical modes arising from the vibrations of the Tl atoms play an important role in causing low lattice thermal conductivity of $TlInTe_2$.

Grüneisen parameter (γ) quantifies the strength of anharmonicity in a solid. We have determined the k-dispersion of mode Grüneisen parameters (γ_i) for the three lowest branches using phonon dispersions calculated at two different volumes in a finite-difference method (Fig. 9.7(b)). The lowest frequency flat phonon branch shows anomalously high γ_i of 60 along M-Γ path; this large value of γ_i possibly arises from (a) large rattling vibration of Tl atoms and (b) modification of restoring force acting on Tl atoms via electrostatic repulsion between Tl and the surrounding Te atoms. In the high-temperature regime

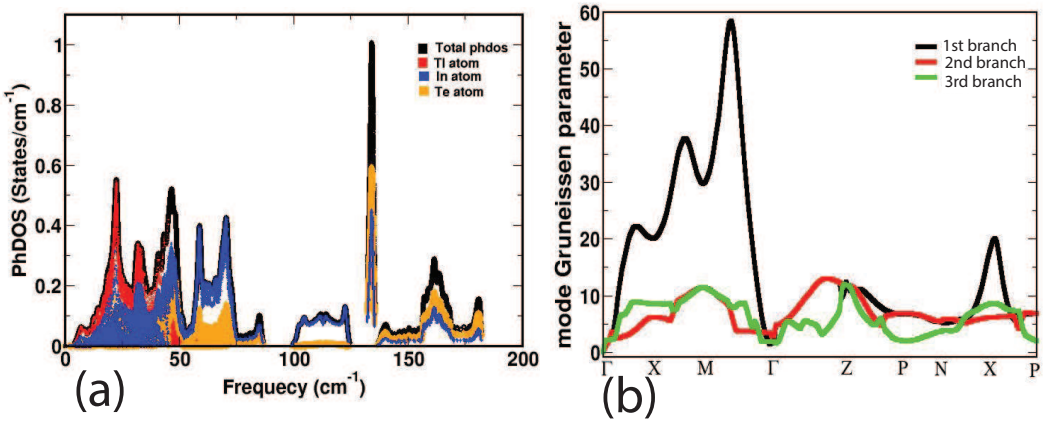

Figure 9.7: (a) Atom projected phonon density of states and (b) Grüneisen parameters (γ_i) for the lowest three phonon branches of $TlInTe_2$. The black line in (b) corresponds to γ_i of the lowest frequency phonon branch *i.e.*, the flat optic phonon branch (rattling mode) which shows anomalously large value of γ_i along M-Γ direction.

where the Umklapp phonon scattering is dominant, κ_l decays as γ_i^2. Therefore, such a high value of γ_i indeed reflects strong anharmonicity and phonon-phonon interactions in $TlInTe_2$ [254] and also asserts the dominant role of single-frequency rattling mode of Tl atoms in the reduction of lattice thermal conductivity of $TlInTe_2$.

9.2.5 Conclusions

In summary, $TlInTe_2$ manifests hierarchical chemical bonding with a rigid covalent framework interlocked with the weakly bound ionic substructure comprising of Tl^+ cations. The latter act as an intrinsic rattlers akin to guest-rattlers in filled-skutterudites. The large displacement of Tl atom along the z-axis is driven by electrostatic repulsion between localized electron clouds around Tl and surrounding Te-atoms. Phonon dispersion of $TlInTe_2$ reveals large optical-acoustic coupling (avoided-crossing) that results in a strongly anharmonic vibration of Tl-cations along the z-axis, which is ineffective of heat-transport. Thus, anharmonic optical-acoustic coupling together with the low sound velocities lead to a very low value of κ_l in $TlInTe_2$.

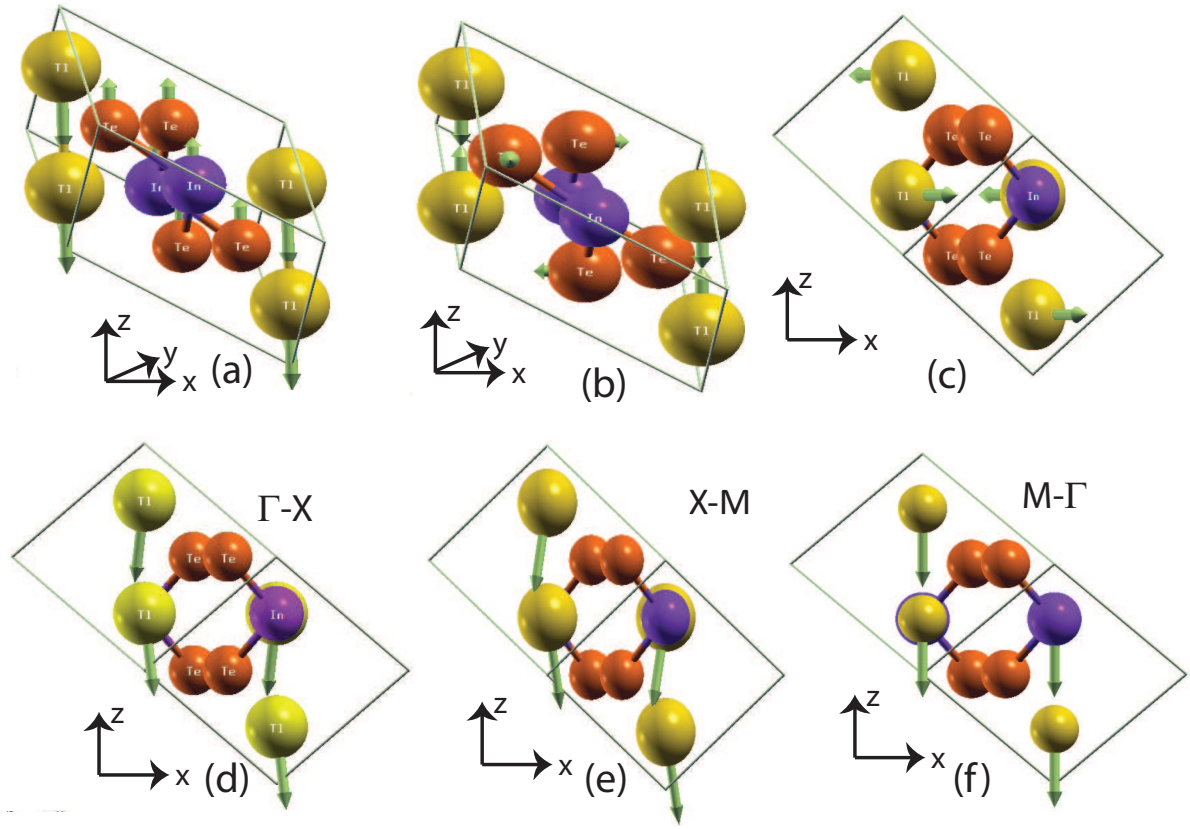

Figure 9.8: Atomic displacements pattern of the lowest three optical phonons at Γ point corresponding to 12.4 cm^{-1} (a), 19.8 cm^{-1} (b), and 21.8 cm^{-1} (c) modes are shown in the primitive unit cell of $TlInTe_2$. Phonon modes associated with the lowest-frequency flat phonon branch, visualized at the mid points of Γ-X line (d), X-M line (e), and M-Γ line (f) showing dominant vibrations of Tl^+ cations parallel to z-axis. Yellow, violet and orange spheres denote Tl, In and Te atoms respectively.

Chapter 10

Summary

The primary focus of this dissertation has been the study of materials with nontrivial electronic topology and their electronic topological transition (ETT) as a function of pressure or strain that tunes the relative strength of spin-orbit coupling, a crucial ingredient for compounds with nontrivial electronic topology. Learning from the physics at the ETT, its origin and associated anomalies in measurable properties of the bulk, we have predicted distinct nontrivial phases of matter belonging to different symmetry and topological classes *e.g.*, strong topological insulator, weak topological insulator, topological Dirac semimetal. We have proposed useful applications based on their exotic properties *e.g.*, strain sensor and valley Hall devices. As many good thermoelectrics are found to be topological insulators, we systematically investigated the thermoelectric properties of topological nontrivial and related materials, uncovering the connection between thermoelectricity and electronic topology.

The nontrivial electronic topology of a topological insulator is encoded into its bulk electronic wavefunctions and it manifests robust metallic state at the surface. Detection of topological insulating phase relies on mapping these topological surface states though angle resolved photo emission spectroscopy (ARPES) which is quite sophisticated and expensive. In part (a) of the 1st chapter of this thesis, we predicted pressure induced

electronic topological transition from band to topological insulating phase in the rhombohedral crystal structure of Sb_2Se_3. We establish vibrational anomalies in Raman spectra of the bulk that signify changes in electronic topology, where an E_g^2 phonon softens unusually and its linewidth exhibits an asymmetric peak at the pressure induced ETT in Sb_2Se_3. Within a four-band model of topological insulators, we show a breakdown of adiabatic approximation due to strongly coupled dynamics of phonons and electrons, and elucidate how nonadiabatic renormalization of phonons constitutes readily measurable bulk signatures of an ETT. This will facilitate efforts to develop topological insulators by modifying a band insulator.

Learning about the effect of spin-orbit coupling (SOC) in inducing topologically nontrivial phase and its tunability with external perturbation such as pressure in part (a) of Chapter 1, we predicted strain induced Z_2 topological insulating phase in β-As_2Te_3 in part (b), which shares the same rhombohedral crystal structure as that of Sb_2Se_3. Using density functional theory, we showed that ETT in β-As_2Te_3 occur at the uniaxial strain ϵ_{zz}=0.05 ($\sim \sigma_{zz}$=1.77 GPa), which passes through a Dirac semi-metallic state with a single Dirac cone in its electronic structure at the Γ point. Based on its electronic structure and phonon dispersion, we proposed ultra-thin films of As_2Te_3 to be promising for use in ultra-thin stress sensors, charge pumps, and thermoelectrics.

In part (c) of the 1st chapter, we revisited the low pressure phase transition in Bi_2Se_3 and clarified that the transition near P_c= 3 GPa is not an electronic topological transition, as there is no change in Z_2 topological invariants of the bulk across P_c. Our first-principles density functional theory calculations capture anomalous changes in its lattice parameters (*e.g.*, a minimum in the c/a ratio) and change in the slope of the Raman active modes at P_c. Hence, we argued that this low pressure transition should better be termed as an iso-structural transition rather than ETT.

So far, experiments on three dimensional topological insulators have mainly focused on

their properties and electronic structure of the surfaces. Measurements of their bulk properties relevant to the electronic topology have remained relatively scarce. Recent experiments on Sb_2Te_3 have revealed an intriguing anomaly in its thermal expansion coefficient along the hexagonal c-axis in the temperature range of 200-250K, with no accompanying signatures in the specific heat. In Chapter 4, using first-principles density functional theoretical analysis, we established that the observed temperature dependent anomalies can be explained with a mechanism of formation of energetically favorable stacking faults above 200 K. As similar anomaly in thermal expansion coefficient is also observed in other chalcogenides (e.g, Bi_2Se_3, Bi_2Te_3) in the same crystal family, the proposed mechanism is applicable for these layered strong topological insulators as well.

Topological Dirac semi-metal (TDSM), a novel quantum state of matter with exotic transport, magnetic, chiral and superconducting properties, has been a subject of intense research in recent years. TDSM is a 3-dimensional analogue of graphene, and is also interesting as a parent to other topological states. Learning from the physics and associated phenomena involved at an ETT in Chapter 1, we found that the transient DSM state is not stable for detailed study and hence, we need to find robust topological Dirac semimetallic state that can be used in devices for practical applications. Using first-principles theoretical analysis, we suggest here (in Chapter 5 & 6) new routes to achieve TDSM state both in centrosymmetric Zintl and non-centrosymmetric half-Heusler compounds through strain engineering. Although half-Heusler (HH) compounds were shown to exhibit rich topological phases, a robust TDSM phase in them is yet to be discovered. In Chapter 5, we presented a generic topological phase diagram of a large family of HH compounds with strained structures maintaining a three-fold symmetry, and discover their highly robust non-centrosymmetric TDSM state. Using an existing, stable half-Heusler LiMgBi as a model system in first-principles theoretical analysis we showed that topological semi-metal, topological Dirac semi-metal, normal and topological insulating states are common to strained structures of these materials which can be realized experimentally through epitaxially grown hetero-structures. Uncovering many half-Heuslers exhibiting

Dirac semi-metallic and other topological states upon epitaxial constraints, our work should open up tremendous possibilities and exciting science of interfaces between TDSM and other topological phases that involve chirality, polarity and topology, and have the potential for novel technologies.

In Chapter 6, we predicted that alkaline earth based Bi_2Mg_2X (X = Mg, Ca, Sr, Ba) Zintl compounds exhibit topologically nontrivial electronic states at ambient conditions. We showed that Bi_2Mg_3 is a topological semimetal, whereas Bi_2Mg_2Ca and Bi_2Mg_2Sr are topological insulators with narrow band gaps. With relatively larger ionic radius of Ba^{2+}, Bi_2Mg_2Ba is a topological Dirac semimetal with linearly dispersed doubly degenerate bands of distinct symmetry crossing at wavevectors (0, 0, $\pm k_0$) that are invariant under three-fold rotational symmetry. From the calculated phonon and electronic spectra, we predicted some of these compounds to exhibit very low lattice thermal conductivity and high Seebeck coefficients, similar to some of the known topological insulators. We believe that our work should stimulate experimental work to realize the tunable topological states in epitaxial films of these Zintl compounds, and guide in exploration of materials with nontrivial electronic topology.

Topological nontrivial phases in insulators can be divided into strong or weak topology depending on their (a) topological indices and (b) appearance of surface states. For a strong topological insulator (STI) (*e.g.*, Bi_2Se_3), Z_2 invariants are ($\nu_0;\nu_1\nu_2\nu_3$= 1;000) and they exhibit gapless metallic states on all surfaces. For a weak topological insulator (WTI), $\nu_0 = 0$ and at least one of the other three indices $\nu_i (i = 1, 2, 3)$ must be 1. The appearance of topological surface states in a WTI depend on specific surface termination unlike strong TI. In Chapter 7, we predicted emergence of weak topological insulating phase in BiSe which consists of a bismuth bilayer (Bi_2) sandwiched between two Bi_2Se_3 quintuple layers. Using first-principles calculations based on density functional theory we showed that even number of band inversions at Γ and A points drive BiSe into weak topological insulating phase. we determined the Z_2 invariants of BiSe, which are (0;001). Calculation of surface states on the (100) side surface reveals an even number of Dirac

points as expected of a WTI, confirming the WTI phase of BiSe.

Materials with good thermoelectric (TE) properties such as Bi_2Te_3 and SnTe have recently come to be known as topological insulators (TIs). It is fundamentally interesting to explore if other materials with nontrivial topology may also exhibit good TE properties. In this work (Chapter 8), we used first-principles density functional theoretical calculations to determine and assess the electronic contribution to the thermoelectric performance of topological insulators (β-As_2Te_3, BiTeCl, PbTe), topological Dirac semimetal (Na_3Bi) and Weyl semimetal (TaAs) and semimetallic YPtBi, belonging to different symmetry and topological classes. We found that multiple sub-band structure, small band gap of a topological insulator, and vicinity to a metallic state associated with an electronic topological transition are responsible for their superior TE performance. In addition, sensitivity of their electronic structure to strain makes their thermoelectric properties highly tunable. Since the spin-orbit coupling is often responsible for nontrivial electronic topology, many of these compounds involve heavy elements, and hence have low elastic moduli and thermal conductivity that further enhance their thermoelectric efficiency. We predicted TaAs to be a promising TE for experimental exploration, and proposed that the thermoelectric modulators based on TIs such as SnTe and PbTe are expected to be more efficient under mechanical load.

An important paradigm in design of materials with high thermoelectric efficiency has been to reduce the lattice thermal conductivity. In Chapter 9, we explained the microscopic mechanism of ultralow lattice thermal conductivity (κ_l) in mixed valence InTe ($In^{+}In^{3+}Te_2^{2-}$) and $TlInTe_2$ ($Tl^{+}In^{3+}Te_2^{2-}$) at room temperature. These compounds share similar crystal structures consisting of rigid anionic and loosely bound cationic substructures showing the characteristics of part-crystalline part-liquid-like materials. We uncovered that the rattling vibrations of the weakly bound cations In^{+} and Tl^{+} in InTe and $TlInTe_2$, respectively, are mainly responsible in the reduction of κ_l through a scattering mechanism. The In^{+} and Tl^{+} atoms act as intrinsic rattlers which scatter the heat carrying acoustic phonons through phonon-phonon interactions. We also found significant

lattice anharmonicity in these compounds, as revealed by the high values of Grüneisen parameters of the localized flat phonon branch relevant to the rattling vibrations. We believe that our work will help in designing materials with improved thermoelectric performance.

Finally, we present a thematic summary of the thesis in Fig. 10, that brings out the commonality and central theme of the topics covered in this dissertation. We have highlighted how electronic topological transition from band to Z_2 topological insulator led us to uncover a plethora of distinct topological phases of matter, and propose devices based on their exotic, often unusual and fascinating properties. Thus, our work should guide experimentalists in the design of these materials in laboratory, tune their properties and make useful devices based on their novel properties.

There is a tremendous scope to take the ideas forward into future work. As TDSMs are newly discovered materials, our work should guide in discovery new TDSMs. Secondly, one can combine topology with other interesting properties like thermoelectricity, and group-IV chalcogenides are attractive systems for this. Finally, the properties of thermoelectric and catalytic activity may have correlation with electronic topology, and are worth deeper investigation.

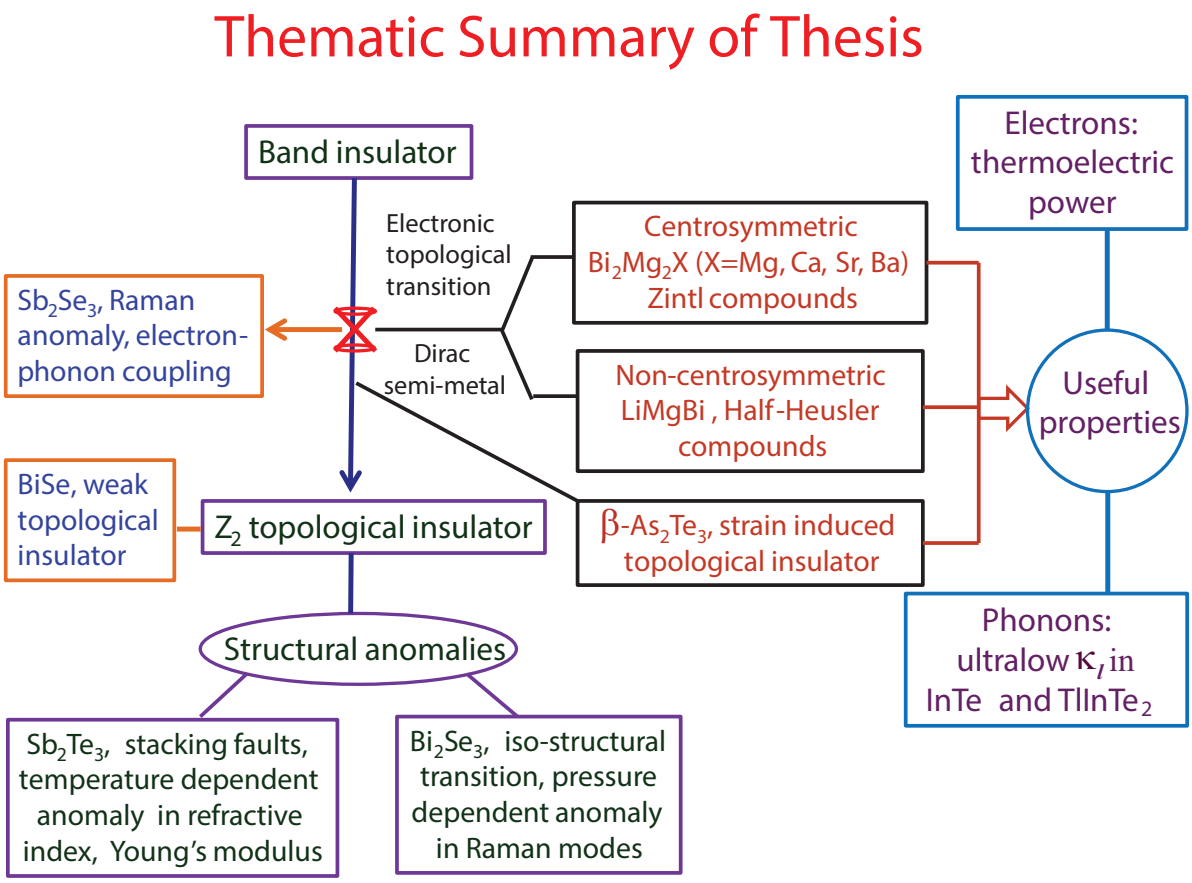

Figure 10.1: A schematic summarizing the ideas and work presented in this thesis.

Bibliography

[1] Y. Nambu and G. Jona-Lasinio, Phys. Rev. **122**, 345 (1961).

[2] P. W. Anderson, Phys. Rev. **130**, 439 (1963).

[3] L. D. Landau and E. M. Lifshitz, *Course of theoretical physics* (Elsevier, Oxford, 2013).

[4] D. C. Tsui, H. L. Stormer, and A. C. Gossard, Phys. Rev. Lett. **48**, 1559 (1982).

[5] R. B. Laughlin, Phys. Rev. Lett. **50**, 1395 (1983).

[6] K. v. Klitzing, G. Dorda, and M. Pepper, Phys. Rev. Lett. **45**, 494 (1980).

[7] F. D. M. Haldane, Phys. Rev. Lett. **61**, 2015 (1988).

[8] B. A. Bernevig and S.-C. Zhang, Phys. Rev. Lett. **96**, 106802 (2006).

[9] H. Zhang *et al.*, Nature Physics **5**, 438 (2009).

[10] Y. Xia *et al.*, Nature Physics **5**, 398 (2009).

[11] H. Lin *et al.*, Phys. Rev. Lett. **105**, 036404 (2010).

[12] Y. L. Chen *et al.*, Phys. Rev. Lett. **105**, 266401 (2010).

[13] N. Marzari *et al.*, Reviews of Modern Physics **84**, 1419 (2012).

[14] A. A. Soluyanov and D. Vanderbilt, Physical Review B **83**, 235401 (2011).

[15] D. Thouless, M. Kohmoto, M. Nightingale, and M. Den Nijs, Physical Review Letters **49**, 405 (1982).

[16] F. Haldane, Physical Review Letters **50**, 1153 (1983).

[17] Q. Niu, D. J. Thouless, and Y.-S. Wu, Physical Review B **31**, 3372 (1985).

[18] D. R. Nelson and J. Kosterlitz, Physical Review Letters **39**, 1201 (1977).

[19] F. Pollmann and A. M. Turner, Physical Review B **86**, 125441 (2012).

[20] B. A. Bernevig and T. L. Hughes, *Topological insulators and topological superconductors* (Princeton University Press, Princeton and Oxford, 2013).

[21] X.-L. Qi and S.-C. Zhang, Rev. Mod. Phys. **83**, 1057 (2011).

[22] M. Ezawa, Y. Tanaka, and N. Nagaosa, Scientific reports **3**, 2790 (2013).

[23] S. Chadov *et al.*, Nature Materials **9**, 541 (2010).

[24] H. Lin *et al.*, Nature Materials **9**, 546 (2010).

[25] Z. Wang *et al.*, Physical Review B **85**, 195320 (2012).

[26] B. Lv *et al.*, Physical Review X **5**, 031013 (2015).

[27] H. Li *et al.*, Nature communications **7**, 10301 (2016).

[28] T. Liang *et al.*, Nature Materials **14**, 280 (2015).

[29] J. Xiong *et al.*, Science **350**, 413 (2015).

[30] S. Nadj-Perge *et al.*, Science **346**, 602 (2014).

[31] K. v. Klitzing, G. Dorda, and M. Pepper, Phys. Rev. Lett. **45**, 494 (1980).

[32] C. L. Kane and E. J. Mele, Phys. Rev. Lett. **95**, 226801 (2005).

[33] D. J. Thouless, M. Kohmoto, M. P. Nightingale, and M. den Nijs, Phys. Rev. Lett. **49**, 405 (1982).

[34] K. S. Novoselov *et al.*, science **306**, 666 (2004).

[35] Z. Qiao *et al.*, Phys. Rev. Lett. **112**, 116404 (2014).

[36] C.-Z. Chang *et al.*, Nature Materials **14**, 473 (2015).

[37] C. L. Kane and E. J. Mele, Phys. Rev. Lett. **95**, 146802 (2005).

[38] M. König *et al.*, Science **318**, 766 (2007).

[39] Z. Ringel, Y. E. Kraus, and A. Stern, Physical Review B **86**, 045102 (2012).

[40] Y. Ran, Y. Zhang, and A. Vishwanath, Nature Physics **5**, 298 (2009).

[41] R. S. Mong, J. H. Bardarson, and J. E. Moore, Physical Review Letters **108**, 076804 (2012).

[42] C.-X. Liu, X.-L. Qi, and S.-C. Zhang, Physica E: Low-dimensional Systems and Nanostructures **44**, 906 (2012).

[43] L. Fu, Physical Review Letters **106**, 106802 (2011).

[44] T. H. Hsieh *et al.*, Nature communications **3**, 982 (2012).

[45] P. Dziawa *et al.*, Nature Materials **11**, 1023 (2012).

[46] S. M. Young *et al.*, Physical Review Letters **108**, 140405 (2012).

[47] Z. Liu *et al.*, Science **343**, 864 (2014).

[48] X. Wan, A. M. Turner, A. Vishwanath, and S. Y. Savrasov, Physical Review B **83**, 205101 (2011).

[49] H. Weng *et al.*, Physical Review X **5**, 011029 (2015).

[50] S.-Y. Xu *et al.*, Science advances **1**, e1501092 (2015).

[51] S.-Y. Xu *et al.*, Preprint at http://arxiv. org/abs/1504.01350 (2015).

[52] S.-M. Huang *et al.*, arXiv:1501.00755 (2015).

[53] M. Franz and L. Molenkamp, *Topological Insulators* (Elsevier, Amsterdam, 2013), Vol. 6.

[54] F. Wilczek and A. Zee, Phys. Rev. Lett. **52**, 2111 (1984).

[55] M. Gradhand *et al.*, Journal of Physics: Condensed Matter **24**, 213202 (2012).

[56] L. Fu, C. L. Kane, and E. J. Mele, Physical Review Letters **98**, 106803 (2007).

[57] L. Fu and C. L. Kane, Phys. Rev. B **74**, 195312 (2006).

[58] R. Yu *et al.*, Physical Review B **84**, 075119 (2011).

[59] B. Yan, L. Müchler, and C. Felser, Physical Review Letters **109**, 116406 (2012).

[60] V. S. Mathur and S. Singh, *Concepts in quantum mechanics* (CRC Press, Boca Raton, 2008).

[61] B. H. Bransden and C. J. Joachain, *Quantum mechanics* (Pearson Education, London, 2000).

[62] A. Mildred, S. Dresselhaus, and G. Dresselhaus, Group theory: application to the physics of condensed matter, 2008.

[63] M. Born and R. Oppenheimer, Annalen der Physik **389**, 457 (1927).

[64] S. Baroni, S. De Gironcoli, A. Dal Corso, and P. Giannozzi, Reviews of Modern Physics **73**, 515 (2001).

[65] J. Bhattacharjee and U. V. Waghmare, Physical Review B **71**, 045106 (2005).

[66] S. Pisana *et al.*, Nature Materials **6**, 198 (2007).

[67] R. P. Feynman, Physical Review **56**, 340 (1939).

[68] J. Kohanoff, *Electronic structure calculations for solids and molecules: theory and computational methods* (Cambridge University Press, Cambridge, 2006).

[69] P. Hohenberg and W. Kohn, Phys. Rev. B **136**, 864 (1964).

[70] W. Khon and L. Sham, Phys. Rev **140**, A1133 (1965).

[71] L. H. Thomas, in *Mathematical Proceedings of the Cambridge Philosophical Society* (Cambridge University Press, Cambridge, 1927), No. 05, pp. 542–548.

[72] E. Fermi, Rend. Accad. Naz. Lincei **6**, 32 (1927).

[73] P. A. M. Dirac, in *Proc. Cambridge Philos. Soc* (Cambridge Philosophical Society, Cambridge, 1931), Vol. 26, pp. 376–385.

[74] E. Wigner, Transactions of the Faraday Society **34**, 678 (1938).

[75] J. Slater, Physical Review **51**, 846 (1937).

[76] C. Herring, Physical Review **57**, 1169 (1940).

[77] J. C. Phillips and L. Kleinman, Physical Review **116**, 287 (1959).

[78] O. K. Andersen, Physical Review B **12**, 3060 (1975).

[79] J. C. Slater, Physical Review **81**, 385 (1951).

[80] R. M. Martin, *Electronic structure: basic theory and practical methods* (Cambridge university press, Cambridge, 2004).

[81] A. Dal Corso and A. M. Conte, Physical Review B **71**, 115106 (2005).

[82] P. Novák *et al.*, Physical Review B **63**, 235114 (2001).

[83] A. MacDonald, W. Picket, and D. Koelling, Journal of Physics C: Solid State Physics **13**, 2675 (1980).

[84] S. Baroni, P. Giannozzi, and A. Testa, Physical Review Letters **58**, 1861 (1987).

[85] S. Baroni, P. Giannozzi, and A. Testa, Physical Review Letters **59**, 2662 (1987).

[86] G. H. Wannier, Physical Review **52**, 191 (1937).

[87] W. Kohn, Physical Review **115**, 809 (1959).

[88] J. Des Cloizeaux, Physical Review **129**, 554 (1963).

[89] N. Marzari and D. Vanderbilt, Physical Review B **56**, 12847 (1997).

[90] R. King-Smith and D. Vanderbilt, Physical Review B **47**, 1651 (1993).

[91] R. Resta, Reviews of Modern Physics **66**, 899 (1994).

[92] G. Mahan and J. Sofo, Proceedings of the National Academy of Sciences **93**, 7436 (1996).

[93] J. Yang *et al.*, Advanced Functional Materials **18**, 2880 (2008).

[94] G. K. Madsen and D. J. Singh, Computer Physics Communications **175**, 67 (2006).

[95] A. Bera *et al.*, Physical Review Letters **110**, 107401 (2013).

[96] J. E. Moore, Nature **464**, 194 (2010).

[97] M. Z. Hasan and C. L. Kane, Reviews of Modern Physics **82**, 3045 (2010).

[98] D. Culcer, Physica E: Low-dimensional Systems and Nanostructures **44**, 860 (2012).

[99] A. M. Essin, J. E. Moore, and D. Vanderbilt, Physical Review Letters **102**, 146805 (2009).

[100] A. M. Essin, A. M. Turner, J. E. Moore, and D. Vanderbilt, Physical Review B **81**, 205104 (2010).

[101] J. E. Moore and L. Balents, Physical Review B **75**, 121306 (2007).

[102] K. Rabe and U. Waghmare, Ferroelectrics **136**, 147 (1992).

[103] A. Das *et al.*, Nature nanotechnology **3**, 210 (2008).

[104] W. Zhang *et al.*, New Journal of Physics **12**, 065013 (2010).

[105] A. Polian *et al.*, Physical Review B **83**, 113106 (2011).

[106] R. Vilaplana *et al.*, Physical Review B **84**, 104112 (2011).

[107] R. Vilaplana *et al.*, Physical Review B **84**, 184110 (2011).

[108] B. Li *et al.*, arXiv:1611.04688 (2016).

[109] W. Liu *et al.*, Physical Review B **84**, 245105 (2011).

[110] O. Gomis *et al.*, Physical Review B **84**, 174305 (2011).

[111] A. Bera *et al.*, Journal of Physics: Condensed Matter **28**, 105401 (2016).

[112] P. Giannozzi *et al.*, Journal of physics: Condensed matter **21**, 395502 (2009).

[113] X. Hua, X. Chen, and W. Goddard, Physical Review B **55**, 16103 (1997).

[114] J. P. Perdew, K. Burke, and M. Ernzerhof, Physical Review Letters **77**, 3865 (1996).

[115] C.-X. Liu *et al.*, Physical Review B **82**, 045122 (2010).

[116] M. Lazzeri and F. Mauri, Physical Review Letters **97**, 266407 (2006).

[117] M. Lazzeri *et al.*, Physical review B **73**, 155426 (2006).

[118] K. Pal and U. V. Waghmare, Applied Physics Letters **105**, 062105 (2014).

[119] D. Hsieh *et al.*, Physical Review Letters **103**, 146401 (2009).

[120] L. Fu and C. L. Kane, Physical Review Letters **100**, 096407 (2008).

[121] T. Harman, B. Paris, S. Miller, and H. Goering, Journal of Physics and Chemistry of Solids **2**, 181 (1957).

[122] J. Black, E. Conwell, L. Seigle, and C. Spencer, Journal of Physics and Chemistry of Solids **2**, 240 (1957).

[123] E. Yarembash and E. Vigileva, Russian Journal of Inorganic Chemistry **7**, 1437 (1962).

[124] T. Scheidemantel, J. Meng, and J. Badding, Journal of Physics and Chemistry of Solids **66**, 1744 (2005).

[125] S. Toscani, J. Dugué, R. Ollitrault, and R. Céolin, Thermochimica acta **186**, 247 (1991).

[126] T. Scheidemantel and J. Badding, Solid state communications **127**, 667 (2003).

[127] K. Yang *et al.*, Nature Materials **11**, 614 (2012).

[128] P. Blaha *et al.*, An augmented plane wave+ local orbitals program for calculating crystal properties (2001).

[129] A. Jain *et al.*, Apl Materials **1**, 011002 (2013).

[130] S. M. Young *et al.*, Physical Review B **84**, 085106 (2011).

[131] M. Endo, S. Iijima, and M. S. Dresselhaus, *Carbon nanotubes* (Elsevier, Amsterdam, 2013).

[132] P. Ghaemi, R. S. Mong, and J. E. Moore, Physical Review Letters **105**, 166603 (2010).

[133] Z. Fan, J. Zheng, H.-Q. Wang, and J.-C. Zheng, Nanoscale Research Letters **7**, 1 (2012).

[134] Y. Saeed, N. Singh, and U. Schwingenschlögl, Applied Physics Letters **104**, 033105 (2014).

[135] Y. Yang *et al.*, Applied Physics Letters **99**, 182101 (2011).

[136] Y. Wang *et al.*, Physical Review Letters **107**, 207602 (2011).

[137] H. Steinberg, D. R. Gardner, Y. S. Lee, and P. Jarillo-Herrero, Nano Letters **10**, 5032 (2010).

[138] D. Kim *et al.*, Nature Physics **8**, 459 (2012).

[139] D. Kim *et al.*, Nano Letters **14**, 1701 (2014).

[140] M. Einaga *et al.*, in *Journal of Physics: Conference Series* (IOP Publishing, Bristol, 2010), No. 1, p. 012036.

[141] J. Zhang *et al.*, Proceedings of the National Academy of Sciences **108**, 24 (2011).

[142] A. Das *et al.*, Nature Physics **8**, 887 (2012).

[143] E. Wang *et al.*, Nature Physics **9**, 621 (2013).

[144] S. V. Ovsyannikov *et al.*, Journal of Applied Physics **104**, 053713 (2008).

[145] J. Hamlin *et al.*, Journal of Physics: Condensed Matter **24**, 035602 (2011).

[146] I. Lifshitz *et al.*, Sov. Phys. JETP **11**, 1130 (1960).

[147] G. Sosso, S. Caravati, and M. Bernasconi, Journal of Physics: Condensed Matter **21**, 095410 (2009).

[148] S. Nakajima, Journal of Physics and Chemistry of Solids **24**, 479 (1963).

[149] W. Richter and C. Becker, physica status solidi (b) **84**, 619 (1977).

[150] H. Köhler and C. R. Becker, Physica Status Solidi (b) **61**, 533 (1974).

[151] G. Liu *et al.*, The Journal of Physical Chemistry C **117**, 10045 (2013).

[152] J. Zhao *et al.*, Journal of Physics: Condensed Matter **25**, 125602 (2013).

[153] I. Nechaev *et al.*, Physical Review B **87**, 121111 (2013).

[154] Y. Zhang *et al.*, Nature Physics **6**, 584 (2010).

[155] T. Förster, P. Krüger, and M. Rohlfing, Physical Review B **92**, 201404 (2015).

[156] K. L. Wang, M. Lang, and X. Kou, in *Handbook of Spintronics*, edited by Y. Xu, D. D. Awschalom, and J. Nitta (Springer Netherlands, Dordrecht, 2016), pp. 431–462.

[157] Y. Chen *et al.*, Science **325**, 178 (2009).

[158] P. Dutta *et al.*, Applied Physics Letters **100**, 251912 (2012).

[159] X. Chen *et al.*, Applied Physics Letters **99**, 261912 (2011).

[160] L. Ping-Yuan *et al.*, Acta Phys. Sin. **63**, 11730 (2014).

[161] Y. Kim *et al.*, Applied Physics Letters **100**, 071907 (2012).

[162] H. Dittrich and M. Wohlfahrt-Mehrens, International Journal of Inorganic Materials **3**, 1137 (2001).

[163] C.-Z. Li *et al.*, Nature Communications **6**, 10137 (2015).

[164] L. Aggarwal *et al.*, Nature Materials **15**, 32 (2016).

[165] Z. Liu *et al.*, Nature Materials **13**, 677 (2014).

[166] J. Liu and D. Vanderbilt, Phys Rev B **90**, 155316 (2014).

[167] M. Ezawa, Y. Tanaka, and N. Nagaosa, Scientific Reports **3**, 2790 (2013).

[168] T. Graf, S. S. Parkin, and C. Felser, Magnetics, IEEE Trans **47**, 367 (2011).

[169] Q. Gibson *et al.*, Physical Review B **91**, 205128 (2015).

[170] B.-J. Yang and N. Nagaosa, Nature Communications **5**, 4898 (2014).

[171] H. Nowotny and F. Holub, Monatsh Chem **91**, 877 (1960).

[172] A. Roy, J. W. Bennett, K. M. Rabe, and D. Vanderbilt, Phys Rev Lett **109**, 037602 (2012).

[173] S. Dupke, H. Eckert, F. Winter, and R. Pöttgen, Prog Solid State Chem **42**, 57 (2014).

[174] H. C. Kandpal, C. Felser, and R. Seshadri, J Phys D: Appl Phys **39**, 776 (2006).

[175] A. Belsky, M. Hellenbrandt, V. L. Karen, and P. Luksch, Acta Cryst Sec B: Struct Sci **58**, 364 (2002).

[176] D. Xiao *et al.*, Phys Rev Lett **105**, 096404 (2010).

[177] D. Gresch *et al.*, arXiv preprint arXiv:1610.08983 (2016).

[178] A. A. Mostofi *et al.*, Computer Physics Communications **178**, 685 (2008).

[179] W. Al-Sawai *et al.*, Physical Review B **82**, 125208 (2010).

[180] X. Wang *et al.*, Phys Lett A **378**, 1662 (2014).

[181] S. Zaheer *et al.*, Physical Review B **87**, 045202 (2013).

[182] Z. Zhu *et al.*, Physical Review X **6**, 031003 (2016).

[183] C. Shi *et al.*, Phys Stat Solid (b) **252**, 357 (2015).

[184] A. Bansil, H. Lin, and T. Das, Reviews of Modern Physics **88**, 021004 (2016).

[185] H. Zhang and S.-C. Zhang, Physica Status Solidi (RRL)-Rapid Research Letters **7**, 72 (2013).

[186] B. Yan *et al.*, Euro Physics Letters **90**, 37002 (2010).

[187] K. Kuroda *et al.*, Physical Review Letters **105**, 146801 (2010).

[188] H. B. Nielsen and M. Ninomiya, Nuclear Physics B **185**, 20 (1981).

[189] Z. Wang *et al.*, Physical Review B **88**, 125427 (2013).

[190] J. Chang, L. F. Register, S. K. Banerjee, and B. Sahu, Physical Review B **83**, 235108 (2011).

[191] E. Zintl and E. Husemann, Phys. Chem. Abt **B21**, 138 (1933).

[192] K. Deller and Z. Eisemann, Z. Naturforsch B **32b**, 612 (1977).

[193] C. Zheng, R. Hoffmann, R. Nesper, and H. G. Von Schnering, Journal of the American Chemical Society **108**, 1876 (1986).

[194] A. F. May *et al.*, Inorganic Chemistry **50**, 11127 (2011).

[195] Y. Sun *et al.*, Physical Review B **84**, 165127 (2011).

[196] Z. Zhu, M. Li, and J. Li, Physical Review B **94**, 155121 (2016).

[197] K. Pal, S. Anand, and U. V. Waghmare, Journal of Materials Chemistry C **3**, 12130 (2015).

[198] A. Dal Corso, Computational Materials Science **95**, 337 (2014).

[199] G. F. Koster, *Properties of the thirty-two point groups* (The MIT Press, MIT, 1963), Vol. 24.

[200] G. Pikus and G. Bir, J. Wiley, New York (1974).

[201] M. K. Jana, K. Pal, U. V. Waghmare, and K. Biswas, Angewandte Chemie International Edition **55**, 7792 (2016).

[202] E. S. Toberer *et al.*, Dalton Transactions **39**, 1046 (2010).

[203] X.-J. Wang *et al.*, Applied Physics Letters **94**, 092106 (2009).

[204] S. M. Kauzlarich, S. R. Brown, and G. J. Snyder, Dalton Transactions 2099 (2007).

[205] J. Shuai *et al.*, Proceedings of the National Academy of Sciences **113**, E4125 (2016).

[206] B. Poudel *et al.*, Science **320**, 634 (2008).

[207] R. Roy, Physical Review B **79**, 195322 (2009).

[208] K.-I. Imura, Y. Takane, and A. Tanaka, Physical Review B **84**, 035443 (2011).

[209] Y. Yoshimura, A. Matsumoto, Y. Takane, and K.-I. Imura, Physical Review B **88**, 045408 (2013).

[210] P. Tang *et al.*, Physical Review B **89**, 041409 (2014).

[211] B. Rasche *et al.*, Nature Materials **12**, 422 (2013).

[212] T. Valla *et al.*, Physical Review B **86**, 241101 (2012).

[213] S. Murakami, Physical Review Letters **97**, 236805 (2006).

[214] F. Yang *et al.*, Physical Review Letters **109**, 016801 (2012).

[215] Z. Liu *et al.*, Physical Review Letters **107**, 136805 (2011).

[216] H. J. Choi *et al.*, Nature **418**, 758 (2002).

[217] K. Govaerts *et al.*, Physical Review B **90**, 155124 (2014).

[218] X. He *et al.*, Physical Review Letters **110**, 156101 (2013).

[219] M. Wada, S. Murakami, F. Freimuth, and G. Bihlmayer, Physical Review B **83**, 121310 (2011).

[220] G. J. Snyder and E. S. Toberer, Nature Materials **7**, 105 (2008).

[221] D. Kraemer *et al.*, Nature Materials **10**, 532 (2011).

[222] T. M. Tritt and M. Subramanian, MRS bulletin **31**, 188 (2006).

[223] H. Böttner, G. Chen, and R. Venkatasubramanian, MRS bulletin **31**, 211 (2006).

[224] G. Wiedemann and R. Franz, Ann. Phys. Chem **165**, 497 (1853).

[225] M. Cutler and N. F. Mott, Physical Review **181**, 1336 (1969).

[226] J. P. Heremans *et al.*, Science **321**, 554 (2008).

[227] P. Barone *et al.*, Physical Review B **88**, 045207 (2013).

[228] L. Müchler *et al.*, Physica Status Solidi (RRL)-Rapid Research Letters **7**, 91 (2013).

[229] X. Chen, D. Parker, and D. J. Singh, arXiv preprint arXiv:1310.5547 (2013).

[230] A. Banik *et al.*, Chemistry of Materials **27**, 581 (2015).

[231] Y. Pei *et al.*, Nature **473**, 66 (2011).

[232] G. Tan *et al.*, Journal of the American Chemical Society **136**, 7006 (2014).

[233] Y. Xu, Z. Gan, and S.-C. Zhang, Physical Review Letters **112**, 226801 (2014).

[234] M. König *et al.*, Science **318**, 766 (2007).

[235] J.-B. Vaney *et al.*, Advanced Electronic Materials **1**, (2015).

[236] T. Scheidemantel *et al.*, Physical Review B **68**, 125210 (2003).

[237] G. K. Madsen, Journal of the American Chemical Society **128**, 12140 (2006).

[238] L. Chaput, P. Pécheur, J. Tobola, and H. Scherrer, Physical Review B **72**, 085126 (2005).

[239] X. Gao *et al.*, Physical Review B **72**, 125202 (2005).

[240] C. Uher *et al.*, Physical Review B **59**, 8615 (1999).

[241] Q. Shen *et al.*, Applied Physics Letters **79**, 4165 (2001).

[242] S. Bhattacharya *et al.*, Applied Physics Letters **81**, 43 (2002).

[243] S. Sakurada and N. Shutoh, Applied Physics Letters **86**, 082105 (2005).

[244] K. Kuroki and R. Arita, Journal of the Physical Society of Japan **76**, 083707 (2007).

[245] J. R. Sootsman, D. Y. Chung, and M. G. Kanatzidis, Angewandte Chemie International Edition **48**, 8616 (2009).

[246] L.-D. Zhao, V. P. Dravid, and M. G. Kanatzidis, Energy & Environmental Science **7**, 251 (2014).

[247] K. Biswas *et al.*, Nature **489**, 414 (2012).

[248] K. Biswas *et al.*, Nature chemistry **3**, 160 (2011).

[249] W. Qiu *et al.*, Proceedings of the National Academy of Sciences **111**, 15031 (2014).

[250] H. Euchner *et al.*, Physical Review B **86**, 224303 (2012).

[251] W. Schweika *et al.*, Physical Review Letters **99**, 125501 (2007).

[252] L. Bjerg, B. B. Iversen, and G. K. Madsen, Physical Review B **89**, 024304 (2014).

[253] D. Morelli, V. Jovovic, and J. Heremans, Physical Review Letters **101**, 035901 (2008).

[254] M. D. Nielsen, V. Ozolins, and J. P. Heremans, Energy & Environmental Science **6**, 570 (2013).

[255] S. N. Guin *et al.*, Energy & Environmental Science **6**, 2603 (2013).

[256] S. N. Guin, V. Srihari, and K. Biswas, Journal of Materials Chemistry A **3**, 648 (2015).

[257] L. Pan, D. Berardan, and N. Dragoe, Journal of the American Chemical Society **135**, 4914 (2013).

[258] S. N. Guin and K. Biswas, Chemistry of Materials **25**, 3225 (2013).

[259] W. Lai, Y. Wang, D. T. Morelli, and X. Lu, Advanced Functional Materials **25**, 3648 (2015).

[260] Y. Dong *et al.*, ChemPhysChem **16**, 3264 (2015).

[261] S. Wang *et al.*, Chemistry of Materials **27**, 1071 (2015).

[262] M. Beekman and G. Nolas, Journal of Materials Chemistry **18**, 842 (2008).

[263] G. Nolas, D. Morelli, and T. M. Tritt, Annual Review of Materials Science **29**, 89 (1999).

[264] J. Hogg and H. Sutherland, Acta Crystallographica Section B: Structural Crystallography and Crystal Chemistry **32**, 2689 (1976).

[265] A. Panich, Journal of Physics: Condensed Matter **20**, 293202 (2008).

[266] Ş. Ellialtioğlu *et al.*, Physical Review B **70**, 195118 (2004).

[267] D. G. Cahill, S. K. Watson, and R. O. Pohl, Physical Review B **46**, 6131 (1992).

[268] X. Shi *et al.*, Journal of the American Chemical Society **133**, 7837 (2011).

[269] T. Takabatake, K. Suekuni, T. Nakayama, and E. Kaneshita, Reviews of Modern Physics **86**, 669 (2014).

[270] H. Liu *et al.*, Nature Materials **11**, 422 (2012).

[271] S. Lee *et al.*, Nature communications **5**, 3525 (2014).

[272] D. Voneshen *et al.*, Nature Materials **12**, 1028 (2013).

[273] P. Ying *et al.*, Advanced Functional Materials **27**, (2017).

[274] L.-D. Zhao *et al.*, Nature **508**, 373 (2014).

[275] H. Liu *et al.*, Journal of Materiomics **2**, 187 (2016).